GA-A15406
UC-77

GAS-COOLED FAST BREEDER REACTOR

QUARTERLY PROGRESS REPORT FOR THE PERIOD FEBRUARY 1, 1979 THROUGH APRIL 30, 1979

by
PROJECT STAFF

Prepared under
Contract DE-AT03-76SF71023
for the San Francisco Operations Office
Department of Energy

GENERAL ATOMIC PROJECT 6114
DATE PUBLISHED: MAY 1979

GENERAL ATOMIC COMPANY

PROGRESS REPORT SERIES

GA-5537	November 1, 1963 through July 31, 1964
GA-6667	August 1, 1964 through July 31, 1965
GA-7645	August 1, 1965 through July 31, 1966
GA-8107	August 1, 1966 through July 31, 1967
GA-8787	August 1, 1967 through July 31, 1968
GA-8895	August 1, 1968 through October 31, 1968
GA-9229	November 1, 1968 through January 31, 1969
GA-9359	February 1, 1969 through April 30, 1969
GA-9639	May 1, 1969 through July 31, 1969
GA-9811	August 1, 1969 through October 31, 1969
GA-9838	November 1, 1969 through January 31, 1970
GA-10517	February 1, 1970 through January 31, 1971
GA-10645	February 1, 1971 through April 30, 1971
GA-A10803	May 1, 1971 through July 31, 1971
GA-A10906	August 1, 1971 through July 31, 1972
GA-A12003	November 1, 1971 through January 31, 1972
GA-A12165	February 1, 1972 through April 30, 1972
GA-A12252	May 1, 1972 through July 31, 1972
GA-A12421	August 1, 1972 through October 31, 1972
GA-A12530	November 1, 1972 through January 31, 1973
GA-A12635	February 1, 1973 through April 30, 1973
GA-A12728	May 1, 1973 through July 31, 1973
GA-A12824	August 1, 1973 through October 31, 1973
GA-A12894	November 1, 1973 through January 31, 1974
GA-A13021	February 1, 1974 through April 30, 1974
GA-A13148	May 1, 1974 through July 31, 1974
GA-A13238	August 1, 1974 through October 31, 1974
GA-A13379	November 1, 1974 through January 31, 1975
GA-A13458	February 1, 1975 through April 30, 1975
GA-A13565	May 1, 1975 through July 31, 1975

GA-A13766	August 1, 1975 through October 31, 1975
GA-A13815	November 1, 1975 through January 31, 1976
GA-A13868	February 1, 1976 through April 30, 1976
GA-A13975	May 1, 1976 through July 31, 1976
GA-A14112	August 1, 1976 through October 31, 1976
GA-A14240	November 1, 1976 through January 31, 1977
GA-A14358	February 1, 1977 through April 30, 1977
GA-A14492	May 1, 1977 through July 31, 1977
GA-A14613	August 1, 1977 through October 31, 1977
GA-A14771	November 1, 1977 through January 31, 1978
GA-A14928	February 1, 1978 through April 30, 1978
GA-A15054	May 1, 1978 through July 31, 1978
GA-A15144	August 1, 1978 through October 31, 1978
GA-A15237	November 1, 1978 through January 31, 1979

ABSTRACT

The tasks of the gas-cooled fast breeder reactor (GCFR) program that are supported by the Department of Energy include development of GCFR fuel, blanket, and control assemblies; development of the pressure equalization system for GCFR fuel; out-of-pile loop facility test programs; fuels and materials development; fuel, blanket, and control rod analyses and development; nuclear analysis and reactor physics for GCFR core design; shielding requirements for the GCFR; reactor engineering to assess the thermal, hydraulic, and structural performance of the core and the core support structure; plant systems control; systems engineering; development of reactor components, including reactor vessel, control and locking mechanisms, fuel handling equipment, core support structure, shielding assemblies, main helium circulator, steam generator, circulator test facility, and auxiliary circulator; development of a helium circulator test facility; reactor safety, environment, and risk analyses, including planning and support of an in-pile and out-of-pile safety test program; nuclear island engineering design; and development of a reliability data bank.

CONTENTS

FIGURES

FIGURES (Continued)

FIGURES (Continued)

FIGURES (Continued)

TABLES

TABLES (Continued)

TABLES (Continued)

1.0. NUCLEAR STEAM SUPPLY SYSTEM

1.11. REACTOR VESSEL SYSTEM

The purpose of this subtask is to design the prestressed concrete reactor vessel (PCRV) and related components which contribute to the integrity of the pressure boundary and to ensure, by analyses and tests, that they meet the design criteria.

As part of the international nuclear energy cooperative effort, review meetings were held during the previous quarter by General Atomic (GA) and Kraftwerk Union (KWU) to develop a common reactor design. During this quarter, a PCRV arrangement was prepared which features an up-flow design as agreed to between GA and KWU (Fig. 1-1). The PCRV configuration was revised to have horizontal cooling ducts as shown in Fig. 1-2, to accommodate redesign of radial shielding. The redesign of radial shielding was required to reduce the irradiation of the liner in the sloped ducts of the previous arrangement.

As part of the up-flow/down-flow core evaluation study, the arrangement of the PCRV for the reference design down-flow core was revised to incorporate the updated designs of reactor core components. The previous reference design PCRV arrangement is shown in Fig. 1-2. The updated PCRV arrangement in Fig. 1-3 incorporates a new core configuration with revised core support structure and radial shielding. In addition, the central cavity and hold-down system were revised, a bayonet-type core auxiliary heat exchanger (CAHE) was incorporated, and a main helium circulator of radial type with electric motor drive was used.

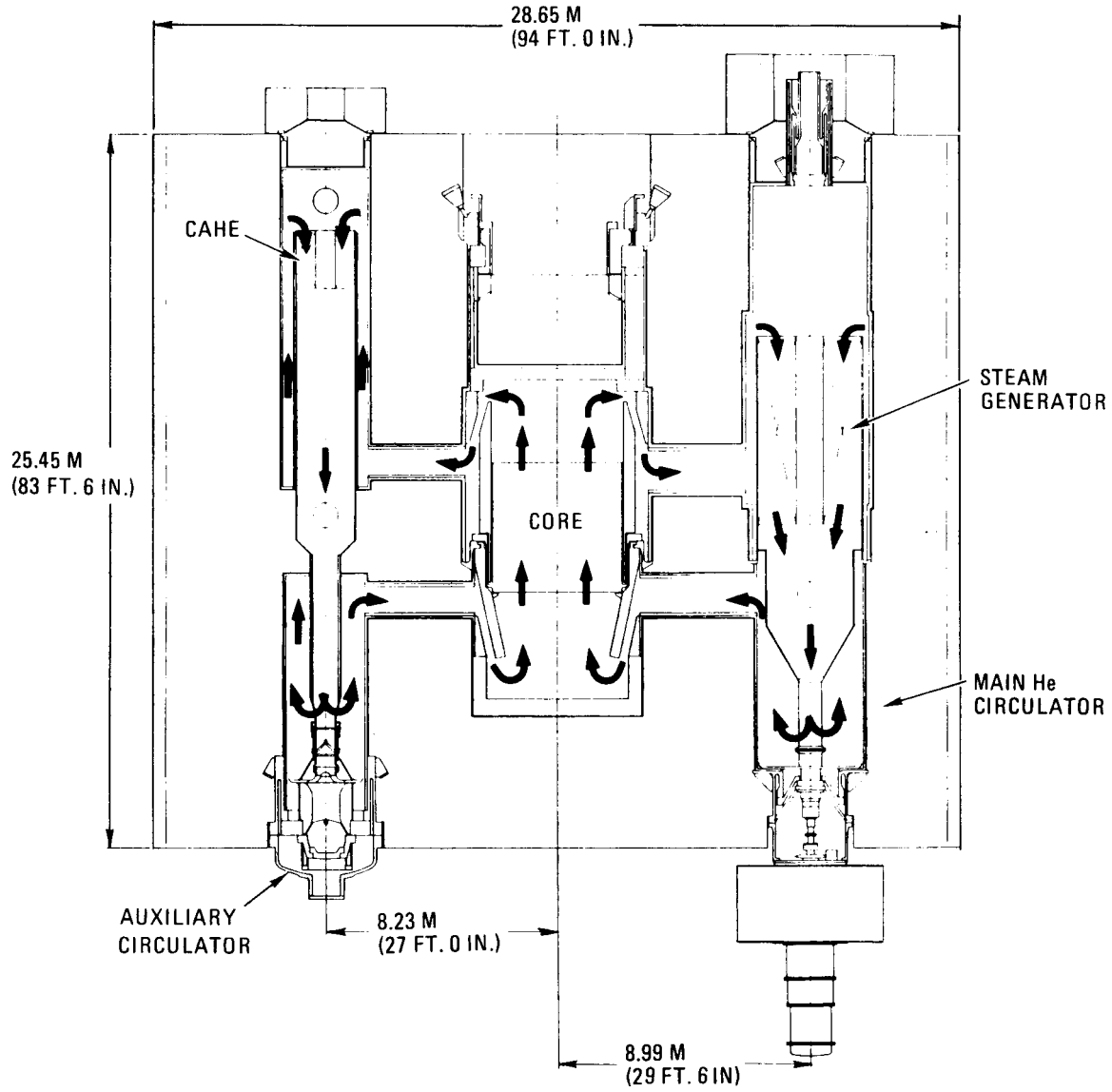

Fig. 1-1. 300-MW(e) GCFR PCRV configuration NEU-D2 (up-flow core)

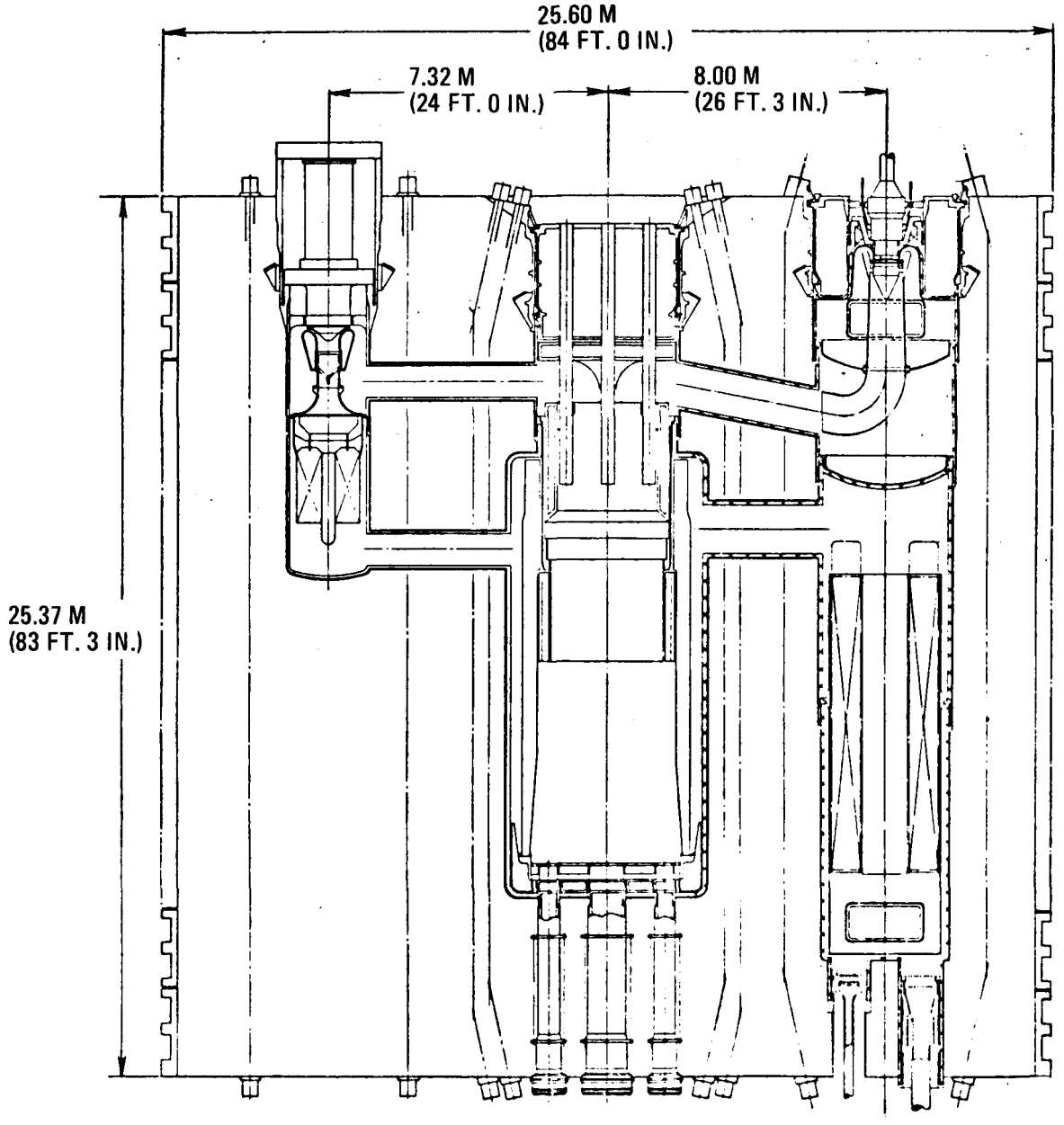

Fig 1-2. 300-MW(e) GCFR PCRV reference design arrangement

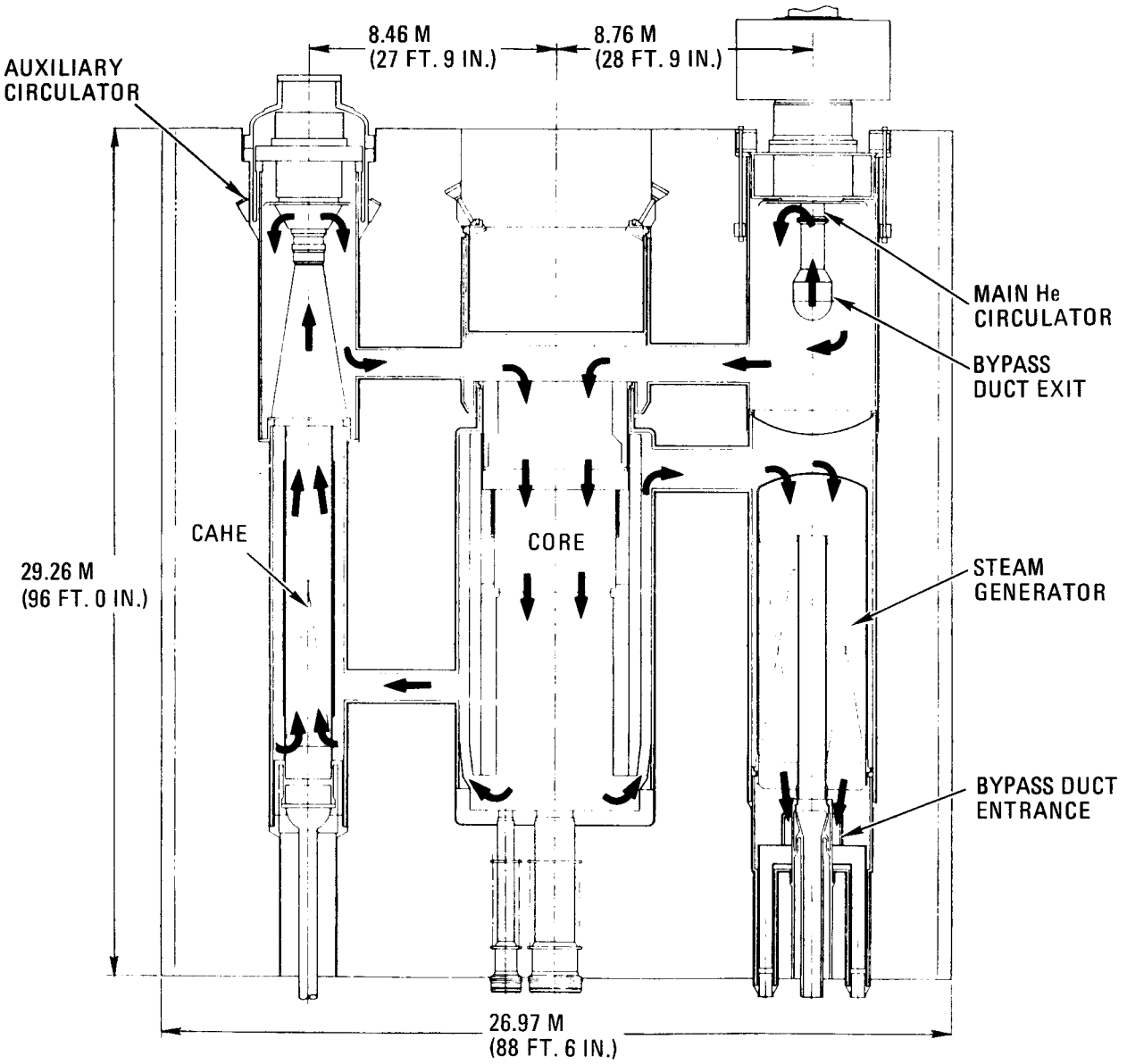

Fig. 1-3. 300-MW(e) GCFR PCRV configuration G-1 (down-flow)

A study to determine the feasibility of incorporating horizontal circulators in the PCRV for a six-loop commercial plant was initiated. The three schemes investigated were:

1. Horizontal circulator located below PCRV bottom head in support structures.

2. Horizontal circulator located in PCRV bottom head with top steam exhaust.

3. Horizontal circulator located in PCRV bottom head with bottom steam exhaust.

All three schemes are thought to be technically feasible. Additional analytical and layout interface studies, which are under way, are required to confirm this conclusion.

Work on liners, penetrations, and closures in support of the up-flow/down-flow decision was completed. From an overall liner viewpoint, the up-flow configuration was preferable except for the rotating plug. Because of problems associated with seals and service lines, the rotating plug design was not considered to be practical, although the design appears feasible. Drawings of the rotating plug arrangement (Fig. 1-4) and method of operation were produced. A tolerance study was performed to determine construction feasibility. The study showed the critical area to be in the gaps between plug, side shielding, and liner. A 2.54-cm (1-in.) gap, which is the maximum permissible from radiation streaming consideration, appears to be adequate. The required tolerances are tighter than desirable but not unrealistic.

A tolerance study was also performed to determine the feasibility of a rotating plug design that used seals on inclined surfaces, as proposed by KWU. A design of that type would be attractive because there are no

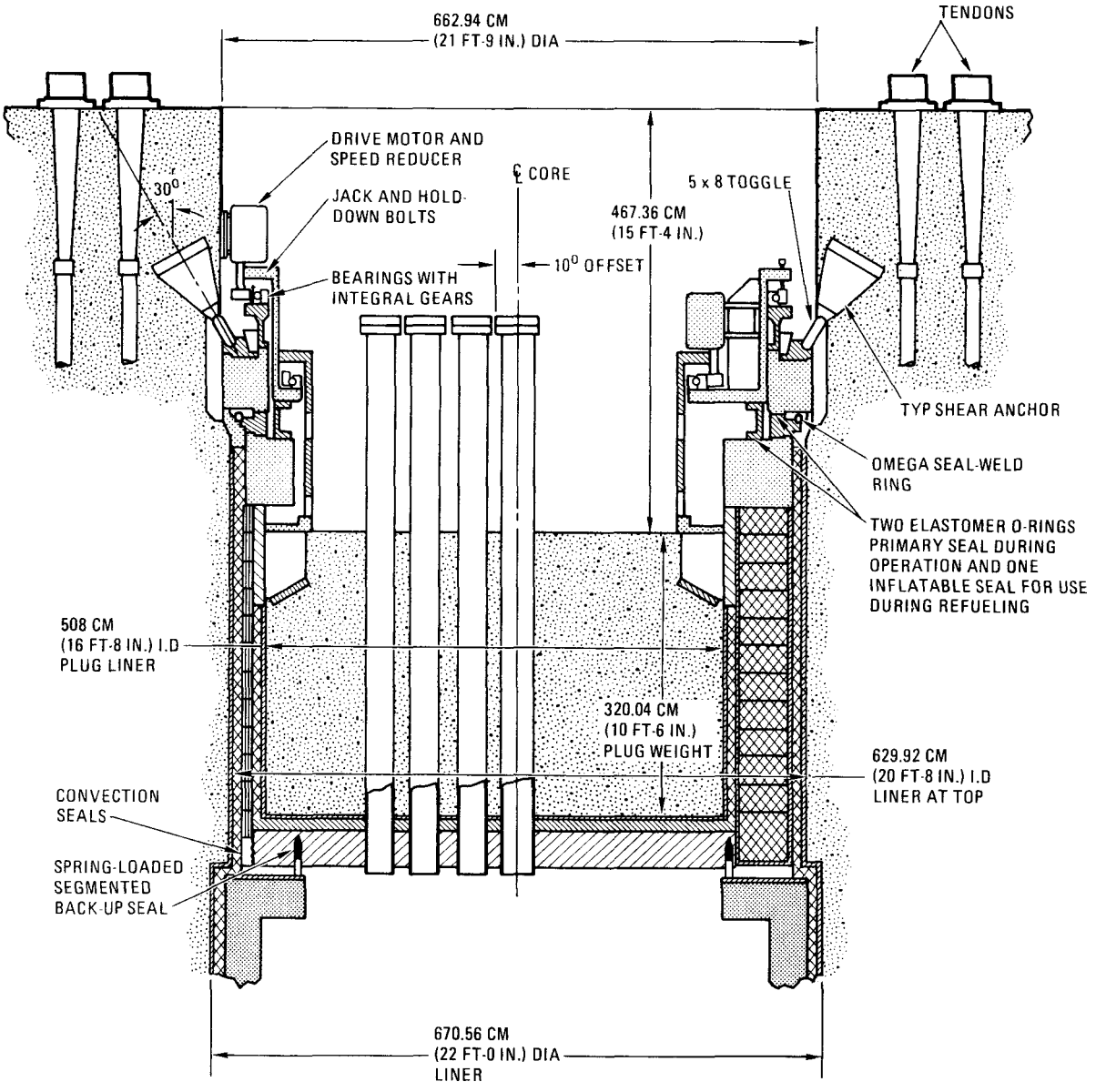

Fig. 1-4. Rotating core closure for GCFR up-flow core

large forgings, and a direct load path from closure to supporting concrete is provided. The study showed that even after field machining of large diameters to relatively small tolerances, potential gaps at O-rings would exceed recommended values by a large factor. To achieve the maximum allowable gaps, it would be necessary to field machine all parts of the plug and liner near the 6.4-m (21-ft) diam sealing surfaces to a tolerance of approximately 0.0051 cm (0.002 in.), and to install all rotating parts to be concentric within approximately 0.01 cm (0.004 in.). Attainment of these tolerances was not considered feasible, and it was concluded that a design using elastomer seals on inclined surfaces is not feasible.

The core cavity closure for the down-flow design was modified to reflect the introduction of a core restraint structure. The restraint structure necessitated the use of removable shielding, which in turn led to a larger closure to accommodate the additional penetrations for the shielding locking mechanisms. The number of penetrations totalled 67, and the plug diameter increased to 5.90 m (19 ft 4 in.). For scalability, a toggle hold-down system similar to that used with the rotating plug was provided. The general arrangement of the enlarged down-flow closure is shown in Fig. 1-5.

Liner, penetration, and closure arrangement drawings were prepared for both up-flow and down-flow plant configurations (Figs. 1-6 and 1-7). Major closure differences between the two configurations are given in Table 1-1. For the liners, major differences between the two configurations lie in the many bends and offsets and the lack of a return duct from top to bottom of the steam generator cavity for the up-flow plant as compared to the down-flow plant. As previously indicated, the overall assessment favored the up-flow plant configuration, except for the rotating plug. Estimates of the cost differences between the two configurations were in agreement with this assessment.

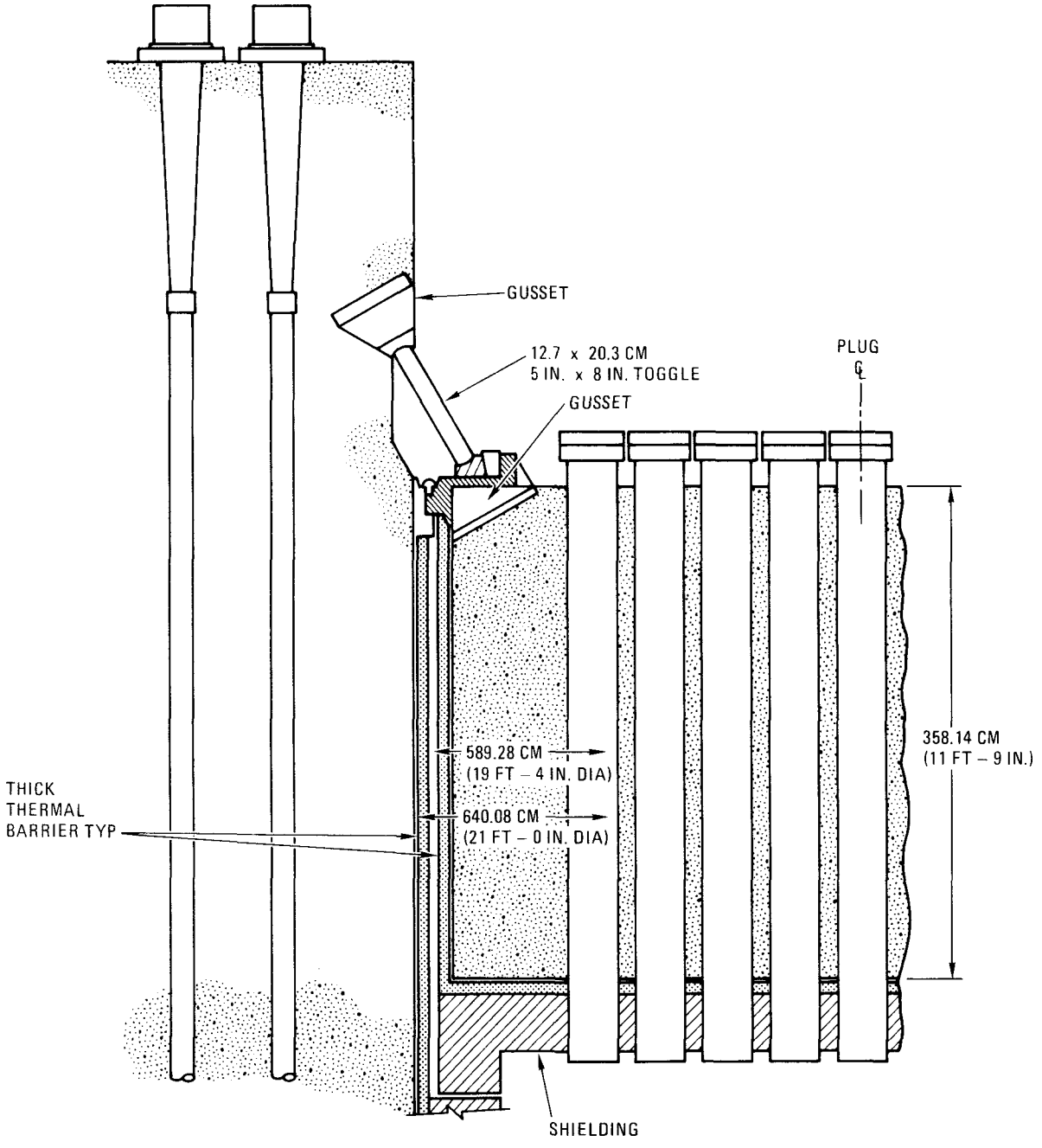

Fig. 1-5. Closure for GCFR down-flow core cavity

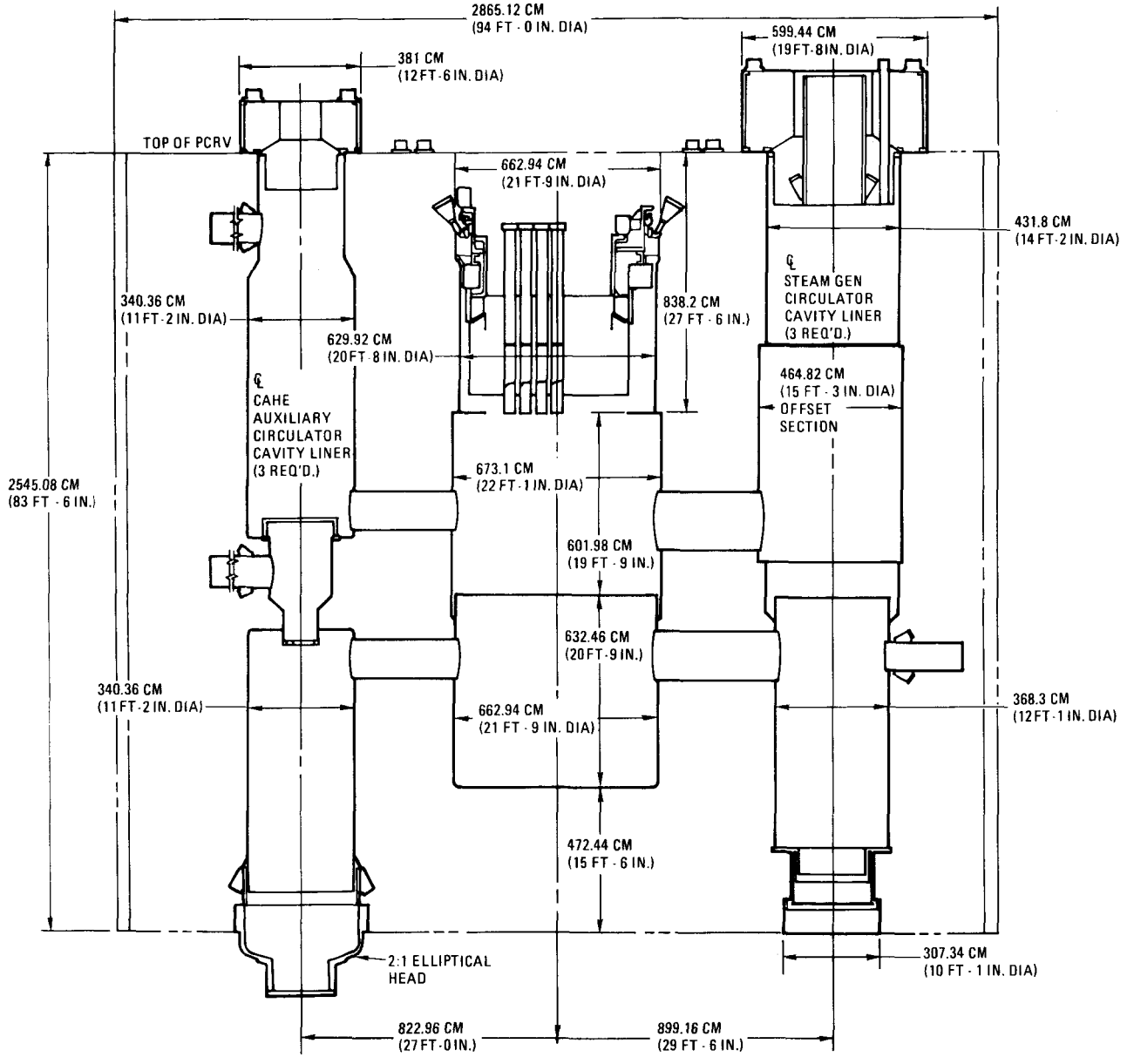

Fig. 1-6. Liner arrangement for GCFR up-flow core

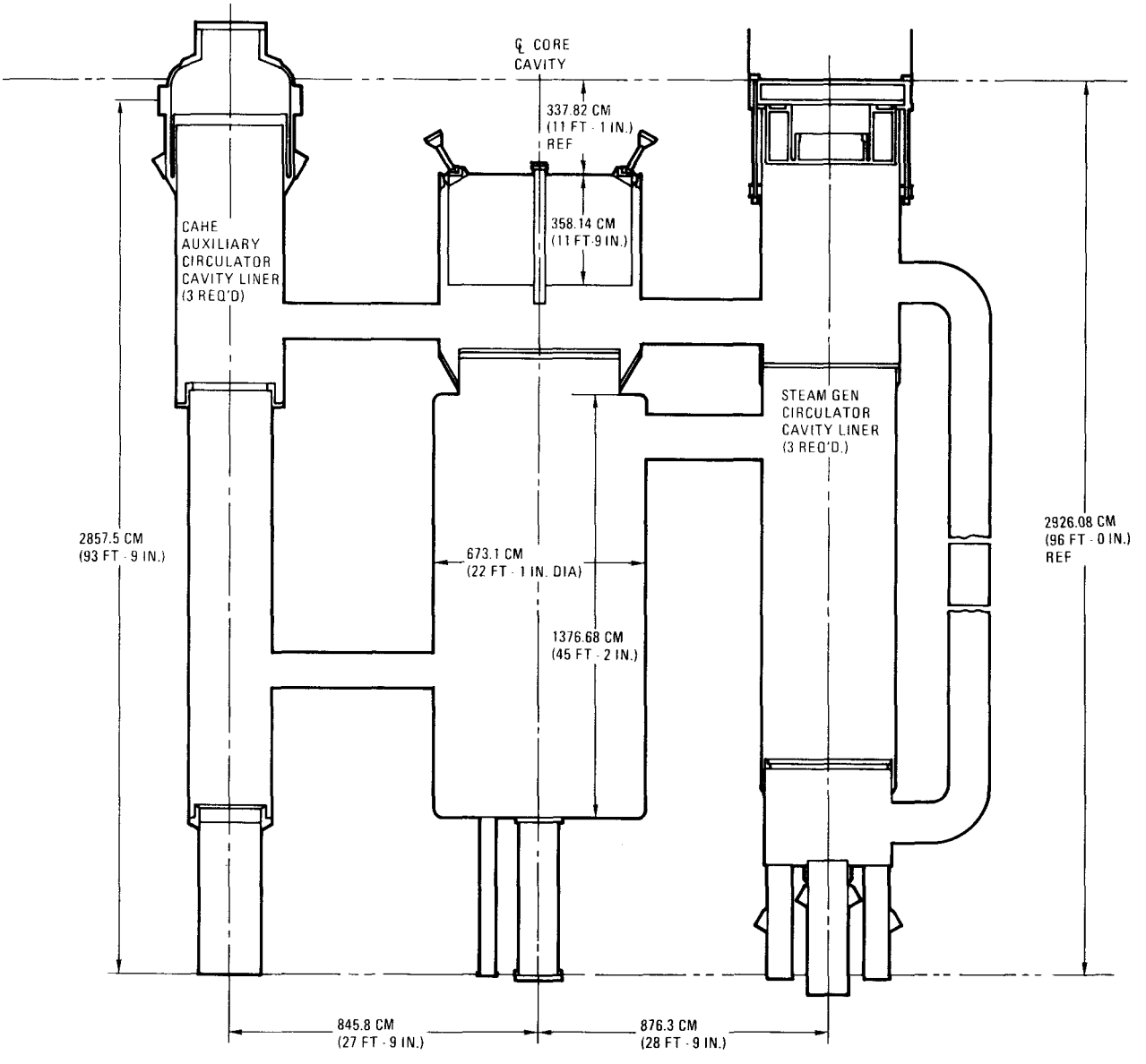

Fig. 1-7. Liner arrangement for GCFR down-flow core

TABLE 1-1
MAJOR GCFR CLOSURES

Location	Up-Flow Plant	Down-Flow Plant
Core cavity	Double rotating concrete plug with control rod penetrations	Stationary concrete plug with control rod penetrations
Steam generator upper closure	Concrete plug with superheat penetration in plug	Steel plug with circulator penetration in plug
Steam generator lower penetration	Circulator penetration closure and flow restrictor	Superheat penetration and flow restrictor
Auxiliary cooling loop upper closure	Concrete plug	Steel circulator closure and flow restrictor
Auxiliary cooling loop lower closure	Steel circulator closure and flow restrictor	CAHE tubesheet

In other liner-related work, a brief study of the feasibility and practicality of a natural convection liner cooling system for an internal postaccident fuel containment system liner following a postulated core meltdown was completed. The conclusion of the study is that a natural convection system, with the necessary large cooling tubes [approximately 7.6 cm (3 in.)], is feasible from a fabrication standpoint, but that significant additional development work is required.

A drawing of a prototype core cavity closure plug was prepared to initiate ORNL small-scale development tests of this closure. The prototype was a hybrid configuration with selected features of both the up-flow and down-flow plant plugs. A depth-to-diameter ratio of 0.5 was selected for the first 1/20-scale reactor core cavity closure (RCCC) model to be tested. The selection was primarily based on the results of Oak Ridge National Laboratory (ORNL) analysis which indicated that an RCCC of this geometry would have an ultimate pressure capacity of 4 MCP and an allowable pressure of 1.2 MCP. The drawing was transmitted to ORNL. Design of the model is in progress at ORNL.

Tentative parameters were recommended for the first large GCFR plants. Closure sizes were established and preliminary PCRV top head tendon layouts were made for 9- and 12-MPa (90- and 120-bar) nominal cavity pressures. On the basis of this work, it is recommended that a nominal cavity pressure of 10 MPa (100 bars) be selected for the six-loop 3600-MW(t) plant. Work to confirm the feasibility of this recommendation is essential.

A two-phase program plan for development of a floodable thermal barrier was completed. Phase I of this program is essentially a series of short-term wet properties tests that will identify the weaknesses of the present thermal barrier design when subjected to flooding and draining. This phase will conclude with testing of alternate design features that are expected to improve accommodation of flooding.

The final phase of this program will apply the knowledge gained in Phase I toward design development studies and analyses that will include detail design, subsequent manufacturing, and proof testing of a full-scale representative section of the most promising floodable thermal barrier configuration.

Thermal barrier general arrangement drawings (see Figs. 1-8 and 1-9 and Tables 1-2 and 1-3) for the proposed up-flow and down-flow vessels were completed to provide bases for the cost analysis input to up-flow/down-flow evaluation.

The total surface area of thermal barrier for the up-flow configuration was about 500 m^2 (5400 ft^2) less than for the down-flow. No major difference that could be considered to favor either configuration was identified.

Conceptual design studies of the postaccident fuel retention system at the bottom of the core cavity were completed for both proposed up-flow and down-flow vessels (see Figs. 1-10 and 1-11).

To ensure equitable comparison in the evaluation of up-flow versus down-flow, these postaccident fuel retention system designs were based on the same guidelines and design criteria wherever possible. The minimum containment volume necessary to confine all the molten core materials was used to determine containment height; then, in both cases, 230 mm (9 in.) was added for spill contingency margin.

The materials of this composite structure include stainless steel castings, magnesia bricks, and boron carbide (B_4C) pellets dispersed in a magnesia (MgO) matrix. This material combination was selected to meet the twofold requirements of thermal barrier and irradiation shielding during normal operation in addition to withstanding the severe structural and heat transfer requirements of a nondesign-basis, postulated core meltdown. From the MFC viewpoint, the most significant difference between the up-flow and down-flow vessels is the refueling penetrations in the bottom

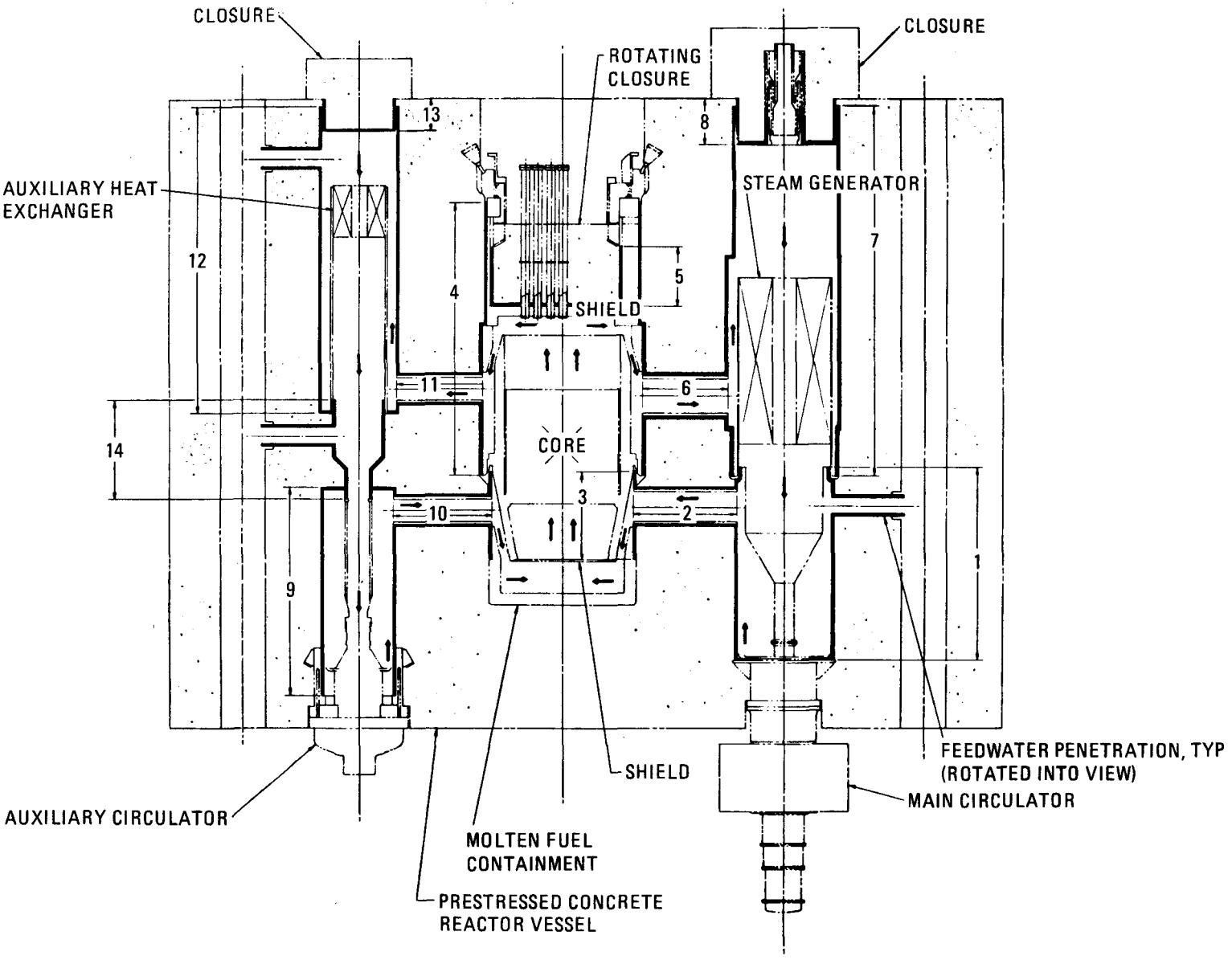

Fig. 1-8. Thermal barrier general arrangement for GCFR up-flow configuration

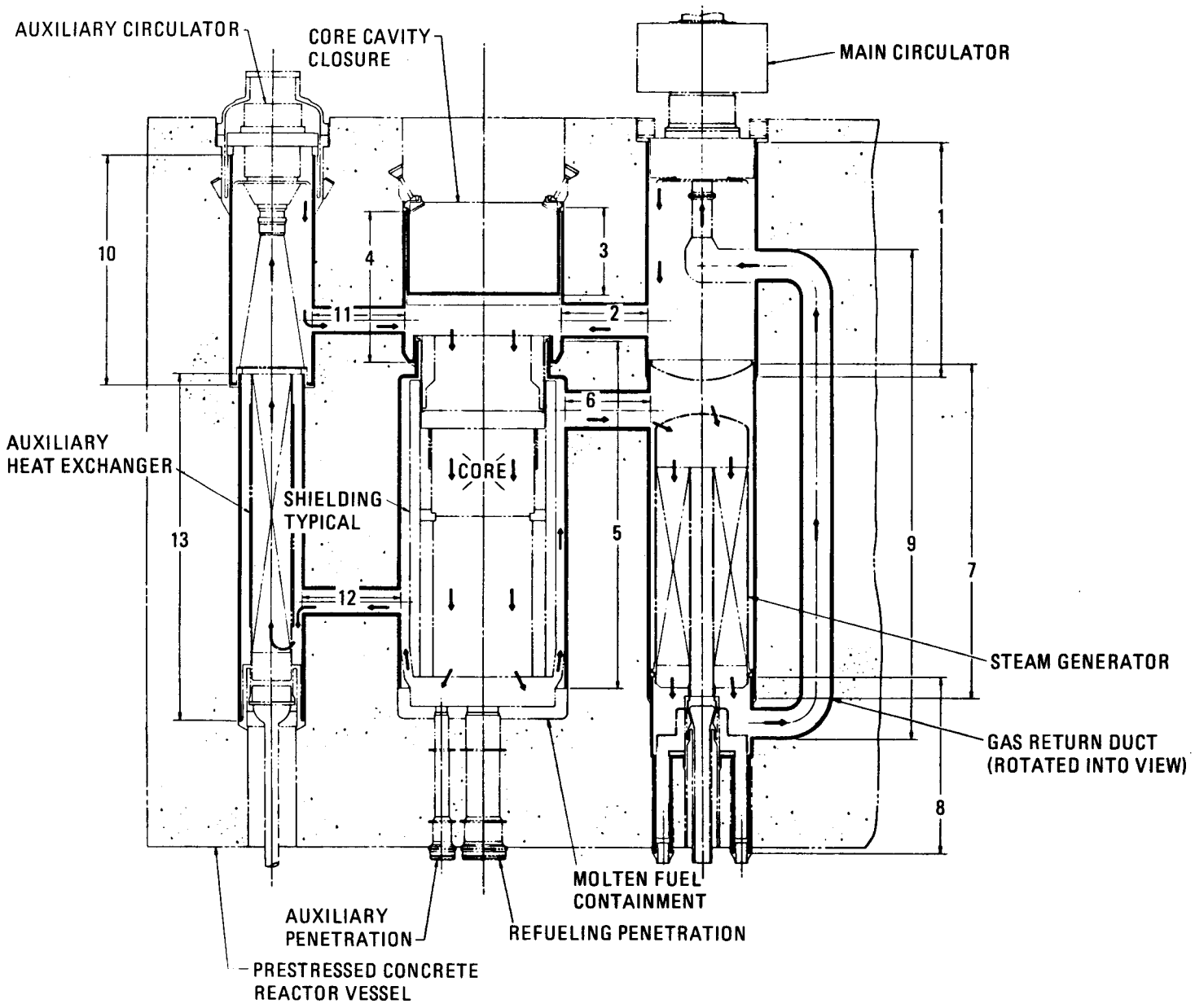

Fig. 1-9. Thermal barrier general arrangement for GCFR down-flow configuration

TABLE 1-2
THERMAL BARRIER DATA FOR GCFR UP-FLOW CONFIGURATION

Zone	Class[a]	Quantity	Thickness[b] (mm)	Area[c] (m^2)	Description
1	A	3	76	319	Circulator cavity
2	A	3	76	66	Lower main cross duct
3	A	1	76	82	Lower core cavity
4	B1	1	102	204	Upper core cavity
5	B1	1	102	55	Core closure - rotating
6	B1	3	102	61	Upper main cross duct
7	B1	3	102	634	Steam generator cavity
8	B1	3	102	84	Closure, steam generator cavity
9	A	3	76	294	Auxiliary heat exchanger circulator cavity
10	A	3	76	42	Lower auxiliary cross duct
11	B2	3	102	41	Upper auxiliary cross duct
12	B2	3	102	314	Auxiliary heat exchanger cavity
13	B2	3	102	35	Closure, auxiliary heat exchanger cavity
14	B1	3	102	74	Feedwater plenum

Class A = 802 m^2, 35%
Class B1 = 1112 m^2, 48%
Class B2 = 390 m^2, 17%
Total Area = 2304 m^2

[a] Class A = carbon steel (AISI type 1020)
Class B1 = stainless steel (AISI type 316)
Class B2 = Hastelloy-X

[b] Does not include attachment fixture protrusion of 25.4 mm maximum beyond cover plate surface.

[c] Area given is total area per reactor and is measured at linear surface.

TABLE 1-3
THERMAL BARRIER DATA FOR GCFR DOWN-FLOW CONFIGURATION

Zone	Class[a]	Quantity	Thickness[b] (mm)	Area[c] (m^2)	Description
1	A	3	76	349	Circulator cavity
2	A	3	76	45	Upper main cross duct
3	A	1	76	95	Closure, core cavity
4	A	1	76	133	Upper core cavity
5	B1	1	102	297	Core cavity
6	B1	3	102	42	Lower main cross duct
7	B1	3	102	514	Steam generator cavity
8	A	3	102	202	Lower plenum and penetration, steam generator cavity
9	A	3	102	412	Gas return duct
10	A	3	76	303	Auxiliary heat exchanger circulator cavity
11	A	3	76	37	Upper auxiliary cross duct
12	B2	3	102	39	Lower auxiliary cross duct
13	B2	3	102	333	Auxiliary heat exchanger cavity

Class A = 1578 m^2, 56.3%
Class B1 = 853 m^2, 30.4%
Class B2 = 372 m^2, 13.3%
Total Area = 2802 m^2

---

[a] Class A = carbon steel (AISI type 1020)
Class B1 = stainless steel (AISI type 316)
Class B2 = Hastelloy-X

[b] Does not include attachment fixture protrusion of 25 mm maximum beyond cover plate surface.

[c] Area given is total area per reactor and is measured at linear surface.

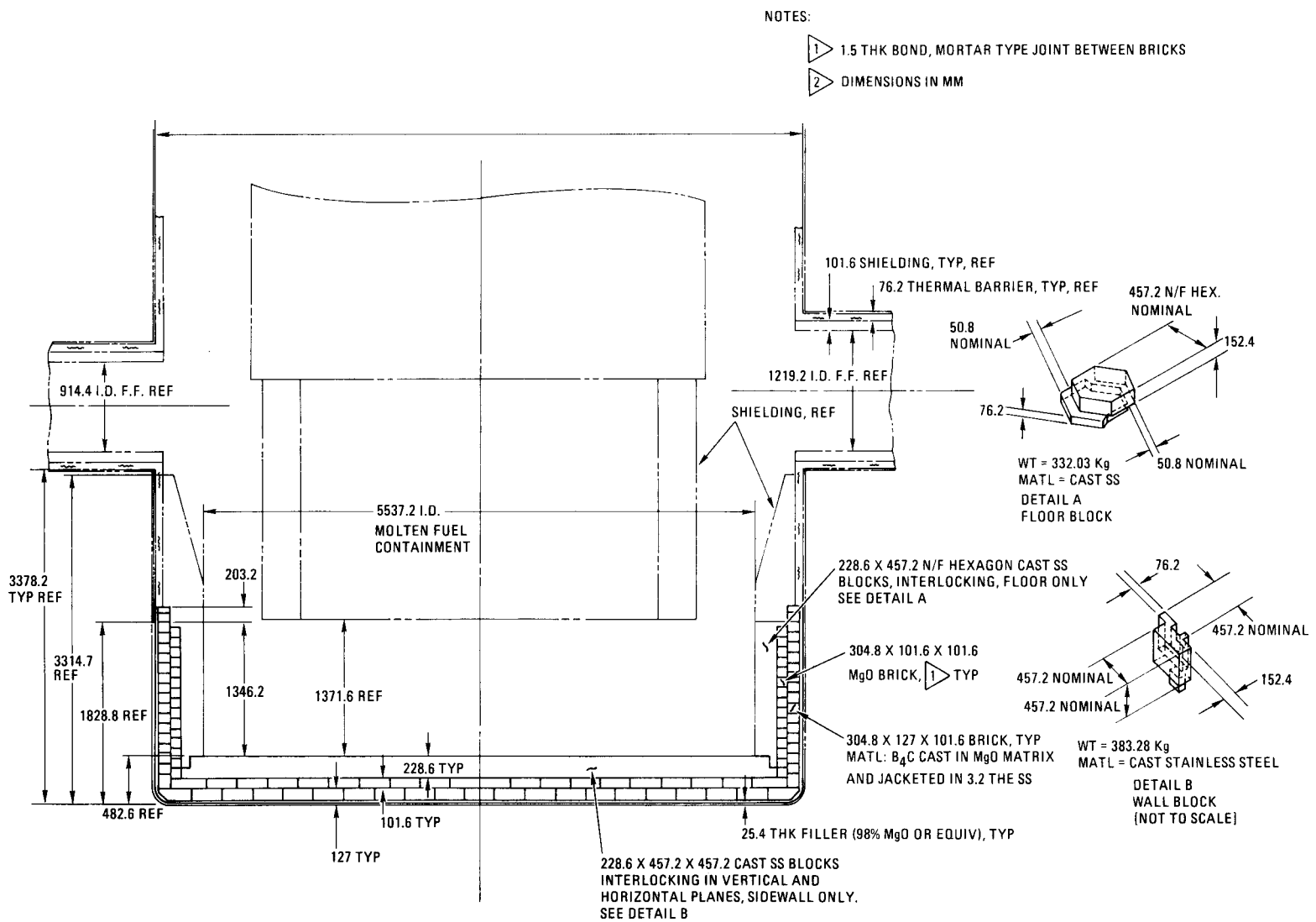

Fig. 1-10. Molten fuel containment for GCFR up-flow core

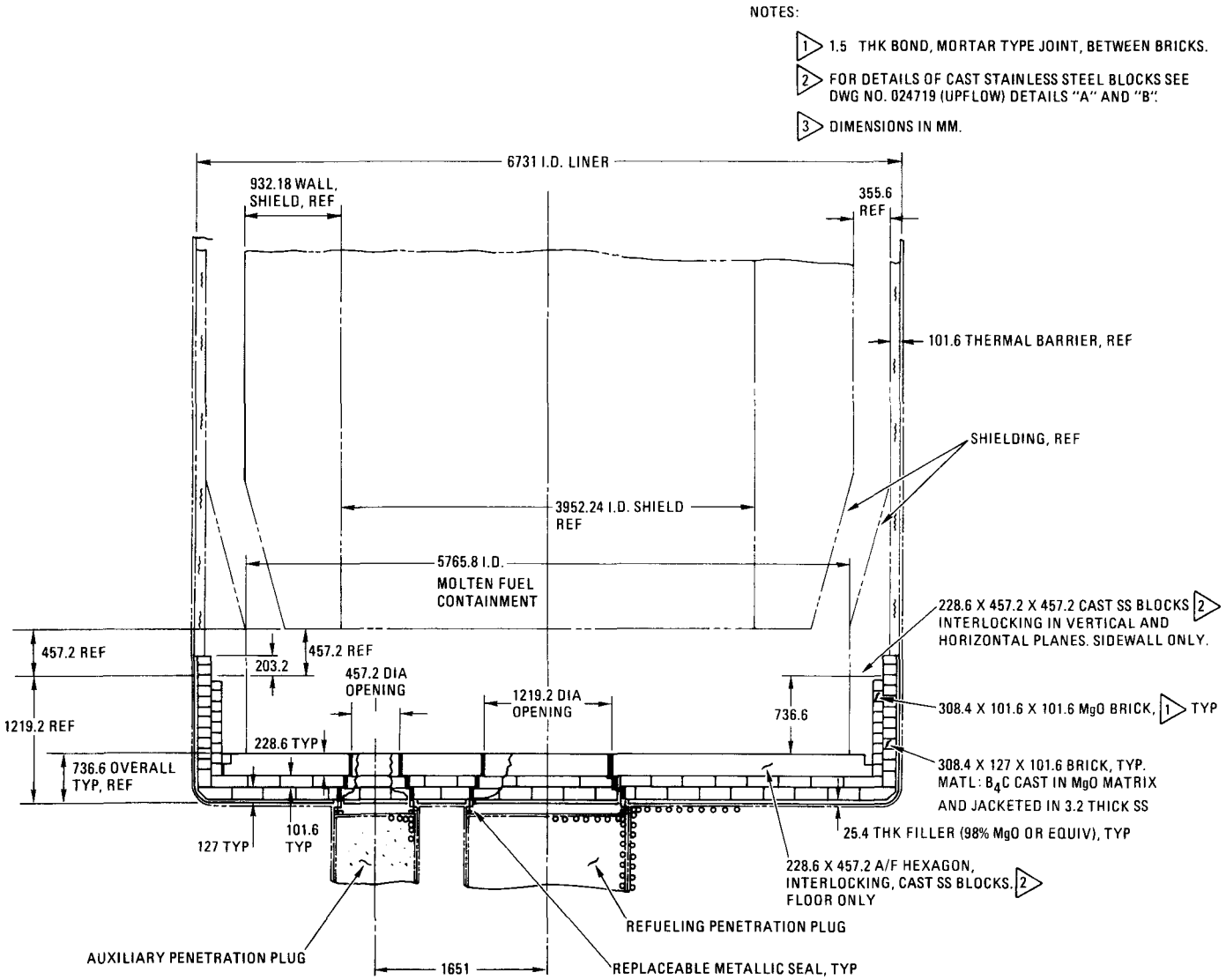

Fig. 1-11. Molten fuel containment for GCFR down-flow core

head of the down-flow configuration. The large plugs needed in these penetrations represent an added technical risk and complexity disadvantage, in comparison with the simpler, uninterrupted up-flow containment. Neither design alternative, however, was judged infeasible.

1.12. CONTROL AND LOCKING MECHANISMS

A backup design concept for the up-flow core to provide control rod drive guidance and thermocouple access without the need of a special support structure spanning the top of the core was developed. The incentive for considering an alternate approach to the guide and support structure concept was to provide a refueling option (seven-element patch), if the tentatively selected rotating plug concept did not prove feasible.

The design provides for a telescoping instrument tree and control rod driveline guide tube that is registered and supported by the central assembly in each seven-element core patch. The instrument tree can move freely up and down with the central assembly axial thermal and irradiation growth.

The telescoping instrument tree approach also provides an alternative to the guide and support structure employed in the rotating plug refueling concept. For this application, the instrument trees would be provided with a motor-powered retraction mechanism within the top head vessel penetrations. These retraction drives would allow the instrument trees to be raised free of their engagement to the core, allowing the top head plug to rotate for the refueling operation.

Having the instrument tree axially supported by the central assembly of a seven-assembly core region provides the potential for a simple mechanical backup hold-down of the core. By utilizing engaging axial stops between the central assembly and its six surrounding core assemblies, the weight of the instrument tree and the central assembly would be transferred to these adjacent core assemblies. The engaging stops would be located at the lower ends of the core assemblies, where differential thermal and irradiation growth interaction would be minimal. Removal and replacement of the core assemblies in a region would require the prior removal of the central assembly.

The telescoping instrument tree has been recommended as the preferred design for providing thermocouple access to the upflow core concepts being evaluated.

A study was made on alternate ways to prevent a control rod ejection that would not require dependence on mechanisms supplementary to the normal actuating and controlling components of a drive assembly. Control rod ejection is based on a postulated loss of pressure that suddenly occurs in a control rod drive housing and its surrounding penetration, whereby reactor cavity pressure causes a large upward force on the penetration internals.

Since the current top head penetration arrangement incorporates hold-down plates above the primary closure plates, ejection of the control rod drive assemblies is not possible. However, the driveline member and its attached control rod has a potential for ejection, specifically during or shortly after a free-fall reactor trip insertion, if a pressure loss is also assumed within the drive housing.

The most promising solution to prevent this ejection potential was to assure a continuous pressure-balancing force on the driveline. Such a feature has been incorporated into the control rod drive design concept. This was readily accomplished by providing a direct gas flow passage inside the driveline, communicating directly between the reactor cavity and the guide tube cavity enclosing the upper end of the driveline.

1.13. FUEL HANDLING SYSTEM

At the conclusion of the previous quarter a decision was made to concentrate the refueling effort for the up-flow/down-flow core evaluation on three specific refueling arrangements. For the up-flow study, two alternate concepts were defined. The first, designated concept F, is associated with a rotating top head plug. The alternate concept, B_3, is associated with a nonrotating plug. Possible arrangements for a down-flow core are somewhat limited by the need to minimize the number of bottom head penetrations, and for this reason only one concept has been developed for evaluation.

Concept F for an up-flow core is based on an arrangement where the refueling penetrations are contained in a rotatable structure or plug located in the top head of the PCRV. The arrangement of the rotatable structure is such that when a fuel handling machine is placed over one of several dedicated penetrations, it can be axially aligned with the required element in the core. This technique provides a desirable straight-shot approach to fuel handling and at the same time places the fuel handling machine in a readily accessible position outside the PCRV.

Figure 1-12 shows a typical arrangement of a rotatable plug. The plug consists of two eccentric components. The primary or inner component is the plug proper and contains all the necessary control rod drive and instrument tree penetrations, together with any additional dedicated penetrations. The center of rotation of the assembly is offset from the center of the core by one-half the total required eccentricity. Surrounding the plug assembly is a secondary eccentric component in the form of an annulus which, when separately rotated, causes displacement of the plug assembly, resulting in the required total displacement of the penetrations. Both the primary and secondary components are supported on ball bearings. Each component is individually driven by electric motors and gear reducers.

The fuel handling machine (FHM) is carried above the rotatable plug on a trolley traversing a polar bridge in such a manner that the machine can be positioned over the appropriate penetration. The control rod drive or instrument tree is first removed from the penetration through which access to the core is to be made, and an isolation valve is installed. The plug assembly is rotated to place the axis of the penetration directly over the axis of the appropriate core element. The FHM is moved into position and sealed to the isolation valve.

The FHM and its functions are illustrated diagrammatically in Figs. 1-13 through 1-16. The machine consists of two telescoping sleeves, each actuated by a pair of ball screws. An element grapple head, coupled in the inner sleeve by a latching arrangement, is carried by a separate hoist.

Following engagement of the FHM with the isolation valve and subsequent interspace purging, the outer sleeve is driven downward until it contacts the six elements surrounding the element to be withdrawn. This restrains the adjacent elements if frictional forces develop during withdrawal that tend to raise them along with the grappled element. The outer sleeve also serves as a guide for the inner sleeve, which is next lowered into position along with the grapple head.

When a core element has been grappled, the sleeves are retracted in reverse sequence, the isolation valves are closed, and the FHM is disconnected. The machine is then moved to an inclined chute and carrier arrangement connecting directly to the storage pool. From this position, the grapple head is uncoupled from the inner sleeve and the element lowered down the transfer chute by the FHM hoist.

The arrangement described above enables substantial axial forces to be developed from the ball screws to both withdraw and insert elements. The necessary longer travel through the transfer chute is provided by the hoist.

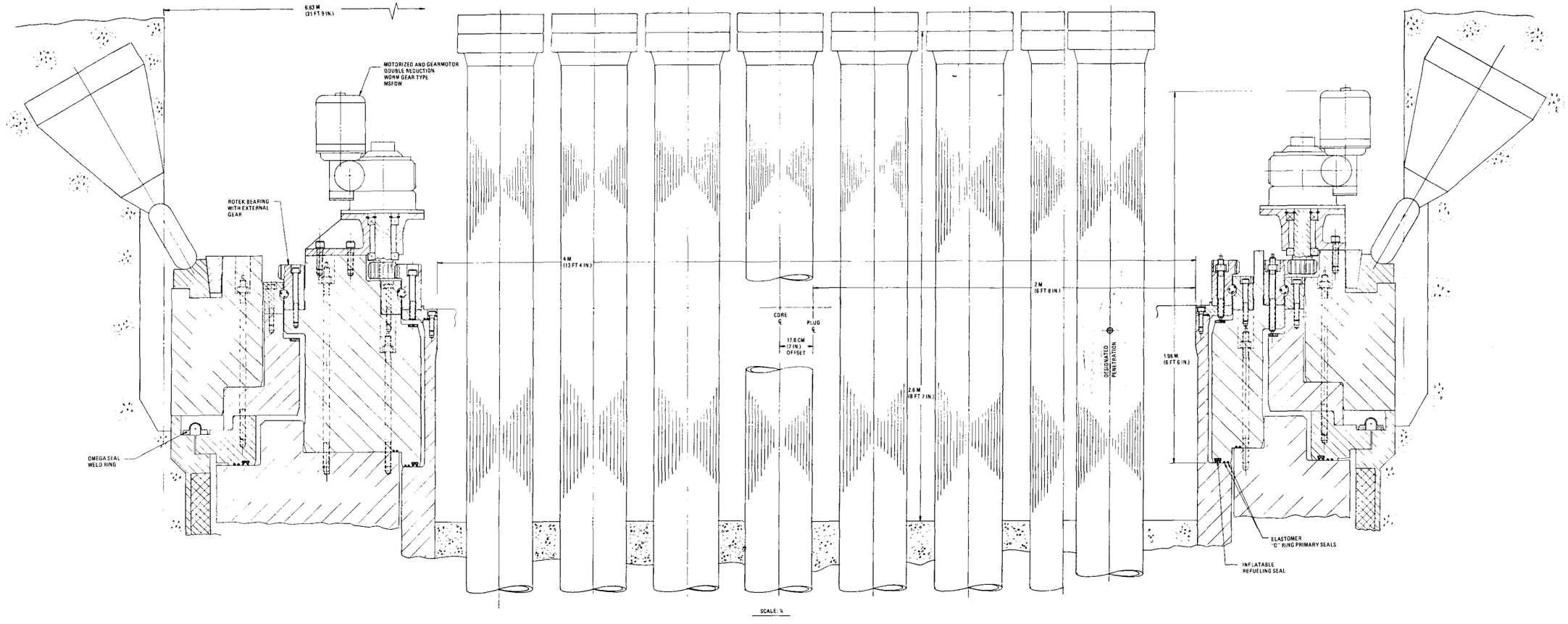

Fig. 1-12. Rotatable plug typical arrangement

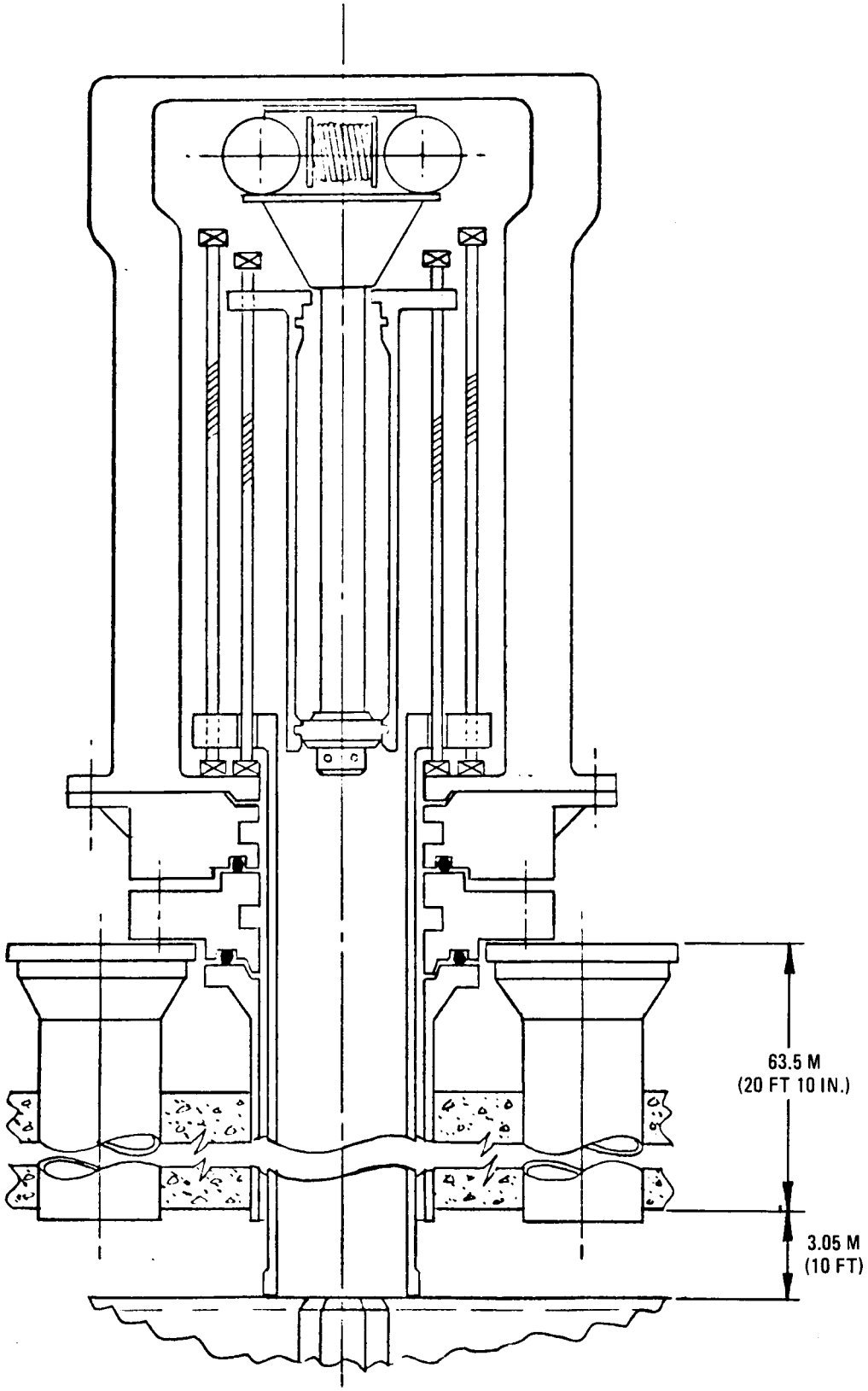

Fig. 1-13. Fuel handling machine with restraint sleeve extended

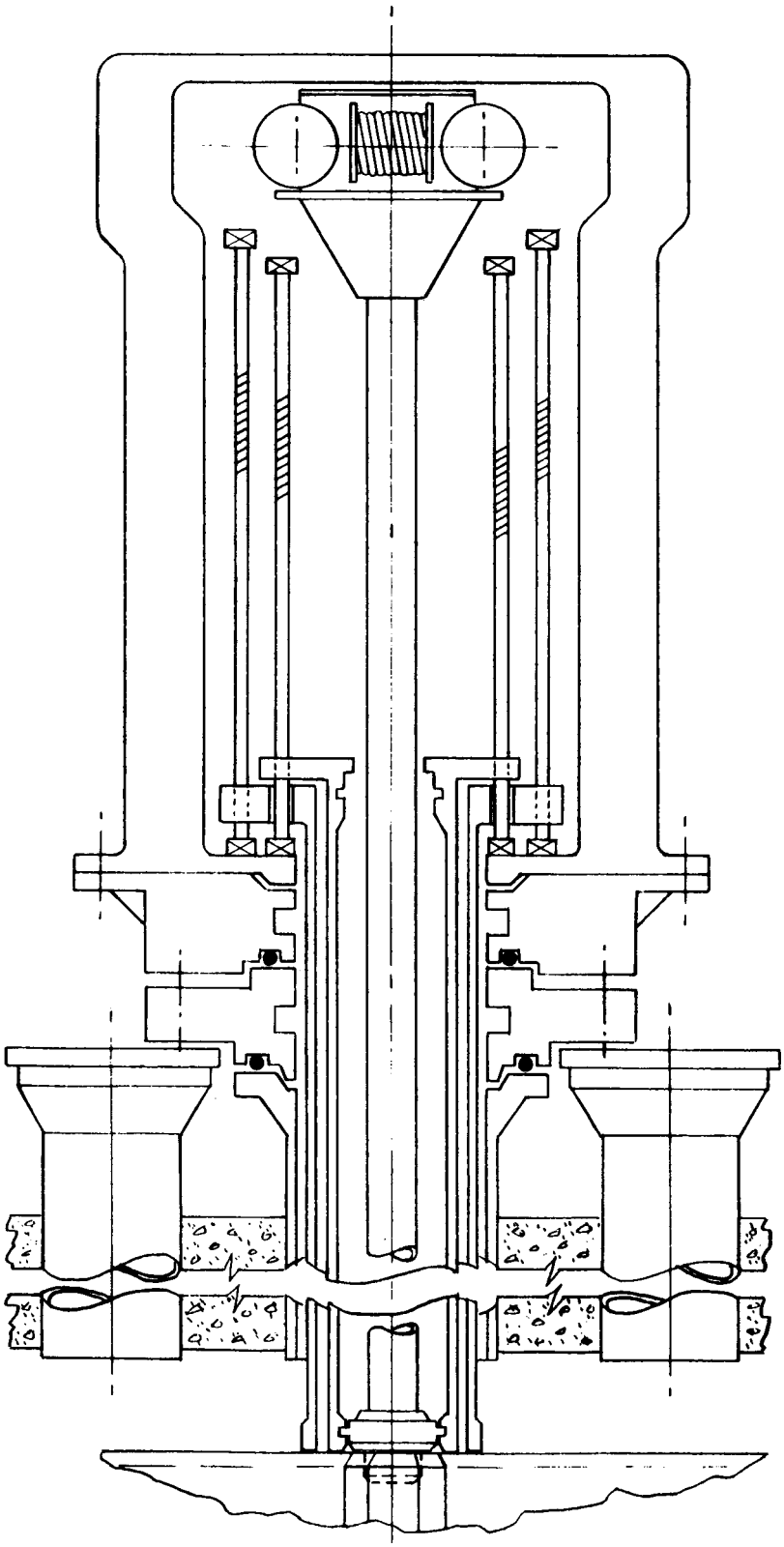

Fig. 1-14. Fuel handling machine with element grappled

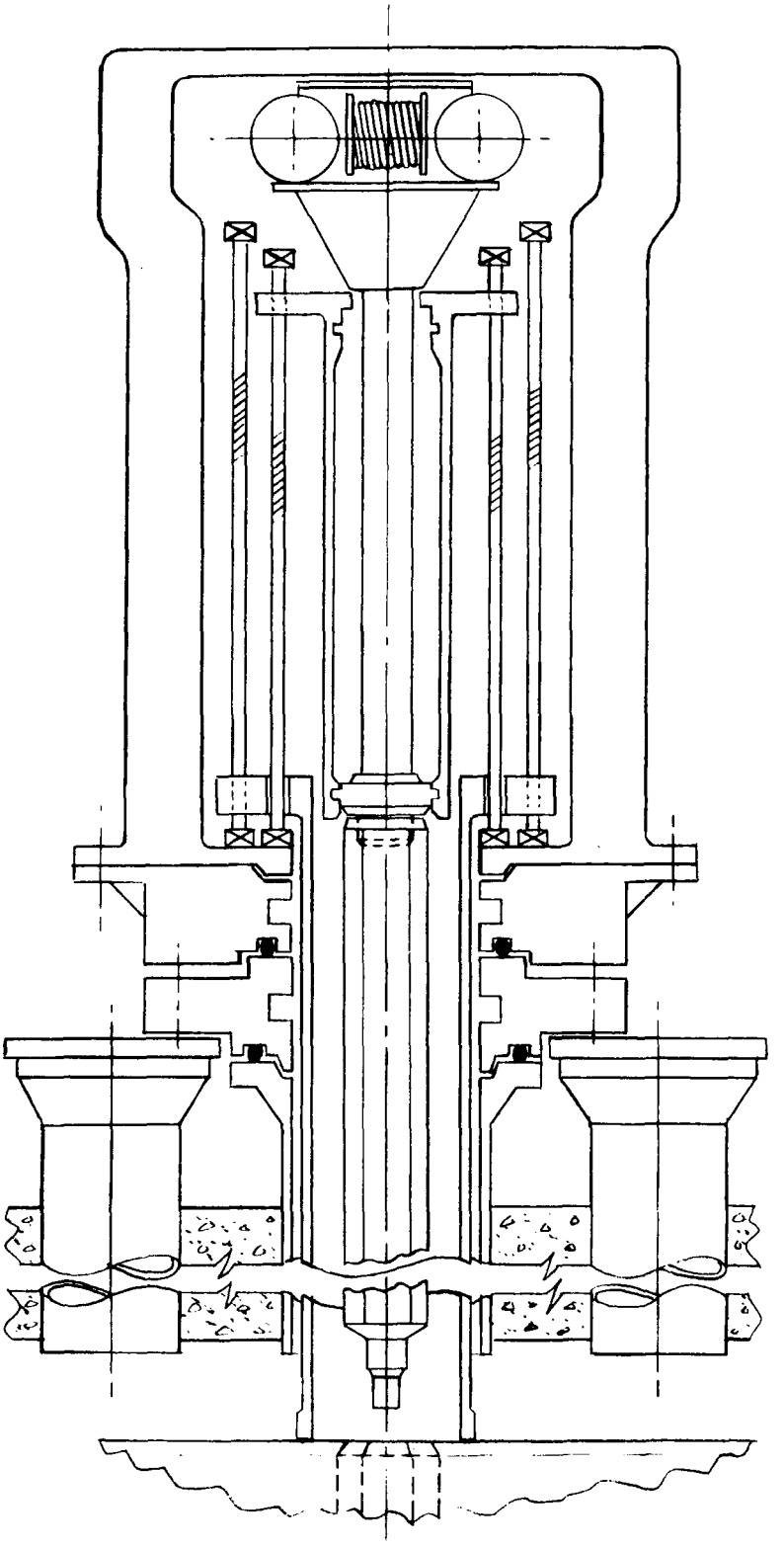

Fig. 1-15. Fuel handling machine with element removed from core

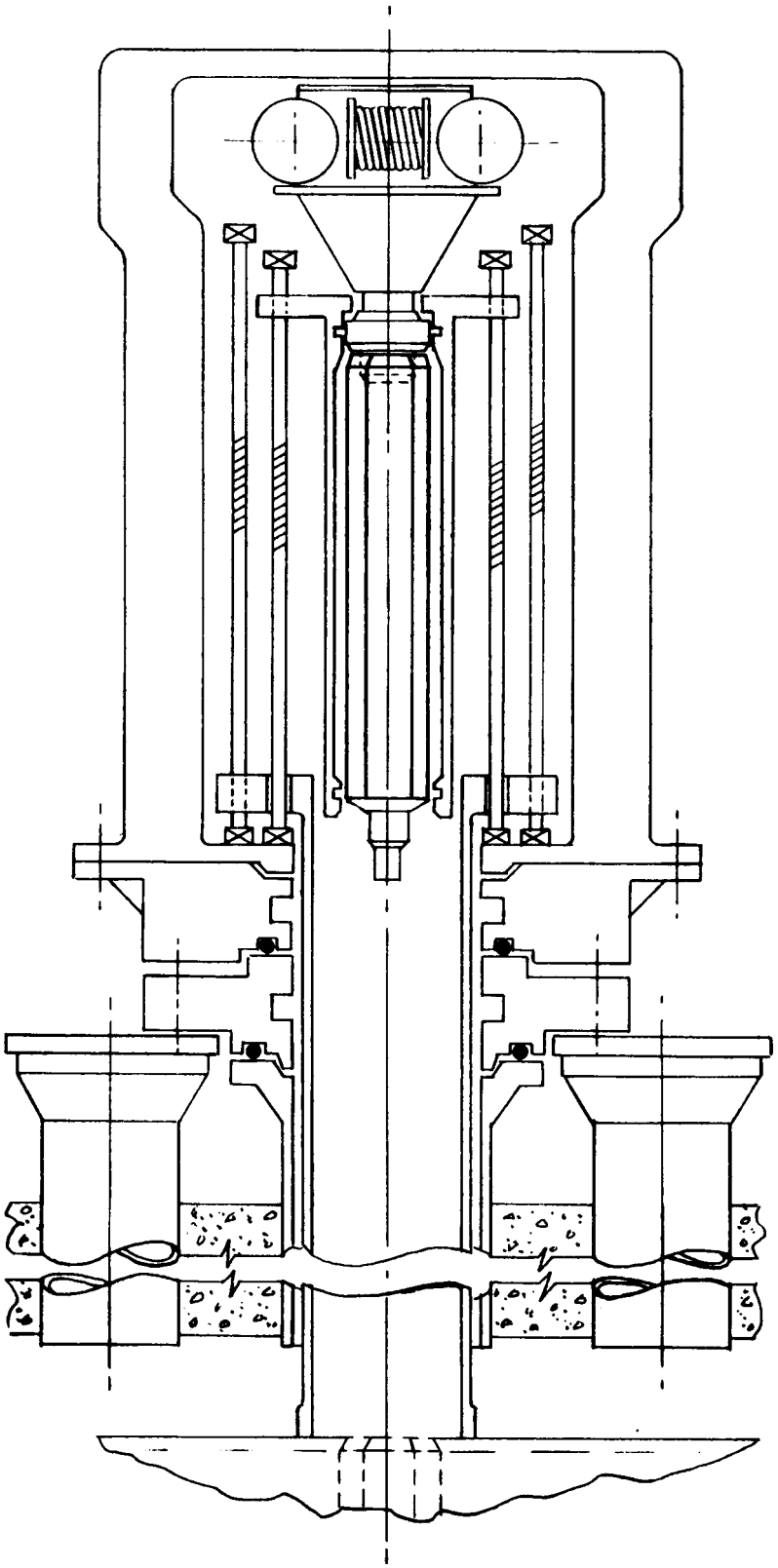

Fig. 1-16. Fuel handling machine with element raised into cask

The machine incorporates a closed-loop helium system for cooling elements during movement between the penetration and the transfer chute. This system is backed up by connections to the plant purification and/or the main helium supply. During periods when an element is being raised into the FHM, or lowered through the inclined chute, this flow is diverted to provide cooling during transit. Figures 1-17 and 1-18 depict alternate general arrangements of the refueling system and Fig. 1-19 shows a typical installation of the FHM itself.

Concept B_3 for an up-flow core necessitates a top head penetration located directly above the center of each seven-element patch of core elements. This results in a total of 67 penetrations for the demonstration plant. The penetrations can be contained in either a fixed plug or a cast-in-place PCRV head. Once inserted into a penetration, the fuel handling machine must deploy to reach any one of the six elements surrounding the central element.

The FHM consists of two telescoping tubes; this is referred to as a "hockey stick" approach. The lower tube is open on one side and incorporates a ballscrew-driven carrier and guide rails. A detachable grapple is carried on a supporting structure suitably pivoted to provide the offset necessary to reach the surrounding six elements. Figures 1-20 through 1-24 show the various machine functions which must be performed to remove an element. Element cooling is handled in a manner similar to that of concept F.

Figure 1-24 shows a proposed fuel handling system; a typical refueling sequence following cool-down is as follows:

1. Remove penetration closure and install isolation valve.

2. Install auxiliary service cask and purge interspaces.

3. Remove control rod drive (CRD) (or instrument tree assembly), close isolation valve purge, and remove auxiliary service cask to CRD storage wall.

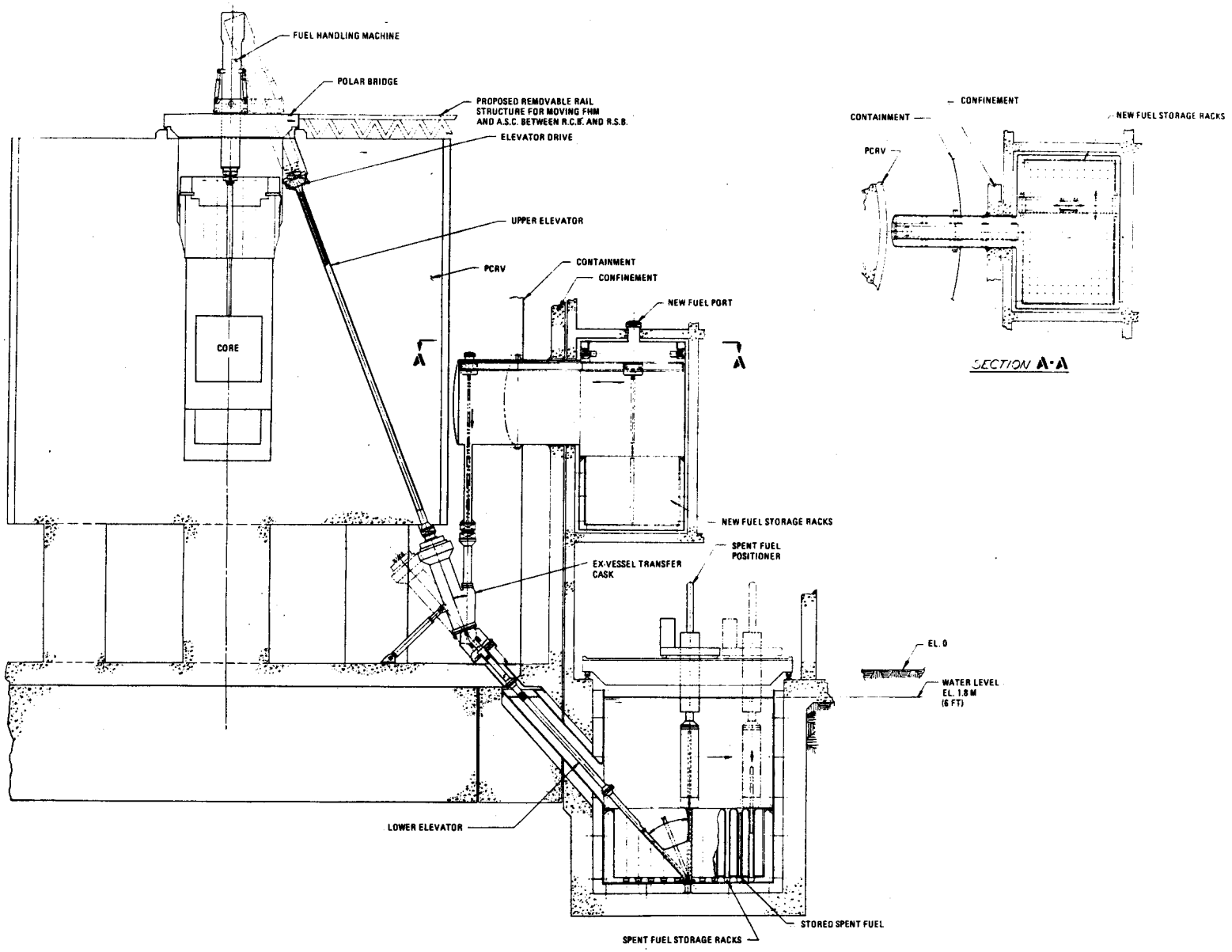

Fig. 1-17. Refueling system general arrangement for up-flow GCFR

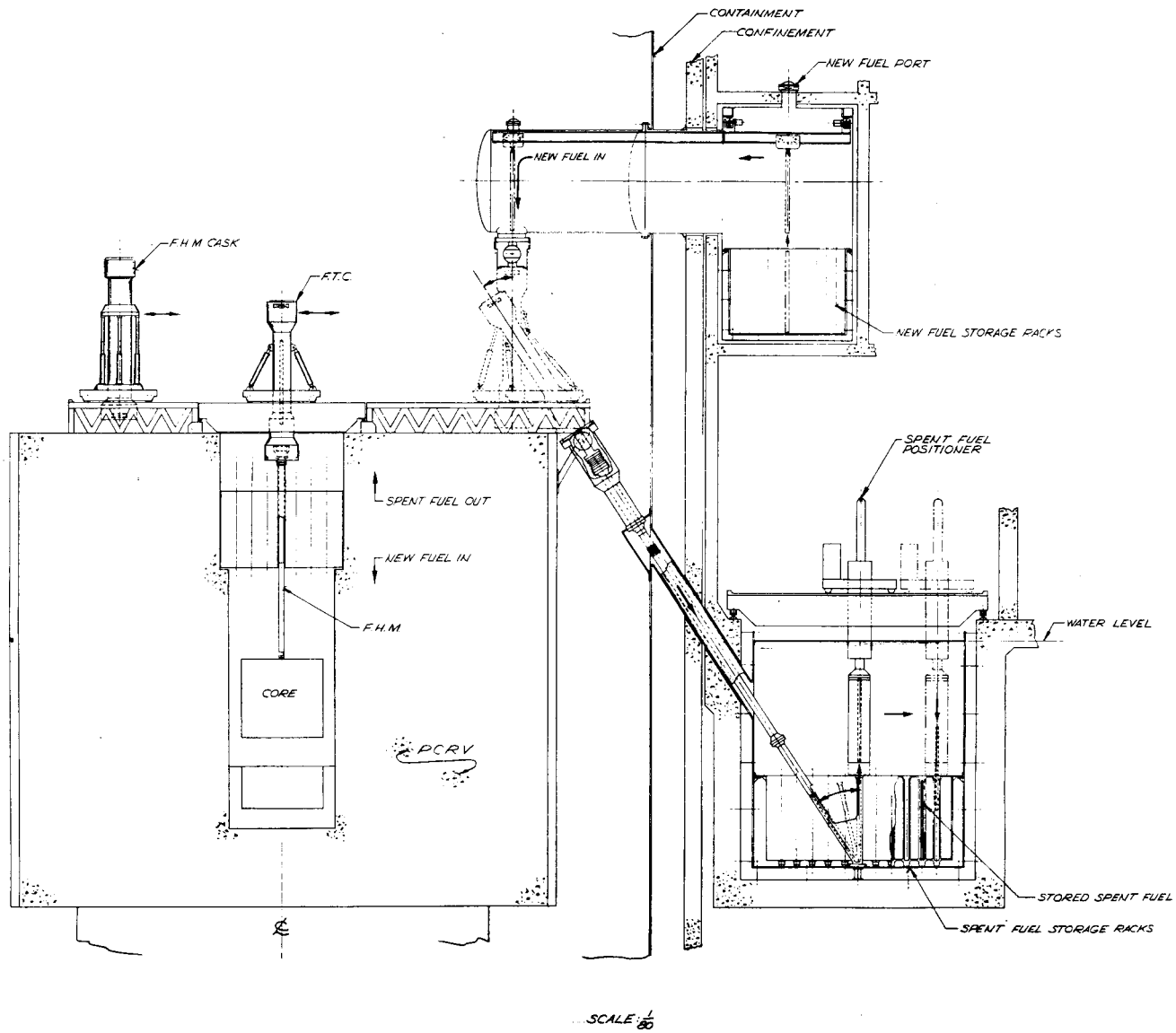

Fig. 1-18. Refueling system alternate general arrangement for up-flow GCFR

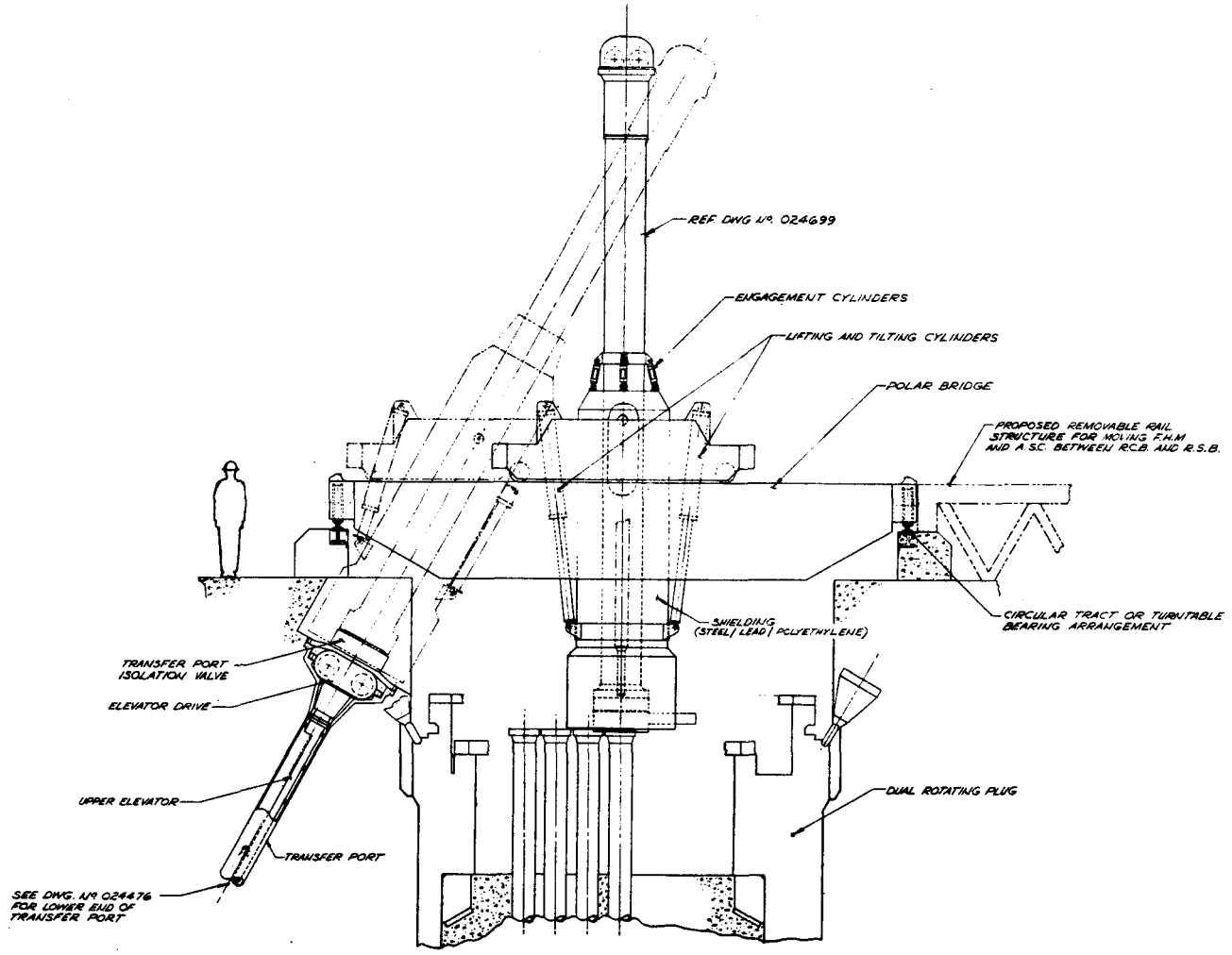

Fig. 1-19. Fuel handling machine installation for rotating plug concept F

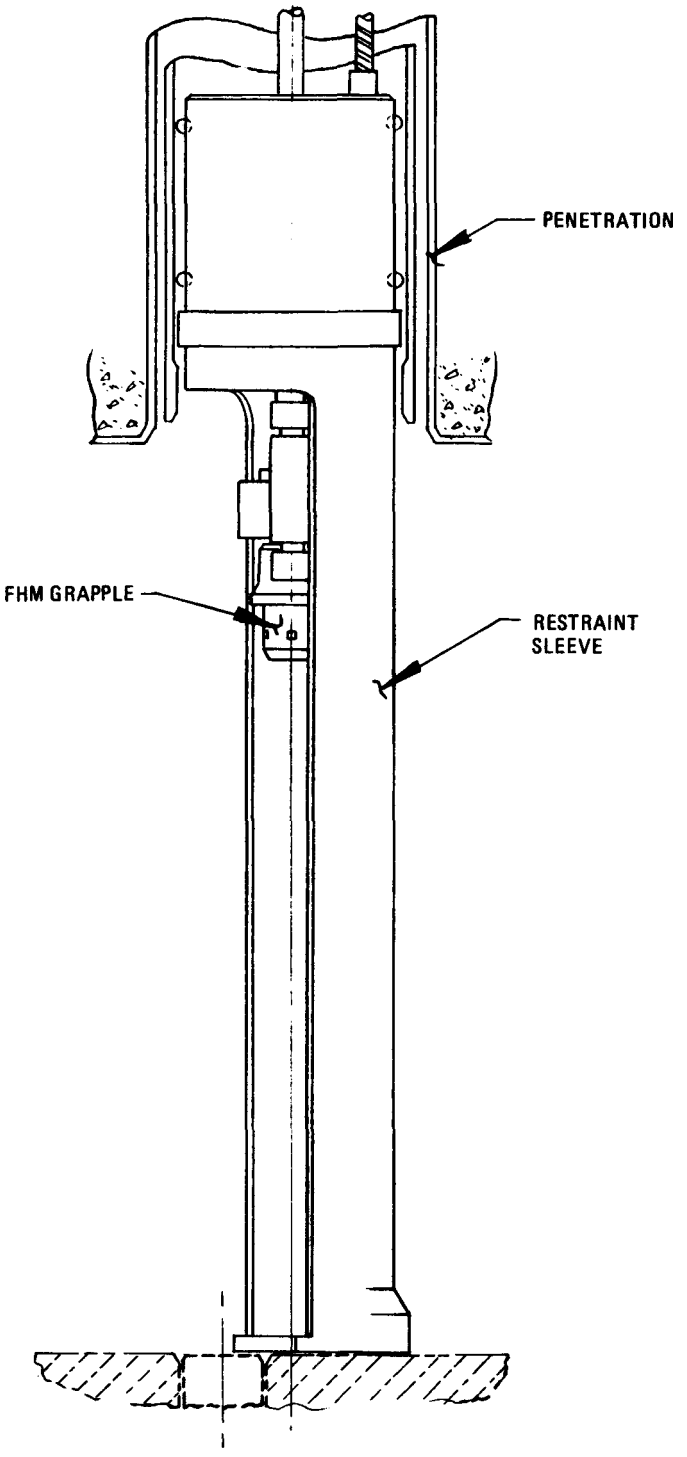

Fig. 1-20. Fuel handling machine installed

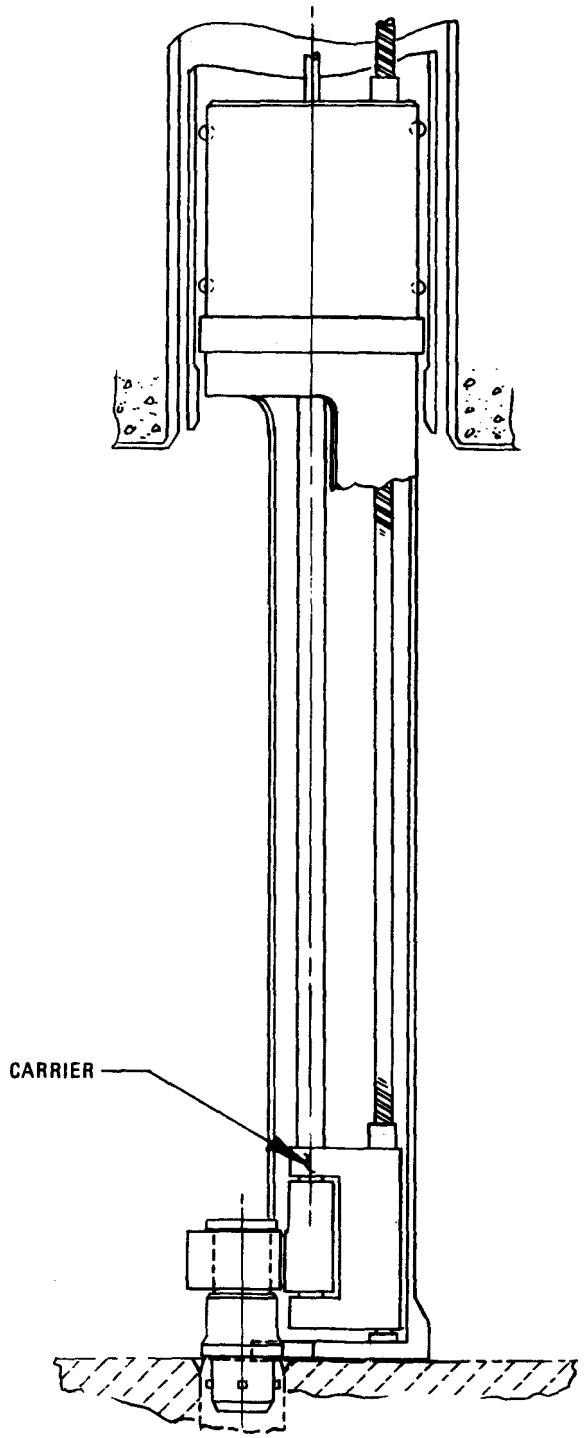

Fig. 1-21. Fuel handling machine grapple engaged

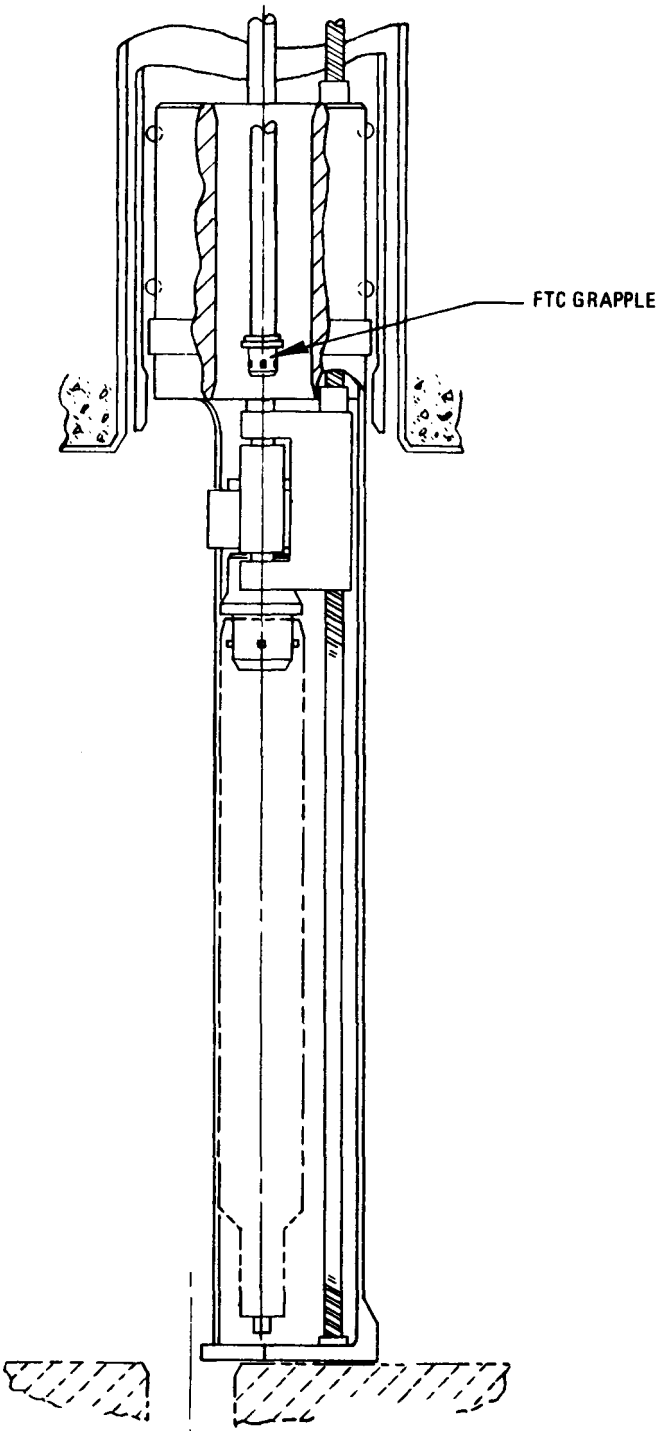

Fig. 1-22. Fuel handling machine grapple withdrawn and centered

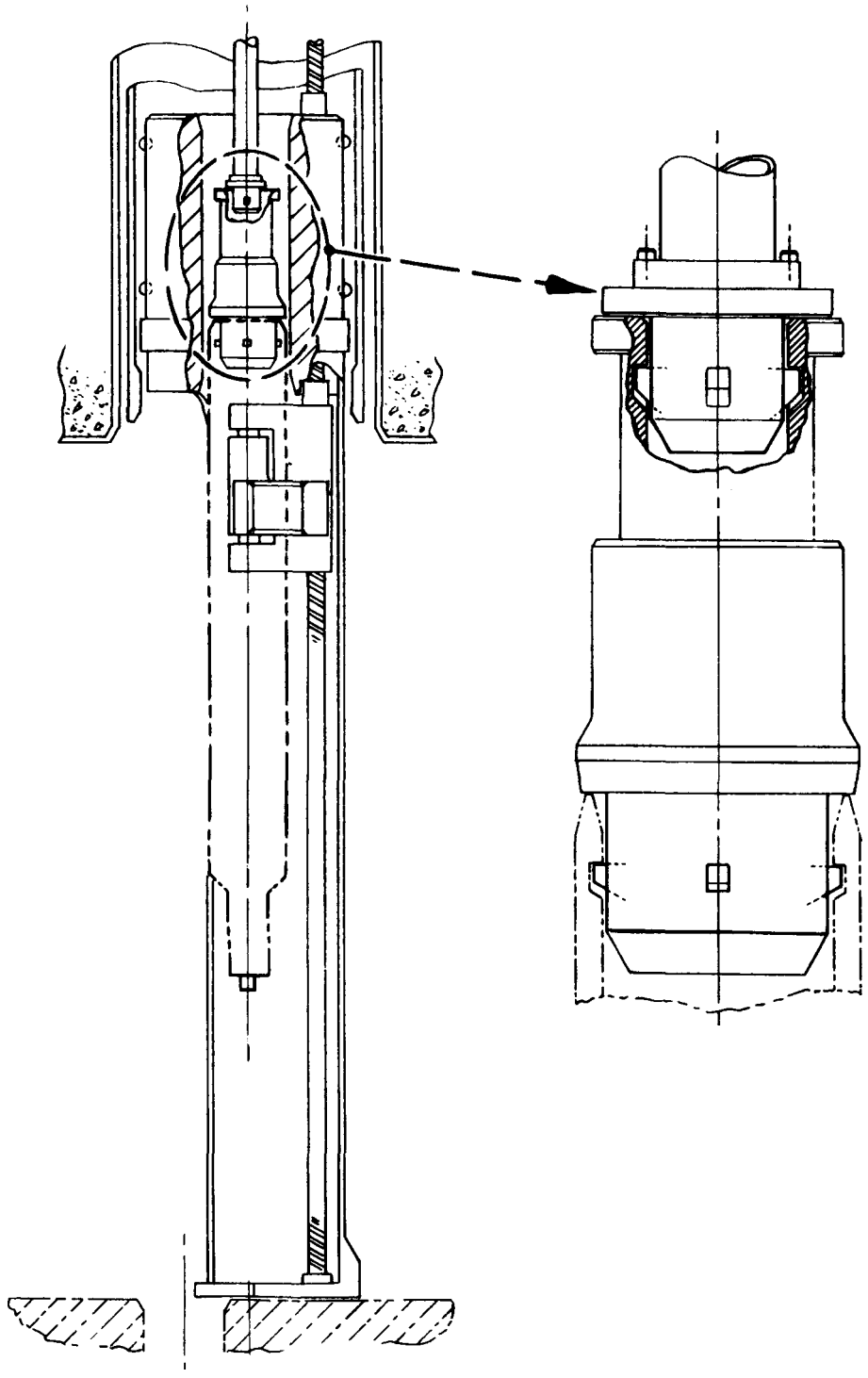

Fig. 1-23. Fuel transfer cask and fuel handling machine with grapples engaged

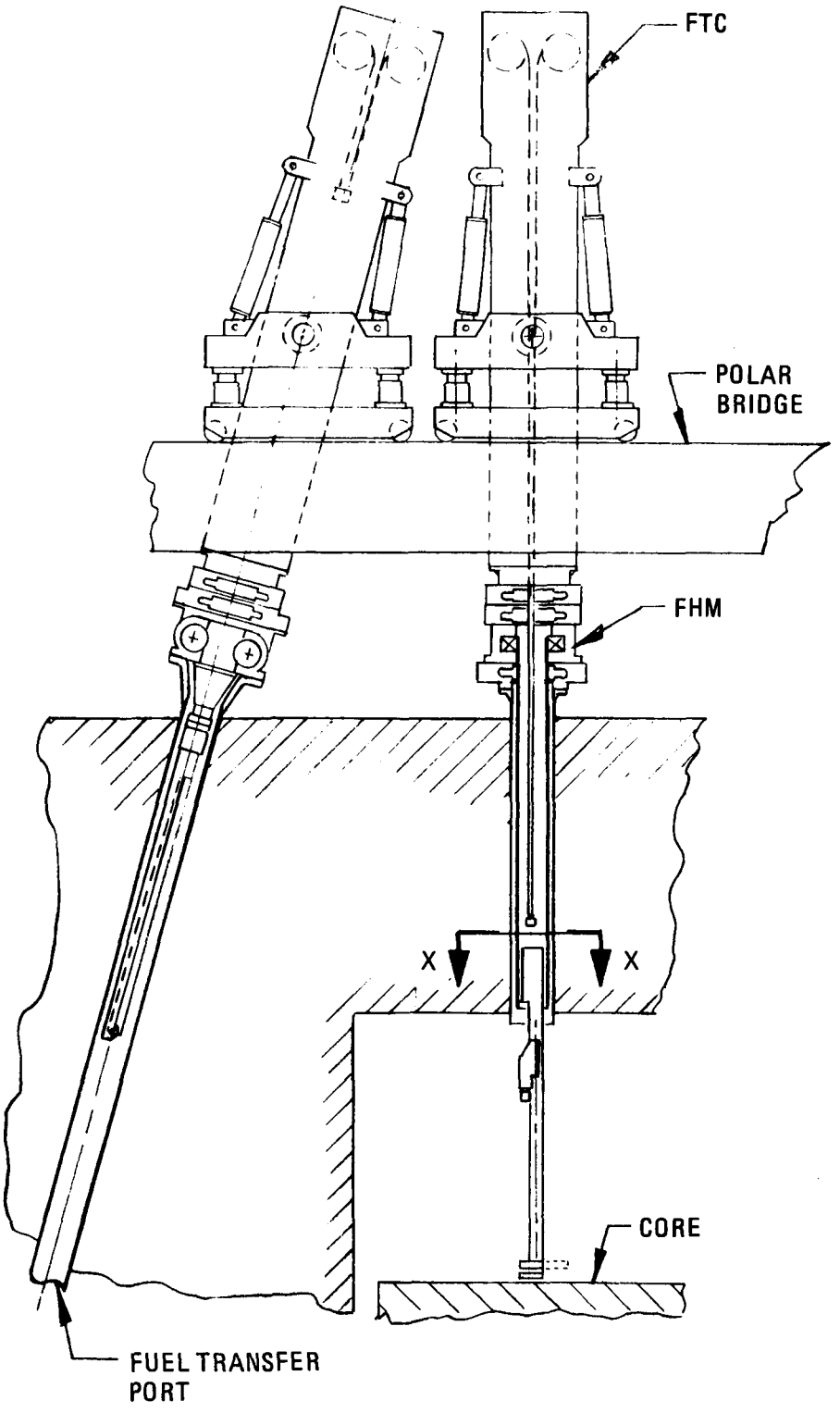

Fig. 1-24. Concept B up-flow core general arrangement

4. Install FHM cask, purge interspaces, and open isolation valves.

5. Lower FHM from cask into penetration, secure, connect services, and close isolation valve.

6. Orient FHM and lower inner sleeve to contact top of core.

7. Install fuel transfer cask (FTC), purge interspaces, and open isolation valves.

8. Deploy grapple arm, and lower carrier to engage grapple with element.

9. Raise element above core, and return grapple arm to central position.

10. Lower FTC grapple, and engage top of FHM grapple.

11. Unlock FHM grapple from grapple arm, and rotate arm to clear.

12. Raise element into FTC.

13. Close isolation valves and purge interspaces.

14. Disengage FTC, move to inclined transfer chute, engage, purge, and open isolation valves.

15. Deposit element in pool, pick up new element, and return FTC to penetration.

In the down-flow refueling concept, the FHM operates in a central penetration in the bottom head of the PCRV and consists of two telescoping elements. The lower element is cylindrical and is locked into the penetration during refueling. The upper element is an open-sided cylinder or

U-shaped member and incorporates a folding radial arm, a grapple assembly, and a grapple and hoist assembly. The radial arm is hinged in such a manner that it can be rotated through 90 deg and locked in a horizontal position. The beam carries with it the assembly which grapples and handles the core elements. The grapple assembly runs on ways in the beam; it is ball-screw-actuated and driven by a motor housed in the lower cylindrical element.

The entire upper assembly is rotatable, driven also by motors in the lower element. Thus, by combined rotation of the upper assembly and translation of the grapple assembly along the beam, all element positions in the core can be reached.

The radial arm is a twin beam configuration with the grapple assembly riding between the two beams. A rotating trunnion or turntable arrangement allows the radial arm to be folded while the grapple assembly maintains a vertical attitude. After an element has been traversed to the center it is regrappled either from above or below and lowered downward through the body of the machine into the fuel transfer cask below the PCRV. Figure 1-25 shows the FHM installed, the radial arm extended, and one of the peripheral elements grappled prior to removal. Withdrawal forces, such as might occur with a bowed element, are reacted by grappling an adjacent element with a secondary, fixed grapple. Element cooling is performed in a similar manner to the up-flow concepts.

The following estimated refueling times for a demonstration plant are based on a typical replacement and/or rotation of fuel, blanket, and shield elements. No allowance has been made for replacement or shuffling of side shield elements in the case of the down-flow core. The estimates include allowances for cool-down, start-up, and operating efficiency.

Up-flow, concept F	14.6 24-hr days
Up-flow, concept B_3	17.7 24-hr days
Down-flow	24.0 24-hr days

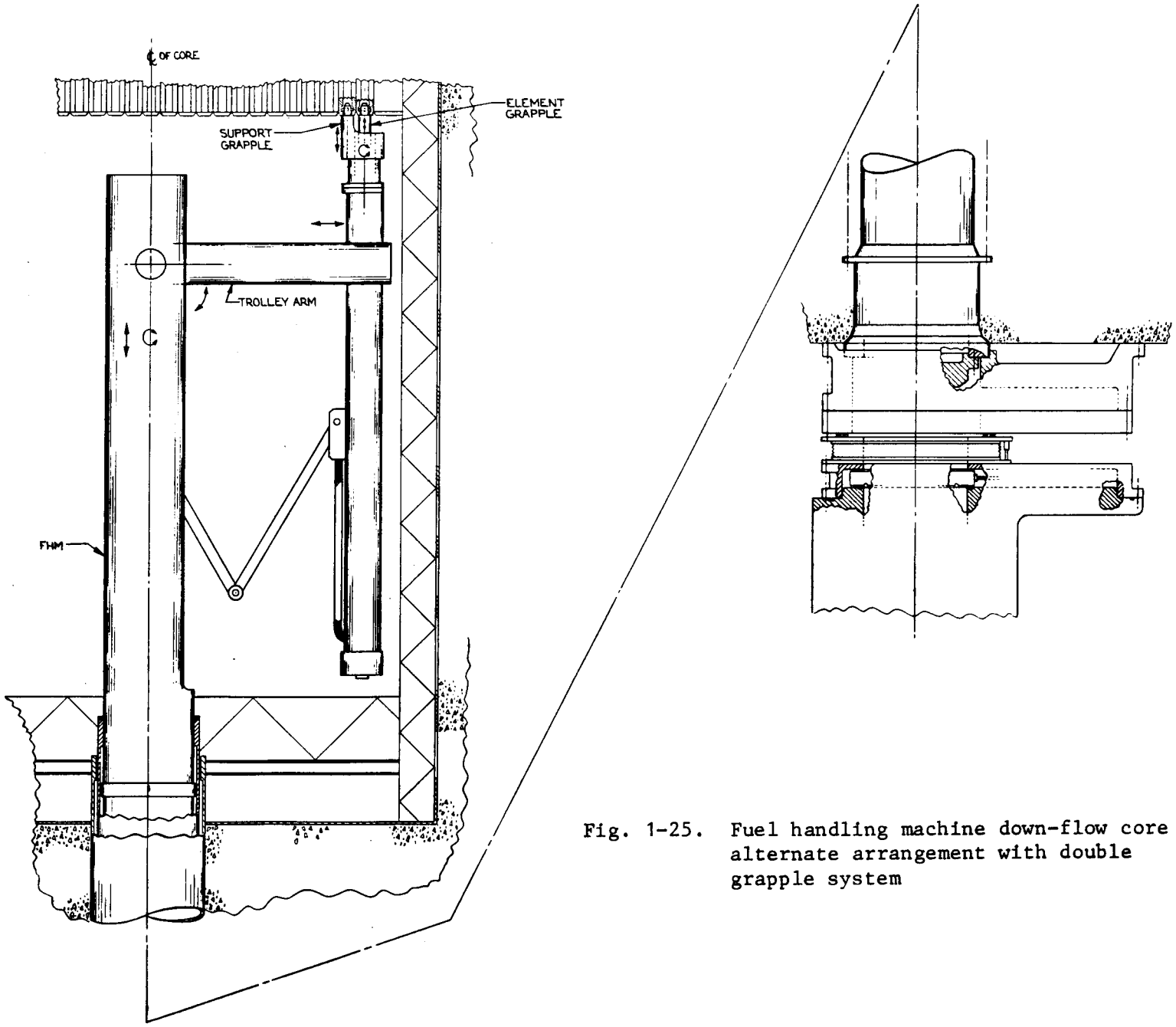

Fig. 1-25. Fuel handling machine down-flow core alternate arrangement with double grapple system

A study report has been prepared which deals with the subject in greater depth and deals also with procedures for handling internals replacement, equipment failures, and element cooling.

1.17. REACTOR INTERNALS SYSTEM

1.17.1. Core Support Structure

The purpose of this subtask is to assure the availability of the structural analysis methods and materials mechanical behavior required to assess the structural integrity of the GCFR core support structure under all anticipated operational and safety-related loading conditions.

Work accomplished during the last quarter included a preliminary evaluation of the effectiveness of the down-flow core seismic restraint in shifting core element natural frequencies to a higher range, and development of a conceptual design for a segmented up-flow core support structure.

During this quarter, preliminary stress analysis of the latest up-flow core support structure conceptual design was performed. Preliminary dynamic analysis of the up-flow grid plate was also performed.

1.17.1.1. Preliminary Stress Analysis of Up-Flow Core Support Structure. A preliminary stress analysis was performed on the latest conceptual design for the up-flow core support structure (Fig. 1-26). Thermally induced loads and estimated seismic loads were included in the analysis. The results indicate that the concept is feasible.

1.17.1.2. Preliminary Dynamic Analysis of the Up-Flow Grid Plate. The up-flow core conceptual design employs a core barrel; hence, the grid plate thickness is not determined by deflection considerations, as in the down-flow reference design, but by the vertical seismic response of the core/core support system. For the purpose of calculating grid plate thickness, the minimum acceptable value for the fundamental vertical frequency of the core/core support system was taken as 1-1/2 times the fundamental vertical frequency of the PCRV.

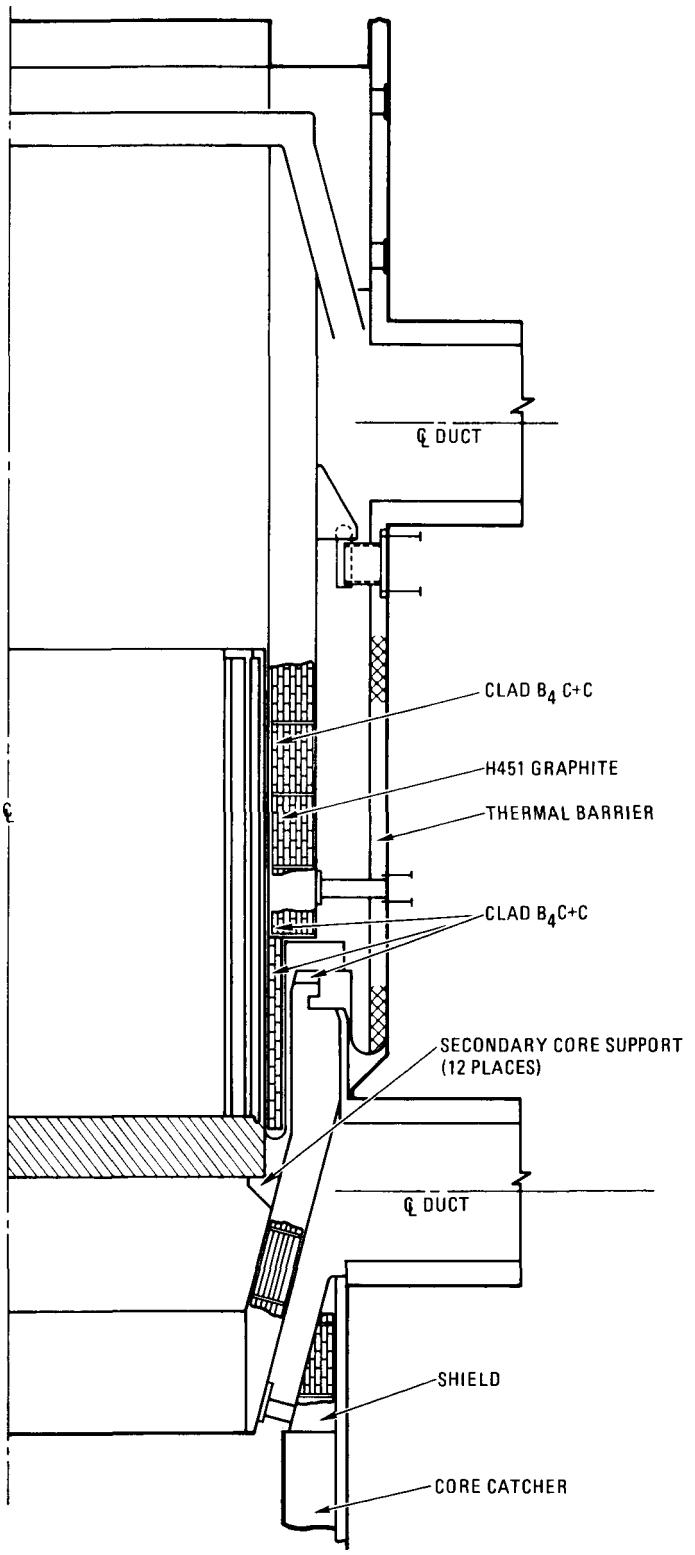

Fig. 1-26. Up-flow shielding conceptual design

Note that Fig. 1-26 shows a one-piece grid plate. The sandwich-type grid plate employing pneumatic hold-down of the fuel elements is no longer part of the up-flow conceptual design.

The fundamental vertical frequency of the PCRV for the worst case soil condition (rock) is presently given as 12.1 Hz. A grid plate thickness of 533 mm (21 in.) results in a core/core support system vertical fundamental frequency of 19 Hz, which satisfies the criterion for 1-1/2 times the PCRV vertical frequency. The grid plate thickness for the up-flow conceptual design is therefore established at 533 mm (21 in.).

1.21. PRIMARY COOLING SYSTEM

1.21.1. Main Helium Circulator, Valve, and Service System

The purpose of this subtask is to develop the helium circulator, its service system, and the main loop isolation valve to demonstrate performance and reliability by testing under anticipated operating conditions. The overall objective for FY-79 is to continue conceptual design and performance analyses of the reference design circulator and support the alternate design studies for an up-flow core. Layouts will be made of the compressor assembly, service system, and loop isolation valve. Test rigs will be designed for (1) testing the bearings, seals, and bearing water supply system and (2) testing a scale-model compressor and loop isolation valve.

1.21.1.1. Circulator for Up-Flow Core Design. The main helium circulator configuration (including the compressor assembly and the electric motor drive) is basically the same for top, horizontal, and bottom mounting. The only significant difference is in the thrust bearing loads. The larger thrust bearing for horizontal installation will be compensated for in reduced motor cost and simpler compressor bearing drain system. The thrust bearing loads in a bottom mounted circulator are undesirably large and will result in additional bearing costs. However, the thrust bearing is not considered a high risk item or high differential cost item. The impact on the PCRV and handling equipment will determine the overall cost effectivity and desirability for main circulator orientation.

Since the top and bottom mounted circulator installation is basically the same as for the down-flow core design, no additional layouts or performance analyses were required for these two installations. The horizontally mounted circulator requires some modification, which is described below.

Because a solid coupling is specified by the electric motor contractor, it is necessary to design a support system in which the motor and compressor assembly move together with movements in the PCRV liner. Two basic installations were investigated, i.e., cantilever off the side of the PCRV and direct support on the PCRV matt, and both appear feasible. In the configuration shown in Fig. 1-27, the motor mount consists of a large pipe surrounding the bottom half of the motor. The pipe has a cutout with mounting pads for supporting the motor and is bolted to the same PCRV liner as the compressor assembly. It is very stiff to provide a natural frequency above the motor operating speed as well as a rigid response during earthquakes. The cutout on top of the pipe allows room for the motor auxiliaries and for servicing the coupling and compressor shaft seal. As an alternate, the PCRV could be extended under the pipe.

A pipe diffuser (Fig. 1-28) was designed in lieu of a vaneless-type diffuser as used for the top mounted circulator. This diffuser has a three-dimensional diffusion which reduces the overall diameter by 0.75 m (2.5 ft). The efficiency is as high as, or better than, that of the vaneless diffuser. At the end of the diffuser pipes is a pipe elbow which turns the helium gas in the direction of the exit duct.

To provide smooth flow into the valve and into the compressor inlet, a long inlet duct would be required, which is not compatible with the steam generator exit duct location. Therefore, it is necessary to design the circulator inlet duct with a bell-mouth entrance located in a large plenum pipe exiting from the steam generator as shown in Fig. 1-29.

It is the conclusion of the circulator installation study that the circulator has no impact on the up-flow core decision. The horizontal installation is the most desirable orientation and has been shown to be feasible. However, the impact on the PCRV design may determine the overall feasibility.

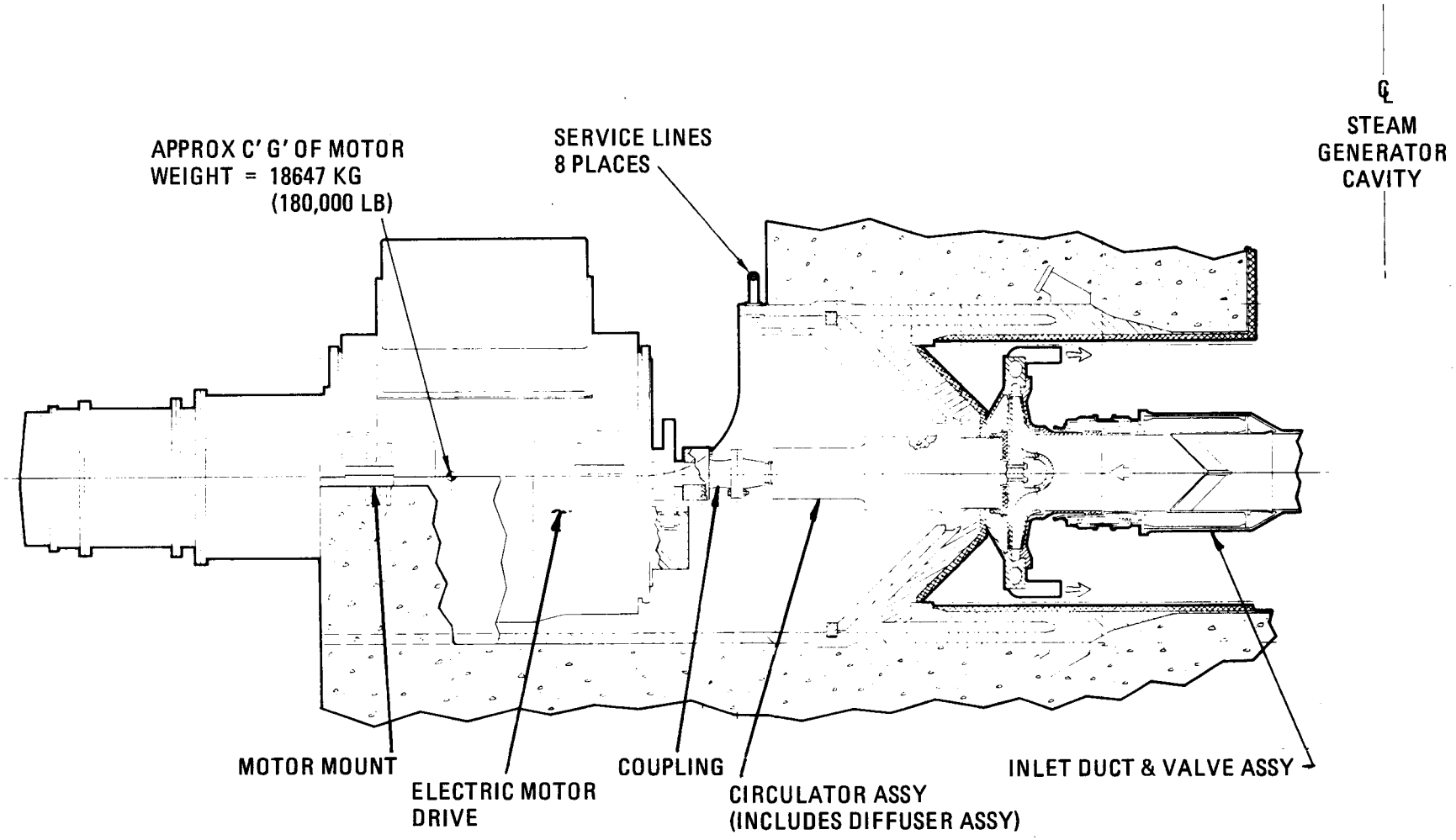

Fig. 1-27. Installation of GCFR main circulator in a horizontal PCRV penetration

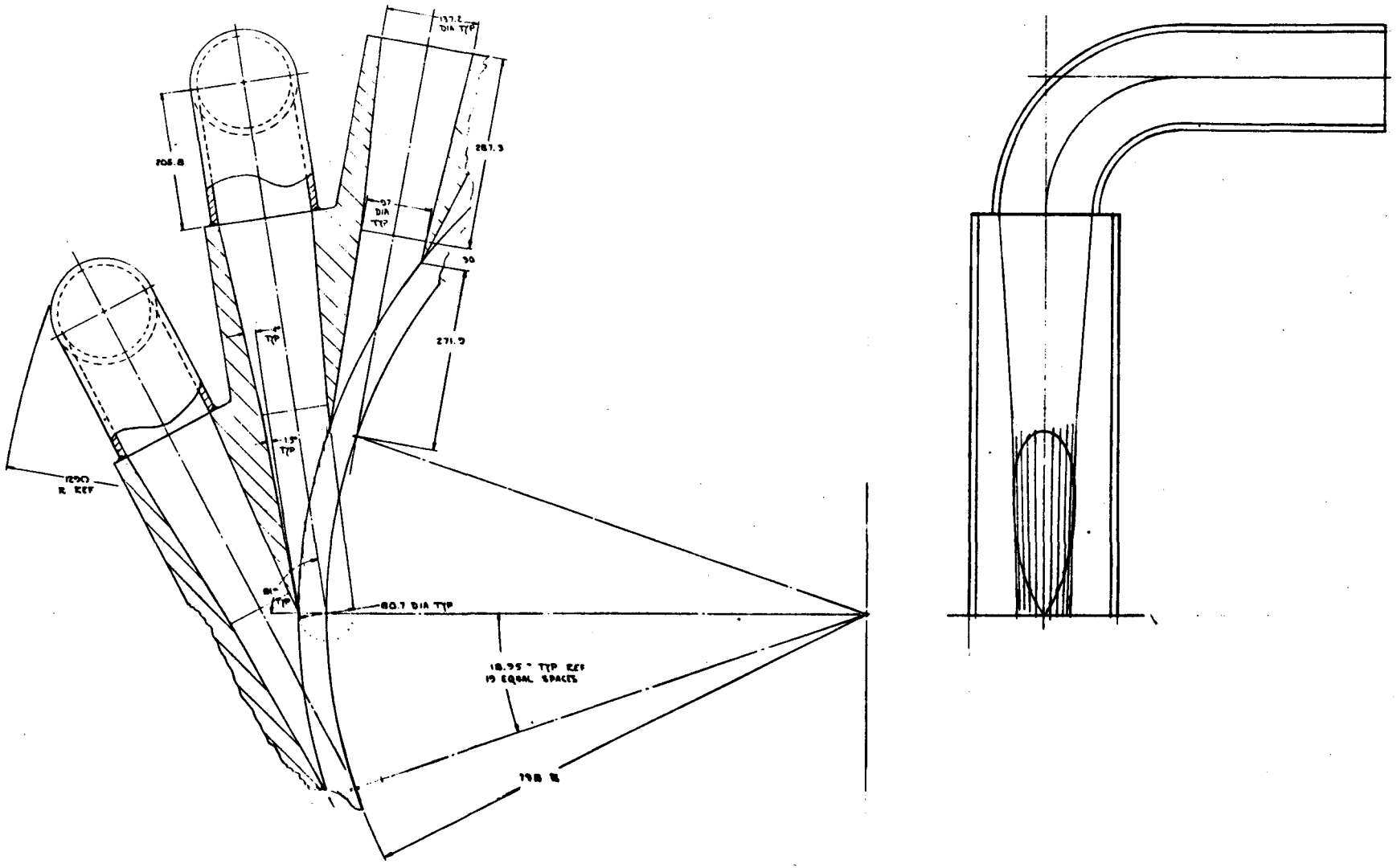

Fig. 1-28. Pipe diffuser

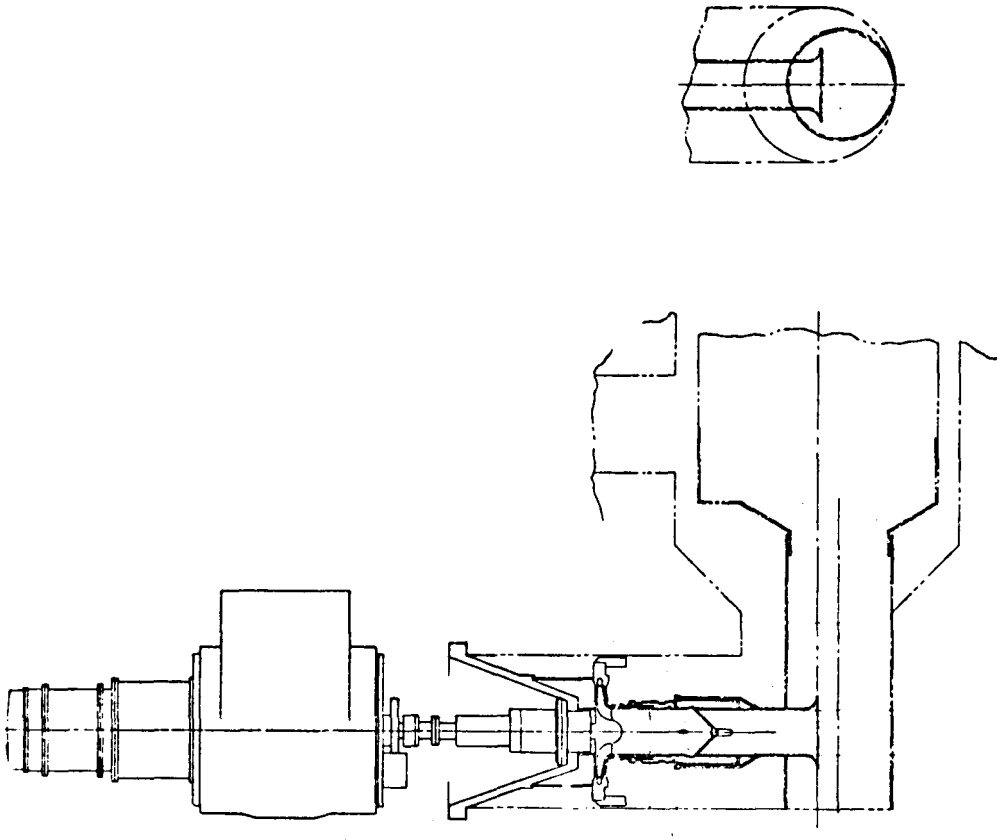

Fig. 1-29. Inlet duct arrangement for GCFR main helium circulator in a horizontal installation

1.21.1.2. Electric Motor Drive. The Westinghouse report for the GCFR main helium circulator electric motor drive was received in December 1978; it was reviewed by GA and Helium Breeder Associates (HBA), and comments were submitted to Westinghouse. Westinghouse consequently revised the report and presented it again in February 1979 in a meeting attended by representatives from Westinghouse, GA, and HBA. The final report was accepted by GA and a request for quotation on Phase II (bearing development) was issued. The final report by Westinghouse contained the following conclusions:

1. The external synchronous drive motor is the most feasible concept, with maximum speed of 3600 rpm.

2. The commercial drive motor is scalable from the demonstration plant drive motor.

3. Submerged drive motors are not recommended because of the higher risk in development and longer development time.

4. A motor bearing development program for the damped bearing is recommended. It will include analytical models, scale model tests, and full-scale tests.

1.21.1.3. Rotor Dynamics, Shaft, and Bearings. A preliminary critical speed analysis was done to evaluate the feasibility of a 37,000-kW (50,000 hp) motor at 3600 rpm as a possible commercial size circulator. This analysis assumed a five-bearing configuration (two on the compressor, two for the motor, and one at the pony motor) with the rotor length increased for the increased power. The first critical speed obtained was greater than the 3600 rpm operating speed when using rigid bearings.

1.21.1.4. Main Loop Isolation Valve. The horizontal installation of the main helium circulator requires a special main loop isolation valve (Fig. 1-30). The valve is a two-blade flapper valve, installed in the horizontal cross duct immediately upstream of the main circulator. The valve is

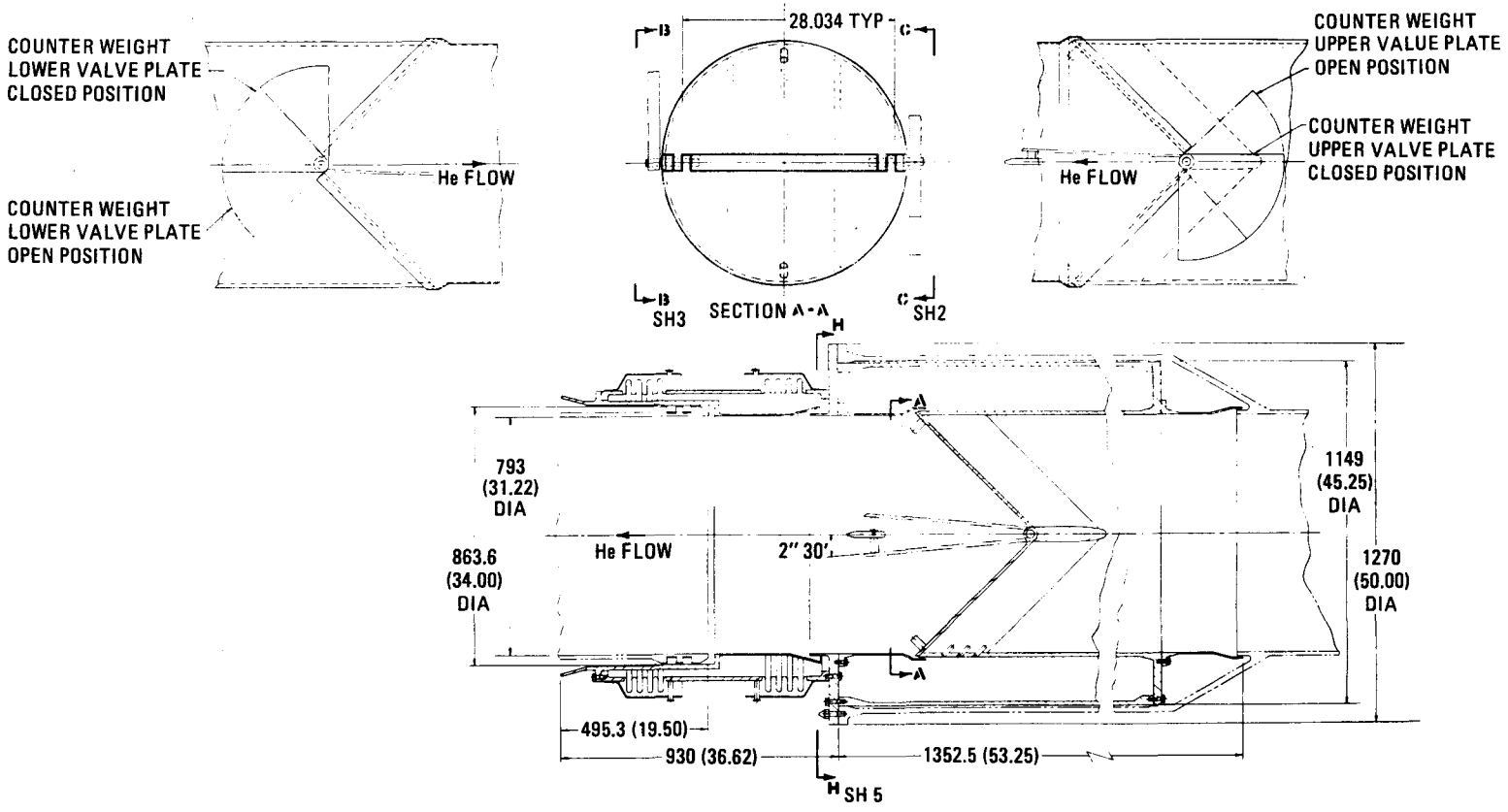

Fig. 1-30. Horizontal valve main loop primary coolant

gravity closing. When the valve is closed, the valve blades form a 45-deg angle with the duct centerline. Each blade has a counterweight attached to a shaft. The counterweight of the upper blade exerts opposite and more torque on the shaft than on the blade, thus providing closing torque. The lower blade exerts more torque on the shaft than the associated counterweight, thus providing closing torque. Both closing torques are of the same amount, determined by counterweights of different size. Suction from the circulator after start-up overpowers closing torque and opens the valve. Gas flow holds the valve open with both blades forced against stops. If flow ceases or reverses, the valve closes automatically. Backflow catches on the aft side of the valve blades, thus helping to close the valve. If one valve blade sticks in the open position, a burst of high-pressure helium through the close-assist jet will generate additional closing torque to free a sticking shaft bearing.

Valve blade position indication is provided through fluidic devices, one for each blade, working on the circumference of the counterweight. As the valve opens, the exit gap in front of the jet increases, thus reducing flow resistance. Jet flow can be measured from the control room. If a counterweight is severed from the shaft or the shaft is sheared off, the control surface runs off the jet exit, thus increasing the jet flow.

The valve is bolted to the end flange of the horizontal inlet duct. Misalignment between the centerline of this duct and the centerline of the circulator assembly are compensated by dual bellows. Overload limiting devices protect the bellows from excess deformation during handling and installation. The attachment bolts are installed and removed by remote handling equipment. After removal of the circulator and the attachment bolts, it is possible to remove and replace the valve if required, using the circulator handling cask.

A metal O-ring seals the area between the valve and inlet duct flange; dual piston rings seal the space between the valve and circulator assembly.

The horizontal inlet duct (Fig. 1-29) attaches to a vertical plenum coming down from the steam generator. A bell-mouth-shaped entry reduces inlet losses to the short inlet duct. Vertical thermal expansion of the plenum is taken in a piston ring seal between the plenum and the outlet cone of the steam generator.

Further study of the flow conditions through the valve and bearing friction forces is required to determine the sizing of the counterweights. Results of the one-third model flow test will be used to verify the analysis. Although the primary function of the valve is to close momentarily in case of a circulator shutdown, it must also open at very low pressure differential during depressurized refueling. For natural convection and pressurized flow, the valve must remain open at 5% flow.

It is concluded that the horizontal valve installation is feasible and that it has no differential cost impact on the up-flow core decision.

1.21.1.5. Aerodynamic Design

Impeller Design

The design of the full-inducer impeller was completed by the definition of a distribution of blade thickness to be added to the blade central surface previously defined. Since the computer program used in the aerodynamic analysis takes into account the curvature of the hub and shroud profiles, the axial velocity distribution predicted for the inlet of the impeller is closer to the actual distribution in that it is nonuniform with radius. This leads to a distribution of relative inlet angle which cannot be accommodated by an inducer with all-radial sections, and the inducer sections have a varying amount of lean from the radial direction as shown in Fig. 1-31.

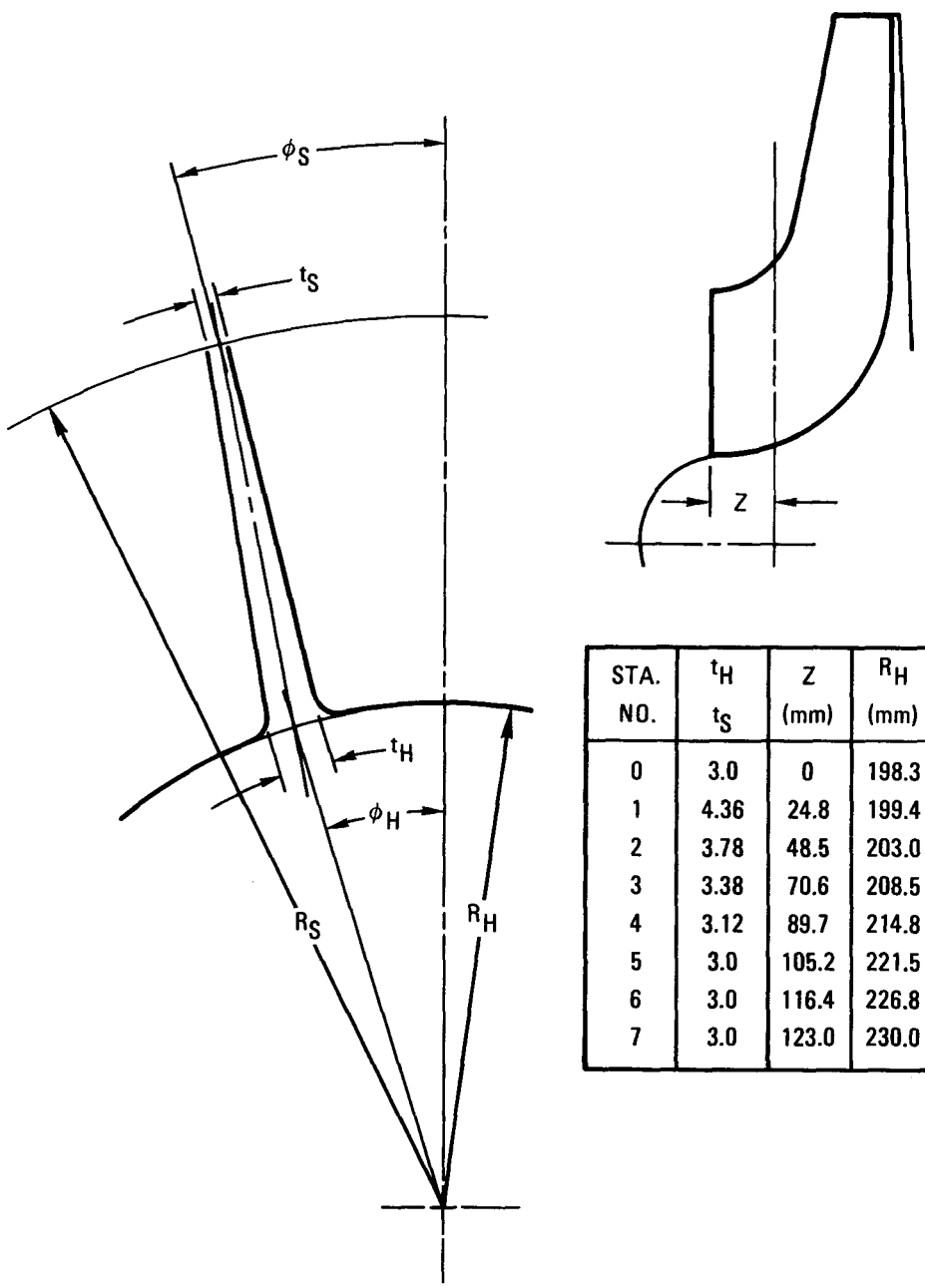

STA. NO.	t_H / t_S	Z (mm)	R_H (mm)	ϕ_H (DEG)	R_S (mm)	ϕ_S (DEG)
0	3.0	0	198.3	$22^0\ 50'$	396.5	$12^0\ 0'$
1	4.36	24.8	199.4	$16^0\ 31'$	399	$8^0\ 37'$
2	3.78	48.5	203.0	$10^0\ 59'$	406.3	$5^0\ 42'$
3	3.38	70.6	208.5	$6^0\ 44'$	418.4	$3^0\ 21'$
4	3.12	89.7	214.8	$4^0\ 0'$	434.5	$1^0\ 43'$
5	3.0	105.2	221.5	$2^0\ 20'$	454.0	$0^0\ 40'$
6	3.0	116.4	226.8	$1^0\ 25'$	476.0	$0^0\ 8'$
7	3.0	123.0	230.0	$1^0\ 2'$	500.0	$0^0\ 0'$

Fig. 1-31. Coordinates for inducer

The thickness distribution of the blade had to be determined from the stress limitations of the material. Since the blade sections in transverse planes as shown in Fig. 1-31 were nonradial, the centrifugal forces on the blade sections produced bending moments in the sections. The resulting stresses were determined first of all for constant taper ratios (t_H/t_s) of 2, 3, and 5, with a constant shroud thickness (normal to the blade surface) of 5 mm. Then several iterations were made for a taper ratio distribution between the stations to give a total stress distribution that was everywhere lower than the allowable stress for 40-year life.

The third iteration of taper ratio distribution was considered to be acceptable and was incorporated in the layout preparatory to final design and analysis. This distribution of taper ratio is shown in Fig. 1-31.

In the actual layout, the hub thickness at stations 0 and 1 was modified from that shown in Fig. 1-31 to give an aerodynamically more efficient leading edge. The leading edge radius was increased linearly with decreasing radius from 2.5 mm at the shroud to 7.5 mm at the hub radius. The blade thickness was faired from the leading edge radius to the calculated thickness at a point near station 1. It is expected that there will be sufficient support for the leading edge from the remainder of the inducer to prevent excessive stress at the leading edge hub radius. More detailed finite-element stress methods should be applied to confirm that this assumption is correct.

Diffuser Design

The standard diffuser assumed for this compressor is a vaneless parallel-sided diffuser. An alternate "pipe" diffuser was also designed as reported below. The vaneless diffuser width is equal to the rotor tip width at the rotor exit, tapers in to a width equal to 98% of the rotor

tip width at a radius equal to 1.2 times the rotor tip diameter, and remains constant at this value to the active section exit radius, which is equal to twice the rotor tip diameter. The diffuser has an active section exit diameter of 3131 mm (10.27 ft). A curving section is added to return the flow to the axial direction. This brings the total exit diameter to 3606 mm (11.96 ft). To reduce this diameter for the horizontal arrangement of the circulator, pipe diffusers were designed.

The pipe diffuser has been used in small gas turbine engines. It consists of a series of holes drilled and taper-reamed in a solid ring surrounding the impeller (Fig. 1-28). Each passage has two sections of differing taper, the first starting at some reference radius slightly greater than the impeller tip radius, where its diameter is equal to the vaneless space width, and extending with a small (around 3 deg) expanding taper angle to just beyond the intersection with the next passage. From this point, where it forms a diffuser throat, the passage diverges further at the diffuser design cone angle to the exit, where the area is as required for the throat to exit the diffuser area. In the main helium circulator, it is necessary to redirect the flow back to the axial direction. To do this, tube corners are added to the diffuser exits.

The diffuser passages are arranged so that the entire space at the entry end is taken up by the diffuser holes; that is, there is no cylindrical surface between the passages at the inner radius or inlet end. The intersections between the passages are sharp-edged ridges of elliptical plan form roughly aligned with the gas flow direction. One of the design objectives is to arrange the passages so that in the section plane containing the passage center lines, the angle between the line bisecting the wedge-shaped areas between the passages and the gas flow direction at the radius of the intersections is minimized. Two diffusers of this type were designed for the GCFR main circulator, one having 19 passages, the other 23. The incidence angles for the two diffusers are -3.28 and +2.89 deg, respectively. Models of these two diffusers will be built and tested in

the compressor scale-model tests to determine which is the better arrangement for the proposed impeller.

1.21.2. Steam Generator

The steam generator function is to transfer heat from the reactor primary coolant (helium) to the secondary coolant (water/steam) during normal plant operation. The steam generator is subject to cyclic or repeated steady and transient operating conditions in its 30-year design life. The objective of this task is to design and develop a steam generator which meets the operational, performance, and safety requirements of the GCFR. The present development consists of the following major item.

1.21.2.1. Up-Flow/Down-Flow Core Selection. The study was focused on top-exhaust steam generator arrangement (Fig. 1-32) for the up-flow core configuration. The task has been completed, and the evaluation has led to the following conclusions:

1. The top-exhaust arrangement satisfies demonstration plant conceptual requirements.

2. Scalability of top-exhaust design is limited by the height restrictions, tube number restrictions, and bimetallic weld envelope allowance.

3. The expansion loop material must be Alloy 800H.

4. The up-flow/down-flow core decision should not be significantly affected by the steam generator design.

The study also recommended that a bottom-exhaust steam generator (Fig. 1-33) be used for the up-flow core. The feasibility of this arrangement requires further study.

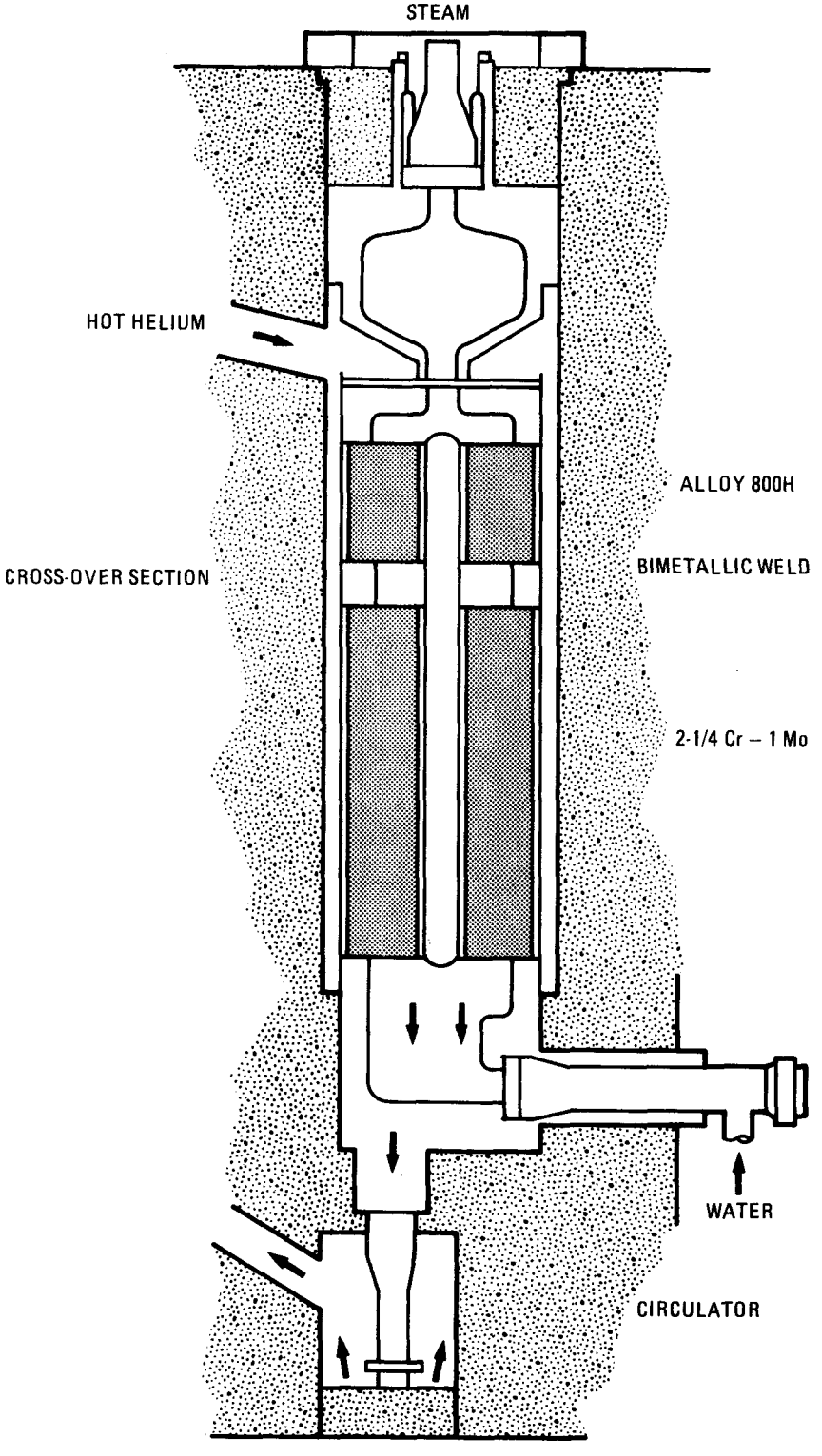

Fig. 1-32. GCFR top exhaust for steam generator up-flow core

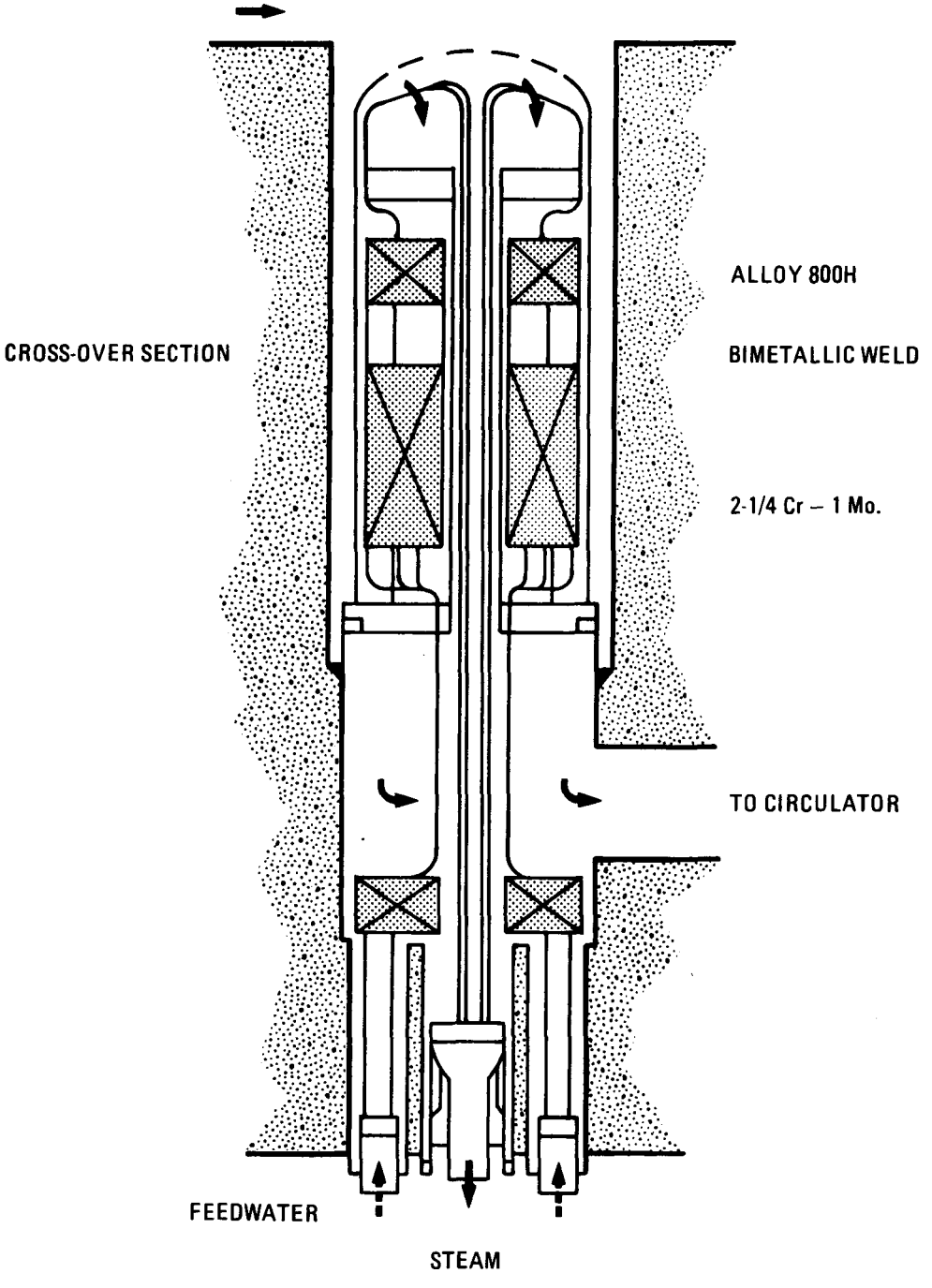

Fig. 1-33. GCFR bottom exhaust for steam generator down-flow core

1.28. CORE AUXILIARY COOLING SYSTEM (CACS)

1.28.1. Auxiliary Circulator, Valve and Service System

Current studies are directed toward evaluation of the impact of several different potential plant system changes and PCRV arrangements on the design of the auxiliary circulator, valve and service system. This work is principally in support of the up-flow/down-flow core studies.

1.28.1.1. Current Reference Design. Latest auxiliary circulator operating parameters for design point conditions [design and depressurization accident with helium ingress (DBDAH)] are shown in Table 1-4. Also shown are parameters for DBDA with air ingress (DBDAA), refueling conditions, and pressurized reactor conditions. The data shown in Table 1-4 together with the general arrangement of the auxiliary circulator will remain the same regardless of circulator orientation in the PCRV.

1.28.1.2. Up-Flow/Down-Flow Support Studies. None of the PCRV configurations proposed for the GCFR up-flow/down-flow studies have much impact as far as the auxiliary circulator and auxiliary loop isolation valve are concerned. In the bottom-mounted circulator arrangements, shaft thrust loads are additive. Bottom mounting should lower the probability of oil ingress from the auxiliary circulator bearing lubrication system because gravity forces are now trying to keep the oil away from the inside of the PCRV.

The auxiliary loop isolation valve can be readily adapted to either top or bottom mounting and with appropriate use of counterweights can be made to either fail open or fail closed. Cost and schedule impact for either configuration appears almost nil as far as the auxiliary circulator and the auxiliary loop isolation valve are concerned.

TABLE 1-4
GCFR AUXILIARY CIRCULATOR PARAMETERS

Item	Parameters[a]	Pressure	DBDAH	DBDAA	Refueling
1	Molecular weight	4.000 (4.000)	4.000 (4.000)	6.170 (6.170)	4.000 (4.000)
2	System pressure, MPa (psi)	8.832 (1280.000)	0.175 (25.300)	0.175 (25.300)	0.101 (14.700)
3	Temperature, K (°F)	613.732 (645.000)	494.278 (430.000)	494.278 (430.000)	366.490 (200.000)
4	Density, m^3 (lbm/ft^3)	6.925 (0.432)	0.170 (0.011)	0.262 (0.016)	0.133 (0.008)
5	System pressure drop, (psi) kPa	1.103 (0.160)	11.673 (1.693)	16.824 (2.440)	5.309 (0.770)
6	Mass flow rate, kg/s (lbm/sec)	14.742 (32.500)	6.591 (14.530)	9.811 (21.630)	4.536 (10.000)
7	Volumetric flow rate, m^3/s (ft^3/sec)	2.128 (75.183)	38.759 (1369.588)	37.406 (1321.769)	34.042 (1202.888)
8	Head delivered, kJ/kg (ft-lbf/lbm)	0.155 (53.299)	66.641 (22979.665)	62.266 (21470.956)	38.679 (13337.623)
9	Driver power, kW (hp)	3.011 (4.038)	580.385 (778.309)	807.262 (1082.557)	231.838 (310.900)
10	Driver torque, N-m (lbf-ft)	147.146 (108.515)	1556.992 (1148.224)	2243.982 (1654.854)	708.142 (522.228)
11	Rotational speed, rad/s (rpm)	20.461 (195.426)	372.732 (3560.000)	359.718 (3435.704)	327.365 (3126.694)
12	Rotor diameter, m (ft)		1.665 (5.463)		
13	Rotor tip width, mm (in.)		72.906 (2.870)		
14	Specific speed, English, nondimensional		0.544 (70.589)		
15	Specific diameter, English, nondimensional		4.326 (1.818)		

[a] Items 1, 2, 3, 5, and 6 are program inputs; items 2, 3, 4, and 7 are circulator inlet conditions.

1.28.2. Core Auxiliary Heat Exchanger (CAHE)

Conceptual CAHE short bayonet arrangements (Fig. 1-34) were developed for up-flow and down-flow cores. Compared with the helical bundle design, the bayonet design has the following advantages:

1. Better in-service inspection capability.
2. Lower tube stresses.
3. Simplified structural analysis.

The helium pressure drop, however, is higher in a bayonet CAHE.

Both bayonet CAHEs developed meet current design requirements. The bayonet tube CAHE for the up-flow core appears to have the disadvantages that the unit is nondrainable, and the tubesheet is exposed to hot helium. Insulation of the tubehseet complicates the tubesheet site weld. The bayonet CAHE is to be evaluated against the helical bundle in selection of a reference concept.

A parametric stress analysis on expansion loops of the helical bundle CAHE was completed. The effort was to determine the support configuration to satisfy dynamic and thermal stress considerations for the conceptual design. The tubing material is assumed to be 2-1/4 Cr-1 Mo, and the MODSAP computer program (Ref. 1-3) was used. The analysis showed that the expansion loop arrangement requires intermediate supports as well as lateral restraints at the tubesheet and at the bundle support plates. This task completes the preliminary evaluation of helical CAHE concept and establishes the helical CAHE as a viable candidate of the reference design for the up-flow core.

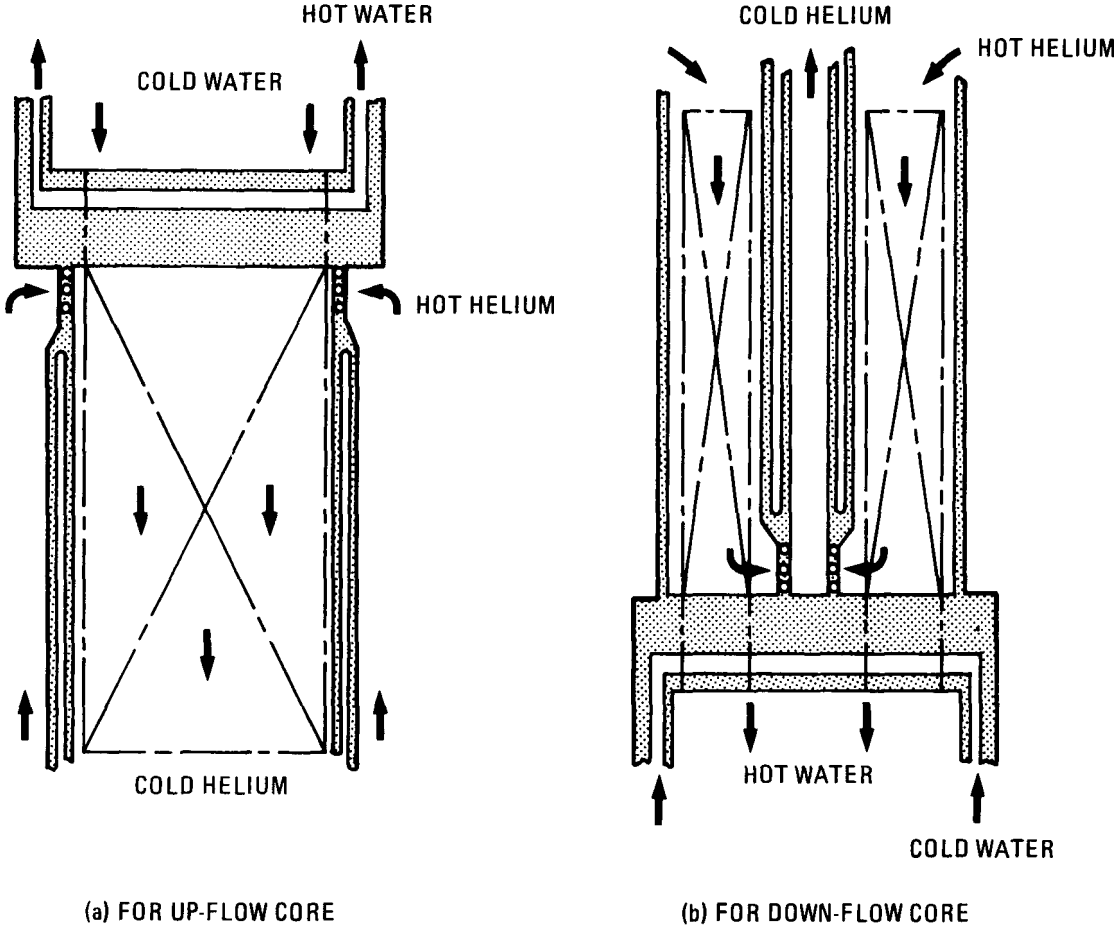

Fig. 1-34. Schematic of bayonet CAHE arrangements

1.32. PLANT PROTECTION SYSTEM

Conceptual plant protective functions were developed during this quarter as follows:

1. Two reactor trip systems to limit damage to core assemblies and preserve the integrity of the primary coolant barrier.

2. A loop isolation and dump system to limit the quantity of water that can leak into the PCRV following a steam generator failure. This system includes a moisture monitoring system.

3. A main loop shutdown system to limit the temperatures of the steam generator tubes following mismatches of primary and secondary coolant flows.

4. A safety cooling system initiation system to start the safety cooling system following a reactor trip and a loss of the main loop cooling system.

5. A core auxiliary cooling system initiation system to start the core auxiliary cooling system following the loss of the main loops or the safety cooling system, or following a primary coolant depressurization accident.

6. A PCRV pressure relief block valve closure interlock to ensure that at least one PCRV relief valve is always available to protect the PCRV and primary coolant boundary.

7. A core auxiliary heat exchanger isolation system to prevent adverse effects of core auxiliary heat exchanger failures.

8. A containment isolation system to limit the pressure buildup in the containment due to secondary system leaks to preserve the integrity of the containment structure.

The design bases and conceptual block diagrams for these functions are discussed in Ref. 1-4.

REFERENCES

1-1. Woo, H. H., "CSTRES. A Computer Program for Evaluating the Thermally Induced Interaction Between Helical Tube Bundles and Their Support Plates," DOE Report GA-A15162, General Atomic Company, December 1978.

1-2. "HTGR Generic Technology Program Safety, Systems and Component Design and Development, Quarterly Progress Report for the Period Ending March 31, 1978," DOE Report GA-A14922, General Atomic Company, April 1978.

1-3. Johnson, J. J., "MODSAP - A Modified Version of the Structural Analysis Program SAP IV for the Static and Dynamic Responses of Linear and Localized Nonlinear Structures," ERDA Report GA-A14006, General Atomic Company, June 1976.

1-4. System Description 903670, General Atomic unpublished data.

2.0. REACTOR CORE

2.1. REACTOR CORE DEVELOPMENT

2.1.1. Materials Development

2.1.1.1. Fuel and Blanket Materials Technology. The purposes of this subtask are to (1) maintain liaison with and surveillance of other DOE and non-DOE programs, especially the liquid metal fast breeder reactor (LMFBR) program, to enable utilization of the information on fuel and blanket materials obtained in these programs in the GCFR design; (2) participate in the fast breeder reactor Fuel Element Development Working Group and its subsidiary task groups; and (3) guide the laboratory and irradiation test programs for the GCFR.

A review of FBR fuel technology data, the planned GCFR irradiation test program, and the potential impact of conceptual design changes on the irradiation program is currently in progress. Upon completion of the review, recommendations for an augmented GCFR irradiation test program will be issued. The revised irradiation program will be designed to provide an adequate supply of irradiated fuel rods for use in the safety and design basis test programs to be carried out in the GRIST-II facility.

2.1.1.2. Cladding Shield and Structural Materials Technology

2.1.1.2.1. Cladding Technology

The GCFR cladding technology program consists of the study of the mechanical and oxidation behavior of GCFR ribbed cladding and advanced alloys. The mechanical behavior test program is being conducted at Argonne National Laboratory (ANL) and the oxidation behavior tests are being performed at GA.

2.1.1.2.1.1 Cladding Oxidation Test Program. The overall objective of the GCFR cladding oxidation test program is to determine the oxidation behavior of ribbed and smooth 20% cold-worked 316 stainless steel and smooth candidate advanced alloy claddings. This includes determination of:

1. The oxidation behavior of reference GCFR ribbed and smooth cladding fabricated by various techniques.

2. The oxidation behavior of smooth candidate advanced alloy claddings.

3. The effect of various pretreatments (i.e., cleaning procedures, passivation, etc.) on the oxidation behavior of ribbed and smooth cladding.

4. The oxidation behavior of the cladding in the range of impurity levels expected in the GCFR demonstration plant.

5. The cladding corrosion wastage allowance for use in the fuel rod design.

Prior to this reporting period, the first oxidation test OX-1 was completed. This test was conducted in an environment containing an H_2/H_2O ratio of 10. Oxidation behavior of all the alloys under test was found to be good to excellent in this type of environment.

During this reporting period, the oxidation test OX-2 was initiated. The test conditions are as follows:

Environment	Helium with impurities
Partial pressure of H_2	100 Pa
Partial pressure of H_2O	400 Pa
Temperatures	600° and 700°C

The environment of test OX-1 (i.e., H_2/H_2O = 10) was expected to preferentially oxidize chromium. In the environment of test OX-2, however, both iron and chromium oxides are stable. The oxidation behavior in the test OX-2 is expected to be very much different from that of test OX-1. Two interim examinations have been conducted, one at 100 hr and the other at 250 hr of exposure. Analysis of the weight gain data indicates:

1. Excessive oxidation of the ferritic alloys, i.e., HT-9 and D-57, was observed at 600°C but not at 700°C. Weight gains of about 2% in 100 hr were observed.

2. All other alloys appear to have good oxidation resistance in this environment.

3. Analysis of the oxide layer by x-ray diffraction shows that this oxide layer is essentially chromium-free iron oxide.

These observations indicate that this environment may be incompatible with ferritic alloys. However, these data and conclusions need to be substantiated by further testing.

The oxide layers of the test specimens from test OX-1 (5000 hr of exposure to an H_2/H_2O ratio of 10) have been partially analyzed by Auger electron spectroscopy. The results show that the oxide layers are chromium rich, as predicted by thermodynamic reasoning. The one exception to this observation is the electrochemically etched ribbed cladding specimen. Here the oxide layer is rich in iron. No explanation has been found for this observation.

2.1.1.2.1.2 ANL Mechanical Testing Program. The objective of the ANL mechanical testing program is to determine the effects of the following

factors on the behavior and mechanical properties of GCFR ribbed and smooth cladding:

1. Ribs, rib geometry, fabrication technique, and stress state.

2. Helium impurity levels typical of the environment expected in the GCFR demonstration plant.

Three biaxial creep rupture tests on unirradiated ribbed and smooth cladding have been completed at ANL. The results indicate that the ribs increase rupture life and do not affect strain at failure. The preparations for start-up of the fourth biaxial creep rupture test (ANL-IV) are still in progress at ANL.

Fifteen smooth and ribbed cladding specimens had been irradiated previously to a fluence of 3×10^{22} to 5×10^{22} n/cm^2 ($E > 0.1$ MeV) at 700°C. These specimens were subjected to biaxial stress rupture tests at the irradiation temperature of 700°C at ANL. Hoop to axial tensile stress ratio of 2 and unity were used in these tests. The overall results indicate that the ribs strengthen the cladding at a stress biaxiality of 2 in the irradiated condition.

Efforts to design an in-reactor creep experiment are under way at ANL. Although the overall experimental test matrix has been formulated, the question of which reactor, i.e., EBR-II or the FTR, should be used has not been decided. This decision will be based on cost estimates and schedule flexibility, which are currently being studied by ANL.

2.1.1.5. Irradiation Testing

2.1.1.5.1. F-1 Fast Flux Irradiation Experiment

The encapsulated fuel rods in the F-1 (X094B) experiment received burnup exposures in the range of 8 to 13.6 at. % [8×10^{26} n/m^2 total fluence and 6.1×10^{26} n/m^2 ($E > 0.1$ Mev)]. Postirradiation examination

(PIE) of the seven fuel rods removed at the termination of the experiment is continuing at ANL, and examination of special components (dosimetry and charcoal traps) continues at GA.

During this quarter, burnup analysis on rod G-8 was repeated on the midplane section and extended to fuel samples from the upper and lower regions in order to resolve an apparent inconsistency reported in earlier data. The current values are consistent with known reactor residence time but about 9% lower than that calculated by codes. The measured values for the upper, mid-, and lower fuel sections are 9.7, 11.5, and 10.6 at. %, respectively; the calculated midplane value is 12.6 at. %.

The final fission gas release results of fission gas sampling of the fuel rod plena in F-1 rods are given in Table 2-1 and Fig. 2-1 as percent fission gas release as a function of rod burnup. In general, the release values are consistent with values reported in the literature for similar irradiation conditions. Fission gas release values for the rods containing active charcoal traps are in the range of 58% to 85%; fuel rods containing sealed traps, G-1, G-2, G-3, and G-8, had release values of 100%, 96%, 65%, and 59%, respectively. Rod G-8 is an apparent anomaly with its high burnup of 11.5% and a release value of only 59%. The mean ratio for the Xe/Kr release fraction for all the rods is 0.90 ± 0.5 (only in the high burnup rod G-4 is the ratio unity). The 0.90 ratio appears to be consistent with diffusion as the rate-controlling mechanism. The remaining F-1 charcoal samples for mass and isotopic analyses have been shipped by GA to Idaho National Engineering Laboratory (INEL).

2.1.1.5.2. GB-10 Vented Fuel Rod Experiment

2.1.1.5.2.1. GB-10 PIE. ANL is proceeding to analyze samples of the GB-10 fuel to determine final fissile atom concentration. These data will permit an estimation of the end-of-life (EOL) power distribution in the GB-10 fuel rod.

TABLE 2-1
RESULTS OF GAS SAMPLING AND ANALYSES FOR F-1 FUEL RODS

Fuel Rod	G-1	G-2	G-3	G-4	G-6	G-8	G-9	G-10	G-11	G-12	G-13
Fission gas volume extracted, cc	117	112	39	264	64	176	133	160	174	157	175
Fission gas released to plenum[a], %	104	96	65	85	64	59	58	67	75	66	76
Rod average burnup, at. %	4.9	4.8	2.5	12.5	4.4	11.7	8.2	9.1	8.9	9.0	8.8
Fuel O/M	1.992	1.971	1.987	1.983	1.972	1.985	1.947	1.968	1.968	1.976	1.973
Clad i.d. max temp, °C	740	730	669	683	662	696	706	722	731	714	759
Centerline fuel temp[b], °C	2487	2485	--	1926	2260	1926	2090	2150	2150	2150	2284
Volumetric fuel temp[c], °C	1368	1305	--	1218	1171	1222	--	1255	1272	1255	1350

[a] Percent release values are based on measured burnup and fission product inventory data.

[b] The centerline fuel temperatures were calculated on run-by-run power data by ANL.

[c] The volumetric fuel temperature was derived from the LIFE-III (Ref. 2-1) code output, using eight radial zone and four axial zone temperature values at approximately the median irradiation residence time.

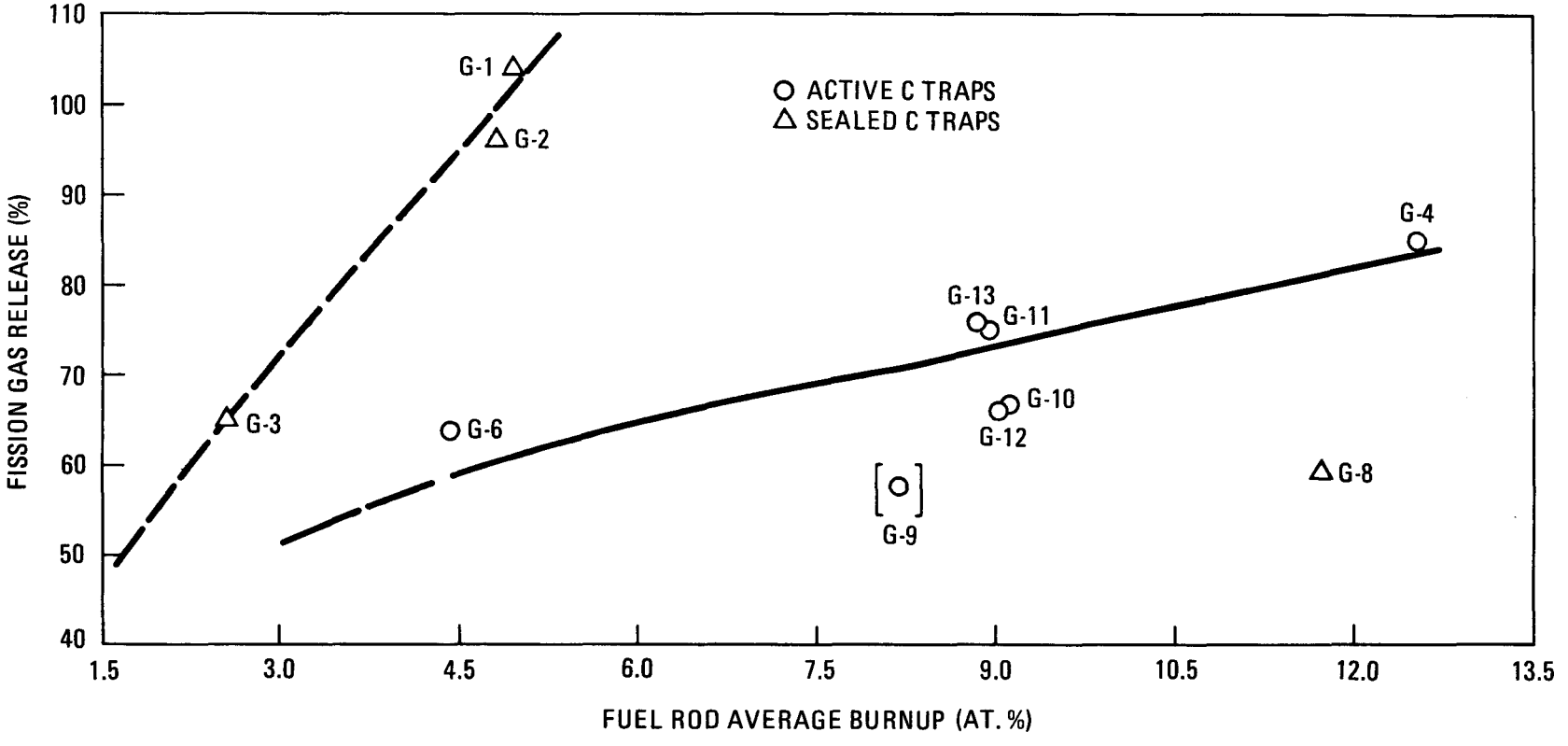

Fig. 2-1. Fission gas release versus fuel rod burnup

2.1.1.5.2.2. GB-10 Data Analysis. Data acquired from irradiation experiments during their operation in the case of vented fuel rods and from PIE of vented and sealed fuels is being assembled and analyzed. Processing and analyses will convert the data to useful forms for (1) understanding the behavior of the fuel and the processes leading to the observed fission product transport and redistribution, (2) application to the design of GCFRs (i.e., design data base), (3) model and code verification, and (4) support of GCFR licensing.

The release of fission gases from the fuel matrix of the mixed U-Pu oxide fuel rod in irradiation capsule GB-10 has been measured as a function of cladding temperature, linear heating rate, and burnup. The measurements have been used to derive diffusion parameters for use in the computer subroutine program GAREL used with the LIFE-III code (Ref. 2-1), and the results have been reported (Ref. 2-2). Nominal o.d. cladding temperatures used to determine the diffusion parameters are known only with large uncertainties, as discussed in Appendix B of Ref. 2-3. The uncertainties arise mainly from changes in the power distribution as a function of burnup in the fuel rod and capsule which were located in the steep thermal neutron flux gradient of the water reflector in the ORR poolside facility, and from possible bowing of the fuel rod. A series of analyses are planned with the aim of reducing the fuel temperature uncertainty to ±25 K. The analyses will use fissile nuclide distributions based on PIE data on the isotopic distribution of uranium and plutonium fissile atoms in the GB-10 rod. Neutronic calculations will provide the EOL power distributions. Thermal analysis of the fuel rod and capsule will then produce the EOL temperature distribution and corrections to be applied to the thermocouple readings. Revised o.d. cladding and fuel temperature distributions can then be incorporated into a thermal rod bowing analysis. Conversely, bowing of the rod, if significant, will affect the temperature distribution. Thus, an iterative solution of the temperature distribution and thermal bowing analyses may be required to find the solution that satisfies both conditions. Comparisons with the EOL calculated temperatures at the thermocouple locations with the thermocouple readings will be made

to evaluate the EOL temperature uncertainties. Finally, interpolation between the beginning-of-life (BOL) and EOL corrections to the thermocouple readings will be used to provide cladding temperatures with smaller uncertainties. The more precise cladding temperatures will permit a more satisfactory analysis of fission gas release measurements at various linear heating rates and burnups during the GB-10 irradiation. If this series of analyses and evaluations succeeds in reducing the uncertainties in the cladding temperatures, then the diffusion release parameters will be redetermined in a manner similar to that described in Ref. 2-3.

2.1.1.5.3. F-5 (X317) Grid Spaced Fuel Rod Bundle Fast Flux Irradiation Experiment

The F-5 irradiation experiment was designed to study the performance of fuel rods irradiated under simulated GCFR conditions to determine (1) the reliability of the GCFR fuel rod design and (2) the effect of a step power increase which simulates a 180-deg rotation of a subassembly at the core blanket interface in the proposed GCFR demonstration plant. The irradiation of the F-5 grid spaced bundle was begun in EBR-II, run 93, in January 1978. Approval has been granted by the EBR-II project for irradiation of F-5 (X317) to about 5 at. % burnup prior to the first interim examination. The first interim examination was started in April 1979. An interim examination plan has been formulated by EBR-II project, ANL, and GA.

The EBR-II reactor is in run 100 at this time. The lead rod in the F-5 bundle has reached a burnup of $\sim$4.0 at. % and the corresponding fluence is $\sim 4.0 \times 10^{26}$ n/m^2 (E > 0.1 MeV).

Work on methods for depressurization, fission gas collection, and resealing of F-5 fuel rods continues. Drilling trials have been completed and components for the rig have been ordered. It was originally planned to perform depressurization and resealing at Hanford Engineering Development Laboratory (HEDL), but recent cost estimates have prompted ANL to consider performing this work at ANL-MSD.

A schedule of tasks to be performed during the interim examination has been established. Depressurization and resealing of fuel rods for reconstitution is the pacing item in this schedule. Reinsertion of the reconstituted 19-rod bundle in EBR-II for the two-cycle low-power irradiation is currently planned for June 20, 1979.

Fabrication of components for the reconstitution of F-5 as a 19-rod bundle following the first interim examination is continuing at GA. Purchase orders for vendor fabrication subcontracts are in review. Criteria for the fuel rod bowing, fuel rod removal and insertion loads, and grid spacer rod clearances and tolerances will be established by the GCFR Core Mechanical Design Branch. This information is needed for guidance in the disassembly for interim examination and for the reconstitution of the experiment as a 19-rod bundle for the low-power phase of its irradiation.

2.1.1.5.4. HELM Bundle Experiments

HELM 2 Fission Gas Release and Venting Analysis

A calculation of the expected release and venting fractions of krypton and xenon isotopes from the HELM 2 bundle has been completed. The calculation used the models and codes developed at GA for fission gas release and venting. Release to birth rate fractions (R/B) were calculated using the LIFE-III code (Ref. 2-1) with the GCFR subroutine GAREL (Ref. 2-2) employing diffusion parameters derived from irradiation capsule GB-10 measurements. Venting to birth rate fractions (V/B) were calculated using the SLIDER code (Ref. 2-4). A detailed description of the methods and assumptions is presented and the sources of uncertainties are discussed. The initial results are gratifying, with all predictions being within a factor of 5 of the measured HELM 2 values. There are, nevertheless, uncertainties and deficiencies in the calculations, many of which are in the process of being actively reduced or eliminated. The results of the detailed calculations are given in Table 2-2, and a comparison of the calculated values with those measured from HELM 2 and 3 are shown in Table 2-3.

TABLE 2-2
ESTIMATED RELEASE AND VENTING FRACTIONS AND TRANSPORT
TIMES FOR GASEOUS FISSION PRODUCTS NEAR THE END OF THE SECOND BR2 CYCLE OF HELM 2 FUEL BUNDLE TEST

		Solid Phase		Gas Phase Region												Vented Bundle		
		Fuel		Fuel		Upper Blanket		Rod Trap[e]		Manifold[f]		Bundle Trap[g]		Bundle Trap Exit Fittings[h]		Venting Fraction V/B[j] (%)	Effective Delay Time[b]	Number of $T_{1/2}$
Isotope[a]	Half Life[b]	R/B[c] (%)	ERDT[d] (%)	RTF[i] (%)	ERDT[d] (%)	RTF[i] (%)	ERDT[d] (%)	RTF[i] (%)	ERDT[d] (%)	RTF[i] (%)	ERDT[d] (%)	RTF[e] (%)	ERDT[d] (%)	RTF[i] (%)	ERDT[d] (%)			
Kr-83m	1.87 h	3.15	21.9	9.63	14.8	15.3	11.9	7.95	16.0	69.4	2.3	1.30	27.5	40.9	5.60	1.4×10^{-5}	42.6 h	22.8
Kr-85m	4.40 h	4.79	25.6	14.9	16.1	34.8	8.90	14.4	16.3	83.5	1.60	3.58	28.0	66.0	3.50	7.0×10^{-4}	75.4 h	17.1
Kr-87	1.27 h	2.64	20.2	7.94	14.0	9.07	13.3	5.97	15.6	61.2	2.78	0.740	27.2	28.6	6.92	1.5×10^{-6}	33.1 h	26.1
Kr-88	2.79 h	3.84	23.6	11.7	15.5	23.7	10.4	10.6	16.3	76.4	1.94	2.16	27.7	53.3	4.56	1.0×10^{-4}	55.6 h	19.9
Xe-131m	12.0 d	48.8	38.3	72.9	16.9	92.7	4.07	68.3	20.3	98.5	0.81	69.9	19.2	99.2	0.42	15	32.4 d	2.70
Xe-133m	2.30 d	29.7	28.1	46.6	17.7	81.0	4.88	42.8	19.7	95.7	1.01	30.3	27.7	95.8	0.91	1.3	14.3 d	6.23
Xe-133	5.27 d	39.1	32.5	60.8	17.2	88.1	4.38	55.1	20.7	97.4	0.92	50.5	23.7	98.1	0.60	5.6	22.0 d	4.17
Xe-135	9.13 h	11.6	24.5	20.1	18.2	69.3	4.13	20.2	18.0	88.2	1.43	6.51	31.0	78.4	2.74	0.01	117 h	12.8

[a] Only isotopes with a venting fraction (V/B) of 10^{-8} < V/B < 0.3 have been included.

[b] h = hours, d = days.

[c] R/B = (release rate from solid fuel to gaseous interstices)/(birth rate in solid fuel).

[d] Effective region delay time = fraction of total delay time attributable to the associated region.

[e] Includes spring chamber and rod trap.

[f] Includes vertical and horizontal manifold passages.

[g] Includes bundle trap and entrance and exit fittings.

[h] Includes vent tube, weld chamber, and miscellaneous fittings.

[i] Region transport fraction = (rate of escape)/(rate of entrance of the associated region).

[j] V/B = (release fraction vented from bundle)/(birth rate in solid fuel regions).

TABLE 2-3
COMPARISON OF PREDICTED AND OBSERVED FISSION GAS BEHAVIOR
IN HELM 2 AND HELM 3 FUEL BUNDLES

	Venting Fraction, V/B (%)		
		OBSERVED	
Isotope	Predicted	HELM 2[(a)]	HELM 3[(b)]
Kr-83m	1.4×10^{-5}	--	--
Kr-85m	7.9×10^{-4}	2.0 (-3)	1.3 (-3)
Kr-87	1.5×10^{-6}	--	--
Kr-88	1.0×10^{-4}	2.0 (-4)	--
Xe-131m	15	--	4.6
Xe-133m	1.3	0.3	--
Xe-133	5.6	2.6	1.8
Xe-135	0.01	2.0 (-3)	3.2 (-3)

(a) Data for UO_2 fueled test after two BR2 cycles.
(b) Data for U/PuO_2 fueled test after one BR2 cycle.

A series of 12-rod pressure-equalized and vented GCFR fuel bundles is being irradiated in the BR2 reactor at Mol, Belgium. The fuel bundles are irradiated in the in-pile section of a high-pressure (60-atm) helium loop called the He-Loop-Mol (HELM). A schematic of the HELM and the HELM fuel bundles (Ref. 2-5) is shown in Fig. 2-2. Fuel bundle data are given in Table 2-4. HELM 2, the first fueled bundle, was urania-fueled and was irradiated for two BR2 reactor cycles or ∿50 effective full-power days to qualify HELM for operation with the plutonium-bearing fuels to be used in the remaining bundles of the series. (HELM 1 contained stainless steel pellets to calibrate HELM for gamma heating, loop-to-reactor heat exchange, and activation of He-3 to tritium.) Venting fractions of the radioactive krypton and xenon fission gases were measured (Ref. 2-6). The calculation described below was the first complete test of the calculational methods planned for application to GCFR vented core assemblies.

Calculation of Release to Birth Rate Fractions (R/B)

The steady-state fission-gas release to birth rate ratios from the HELM 2 irradiation test were calculated using the combination of the fuel rod thermomechanical performance code, LIFE-III (Ref. 2-1), and the isotopic fission-gas release subroutine GAREL (Ref. 2-2). The diffusion coefficients used in the GAREL subroutine were derived from data measured in the GB-10 experiment and expressed in the form

$$D = D_o \exp[-Q/KT]$$

where D_o = 0.12074×10^{9} cm^2/sec for krypton isotopes
= 0.7521×10^{-9} cm^2/sec for xenon isotopes,
Q = 1.53 - 0.00004 t eV/atom for krypton isotopes
= 1.55 - 0.000024 t eV/atom for xenon isotopes,
t = time in hours,
K = Boltzmann constant,
T = absolute temperature.

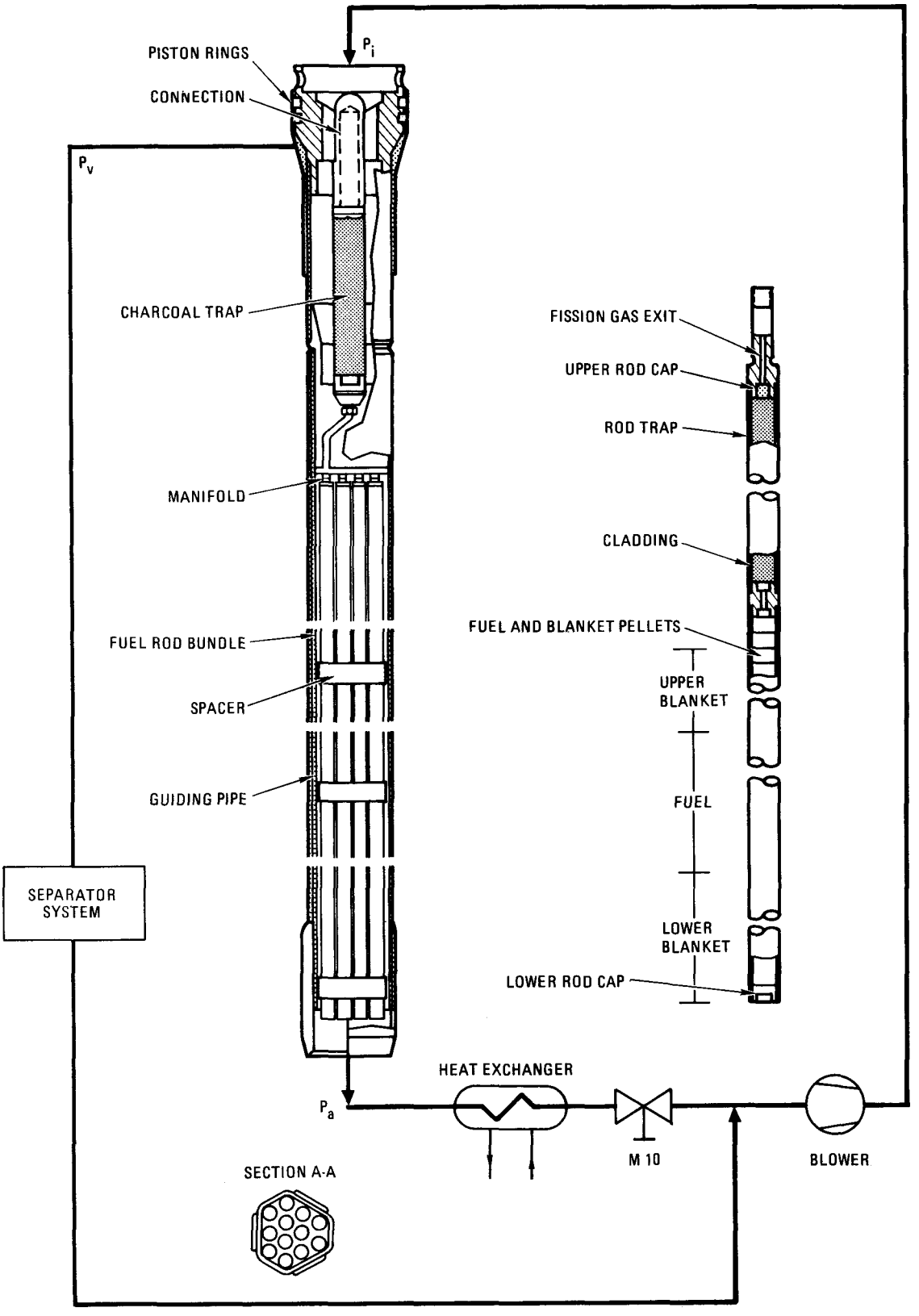

Fig. 2-2. Schematic of fuel element pressure equalization system (He loop - Mol)

TABLE 2-4
DESIGN AND OPERATION DATA FOR HELM FUEL BUNDLES

	BR2 Helium Loop Experiments	
	HELM 2	HELM 3
Fuel pin diameter (smooth), mm	8.0	
Depth of surface roughening, mm	0.1	
Cladding o.d./i.d. ratio (at roughness base)	1.15	
Pin length total, mm	1218.5	
Fuel, mm	600	
Upper blanket, mm	420	
Lower blanket, mm	90	
Roughened surface, mm	630	
Number of fuel pins	12	
Triangular pitch, mm	11.1	
Number of spacers	6	
Duct inside width across flats, mm	(special duct inside profile, outside circular)	
Wall thickness, mm		
Element length total, mm	1450	
Fuel pellet material	UO_2	UO_2/PuO_2
$Pu_{fiss}/(U + Pu)$, %	--	12.6
U-235/U, %	93 (75)[a]	93 (75)[a]
Smear density, % theoretical density	85.1 (84.9)[a]	84.2 (84.0)[a]
Blanket pellet material	UO_2	
U-235/U, %	(natural)	
Cladding and structural material[b]	316 SS (20% cold worked)	
Pin maximum linear heat rating, W/cm	460[c] (500)[d]	
Axial form factor	1.25	
Helium system pressure, bar	65	
Helium outlet temperature, °C	<600	
Maximum mid-cladding temperature, °C	670[c] (700)[d]	
Maximum burnup, MWd/kg (U + Pu)	7	60 (100)[e]
Maximum fast fluence (>0.1 MeV), $10^{21}/cm^2$	~0.6	~5.0 (~8.5)[e]

[a] Two different pin loadings used for power equalization across the bundle.

[b] AISI 316 (US alternative material) used in three pins in HELM 3.

[c] Bundle average value.

[d] Value for pin with highest nominal power.

[e] Extension of HELM 3 to 100 MWd/kg(U+Pu) maximum burnup intended.

The input data (Ref. 2-4) used in the analysis are listed in Table 2-5. The linear power and coolant conditions are given as bundle-averaged values so that the bundle-averaged fission-gas release can be calculated. The power distribution was obtained from Ref. 2-6 and is depicted in Fig. 2-3.

The results of the steady-state release to birth rate ratio for radioactive fission gas isotopes are summarized in Table 2-3 for 50 effective full-power days of irradiation.

SLIDER Modeling

Calculation of venting fractions requires consideration of the following factors which influence the venting process:

1. Venting passage configuration and arrangement in the HELM fuel bundle assembly.

2. Equivalent volume model utilized in the SLIDER code.

3. Modeling of blanket, fuel, rod traps, manifolds, bundle trap, and fittings.

4. Interdiffusion coefficients of krypton and xenon in helium at temperatures and pressures of interest.

5. Release to birth rate fractions of krypton and xenon in the fuel.

Each of these items is addressed individually below.

Design and Configuration of HELM Fuel Bundle Assemblies. Twelve 1460-mm-long fuel rods incorporating UO_2 fuel, UO_2 axial blankets, and charcoal traps are connected in parallel to a manifold. The latter is

TABLE 2-5
LIFE-III INPUT DATA FOR HELM-2 FUEL ROD

Fuel column length, mm	600
Clad o.d., mm	8.00
Clad i.d., mm	6.96
Pellet o.d., mm	6.63
Pellet density, % TD	87.7
Average linear power, kW/m	40
Coolant inlet temperature, °C	275
Coolant outlet temperature, °C	490
Helium system pressure, bar	58.8
Maximum burnup, MWd/kg	7.0

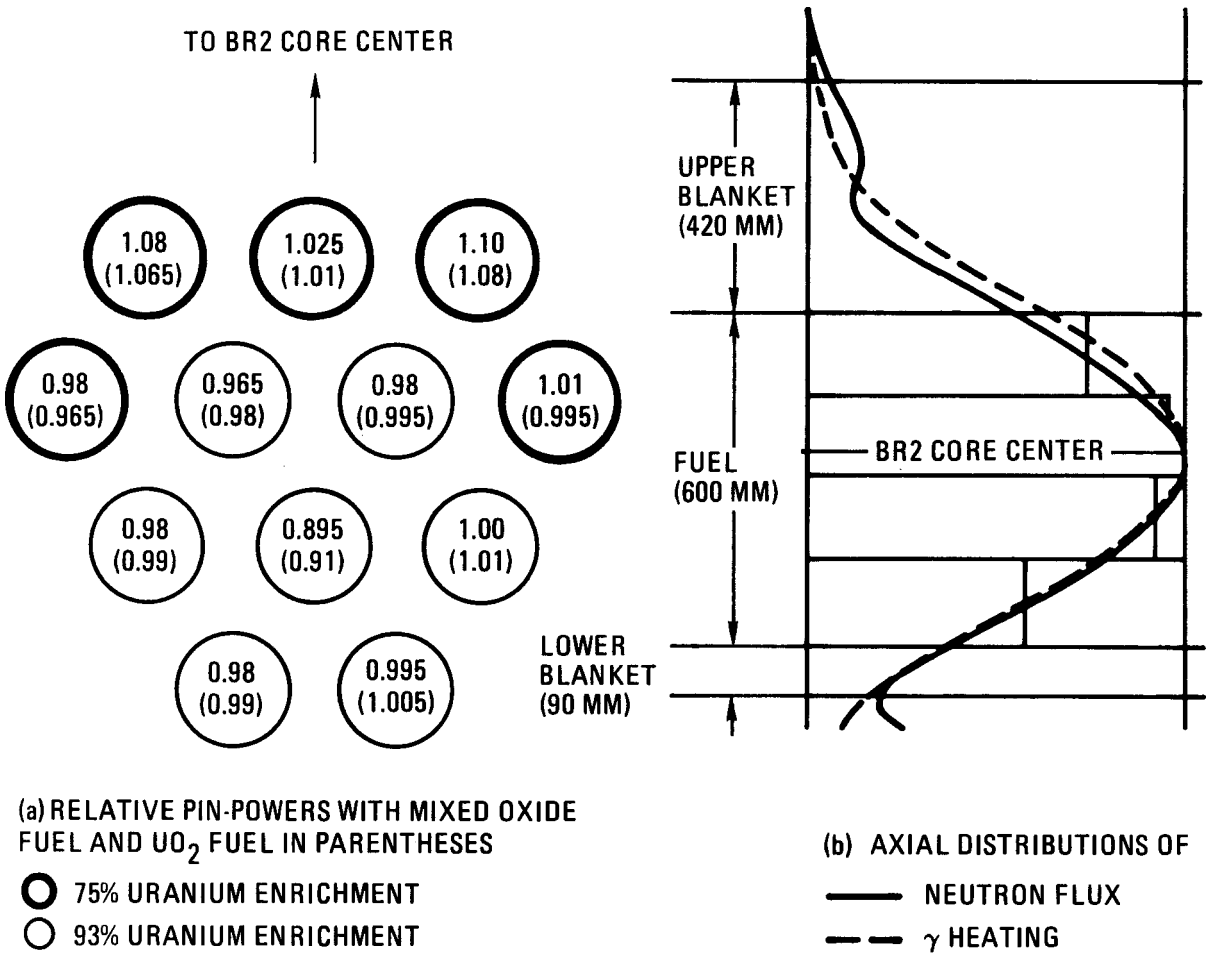

Fig. 2-3. Power distributions in the bundle

connected in series to the bundle charcoal trap and the vent connection via a vent tube. These regions of the fuel rods and the assembly were modeled in the SLIDER code to calculate venting fractions at the vent connection near the end of the second BR2 cycle.

Equivalent Volume Model. The SLIDER code is used to solve the equation (Refs. 2-4, 2-7) which describes the gaseous diffusion transport process:

$$\frac{\partial C(\bar{r},t)}{\partial t} = S(\bar{r},t) - \lambda C(\bar{r},t) - \nabla \cdot \bar{J}(\bar{r},t) \qquad (2\text{-}1)$$

where $C(\bar{r},t)$ = fission product concentration as a function of position and time (atoms/cm^3-s),
$S(\bar{r},t)$ = fission product production rate (atoms/cm^3-s),
$\bar{J}(r,t)$ = fission product current (atoms/cm^2-s),
λ = decay constant of fission product (s^{-1}).

Equation 2-1 is solved in slab geometry when modeling fission gas behavior in the HELM tests. Since SLIDER is a one-dimensional code, the varying cross sections in discrete portions of the transport path must be accounted for in the input data. This is done by ensuring that the system volume and component resistances to gaseous-diffusion transport are conserved. Volume conservation is assured using the equation

$$A_{ot} L_e = A_x L_x \qquad (2\text{-}2)$$

or $$L_e = \frac{L_x}{A_{ot}/A_x}$$

where A_{ot} = cross-sectional area of open tube in SLIDER model (cm^2),
L_e = equivalent length of tube in SLIDER required to produce equal volume of actual component of interest (cm),
A_x = actual cross-sectional area of component of interest (cm^2),
L_x = actual length of component of interest (cm).

Conservation of component resistance to gaseous-diffusion transport results from using the expression

$$R = \frac{L_x}{D_x A_x} = \frac{\frac{L_x}{A_{ot}/A_x}}{\frac{D_x A_x}{A_{ot}/A_x}} = \frac{L_e}{\frac{D_x A_{ot}}{(A_{ot}/A_x)^2}} = \frac{L_e}{D_e A_{ot}} \qquad (2\text{-}3)$$

where R = resistance to release in each region (s/cm^3),

D_x = diffusion coefficient in component of interest corrected for temperature and pressure (cm^2/s),

D_e = effective diffusion coefficient,

$$D_e = \frac{D_x}{(A_{ot}/A_x)^2} \ (cm^2/s).$$

It is worth noting that the actual time constants t_x and the effective time constants t_e associated with each component are equivalent:

$$t_x = \frac{kL_x^2}{D_x} = \frac{kL_x^2 \left(\frac{1}{A_{ot}/A_x}\right)^2}{D_x \left(\frac{1}{A_{ot}/A_x}\right)^2} = \frac{k\left(\frac{L_x}{A_{ot}/A_x}\right)^2}{\frac{D_x}{\left(A_{ot}/A_x\right)^2}}$$

$$= k\frac{L_e}{D_e} = t_e \ .$$

Calculation of L_e and D_e Input to SLIDER. Appropriate values for three experimental variables were required for SLIDER analysis:

1. Component length and open tube/actual tube cross-sectional area ratios.

2. Equivalent lengths of traps taking account of fission product sorption and delay in charcoal beds.

3. Temperature- and pressure-dependent diffusion coefficients for krypton and xenon nuclides in helium.

Component dimensions for each region were obtained from drawings provided by Kraftwerke Union (KWU), fabricators of the HELM bundles. Component lengths are shown in summary form in Table 2-6. The treatment of area ratios requires closer review.

Lower Blanket Region. The cross-sectional area of an open fuel rod tube without fuel or blanket material is 0.462 cm^2 (d = 0.680 cm). The average diameter of the HELM 2 blanket pellets (d = 0.663 cm) results in a cross-sectional area of 0.440 cm^2. The area ratio of an open tube (modeled in SLIDER) to that of the area available for fission gas diffusion in the blanket region is

$$\frac{A_{ot}}{A_x} = \frac{0.462}{0.462 - 0.440} = 20.25.$$

Since the bundle is composed of 12 rods manifolded in parallel, the area ratio is reduced by the amount $A_{ot}/(12)A_x = 1.69$. Note that the differential expansion of the UO_2 pellets can be neglected in this analysis since the blankets are isothermal regions.

Fuel Region. The treatment of the fuel region is analogous to that of the blanket except that the central hole and the effect of differing fuel temperatures must be modeled. As such,

$$\frac{A_{ot}}{A_x} = \frac{A_{ot}}{A_{ot} - \text{area of fuel} + \text{area of central hole}} \qquad (2\text{-}5)$$

$$= \frac{\frac{\pi}{4} d_o^2}{\frac{\pi}{4}\{d_{ot}^2 - [d_{ot}^2 - 2(\text{gap})]^2 + d(\text{central hole})^2\}} .$$

TABLE 2-6
HELM 2 SLIDER MODELING DATA

Region Description	Actual Length (cm)	Area Ratio A_{ot}/A_x	Effective Length (cm)	Temperature (K)	D_e(Kr) (cm^2/s)	D_e(Xe) (cm^2/s)
Lower blanket	8.8	1.69	5.21	763	1.74×10^{-2}	1.47×10^{-2}
Fuel	15.1	0.897	16.84	1372	1.54×10^{-1}	1.31×10^{-2}
	15.1	0.603	25.04	1814	5.29×10^{-1}	4.48×10^{-1}
	15.2	0.587	25.89	2015	6.59×10^{-1}	5.58×10^{-1}
	15.1	1.04	14.52	1801	1.75×10^{-1}	1.48×10^{-1}
Upper blanket	41.8	1.69	24.73	548	1.03×10^{-2}	8.74×10^{-3}
Spring chamber	1.6	0.185	8.65	548	0.861	0.729
Rod trap	5.0	0.0833	120.0	548	2.35	1.99
End cap and vent manifold	2.5	0.963	2.60	548	3.17×10^{-2}	2.68×10^{-2}
Horizontal manifold	1.3	0.963	1.35	548	3.17×10^{-2}	2.68×10^{-2}
Bottom bundle trap fitting	1.8	11.6	0.155	548	2.20×10^{-4}	1.86×10^{-4}
Bundle trap	12.5	0.236	105.9	548	2.93×10^{-1}	2.48×10^{-1}
Top bundle trap fitting	1.7	11.6	0.147	548	2.20×10^{-4}	1.86×10^{-4}
Vent tube	20.6	5.14	4.008	548	1.11×10^{-3}	9.43×10^{-4}
Weld chamber	1.3	11.56	0.113	548	2.20×10^{-4}	1.86×10^{-4}
Miscellaneous	1.7	1.85	0.919	548	8.59×10^{-3}	7.27×10^{-3}

For this analysis, the fuel was divided into four axially equal temperature regions. The corresponding fuel-cladding gaps for each region, starting at the bottom of the fuel region, were 0.0114, 0.0110, 0.0111, and 0.0129 cm. The central hole diameters were taken to be 0.0561, 0.0928, 0.0948, and 0.0251 cm, respectively. From these data, taken from the LIFE III results (Ref. 2-1), and the inclusion of 12 rods in parallel, the area ratios in Table 2-6 were derived.

Upper Blanket. The analysis is identical to that of the lower blanket region.

Spring Chamber. The area ratio was calculated assuming the spring consisted of four turns of 2.0-mm wire. The length of a spring is calculated from the expression

$$\ell_{spring} = n\Pi d_{chamber} + \ell_{chamber} = 10.15 \text{ cm} \qquad (2\text{-}6)$$

where n = number of turns (4),

$d_{chamber}$ = diameter of spring chamber (0.680 cm),

$\ell_{chamber}$ = length of spring chamber (1.6).

The spring volume is

$$V_{spring} = \frac{\Pi}{4} (d^2_{wire}) (\ell_{spring}) = 0.319 \text{ cm}^3. \qquad (2\text{-}7)$$

From this, the area ratio can be calculated from

$$\frac{A_{ot}}{A_x} = \frac{V_{chamber}}{V_{chamber} - V_{spring}} = \frac{\frac{\Pi}{4} (0.680)^2(1.6)}{\frac{\Pi}{4} (0.680)^2(1.6) - 0.319}$$

$$= 2.217.$$

Again correcting for the presence of 12 rods, a value of 0.185 is obtained.

Rod Trap. Neglecting the presence of charcoal (see separate discussion of charcoal traps below), the rod trap area ratio is 1/12 or 0.0833, reflecting the presence of twelve traps of unit cross-sectional area in parallel.

Vertical and Horizontal Manifolds. The vertical and horizontal manifolds are comprised of 12 tubes of 0.2-cm diameter. Since the open tube diameter modeled in SLIDER is equal to the cladding i.d. (0.680 cm), the area ratio is

$$\frac{A_{ot}}{A_x} = \frac{(0.680)^2}{(0.2)^2(12)} = 0.963.$$

Element Bottom and Top Trap Fittings. These fittings are single tubes 0.2 cm in diameter. As such,

$$A_{ot}/A_x = \frac{(0.680)^2}{(0.2)^2} = 11.6.$$

Bundle Trap. The single bundle trap has a diameter of 1.4 cm. Neglecting the presence of charcoal, the area ratio is found to be 0.236.

Vent Tube. This region has a tube diameter of 0.3 cm, resulting in an area ratio of 5.14.

Weld Chamber. The weld chamber is treated analogously to the bundle trap fittings.

Miscellaneous Fittings. A diameter of 0.5 cm is assumed, providing an area ratio of 1.85.

The effective length of each region modeled in SLIDER and presented in Table 2-6 was calculated using the actual length of the region, the area ratio, and Eq. 2-2. The calculated effective length of the charcoal

traps is based on a heuristic model developed for the GB-9 capsule analysis (Ref. 2-6). Since charcoal in the trap adsorbs krypton and xenon molecules in the gas phase, the effect is to reduce the nuclide concentration in the diffusion region of the trap. This result can be modeled by increasing the effective volume of the trap by an amount that provides an accurate simulation of fission gas diffusion times in the traps. Data from Ref. 2-6 revealed that at a pressure of 7.04 MPa (1021 psi), an equivalent rod-trap volume twice that of the actual trap volume resulted in predicted diffusion behavior in agreement with that observed. The factor of two in the volume was included in the calculated values of L_e for the traps shown in Table 2-6. It should be noted that this change increases the diffusion path length in the one-dimensional SLIDER model, whereas a combination of changes in cross-sectional area and the diffusion coefficient is desired. As a consequence, the results are empirical in nature and strictly applicable only to traps having the same diameter as that in GB-9. Although this is not true for the HELM test bundle trap, no other applicable data existed at the time of the analysis.

Interdiffusion Coefficients of Krypton and Xenon in Helium. The diffusion coefficients used in the calculations were obtained for each region using the expression (Ref. 2-8)

$$D_e = D_o\left(\frac{T}{T_o}\right)^x \left(\frac{P_o}{P}\right)^y \left(\frac{1}{A_{ot}/A_x}\right)^2 \qquad (2\text{-}8)$$

where D_e = effective diffusion coefficient at temperature and pressure of interest (cm^2/sec),

D_o = normal value of D at T_o = 273 K and P_o = 0.101 MPa (1 atm), 0.579 cm^2/s,

P = loop pressure, 5.96 MPa (58.8 atm),

T = temperature in region of interest (K),

x,y = constants, 1.57 and 1.0, respectively.

The area ratio correction is included to retain equal resistances to transport in both the actual bundle regions and in the SLIDER model (see Eq. 2-3). The diffusion coefficient in the lower blanket region was calculated with a temperature of 763 K. In all other locations with the exception of the fuel regions, the temperature was 548 K.

The calculation of temperatures in the fuel region required a more sophisticated analysis. Fuel region temperatures can be estimated using the expression

$$T_{fuel} = T_i + \Delta T_g + (\Delta T_{film} + \Delta T_{clad} + \Delta T_{gap} + \Delta T_{fuel}) \qquad (2\text{-}9)$$

where T_{fuel} = temperature of fuel (K),
T_i = inlet temperature of helium coolant, 533 K,
ΔT_g = gas temperature rise axially along fuel rods from inlet, $(T_o - T_i) = (763 - 533) = 230$ K,
ΔT_{film} = temperature rise across bulk gas to cladding film (K),
ΔT_{clad} = temperature rise from conduction in cladding (K),
ΔT_{gap} = temperature rise across clad-pellet gap (K),
ΔT_{fuel} = temperature rise from pellet o.d. to average gas temperature (K).

The ΔT values in parentheses all depend upon the rate of linear heating developed in the fuel and its radial conduction. Axial conduction is negligible.

Predicted values of the latter four terms were obtained from earlier HELM 2 calculations incorporating a reduction in the average power density from 50 to 40 kW/m:

$$T_{fuel} = Ti + \Delta T_g + 40/50\ (\Delta T_o) \qquad (2\text{-}10)$$

where $\Delta T_o = \Delta T_{film} + \Delta T_{clad} + \Delta T_{gap} + \Delta T_{fuel}$.

Using values of ΔT = 1013, 1493, 1673, and 1333 K, the temperatures shown in Table 2-6 were calculated. These values were subsequently used to determine D_e for krypton and xenon in the fuel region, also shown in Table 2-6.

The values of $D_e(Xe)$, the interdiffusion coefficient of xenon in helium, is 0.847 times the corresponding value for krypton. This multiplier was determined from low-temperature, low-pressure experiments carried out in connection with the GB-9 capsule. This ratio also applies at other common conditions of temperature and pressure since the temperature and pressure dependencies of the diffusion coefficients of krypton and xeron are the same (ref. 2-8).

Venting to Birth Rate Ratios (V/B). The SLIDER code provides calculated values of V/R for each region modeled, where V is the rate at which a given nuclide leaves a region and R is the release rate from the solid matrix of the fuel into the fuel region gas phase. Of greater interest is the V/B obtained by using the expression

$$V/B = V/R \cdot R/B \quad . \tag{2-11}$$

Results

The release and venting fractions derived from the calculations are shown in Table 2-2. Results for each of the principal regions of interest are presented, including values of release to birth rate ratios (R/B) derived from LIFE-III, region transport fractions (RTF) (atoms into region/atoms out of region) derived from SLIDER, effective delay times in each region (ERDT) calculated using the expression

$$ERDT = \frac{\ell n\ (RTF)}{\ell n\ (V/B)} \tag{2-12}$$

where RTF and V/B are used as fractions, and effective total delay times derived using the expression

$$\text{effective delay time} = \frac{1}{\lambda_i} \ln (V/B) \qquad (2\text{-}13)$$

where V/B is used as a fraction. A review of ERDT values shows that the bundle trap offers the greatest delay to venting of krypton isotopes, closely followed by solid-state diffusion in the fuel; diffusion in these regions results in about equal holdup times for xenon nuclides. Contrary to previous calculations and observations, the blanket region offers less resistance to venting than either of the above regions or gaseous diffusion in the fuel and rod traps.

The venting fractions derived from the analyses have been compared to observed results for both HELM 2 and HELM 3 (Ref. 2-6) in Table 2-3. The measured venting fractions for the detectable HELM 2 krypton nuclides, Kr-85m and Kr-88, are seen to be a factor of 2.5 and 2.0 less than that predicted. Measured results for Xe-133m, Xe-133, and Xe-135 are factors of 2 to 5 larger than calculated. Although not directly applicable, the results of the HELM 3 experiment after one BR2 cycle showed similar V/B values. THe close agreement of the comparisons provides assurance that the predictive methods to be used with the GCFR demonstration plant are reliable.

Uncertainties

Table 2-2 indicates that krypton and xenon activities vented from HELM 2 are most strongly affected by the processes leading to the release of gases from the solid-state fuel matrix into the interstitial gas space of the fuel and by the bundle charcoal trap. Unfortunately, these are the two areas where the greatest uncertainties lie.

Uncertainties in Fission Gas Release. There are four uncertainties associated with the calculation of the gas release:

1. The uncertainty due to the fact that the diffusion coefficients used in the LIFE-GAREL code were not optimized by comparison with the data obtained in the GB-10 experiment. This is discussed in detail in Ref. 2-2 and thus will not be discussed here.

2. A large uncertainty presently exists in the measured temperature and its associated release fraction (R/B). The assumptions used in establishing the fuel and cladding temperature as a function of burnup are discussed in Ref. 2-3. A temperature uncertainly of ±75°C is estimated. It is expected that, by an analysis of in-pile and PIE data, this temperature uncertainty can be significantly reduced, hopefully to ±15°C. (For some important isotopes, a temperature uncertainty of 50°C corresponds to a factor of 10 in R/B.)

3. HELM 2 was fueled with UO_2, whereas the release data obtained from GB-10 are primarily applicable to mixed oxide (88 U - 12 Pu) fuel.

4. The release fractions calculated by LIFE-GAREL are derived using a single fuel rod to represent the average of all rods in the fuel bundle. The problems in representing 12 rods by a single rod are not trival. The calculation is based upon results from the Kernforschungszentrum Karlsruhe (KFK) SAGAPO* code (Ref. 2-10), which has been used successfully to analyze the electrically heated HELM bundle tests and to determine the heat transfer and fluid flow operating status of the HELM bundles during irradiation.

Uncertainties in Trap Performance. Laboratory tests of krypton adsorption at high pressure have shown that the effective length of a charcoal trap decreases as the helium pressure increases at constant krypton partial pressure. This is interpreted as indicating that the effective adsorption of the krypton on the charcoal is similarly affected. However, this may not be the case since the inter- and intraparticle diffusion rates are also affected by pressure. Temperature effects were regarded as separable and were not tested. Thus, the data are empirical and applicable only to similar trap geometry and conditions or those very near to them. The application of these data to the rod traps of HELM bundles is believed

*Analogous to GA COBRA code (Ref. 2-9)

to result in only a small uncertainty. However, application to the HELM bundle trap, which is very different in geometry, means that significant uncertainties must be considered. Bolch et al. (Ref. 2-11) have performed a number of krypton diffusion experiments in charcoal near 1 atm with traps of grossly different sizes from those tested at GA and with a wide variation of geometry. These results, along with more recent rod trap measurements carried out at elevated temperature and pressure, are expected to remove all significant remaining uncertainties in calculations of the HELM bundle or GCFR assembly trap performances.

Blanket Region Transport Performance

In all previous analyses of rod and bundle release and venting, the blanket regions of the rods were shown to be the most effective component in decreasing vented activities. It is worth noting that this is not the case in HELM bundles, as shown by a review of the data in Table 2-2. The blanket pellet-to-cladding gap in HELM is larger than that present in previous tests. The area ratios* in the blanket region in earlier design analyses were as high as ∿77, whereas in the HELM rods the ratio is ∿22. Since the delay in transport depends inversely on this ratio, as shown in the SLIDER modeling discussed above, the HELM blanket effectiveness in each rod is substantially reduced. In addition, parallel connection of diffusion paths below the manifold further reduced the blanket region effectiveness compared to GB-9 and GB-10 as single rod experiments. The bundle trap, located above the rod manifold and connected in series flow, is greatly increased in relative effectiveness.

Further Analyses

The results of future efforts to reduce or eliminate uncertainties will be incorporated in the analyses of HELM 3 experiment at a burnup of ∿28 MWd/kg or 7 BR2 irradiation cycles. Release constant data from the

*Area ratio is the ratio of the area of the tube i.d. to the annular area between the pellet and the clad. Therefore, the smaller the area ratio, the larger the diffusion rate.

GB-10 experiment await GB-10 temperature analyses using PIE data. These analyses are not expected to be available until the end of FY-79 at the earliest. Nonetheless, the analytical methods are capable of incorporating changes in design and operating conditions, and it is anticipated that new input data can be accommodated quickly and at low computational cost.

2.1.2. Assembly Design Verification and Support

2.1.2.1 Out-of-Pile Tests

2.1.2.1.1 Assembly Thermal-Hydraulic Tests

This task consists of thermal-hydraulic tests at EIR (Switzerland) in air and CO_2 loops and tests at University of California, Santa Barbara, in a water loop. The purpose of these tests is to improve the thermal-hydraulic correlations and to verify the computer codes used for thermal-hydraulic analyses of GCFR core assemblies.

Progress of Tests at EIR. The guidelines for design of AGATHE-III bundle were discussed in the last Quarterly Report (Ref. 2-53). This activity continued with comparison of COBRA*GCFR and EIR analysis results. The final design will be reported in the next quarterly.

UCSB Tests. No activity occurred in this subtask during the reporting period.

2.1.2.1.2 Assembly Mechanical Tests

A series of mechanical tests have been conducted on a 37-cell AGATHE HEX II spacer grid and a 271-cell DMFT spacer grid. The purpose of the tests was to determine the behavior of the spacer grids in response to loads applied normal to the plane of the spacer grid. In addition, miniature strain gages were attached to one 37-cell spacer grid, and both local strain and overall deflection were measured as a function of load.

Two different support conditions were tested: simply supported and fixed. The first condition was established by mounting the spacer grid on six ball bearings at the corner support points and applying a load to the upper surface of the central cell using a fitted ram. The second condition was obtained by clamping the six support points in a stiff fixture. Schematic views of the two configurations are given in Fig. 2-4. Loads were applied to the samples using an Instron 1122 testing machine. Load-deflection data were recorded on a chart recorder, integral with the testing machine. Strain gage data were recorded on a separate two-pen recorder.

Uniaxial-type strain gages were mounted at the lower edge of the webs as indicated on Fig. 2-5. All gages were mounted with the gage direction parallel to the lower edge, except numbers 29 and 30, which were mounted perpendicular to the edge.

Load-deflection data are summarized in Table 2-7. The readings in the table represent stabilized conditions; the results were reproducible to the accuracy of the recorder. The difference between the total deflection and effective deflection values is given in the table and shown in Fig. 2-6. The total deflection includes a nonlinear effect during initial loading, which disappears as the load increases. The effective displacement is determined by extrapolating back to the origin from the linear portion of the curve. The symbol δ shown on Fig. 2-6 indicates the difference between the total and effective deflection. No such difference was indicated on the 271-cell grid.

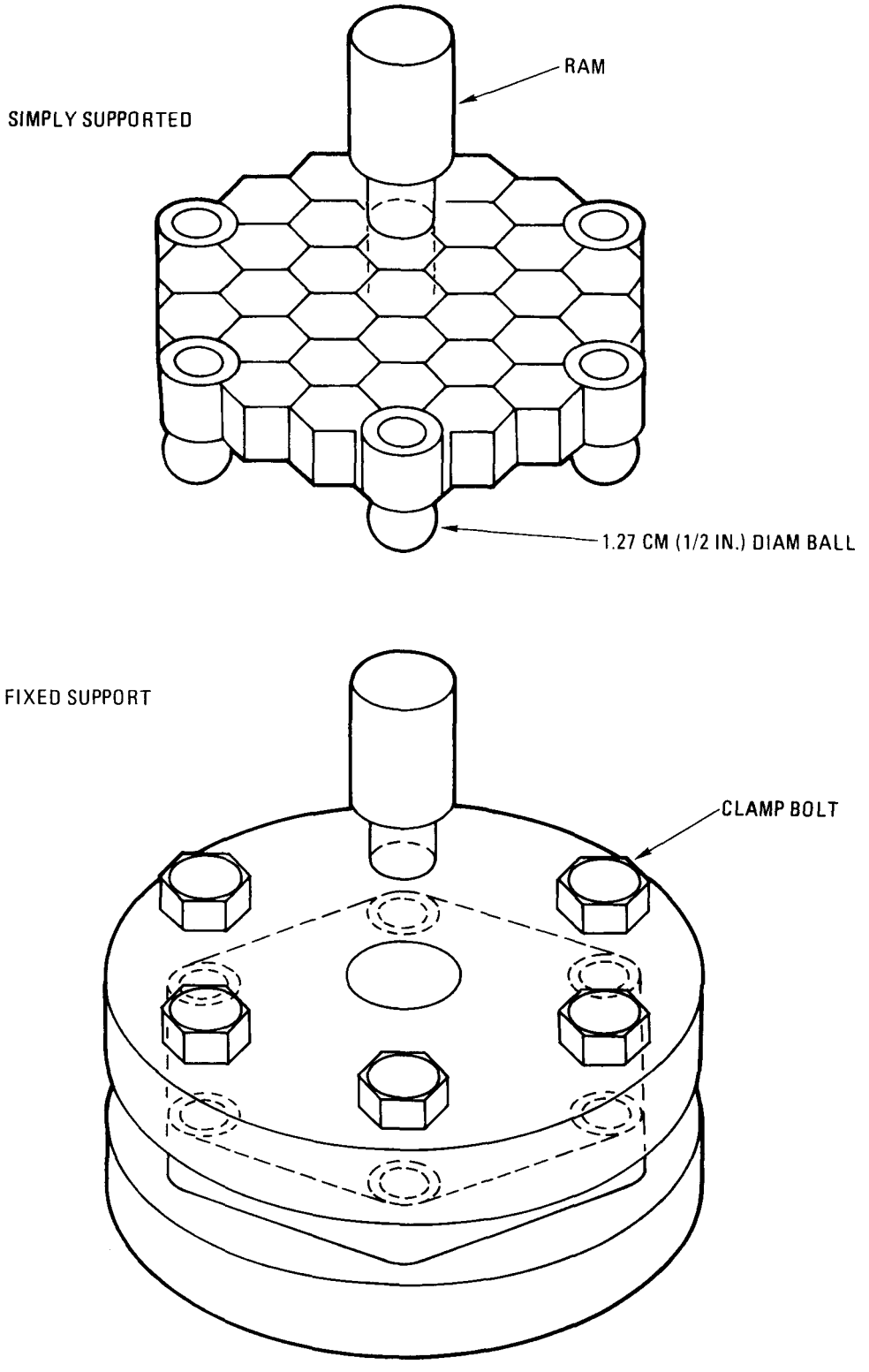

Fig. 2-4. Spacer grid support configurations

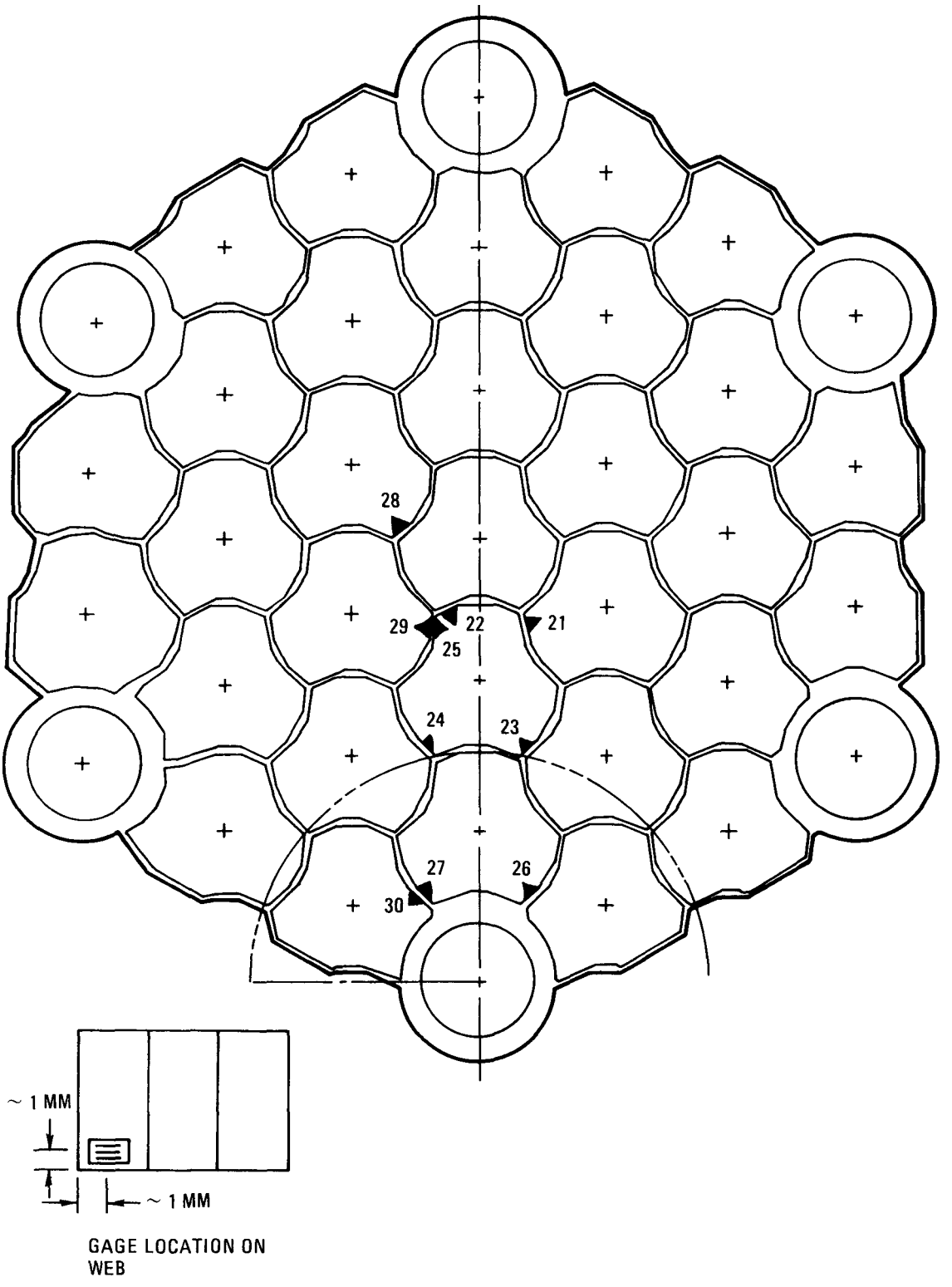

Fig. 2-5. Strain gage locations

TABLE 2-7
LOAD-DEFLECTION DATA

Test	Peak Load (N)	Total Deflection (mm)	Effective Deflection (mm)
37-cell simply supported (AH 28)	445	0.67	0.62
37-cell fixed (AH 28)	445	0.21	0.18
271-cell simply supported	178	1.14	1.12
271-cell fixed	178	1.02	1.02
37-cell simply supported (with strain gages) (AH33)	440	0.71	0.66
37-cell fixed (with strain gages) (AH 33)	227	0.12	0.10

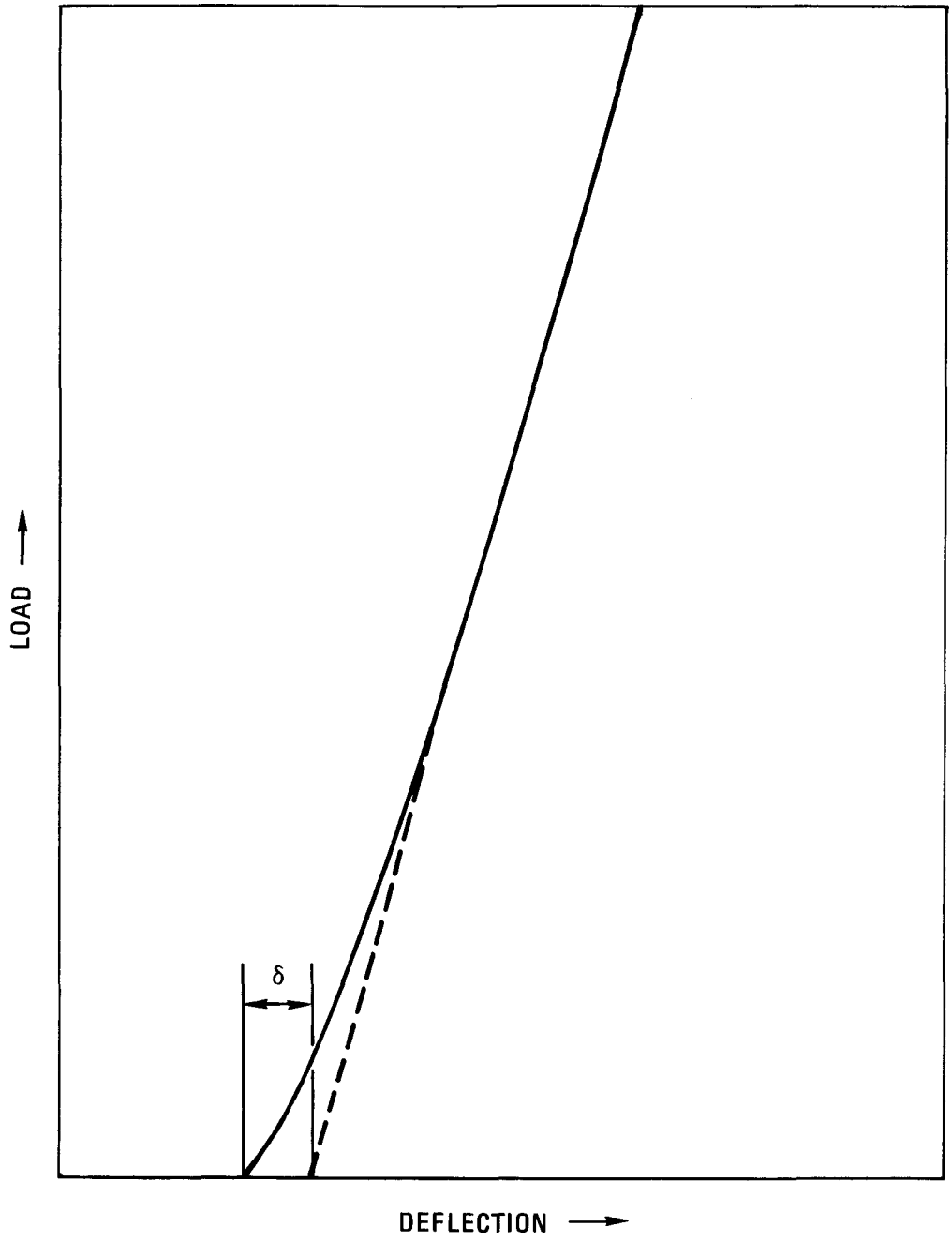

Fig. 2-6. Difference between total and effective deflection

Strain data were obtained for nine of the ten strain gages in both tests, gage number 5 having apparently failed prior to testing. Reduced data are presented in Table 2-8.

One aspect of the load-deflection data requiring discussion is the nonlinearity of the curves on the 37-cell spacer grids. No extensive examinations were carried out to determine the cause of the nonlinearity. It was initially believed that the curvature represented a setting up of the cell in the fixture. This notion is reinforced by the fact that the clamped condition shows much greater uniformity and unloads on nearly an identical path. Because of the good agreement with analytical results, as discussed previously, this discrepancy was not pursued further.

A marked difference was observed between the load deflection data for spacer grid numbers AH-28 and AH-33, the latter being tested with strain gages mounted. Sample measurement of the two grids showed that grid AH-28 contained an average web thickness sufficiently larger than AH-3, which explains the difference.

2.1.2.1.3. Assembly Vibration and Seismic Tests

Helium flow/vibration testing is planned for the design evaluation of single rods, partial assemblies, and full-size core assemblies; Ref. 2-12 describes the need for conducting flow tests on GCFR core assemblies. The objectives of the tests are to determine local and overall pressure drops and local flow distribution and to explore for acoustic excitation phenomena and flow-induced vibration characteristics. The results of these tests will be used to establish satisfactory flow performance of the core assemblies. Therefore, these tests must be accomplished during the preliminary design phase of the core assembly to provide input for completion of the preliminary core design effort. Flow diagrams of the full-size test rig, the major test parameters, and the test section envelope dimensions are given in Ref. 2-13.

TABLE 2-8
LOAD-STRAIN DATA FOR 37-CELL AGATHE HEX II
SPACER GRID SERIAL NO. AH33

Gage No.	Simply Supported Measured Strain at 45 kg (99 lb) Load (%)	"Fixed" Condition at 23 kg (51 lb) Load (%)
21	0.24	0.11
22	0.28	0.09
23	0.14	0.03
24	0.11	0.02
25	--	--
26	0.04	0.07
27	0.03	0.05
28	0.25	0.07
29	0.03	0.01
30	0.00	0.005

Planning has been initiated to build a small rig capable of testing partial assemblies to obtain flow-induced vibration information needed for the core assembly design. These partial assemblies will be comprised of full-length 1-rod and 19-rod bundles. The spacer grid pitch will be adjusted and the rod-spacer diametral clearance will be varied during these tests to obtain data for core assembly design and analyses.

The specific objectives of the partial bundle flow tests are as follows:

1. Determine rod natural frequencies.
2. Determine rod damping.
3. Measure flow-caused amplitude of response.
4. Evaluate effects of rod-spacer clearance.
5. Evaluate effects of spacer grid pitch.

Flow diagrams of the partial-size test rig are shown in Figs. 2-7 and 2-8 and the test schedule is shown in Fig. 2-9.

2.1.2.1.5 Core Flow Test Loop Program

A series of out-of-pile simulation tests will be conducted to (1) demonstrate the ability of the GCFR fuel, control, and blanket assembly designs to meet design goals and (2) verify predictions of analytical models which describe design operation and accident behavior. The tests will measure thermal-structural data for steady-state, transient, and marginal conditions using electrically heated rod bundles in a dynamic helium loop. Final margin tests will progressively be extended to the highest possible temperature until the heater elements fail. The CFTL program plan (Ref. 2-14) describes the requirements for the test program to be conducted in the CFTL, which will be constructed and operated by ORNL.

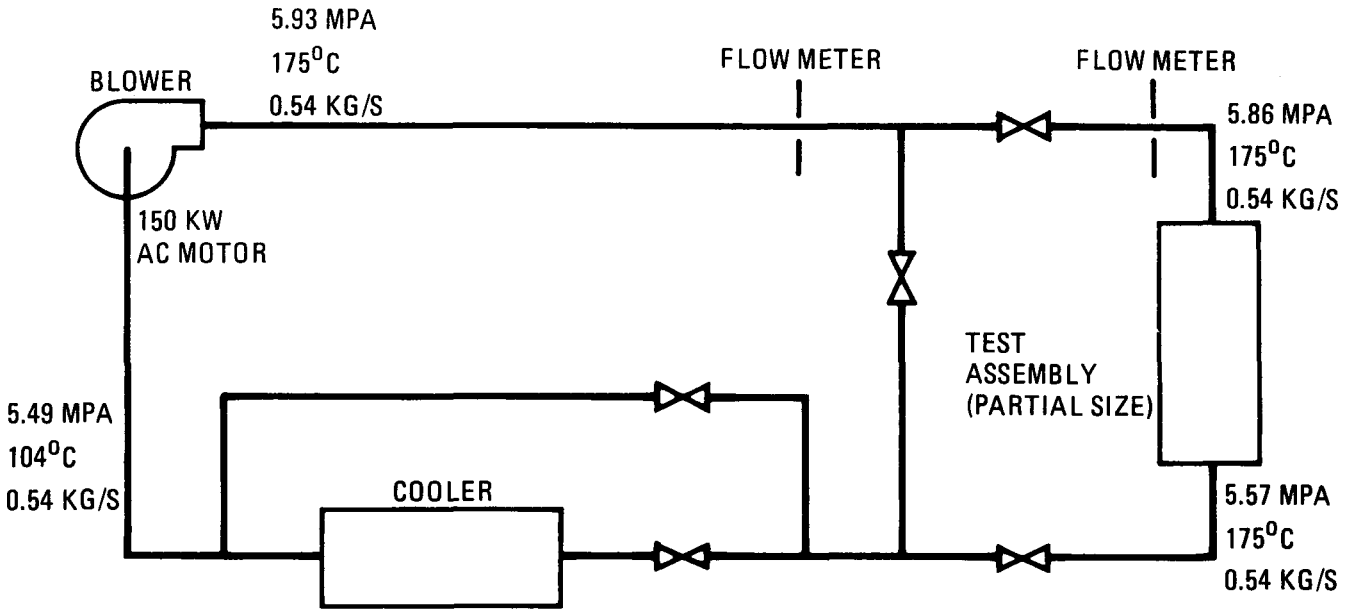

	REACTOR CORE	TEST RIG
TEMPERATURE	300° - 550°C	175°C
PRESSURE (AVERAGE)	8.86 MPA	5.86 MPA
FLOW	5.4 KG/S *	0.54 KG/S
DENSITY (AVERAGE)	6.1 KG/M^3	6.1 KG/M^3
ACOUSTIC VELOCITY	1400 - 1700 M/S	1240 M/S

* ONE FUEL ASSEMBLY

Fig. 2-7. Conceptual design of helium flow test rig

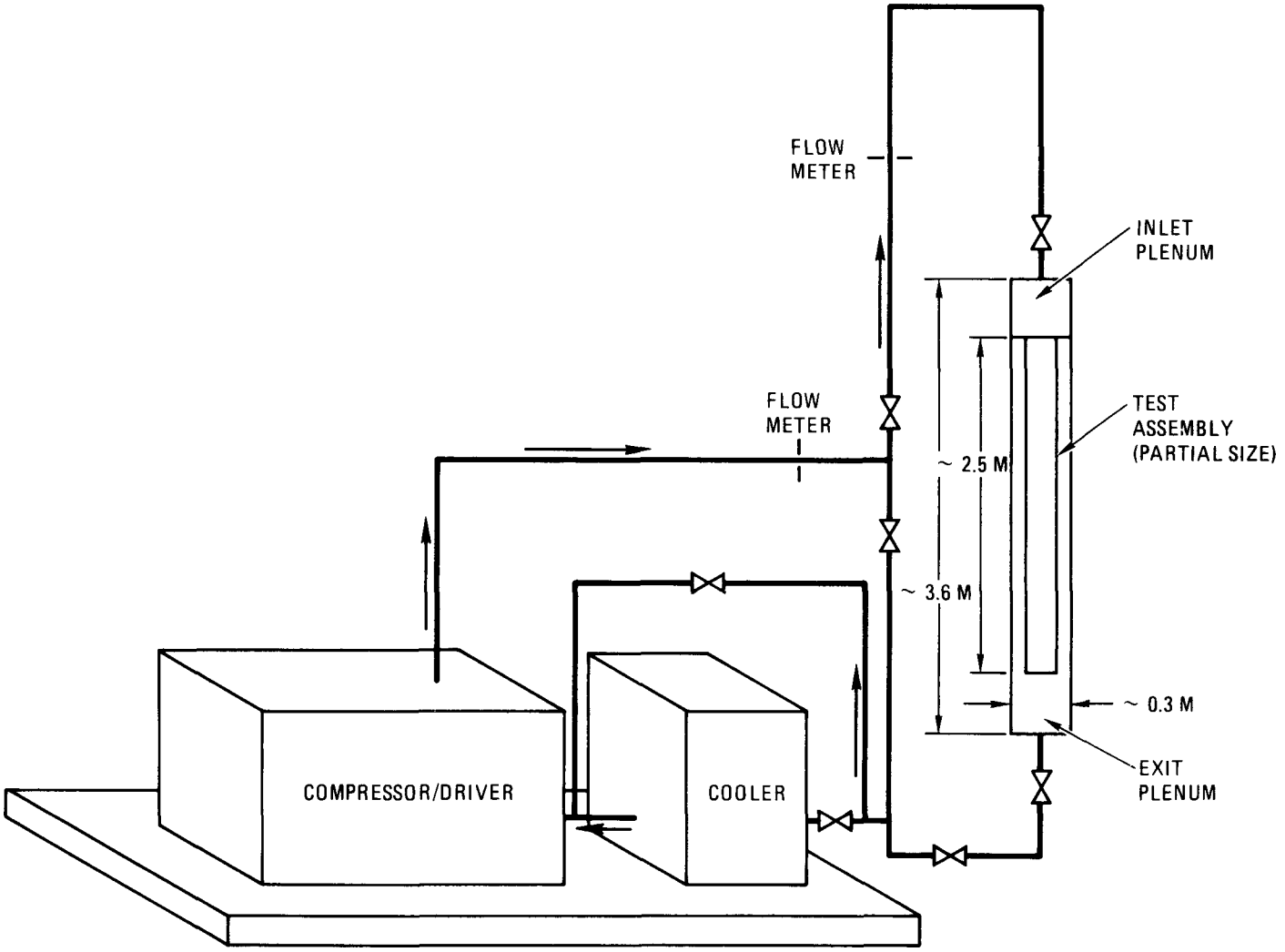

Fig. 2-8. Helium flow test rig

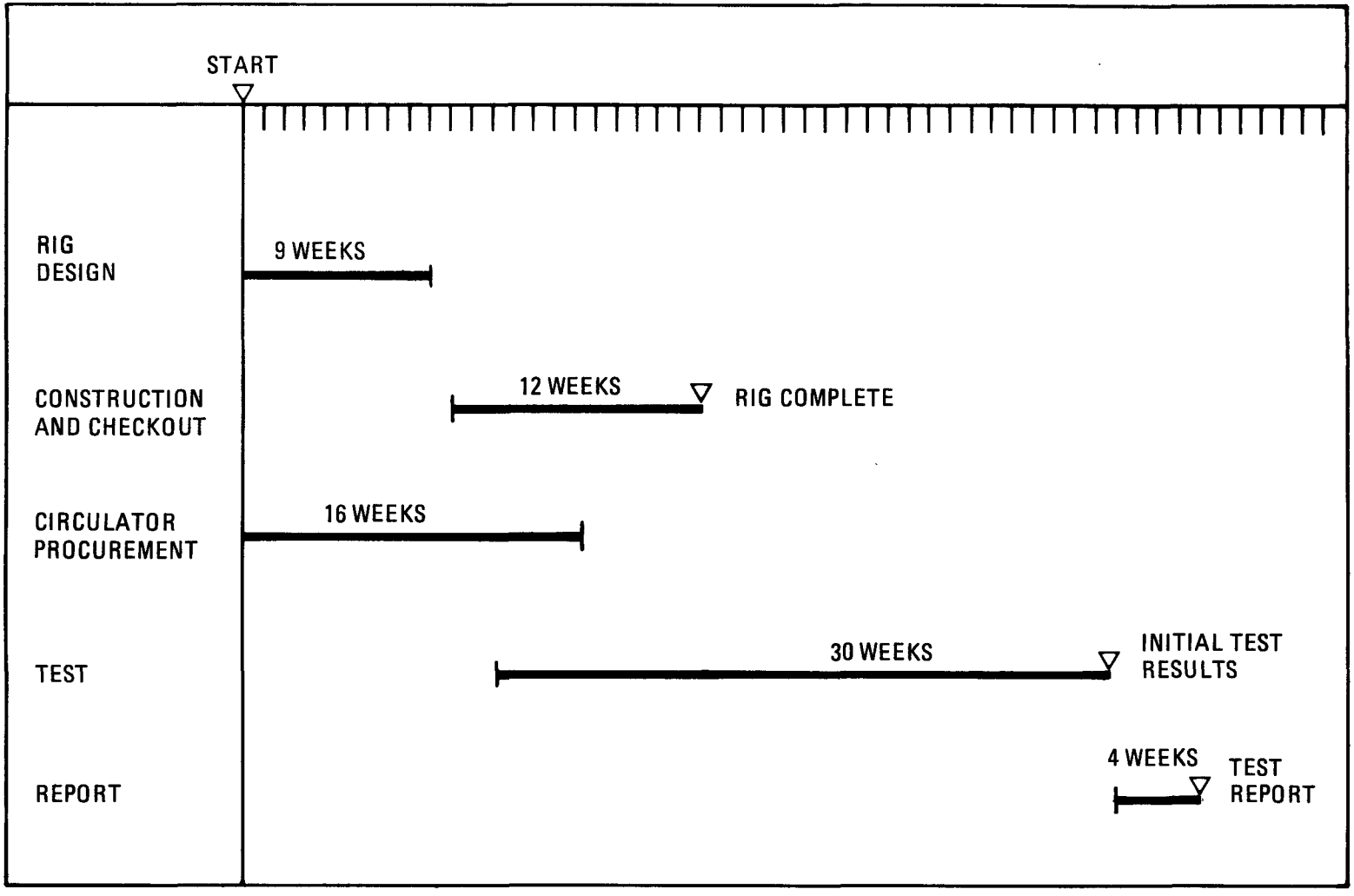

Fig. 2-9. Small helium flow test rig schedule

Program Management

Near-Term Planning. Principal efforts are now directed toward the start of testing in the fall of 1981. This is the target date for ORNL to complete the Stage I configuration of the CFTL. The Stage I CFTL will be capable of performing all 37-rod-bundle AG-1 tests listed in the test specifications except for the depressurizations. Planning has established that top priority be given to achieving the AG-1 milestones for design, analysis, test specification, fabrication, and coordination with ORNL. Figure 2-10 shows the design and fabrication schedule for the first two bundles.

Impact of Up-Flow/Down-Flow Decision. Most of the CFTL development appears to be equally applicable to either an up-flow or down-flow GCFR design. The current reference design is down-flow, and all ORNL work is limited to this concept. During the quarter, the impact of a possible up-flow decision was assessed, and a conservative estimate is that the cost will be $1 million more and there will be a 6-month delay. Many up-flow design details must be completed before a realistic estimate can be developed.

The limits of the problem are defined by a set of options for the loop and the test bundles. If the GCFR core up-flow design is selected, there are three options for Stage I CFTL loop:

Option A. Retain the down-flow design.

Option B. Reverse the flow and construct an up-flow design.

Option C. Design a loop with additional piping to operate in either down-flow or up-flow mode.

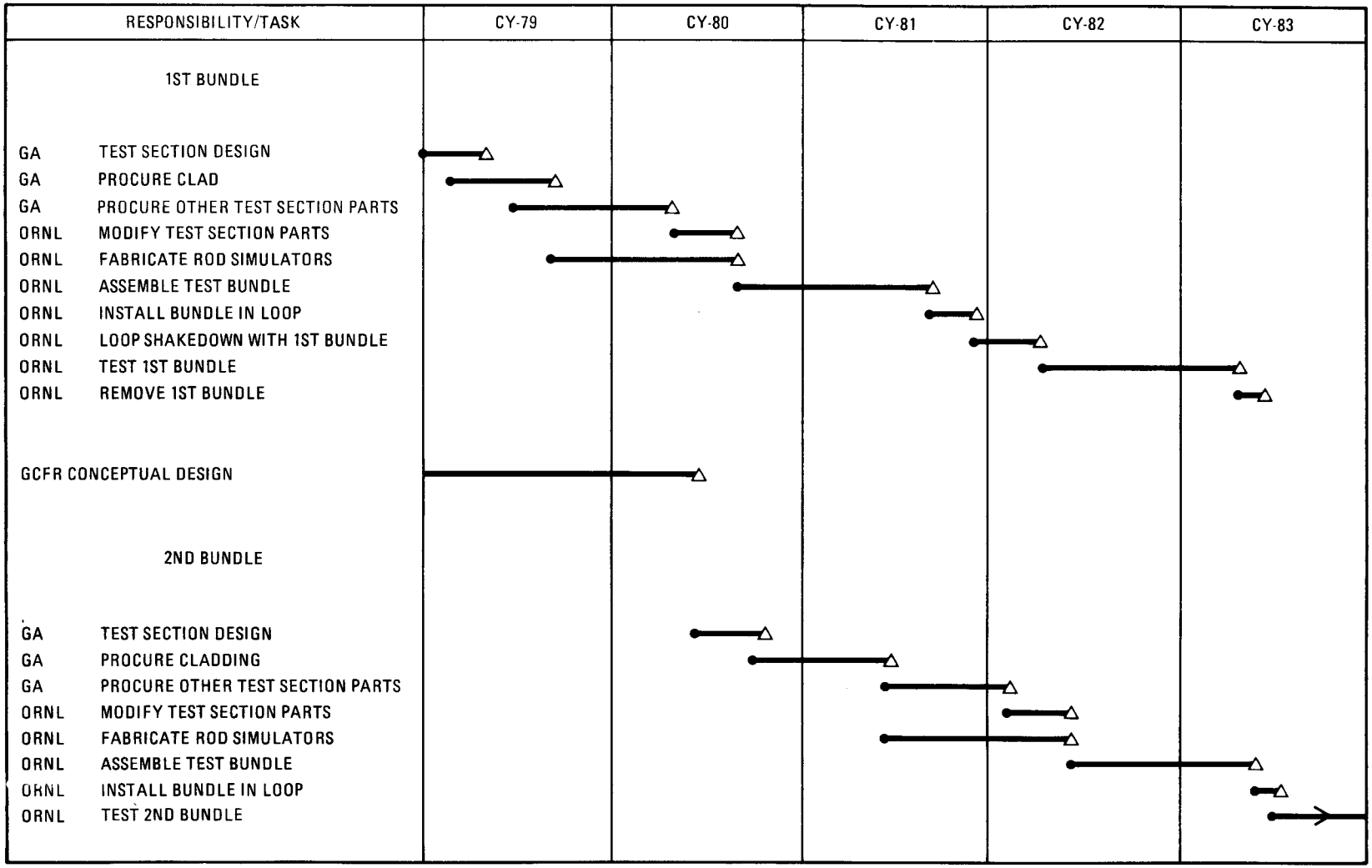

Fig. 2-10. Design and fabrication schedule to support first two CFTL test bundles (minimum $685 K (Rev.) funding level required in FY-80)

Option A will maintain the near-term cost and schedule, while options B and C are better technical approaches. For later stages of loop operation, flow simulation is postulated to require duplication of the GCFR direction.

In addition to the loop options, test bundle options must be considered. If loop option A, down-flow, is assumed, the bundle options are as follows:

1. Continue current design to qualify analysis: down-flow with rods fixed at the top, cold end.

2. Invert the test bundle to model some features of the up-flow design: down-flow with rods fixed at bottom, hot end.

If loop option B, up-flow, is assumed, the bundle options are the following:

1. Redesign the rod electrical connections to penetrate the pressure boundary at the hot, top end (reduces possible operating range).

2. Redesign the rod electrical connections to penetrate the pressure boundary at the cold, bottom end.

For loop option C, all of the above bundle options are possible. Loop option C is recommended if a final decision is not made on schedule or there is the possibility of reversing the decision.

CFTL Documentation. The top level documentation for the CFTL is assembled in the "Control Documents Manual" under the supervision of the CFTL Coordinating Committee. This manual was revised and now includes the following:

1. Management Plan (Rev. 2)

2. Program Plan (Amendment 1)*
3. System Design Description (Rev. 1)
4. Directive (Mod 1)
5. Work Plans and Schedule**
6. Test Section Design Drawings (Initial Issue)
7. Division of Responsibility (Initial Issue)

A computerized task document index (TDI), which contains CFTL reports, letters, and memoranda, was revised to identify current and obsolete documents. The TDI now lists 356 documents, of which 191 are current.

CFTL Analysis

This subtask includes thermal-flow structural analysis of the test models and the loop. A major effort supported the first test bundle design, and this is reported in Sections 2.1.2.3.2 and 2.3.1.3. Other activities include revision of maximum cladding temperature curves for the system design description (SDD) and a visit by J. Conklin of ORNL to coordinate thermal flow analysis.

Maximum Cladding Temperature. The SDD contained a carpet plot with maximum cladding temperature as the independent variable and flow (percent) and power (percent) as the dependent variables. The maximum cladding temperature is shown as a function of power fraction with flow fraction as a parameter in Fig. 2-11. The approximate relationship is given by the empirical equation

$$T_{max} = 286 \times \frac{P\%}{W\%} + 325$$

*At present, the Program Plan requires changes to reflect GCFR design, and this is now being accomplished by correspondence that will modify and refine the plan.

**At a meeting on January 18, 1979, the Committee revised and approved the schedule.

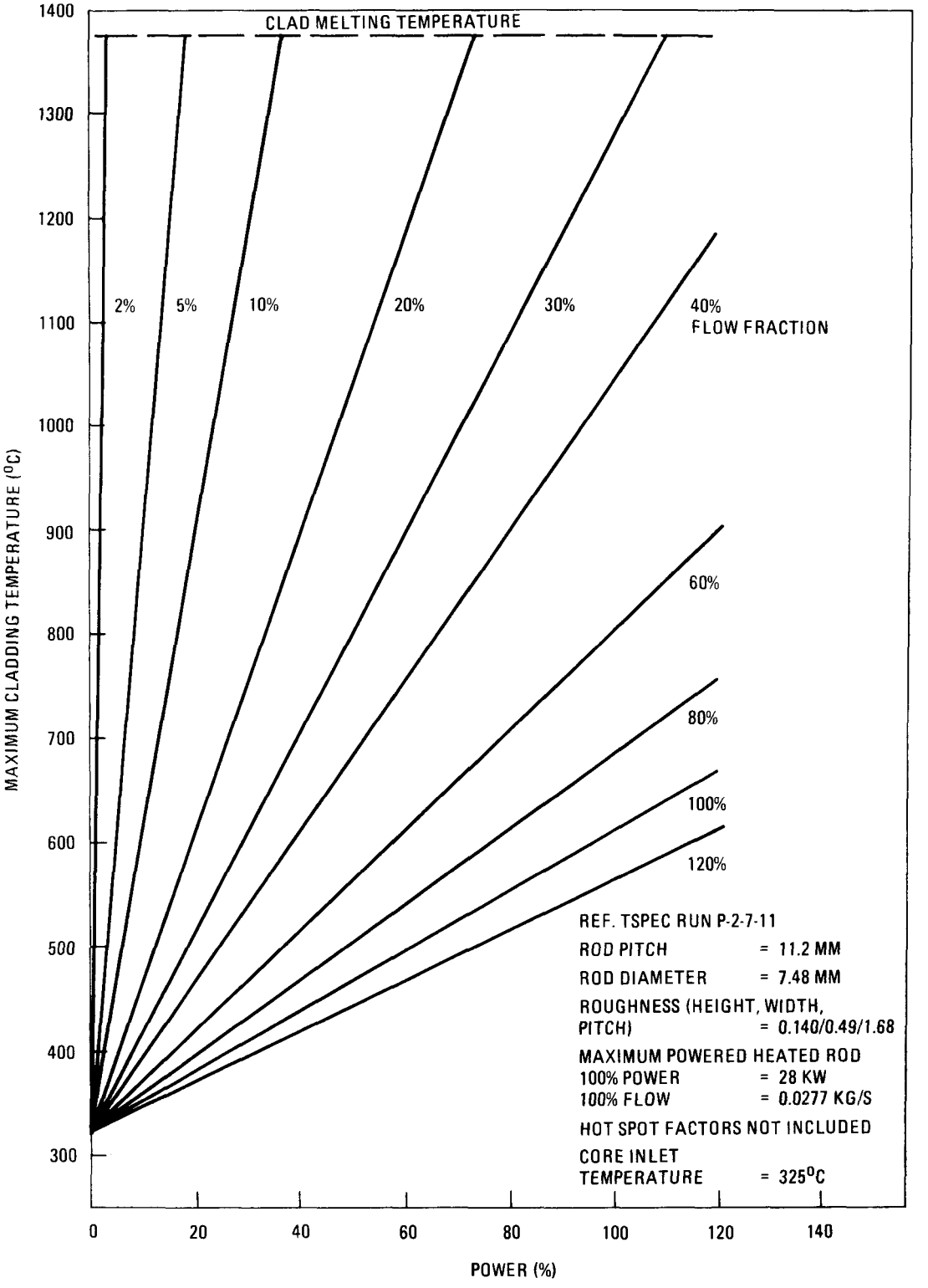

Fig. 2-11. Maximum cladding temperature

where T_{max} = maximum cladding temperature (°C),

P% = power fraction in percent,

W% = flow fraction in percent.

This plot is accurate to greater than 3% when compared with TSPEC calculations (Ref. 2-15) for the range of power and flow conditions from 10% to 110%.

CFTL Design. Revised drawings of the test section assembly and components for the first test bundle, AG-1 (formerly F1), are complete. The drawings incorporate the latest features of GCFR fuel assemblies for use in a down-flow core; e.g., interior tie (hanger) rods replace corner rods (only three will be used in the 37-rod bundle), ribbing of the fuel rod simulator has been lengthened to coincide with the total length and axial location of the heating element, and regular hex spacer grids replace those of modified hex design. The key features are listed in Table 2-9; the spacer is shown in Fig. 2-12.

Procurement specifications for cladding were reviewed and vendors were contacted for input to a cost-effective specification (Ref. 2-16) covering the cladding for the first CFTL test. The basis is ANSI/ASTM Specification A213-76a with modification; e.g., RDT M7-23T is required for chemical composition and ASTM E112-77 for grain size.

GA/ORNL Coordination

Principal program coordination is achieved through the CFTL Coordinating Committee, which has the function of coordinating and reviewing the program. The following actions were taken in January 1979:

1. Endorsed the CFTL schedule for inclusion in the Control Documents Manual.

TABLE 2-9
KEY PARAMETERS OF TEST BUNDLE AG-1

Duct	Hex/straight
Rod o.d., mm	7.46
Rod pitch, mm	11.2
Pitch-to-diameter ratio (based on rod o.d.)	1.5
Roughness height, mm	0.13
Roughness width, mm	0.45
Roughness pitch, mm	1.56
Spacer	Hex/straight
Spacer support	3 interior rods
Support rod roughened[a] sleeve o.d., mm	9.00
Wall spacing, mm	3.0
% of rod to rod gap	80.0
Heated length, mm	1130
Heated length roughened, mm[b]	1150
FRS total length from top of tube sheet to bottom end plug, mm	2220
Duct length, mm	∿2300
Duct across flats, mm	80

[a]Roughness height, width, and pitch of support rod sleeve are identical to heated rod roughness.

[b]10 mm beyond heated length.

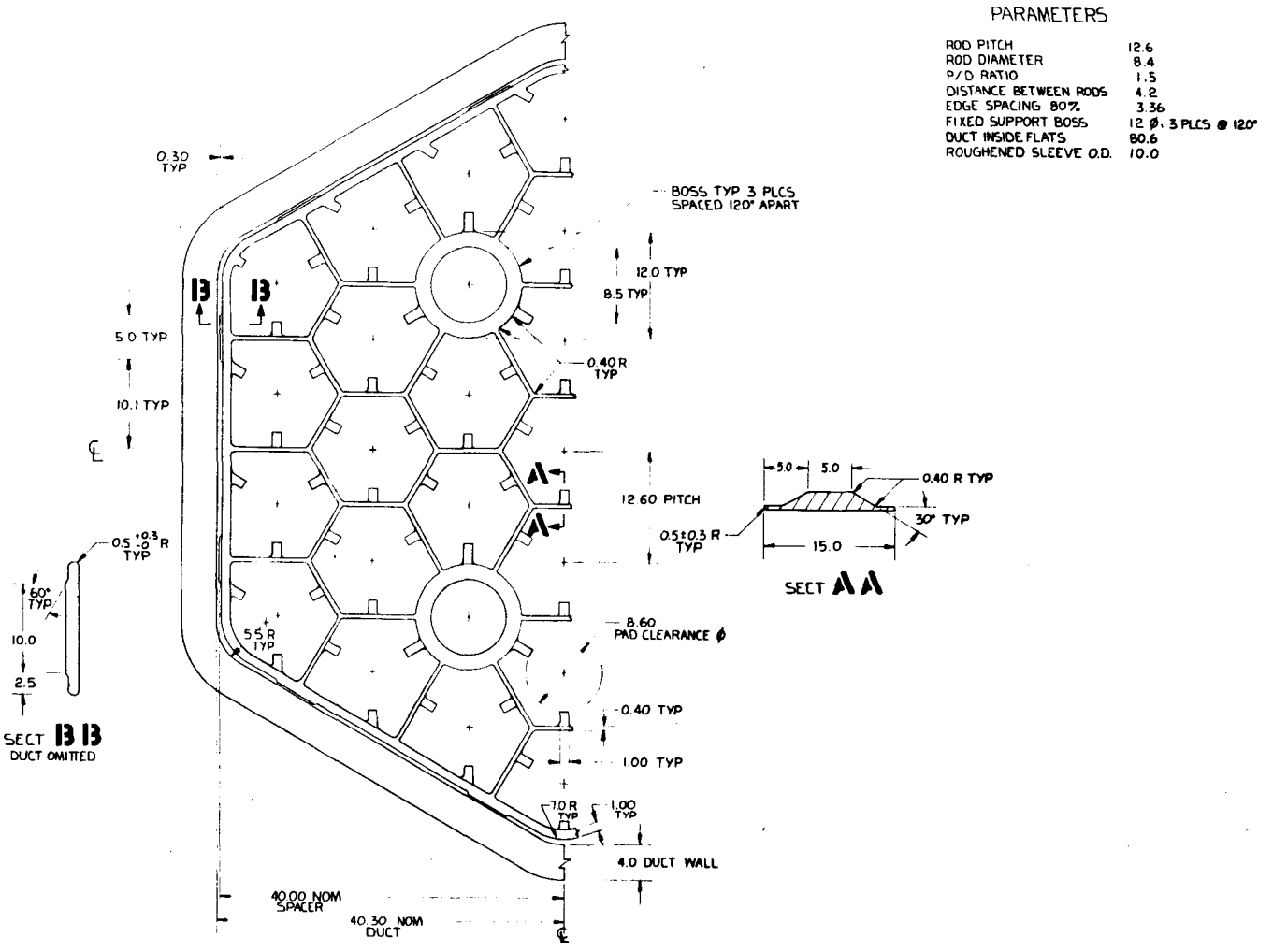

Fig. 2-12. CFTL spacer design

2. Urged ORNL to arrange work so as to minimize the impact of a possible shift from a down-flow to an up-flow core while continuing progress on the reference down-flow design.

3. Authorized ORNL to proceed with the structural-related methods development and analysis.

ORNL and GA are exchanging personnel to coordinate CFTL bundle design and analysis. In January, an ORNL thermal analyst spent a week at GA working on (1) the revised first test section design, (2) the modifications of COBRA*GCFR to consider the effects of circumferential clad thermal conduction and spacer heat transfer enhancement, and (3) consultation with COBRA*GCFR users at GA and attempts to isolate problems in running COBRA* GCFR at ORNL. In February, the GA coordinator spent a week at GA working on loop and bundle requirements for the first test, AG-1. In March, an ORNL designer reviewed and commented on the AG-1 test section design.

2.1.2.1.6 Core Assembly Prototype Tests

Program planning for testing of the prototype core assemblies is continuing on a limited basis because of program stretchout. The tests will be conducted on full-size core assemblies to ensure that they meet design qualification requirements prior to fabrication of the demonstration plant initial core. The prototype assemblies will be the same as the GCFR demonstration plant core assemblies except that the PuO_2-UO_2 fuel in the GCFR fuel rods will be simulated by depleted UO_2. The assemblies will be subjected to maximum GCFR helium flow conditions to simulate the reactor core environment closely; however, there will be no radiation. One assembly of each type (fuel, control, and blanket) will be subjected to the equivalent of approximately 1 year each of reactor operation in the hot helium test loop. The helium test loop temperature will be maintained external to the test section, since fuel rod heating will not be simulated in these tests.

Program Options. The core development plan (Ref. 2-17) and subsequent project work statements (Ref. 2-18) have assumed that the test facility and operation are planned as part of the German contribution to the GCFR program. Several options are being considered, including (1) a new facility which would most likely be situated in Germany, (2) the CARMEN-2 loop at Saclay, France, and (3) upgrading of the proposed GCFR core assembly helium flow test rig.

2.1.2.1.7 Depressurized Accident Condition Test

The depressurized accident condition test (DACT) will provide design basis accident data and core cooling safety margin information under low-pressure, pseudo-steady-state depressurized conditions. Experimental information on potential GCFR core assembly edge channel problems and flow and temperature distributions within the bundles under depressurized conditions will also be provided. In addition, DACT will be capable of investigating natural convection effects within the core assemblies. Since recently developed experimental equipment for the DMFT can be adapted to DACT, it is proposed that the DACT be conducted at LASL, which is including the DACT requirements in the design of the DMFT test vessel. The DACT will be accomplished before the CFTL DBDA tests and will provide the near-term information required for licensing reviews.

The task summary for the preparation of the DACT program plan has been completed. The first goal has been to get approval of the DACT program objectives by the resource and project groups. Preparation of the program plan is under way.

2.1.2.2. Pressure Equalization System (PES)

2.1.2.2.1 PES Seals

2.1.2.2.2. Plateout and Plugging.

Volatile fission products, particularly cesium and iodine, vented from the core assemblies and also produced in the monitor lines by decay of vented noble gas precursors, may plate out on the walls of the monitor lines. These fission products will be swept through the monitor lines into the helium purification system traps by helium entering at the core subassembly vent connections. If deposited material accumulates, it may constrict the sweep gas flow passages and could potentially lead to flow restrictions in the lines. The conditions under which plateout or plugging could occur in the GCFR, the means of minimizing or eliminating these conditions, and the methods for removing any deposits that might form are being investigated.

Insignificant levels of fission metal plateout will exist in PES monitor lines as a result of gaseous precursor (krypton, xenon) decay during transport in the monitor lines. By designing the rod and assembly traps to retain all condensable long-lived or stable metals (principally cesium) under normal and leaking-rod conditions, plugging of the monitor lines will not occur. The plateout and plugging task is being redirected to provide static data on the sorption of cesium on unirradiated and irradiated charcoal used in rod and assembly traps. In addition, the plateout and plugging loop previously designed for this task will be used to study the dynamic behavior of cesium over charcoal during simulated leaking rod conditions.

The potential for plugging of PES monitor lines is being reassessed in light of the accumulating body of in-pile data from fuel rod and subassembly irradiations. Results to date have shown that the fuel rod charcoal

traps are highly retentive of cesium, the volatile fission metal most likely to cause monitor line plugs. These findings raised the following question: assuming that the rod and assembly traps can be designed to retain essentially all of the volatile fission products during normal and leaking-rod conditions, will precursor noble gas decay itself lead to potential monitor line plugging?

This question is addressed in Table 2-10, where precursor and plateout data are summarized for all important nuclides. Xenon and krypton precursors (1) having measurable venting fractions from the fuel assembly, and (2) leading to long-lived or stable condensable daughter products are included. Venting fractions under nonleaking and leaking conditions were derived from in-pile measurements. A worst-case calculation (i.e., all 795 fuel rods serviced by a single monitor line are assumed to leak at the maximum rate) shows that only 0.22 g of condensable metals will plate out in the monitor line over 30 years of reactor operation. Since plateout from precursors will occur uniformly along the monitor line, the inner diameter of the line itself will be uniformly decreased by less than 0.01% (assuming the condensable metals remain unreacted). Under the more realistic design conditions of 1% leaking rods in fuel assemblies, the loading in the lines is reduced two orders of magnitude. These findings demonstrate that precursor decay will not lead to plugging of the monitor lines with the current design parameters. It is worth noting that monitor line plateout activity is directly proportional to transport times in the lines. If the transport time is increased an order of magnitude to 10 s, plateout activity will be increased a like amount.

These results raise additional questions:

1. What fraction of the cesium in the traps could be released before potential plugging becomes a problem?

2. Is it desirable to retain cesium in the traps, as opposed to letting it pass on through to the HPS?

TABLE 2-10
SUMMARY OF PRECURSOR AND PLATEOUT DATA FOR PES MONITOR LINES

Precursor Data								Plateout Data					
						Measured V/B (%)[e]				Plateout in Monitor Lines After 30 Years[f]			
Isotope	$t_{1/2}$[a]	λ (s^{-1})	Fission[b] Yield (%)	Birth[c] (Atoms/s)	R/B[d] (%)	Non-Leaking (HELM 2)	Leaking (GB-10)	Isotope	$t_{1/2}$	No Leaking Rods (Atoms)	1% Leaking Rods (Atoms)	100% Leaking Rods (Atoms)	100% Leaking Rods (g)[g]
Xe-133m	2.19 d	3.66×10^{-6}	0.226	1.44×10^{15}	29.7	0.3	8.5	Cs-133(134)	Stable (2.06 y)	1.5×10^{16}	1.9×10^{16}	4.2×10^{17}	9.3×10^{-5}
Xe-133	5.25 d	1.53×10^{-6}	6.58	4.21×10^{16}	39.1	2.6	11.0	Cs-133(134)	Stable (2.06 y)	1.6×10^{18}	1.7×10^{18}	6.7×10^{18}	1.5×10^{-3}
Xe-135m	15.3 m	7.55×10^{-4}	1.67	1.07×10^{16}	4.5	ND[h]	1.2	Cs-135	2.3 (+6) y	---	9.2×10^{17}	9.2×10^{19}	2.1×10^{-2}
Xe-135	9.09 h	2.20×10^{-5}	7.15	4.58×10^{16}	11.6	0.002	5.0	Cs-135	2.3 (+6) y	1.8×10^{16}	4.8×10^{17}	4.6×10^{19}	1.0×10^{-2}
Xe-137	3.85 m	3.00×10^{-3}	5.96	3.81×10^{16}	2.3	ND	ND	Cs-137	30.2 y	---	3.4×10^{18}	3.4×10^{20}[i]	7.7×10^{-2}
Xe-138	14.2 m	8.13×10^{-4}	4.96	3.17×10^{16}	4.7	ND	1.6	Ba-138	Stable	---	3.9×10^{18}	3.9×10^{20}	8.9×10^{-2}
Kr-85m	4.48 h	4.30×10^{-5}	0.613[j]	3.02×10^{15}	4.8	0.002	3.6	Rb-85	Stable	2.5×10^{15}	4.7×10^{16}	4.4×10^{18}	6.2×10^{-4}
Kr-87	76 m	1.52×10^{-4}	1.06	6.78×10^{15}	2.6	ND	2.2	Rb-87	Stable	---	2.2×10^{17}	2.2×10^{19}	3.2×10^{-3}
Kr-88	2.84 h	6.78×10^{-5}	1.23	7.87×10^{15}	3.8	0.0002	2.5	Sr-88	Stable	1.0×10^{15}	1.3×10^{9}	1.3×10^{17}	1.9×10^{-3}
Kr-89	3.5 m	2.67×10^{-3}	1.32	8.45×10^{15}	1.3	ND	0.32	Y-89	Stable	---	9.4×10^{17}	9.4×10^{19}	1.4×10^{-2}
								Σ Isotopes	---	1.6×10^{18}	1.18×10^{19}	1.0×10^{21}	0.22

[a] D = days, h = hours, m = minutes.

[b] Fast fission of Pu-239.

[c] B = (3.2×10^{10} fissions/W-s) (7.87×10^{8} W in active core) (0.0254-fraction of total birth per monitor line) (fission yield) = 6.40×10^{17} (fission yield).

[d] R/B = release rate from solid fuel to gas-filled interstices/birth rate in solid fuel (derived from beginning-of-life LIFE code calculations).

[e] V/B = release rate from fuel element vent connection/birth rate in solid fuel.

[f] Plateout = (V/B) (B) ($1 - e^{-\lambda t}$) (9.47×10^{8}) where t = transit times in monitor line, ≈1 s and 9.47×10^{8} = seconds per 30 years
= (V/B) (B) (λ) (9.47×10^{8}).

[g] Mass = (plateout)(atomic weight of isotope)/(6.02×10^{23}).

[h] ND = not detected

[i] Derived using V/B (leaking) for Kr-89.

[j] 23% of Kr-85m atoms decay to Kr-85 ($t_{1/2}$ = 10.7 years).

3. Will cesium be swept from the rod and asembly traps during leaking-rod conditions?

To provide answers to these questions, the plateout and plugging task is being redirected to encompass the following objectives:

1. Establish the data base available for cesium behavior on unirradiated and irradiated charcoal and graphite. This compilation will draw on previous studies carried out for the HTGR, as well as any other available sources. It is anticipated that this will principally involve static sorption data.

2. Extend studies of the static sorption of cesium on irradiated charcoal. Charcoal is known to densify in a fast neutron flux. The impact of this effect on the cesium sorptive capacity of charcoal will be defined. Irradiated charcoal free of mixed fission products is currently available from the F-1 capsule. This will be subjected to BET surface area measurements and cesium sorption studies using a pseudoisopiestic technique (Ref. 2-19) currently available at GA. These measurements will provide data on the cesium vapor pressures over irradiated charcoal as a function of temperature.

3. Define the dynamic behavior of cesium over unirradiated charcoal. This work can be carried out by adapting the existing plateout and plugging loop to include samples of charcoal loaded with cesium. In this manner, the rate of desorption of cesium from the trap under leaking rod conditions can be measured. If it can be established that cesium does not desorb under all credible normal operating conditions, plateout and plugging in the monitor lines can be eliminated as a potential problem associated with the PES.

2.1.2.2.3. Fission Product Release and Transport

The purpose of this subtask is to obtain experimental data on (1) interdiffusion of fission gases in helium, and (2) gas and surface back-diffusion of gaseous and volatile fission products into the reactor coolant. The interdiffusion coefficient data will be used to validate or improve the fission product release code that models gas-phase diffusion transport (including radioactive decay). Surface transport and back-diffusion data will be used to establish a model for predicting the importance of these mechanisms in contamination of the reactor coolant system.

Interdiffusion Studies

Studies of gaseous diffusion in simulated GCFR fuel rods are nearing completion, with all planned measurements of krypton and xenon diffusion having been completed. Analyses are in progress to define the diffusion coefficients of these fission gases through charcoal. Knowledge of the diffusion coefficients in charcoal will permit calculation of expected hold-up times in the fuel rod and assembly charcoal traps. These results will permit reliable predictions of fission gas transport by gaseous diffusion in GCFRs under normal and off-normal operating conditions.

Back-Diffusion Studies

The first phase of work aimed at defining the extent of surface and back-diffusion at suction holes, fuel assembly vent connections, and potential fuel rod cladding breaches has begun. Back-diffusion of volatile fission products into the GCFR helium coolant stream is a potential source of circulating activity and plateout contamination in the primary circuit. Several avenues for back-diffusion have been postulated:

1. Counter-diffusion within the boundary layer of helium flowing through the core assembly suction holes.

2. Back-diffusion at the core assembly vent connections.

3. Diffusion through potential cracks and holes in fuel rods with cladding leaks.

Each of these pathways will be investigated in out-of-pile tests. Initial studies are focusing on gaseous fission product back-diffusion through the fuel element suction hole. This pathway was selected for study since it can be readily simulated in the laboratory and has been modeled using first principles.

The suction hole is a passage in the core assemblies that serves a dual function: (1) it permits primary coolant helium to enter the fuel rods to maintain nearly equal pressure on both sides of the fuel rod cladding, and (2) it allows flowing helium to sweep gaseous and volatile fission products venting from the assembly trap into the monitor lines and helium purification system. This study will define the conditions under which back-diffusion will occur in simulated suction holes. Table 2-11 presents a comparison of suction hole dimensions, helium mass flow rates, operating temperatures, and operating pressures for the reference 300-MW GCFR demonstration plant, the HELM 3 in-pile loop test, and the planned experimental apparatus.

Back-diffusion of gaseous and volatile fission products has been treated mathematically. At a PCRV pressure of 8.59 MPa (85 atm), the ratio of gaseous fission products back-diffusing through the suction hole to gaseous fission products swept up the monitor line is $<<10^{-12}$ or zero. These results indicate that no gaseous back-diffusion would be expected under anticipated GCFR operations conditions. An experiment measuring the extent of fission gas venting to the coolant, perhaps by back-diffusion, was conducted in the HELM 3 test. Helium flow rates in the suction hole were substantially reduced below the nominal values while the activity in the bundle coolant was monitored. Only when suction flow had reached essentially zero was there evidence of increasing coolant activity. In

TABLE 2-11
COMPARISON OF SUCTION HOLE PARAMETERS

System	Suction Hole Diam (mm)	Helium Mass Flow in Suction Hole (g/s)	Inlet Temperature (K)	Inlet Pressure (MPa)	Suction Hole ΔP(kPa)
300-MW GCFR demo. plant	To be determined (straight passage)	0.1578	573	8.6	13.7
HELM 3 loop test	1 mm diam x 11 mm + 1 mm diam x 9 mm (at right angles)	0.215	528	6.06	15.2
Experimental apparatus	1 mm diam x 12.7 mm (straight passage)	0.0018 to 0.158	295 (initially)	0.1 to 8.6	0.162 to 13.7

addition, bundle coolant activity showed no significant changes during transient operating conditions.

Experiments

The experimental apparatus simulates the current PES design, which uses a suction hole near the fuel element-to-grid plate connection (see Fig. 2-13). Since the location, length, and diameter of the suction hole have not been fixed, a mock-up of the suction hole has been fabricated which has a diameter of ∿1.0 mm and a length of 12.7 mm (see Fig. 2-14). Liquid-nitrogen-cooled fission gas traps will be used to recover activity from flowing gas streams, as shown in Fig. 2-13. A Canberra NaI(Tℓ) scintillation detector, single-channel analyzer, and accompanying equipment will measure the activity in the traps.

Simulated primary coolant helium supplied by high-pressure tanks will be swept through the reactor coolant side of the apparatus (Fig. 2-13) by opening valves, 1, 2, and 3. A small fraction of this helium will flow through the suction hole to the monitor line when valve 6 is open. The pressure drop across the suction hole will be monitored with a Validyne CD-12 differential pressure transducer. Krypton-85 will be introduced by opening valves 7 and 8 to simulate fission gas venting from the fuel element annular trap. The krypton that back-diffuses through the suction hole will be swept away and collected in trap A. The remaining krypton will be swept up the monitor line by the helium streaming through the suction hole and collected in trap B. The following experimental parameters are to be varied:

1. Helium flow rates in the suction hole.
2. Helium pressure.
3. Pressure drop across the suction hole.
4. Suction hole dimensions.
5. Gaseous fission product concentration in helium.

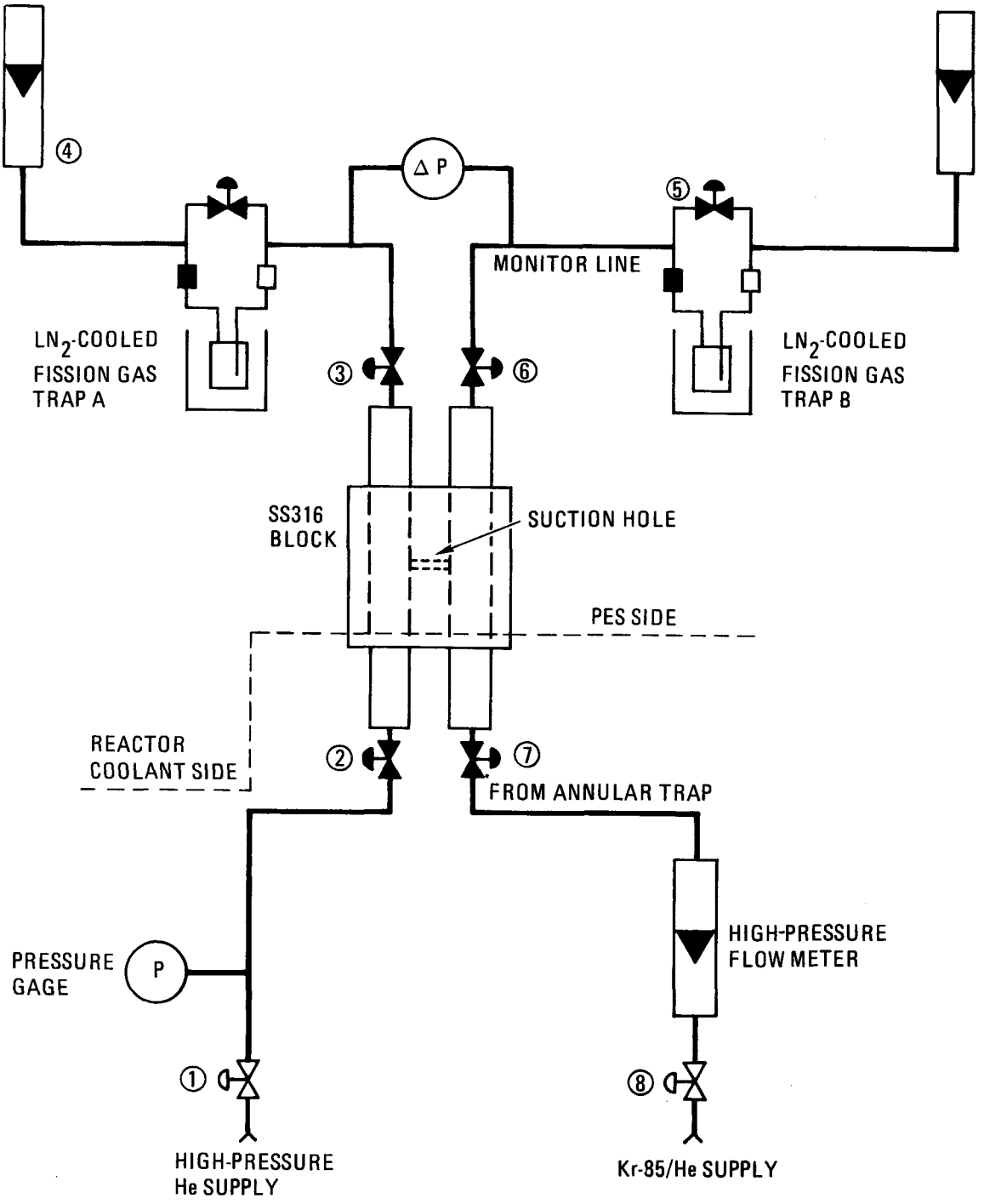

Fig. 2-13. Schematic of gaseous back-diffusion apparatus

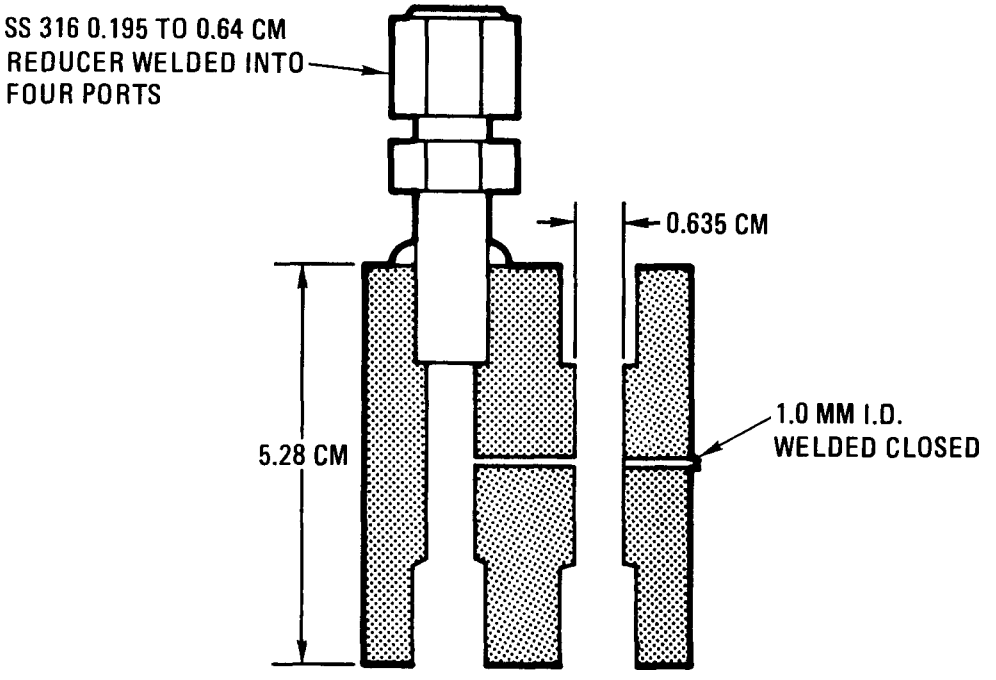

Fig. 2-14. Schematic of suction hole mock-up

It should be noted that experimental conditions deviating significantly from GCFR operating conditions will be required to induce back-diffusion. This comes about because of the very low fraction of gaseous fission products expected to escape under any but the most favorable conditions for back-diffusion. As such, the experimental conditions will use much lower helium velocities and flows in the suction hole and much lower pressures to permit back-diffusion to occur.

2.1.2.2.4. Monitor Station and Instrumentation

Research and development are being conducted to establish design criteria and to acquire design information for the monitor stations of the proposed GCFR demonstration plant and subsequent commercial reactors. The stations monitor the radioactivity of gaseous fission products passing through the lines of the PES after sweeping past the vent holes of the core assemblies. Development and testing must be associated with the fuel irradiation tests.

A monitor station is being assembled for acquisition of radioactivity (photon emission) data from fission product gas mixtures being vented from the GCFR 12-rod fuel bundle (HELM 3) being irradiated in the helium loop in the BR2 reactor at Mol, Belgium (HELM).

The BR2 reactor (and thus HELM) was shut down near the end of 1978 to permit replacement of the beryllium. Irradiation of HELM 3 is expected to resume shortly after the start of CY-80. Thus, completion and delivery of the monitor station have been rescheduled for the end of FY-79 to allow time for its installation and checkout.

During this report period, discussions have been conducted with commercial instrumentation and detector vendors. No commercially available detectors are capable of meeting the photopeak resolution and dynamic counting rate range specified for the HELM monitor station detector. The use of two (high and low range) detectors per station, changeable collimators, or movable detectors may be required to meet the specifications, resulting in a more complex design.

Before designing a more complex station, however, the specified dynamic range is being reevaluated using more recent results from the GCFR fuel irradiation program including those from the GB-10 vented capsule and from the HELM 3 test. The computer code COUNT, under development for monitor station design and analysis, will be used. The current dynamic range specification was developed many years ago when there were few irradiation data. There are indications that the dynamic range required may be substantially less than previously indicated and specified. If a dynamic range of $\leq 10^5$ cps is acceptable, it should be possible to use a single commercial photon detector without the design complications mentioned above.

The expected count rates of GCFR and HELM monitor stations will be calculated using the COUNT code. Count rates corresponding to an individual rod with maximum leakage and to a nonleaking rod are necessary to provide data on the dynamic counting rate range required. Initially, the counting rates will be calculated based on the use of a planar Ge(Li) detector. Later, similar calculations will be done based on the use of planar Ge(I) semiconductor and NaI(Tℓ) scintillation detectors. The dynamic ranges, efficiencies, and resolutions of the detectors will be compared for suitability to the monitor station application. An initial set of input parameters has been selected and a trial run is being evaluated. Results will be compared with HELM data. Some spectral data taken from HELM during the HELM 3 test in both normal and breathing (exhalation) operations have been received along with the HELM instrumentation calibration curves.

The possible use of a cryogenically cooled detector raised questions about the location of the detector in the HELM facility. The Ge(Li) or Ge(I) detectors require cryostats of significant size (e.g., a 30-liter dewar for a dip stick cryostat is ∿450 mm in diam by ∿750 mm high). In contrast, the CdTe(Cl) detector that the Ge detectors might replace are only ∿15 mm in diam by 25 mm high and require no cooling. The well at the HELM in the FR2 facility where the detector is to be located is ∿690 mm wide by 1380 mm long by 840 mm high. The well can easily accommodate the full range of detector sizes of commercial detectors that might be utilized. Thus, it will not be necessary to relocate the detector, the microprocessor, or the spectrometer electronics cabinets from their planned locations regardless of which detector is selected.

2.1.2.3. Assembly Methods Development

2.1.2.3.1. PES Methods Development

A transient PES flow network code (SINDA/PES) is being developed. The PES, described in Ref. 2-20, is a complex flow network. It consists of vented core assemblies which admit gas from the coolant, normally at controlled rates, to sweep the vented fission product gases through interconnected matrices of passages and lines past radioactivity monitors into the dedicated helium purification system. The purified helium is returned to the coolant stream via check valves to the suction sides of the main and auxiliary circulators which power the system.

No progress was made during this report period. Some debugging of the SINDA/PES transient PES flow network code still remains to be done before publication of the code.

2.1.2.3.2 Structural Methods Development

CFTL Structural Analysis Support

Structural Performance Evaluation of GCFR Spacer Grids. Finite element models have been developed to predict the GCFR spacer grid structural performance under loadings caused by mechanical interaction between the fuel rods and the grid. The models were validated by structural tests. Application of the models to the analysis of alternate GCFR spacer grid designs has demonstrated that a grid design composed of regular hexagonal cells and supported at six points located one row in from the edge, midway along the flats, is superior to other configurations and is recommended for use in the GCFR.

Analyses have also shown that the recommended spacer grid can meet the structural functional criteria in the absence of irradiation effects. Further investigations of the irradiation effects on the spacer grid structural behavior are needed to ensure the in-reactor structural integrity of the spacer grid.

A finite element analysis model was developed for the modified hex spacer grid design shown in Fig. 2-15. A model was also developed for a grid of the same overall configuration but having regular hexagonal cells. In the models, the spacer grid was idealized as an assemblage of three-dimensional beam elements having torsion, bending about two axes, and axial and shear deformations. The MODSAP code (Ref. 2-21) was used for the analyses. Only one-sixth of the spacer grid was modeled due to symmetric loading and geometric conditions. In addition to the evaluation of the type of designs (regular versus modified), the effects of the tie rod support location and type of support condition (simple versus clamped) were included in the analyses. Figures 2-16 and 2-17 display the one-sixth models of the spacer grid finite element models for the modified and regular hex, respectively, used in MODSAP. The alternative support locations investigated are also indicated (at the corner, the second row in on the corner, and the second row in on the flat).

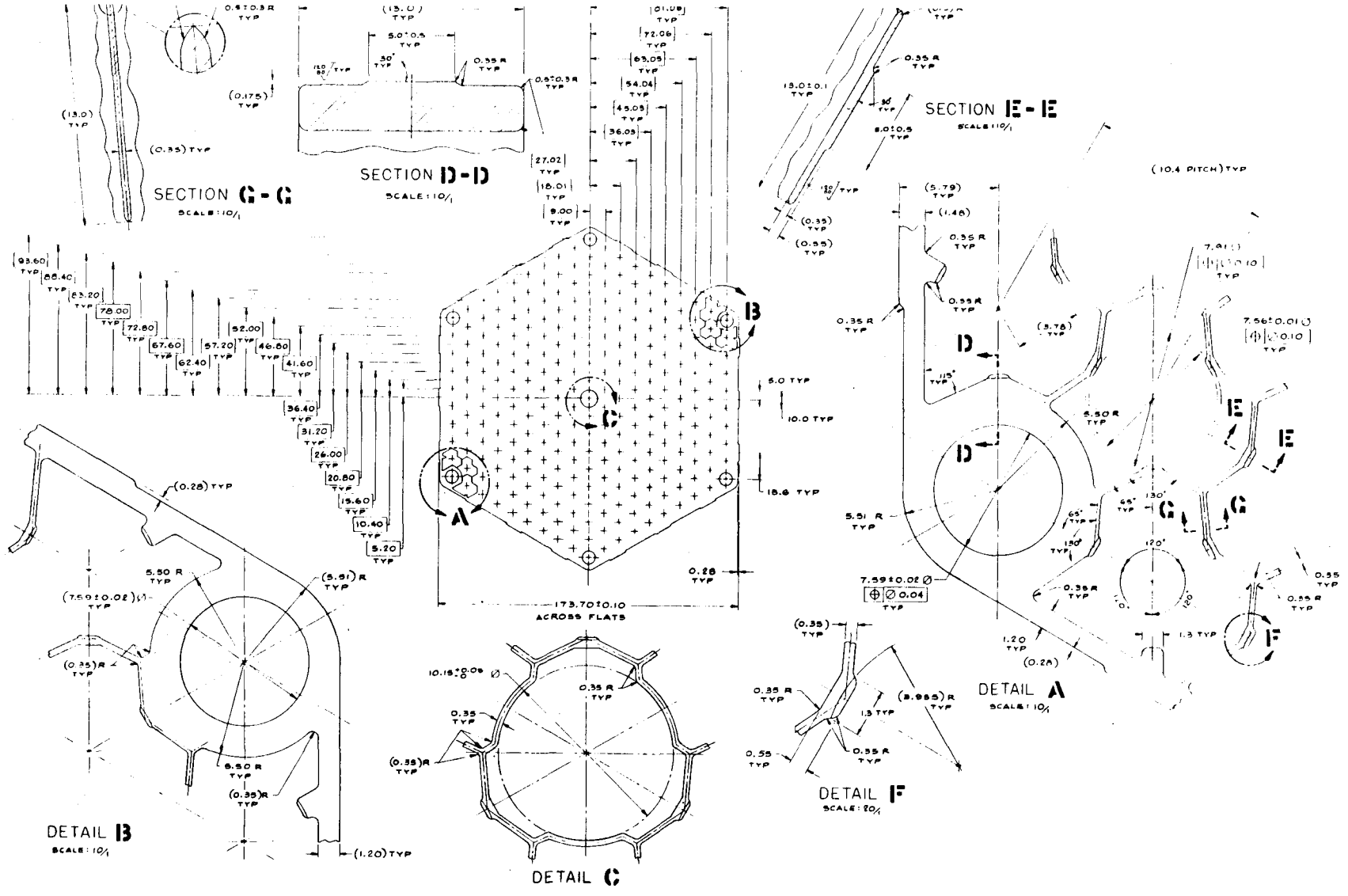

Fig. 2-15. Hex spacer grid design

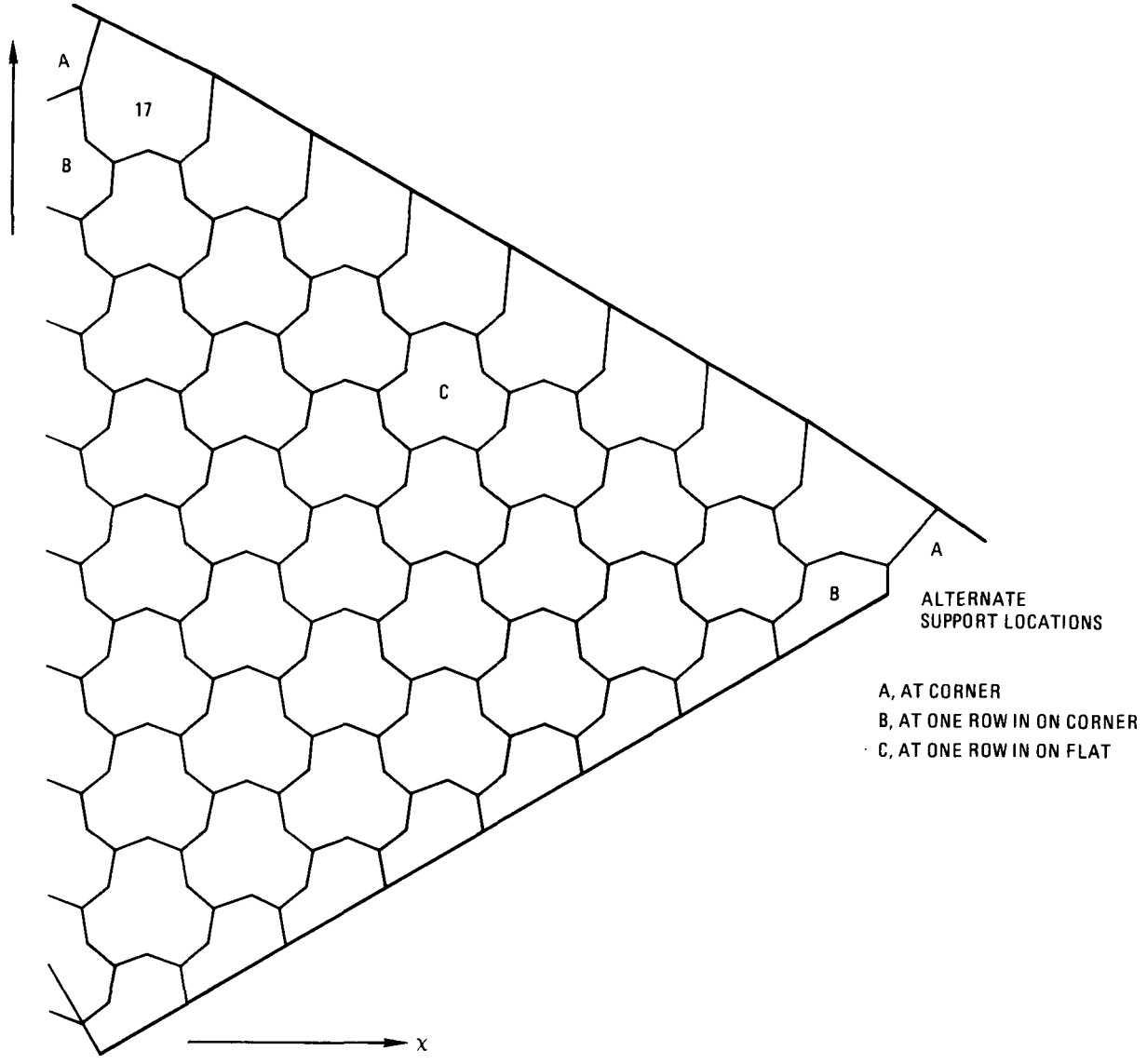

Fig. 2-16. MODSAP model for modified hex spacer grid

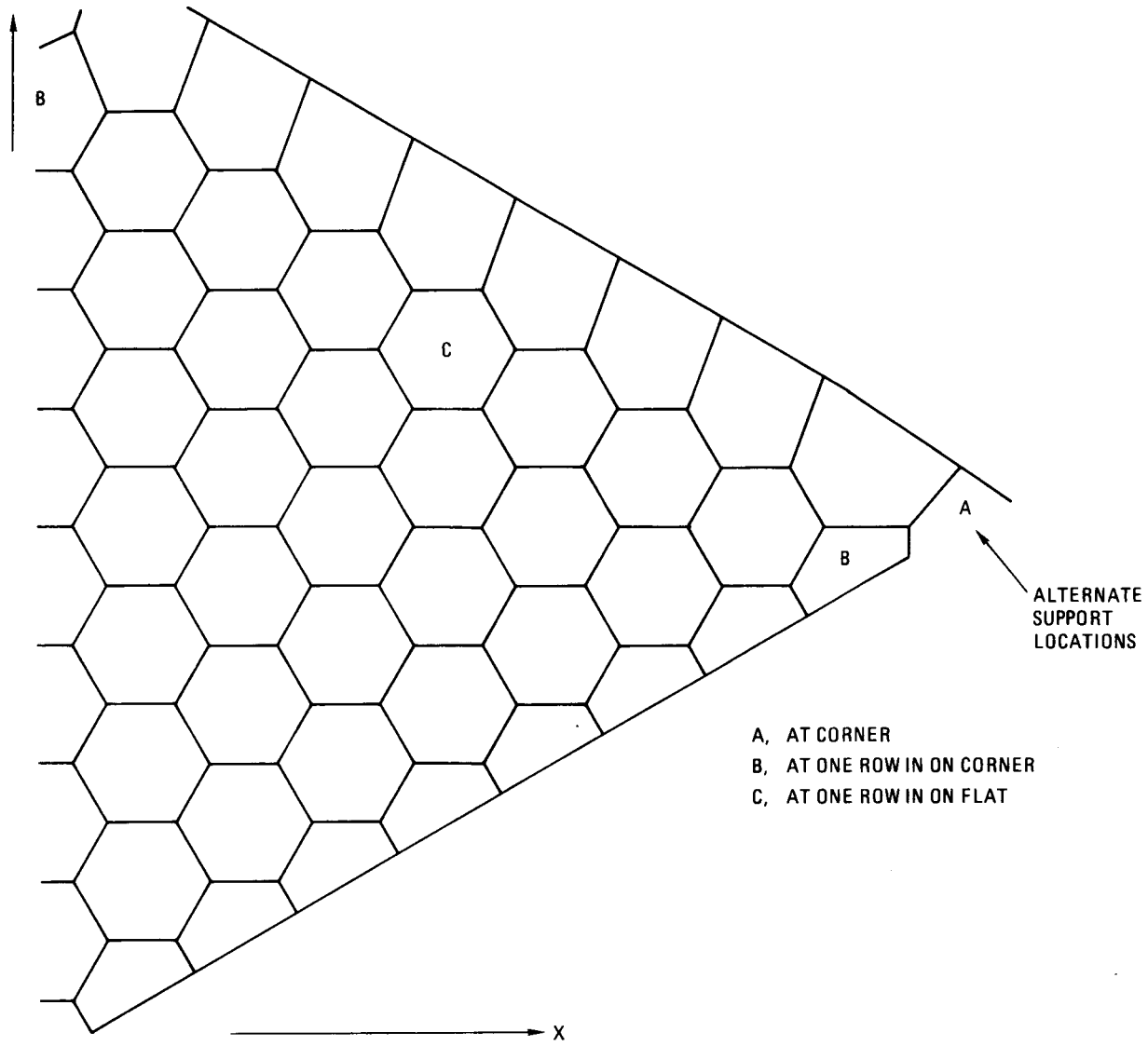

Fig. 2-17. MODSAP model for regular hex spacer grid

Loadings on the spacer grids arise from the mechanical interaction between the fuel rods and the grid due to rod bowing caused by thermal gradients. Lateral interaction loads can be calculated using a thermal bowing code such as CRASIB (Ref. 2-22). Axial forces on each cell were obtained by assuming a friction factor of 1.0 between the fuel rods and the grid. The interaction loads obtained from CRASIB were 9.052 N and 8.593 N for the edge-row rods and the second-row-in rods, respectively. The axial forces for the remaining rows were obtained by linearly extrapolating from 8.593 N at the second row to zero at the central cell, where the interaction between the fuel rod and the grid is absent because of symmetry. In the analyses, two temperatures were used: 427°C (800°F), which is about the mid-core coolant temperature, and 538°C (1000°F), which is about the outlet coolant temperature.

Figure 2-18 shows the deflection curves in the directions of corner-to-corner and flat-to-flat for the modified and regular hex grids, respectively. This shows that the regular hex grid is much stiffer (13.5 times in terms of maximum deflection) than the modified hex grid. Because of the superiority in stiffness, the regular hex design is recommended for the GCFR spacer grid.

Figure 2-19 is a plot of the regular hex spacer grid deflections for the different tie-rod support locations, namely, at the corner, the second row in on the corner, and the second row in on the flat, as indicated by cells A, B, and C, respectively, in Fig. 2-16. Support at the second row in on the flat results in the least deformations. Based on the deformations and stresses, the second row in on the flat location is recommended for the GCFR spacer grid tie-rod support.

The recommended GCFR spacer grid is a regular hex design supported at the second row in from the edge, midway along the flat. The analysis to select the type of spacer grid and support location was performed at a grid temperature of 427°C (801°F), the approximate GCFR mid-core coolant temperature. For conservatism, the design analysis of the recommended

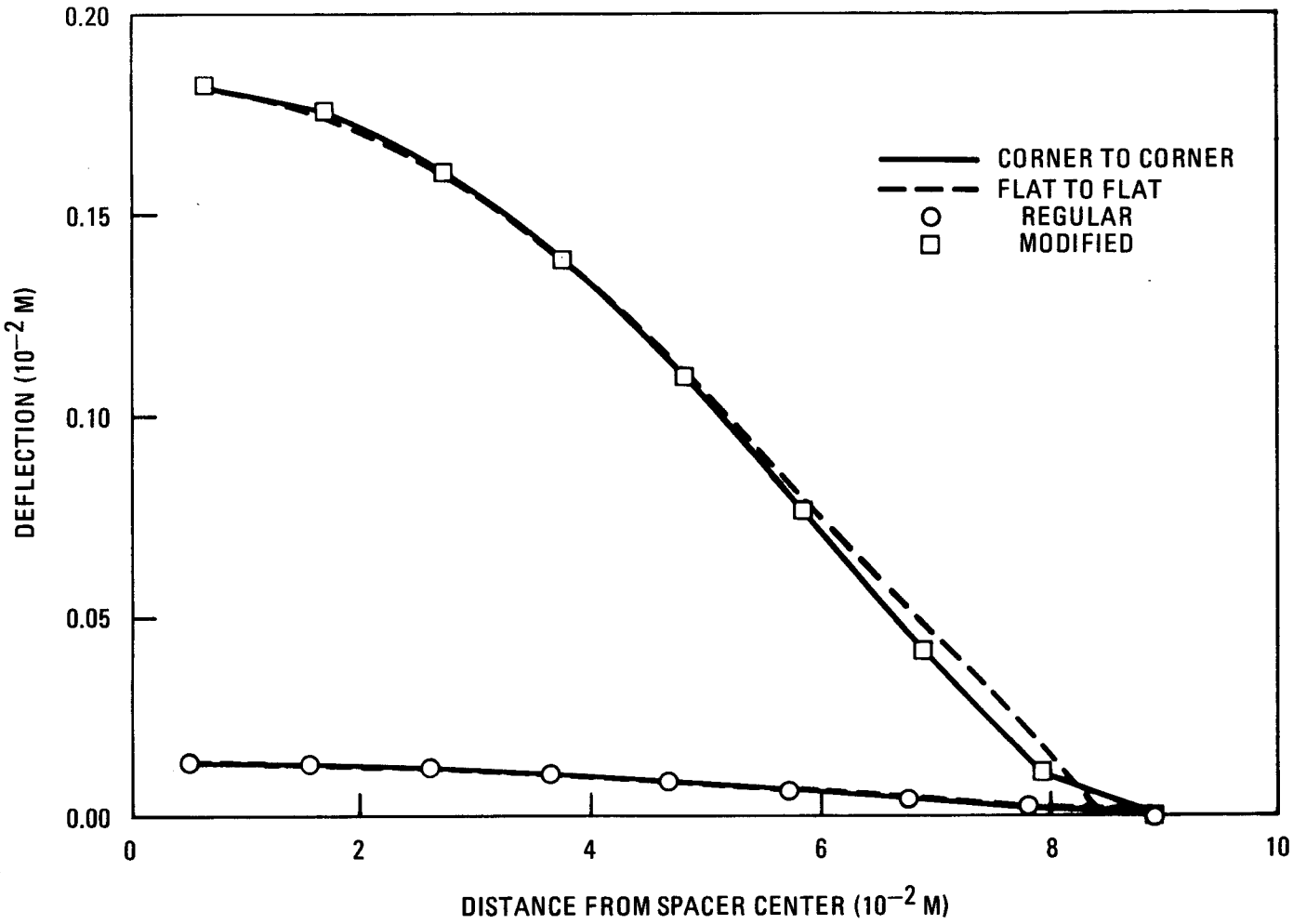

Fig. 2-18. Deflection for hex spacer grid clamped at corner

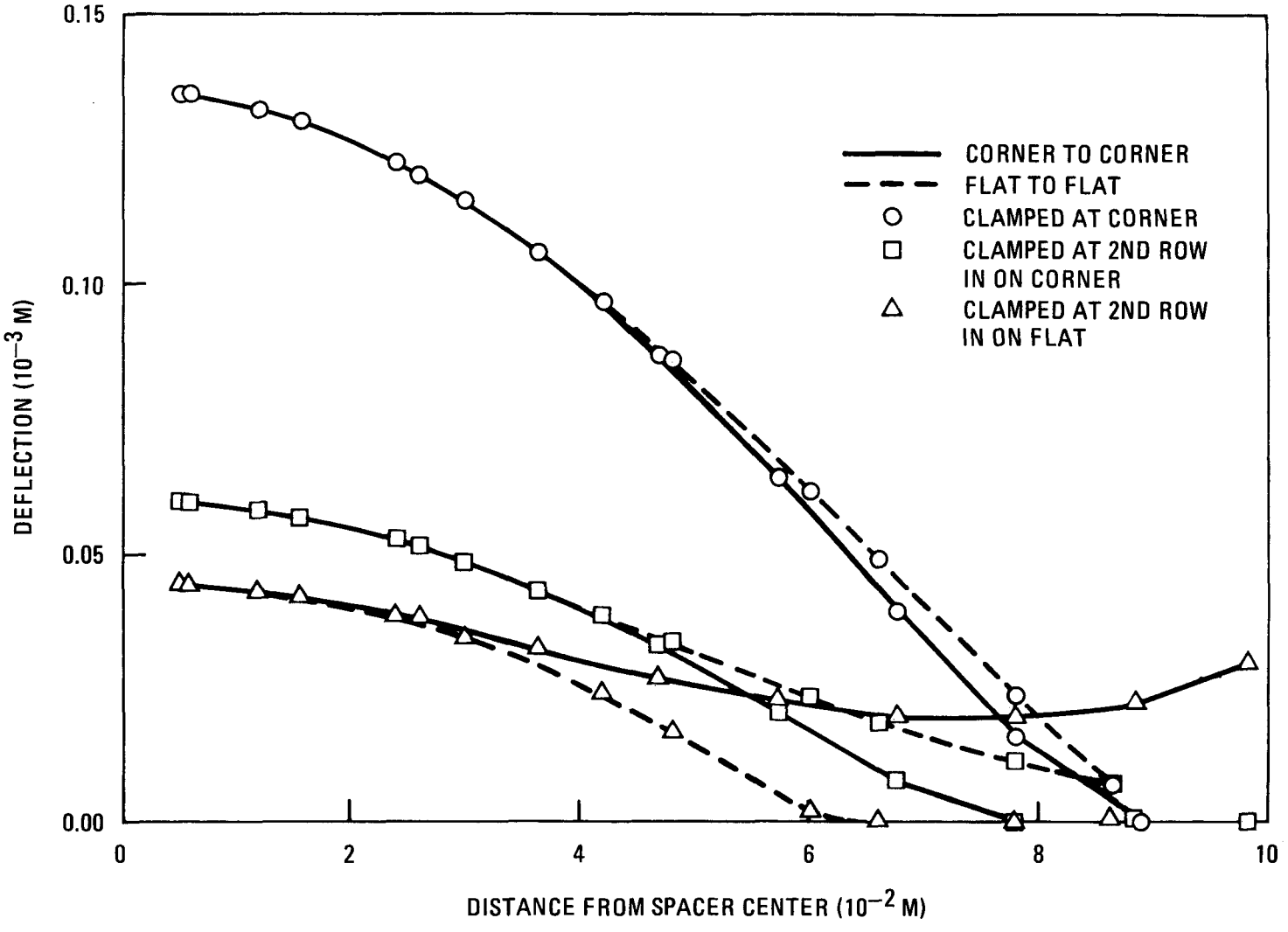

Fig. 2-19. Deflection for regular hex spacer grid

GCFR spacer grid was performed at 538°C (1000°F), the approximate coolant outlet temperature. Figure 2-20 shows the deflection results for the recommended spacer grid for simply supported and clamped conditions. The difference in deflection between the simple and clamped supports is negligibly small, because the support condition behaves as a point support. The analyses of deformation, stresses, and thermal creep ratcheting were found to be well within acceptable limits.

A regular hex spacer grid with the dimensions defined in Fig. 2-15 (web thickness, grid depth) with supports at the second row in on the flat satisfies the structural functional criteria in the absence of irradiation effects. The irradiation effects on the spacer grid structural behavior need further investigations.

The use of an assemblage of beam elements to characterize the spacer grid structural behavior was previously verified using the 37-cell AGATHE HEX II spacer grid, as described below. Although the extension of the 37-cell grid model to the full-size 271-cell GCFR spacer grid is obvious, experiments were performed to reinforce the verification. Tests were performed on a sample duct melting and fall-away test (DMFT) spacer grid as reported in Section 2.4. The comparison of the maximum deflection between the MODSAP predictions and the test measurements is as follows:

	Maximum Deflection (in mm) per 445 N (100 lb)	
	MODSAP	Test
Simple support	2.84	2.80
Clamped support	2.45	2.55

The differences between the MODSAP predictions and test results are within 4%, an excellent agreement.

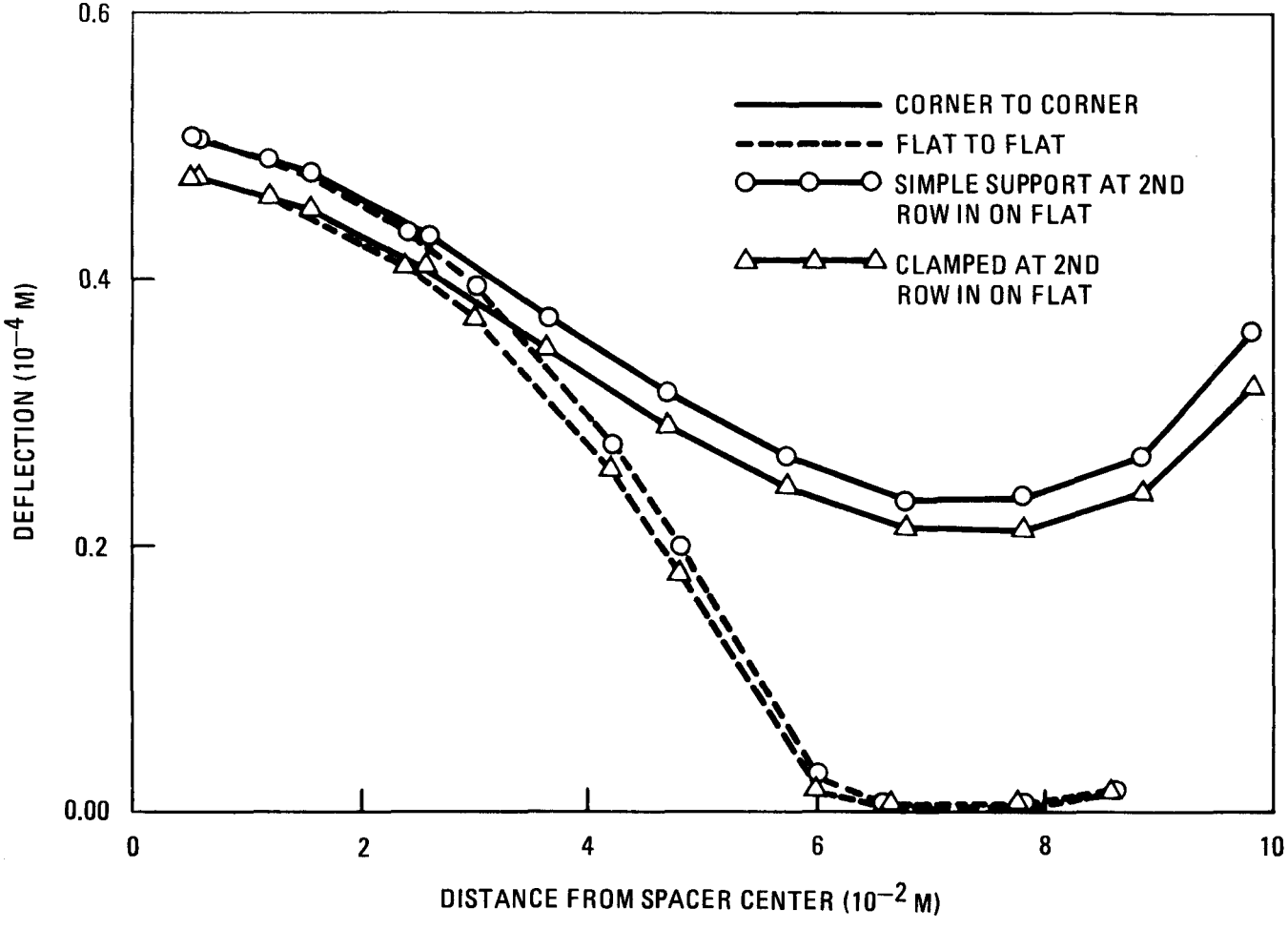

Fig. 2-20. Deflection for regular hex spacer grid at 538°C

Spacer Grid Structural Analysis Model Verification. As part of the program to develop a spacer grid model to support the CFTL bundle AG1 analysis, a finite element model of an AGATHE HEX II spacer grid was developed and the load/deflection characteristics of the model were verified by load/deflection tests of an actual AGATHE-HEX II grid.

Provided that web warping constraint is properly accounted for and actual grid dimensions are employed in the analysis, agreement between analysis and test is excellent, generally within 10% for both simply supported and clamped boundary conditions.

The AGATHE HEX II spacer grid (Fig. 2-21) is a 37-cell grid of the modified hex* type. The six corner rod positions serve as support points. The grid is manufactured from a solid piece of cold-worked 316 stainless steel using the wire electrical discharge machining method. The grid was analyzed using the finite element code MODSAP (Ref. 2-21). One-half of the grid was modeled as an assemblage of linear elastic beam elements capable of extension, torsion, and bending and shear deformation in two directions. The model (Fig. 2-22) consists of 87 nodal points and 98 beam elements. As can be seen, the actual modified hex geometry has been simulated.

The computer code requires input of the following beam geometric property data: axial area, shear areas in two directions, torsional stiffness, and bending moments of inertia in two directions. The determination of all parameters but the torsional stiffness is straightforward. The determination of the correct value for the torsional stiffness is more difficult.

*The webs are not straight but have been given an angle to reduce the size of the spacer pads.

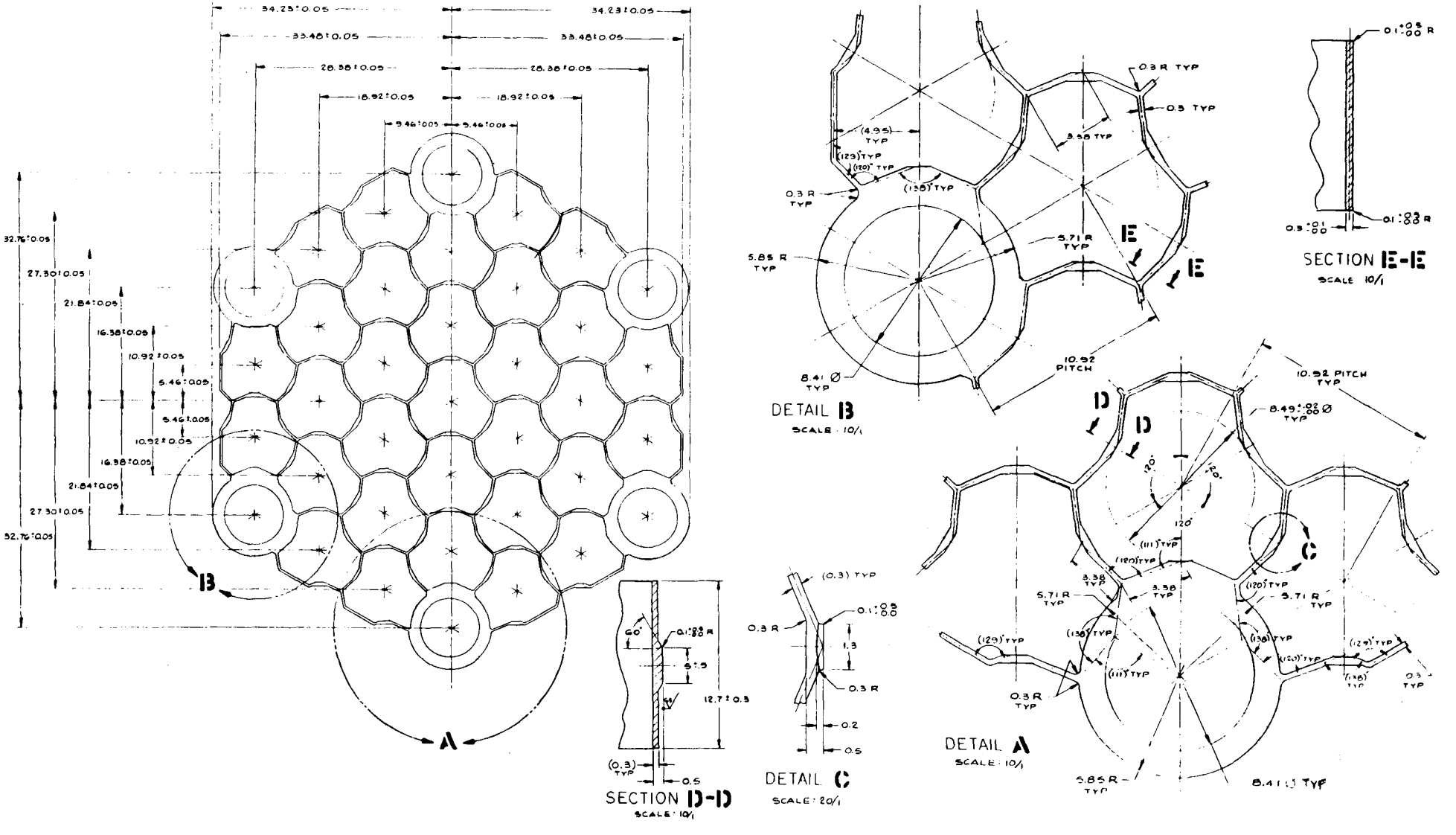

Fig. 2-21. AGATHE HEX II spacer grid

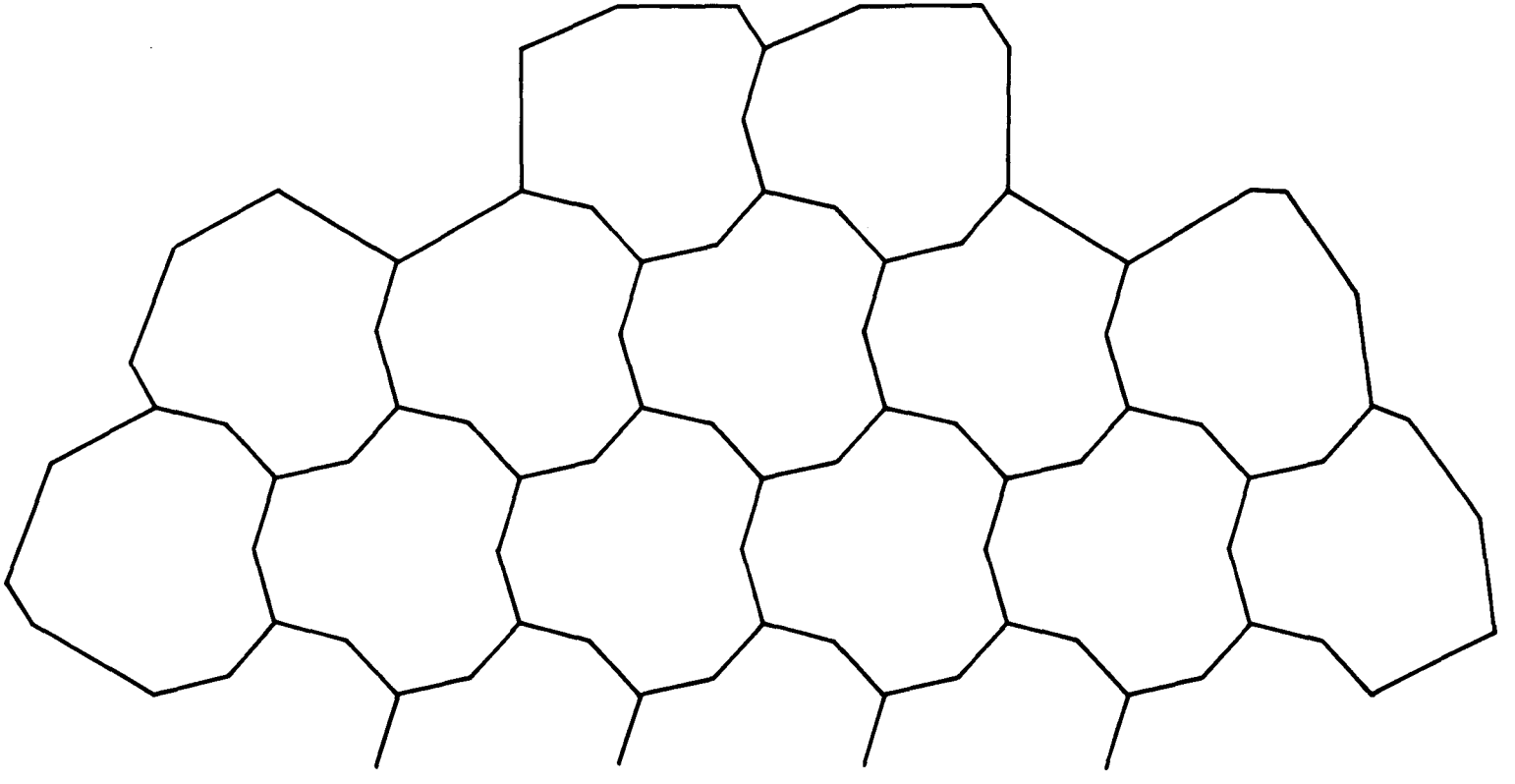

Fig. 2-22. MODSAP AGATHE HEX II spacer grid model

A treatment of warping constraint can be found in Timoshenko (Ref. 2-23), from which a formula for the torsional stiffness factor K can be derived as follows:

$$K = \frac{ab^3}{3}\left[1 - \frac{\sqrt{5(1+\nu)}}{12}\,\frac{a}{\ell}\right]^{-1}$$

where a = web height,

b = web thickness,

ℓ = web length,

ν = Poisson's ratio.

The term to the left of the brackets is the ordinary torsional stiffness factor for a tall slender beam; the factor within the brackets is the modification required to consider end constraint. As indicated above, this latter factor can be significant; for the AGATHE HEX-II grid, it increases K by a factor of about 4.7 and reduces the grid deflection by more than a factor of 2.

Another consideration of importance is the effect of tolerances, particularly the tolerance on web thickness. From Fig. 2-21, it can be seen that the web thickness is given as 0.3 mm, plus 0.1 mm, minus nothing. Scoping runs along the minimum thickness (0.3 mm) and the maximum thickness (0.4 mm) showed that this variation alone could change the grid stiffness by nearly a factor of 2. Thus, measured grid dimensions were used in the final analysis.

The analysis considered the grid loaded at the central cell, and considered both simply supported and clamped boundary conditions at the six corner tie bar locations. A typical deflected shape of a grid diameter is shown in Fig. 2-23.

The comparison between AGATHE HEX II load deflection test results as described in Section 2.4 and the MODSAP finite element predictions is given in Table 2-12. As can be seen from the table, the predicted values

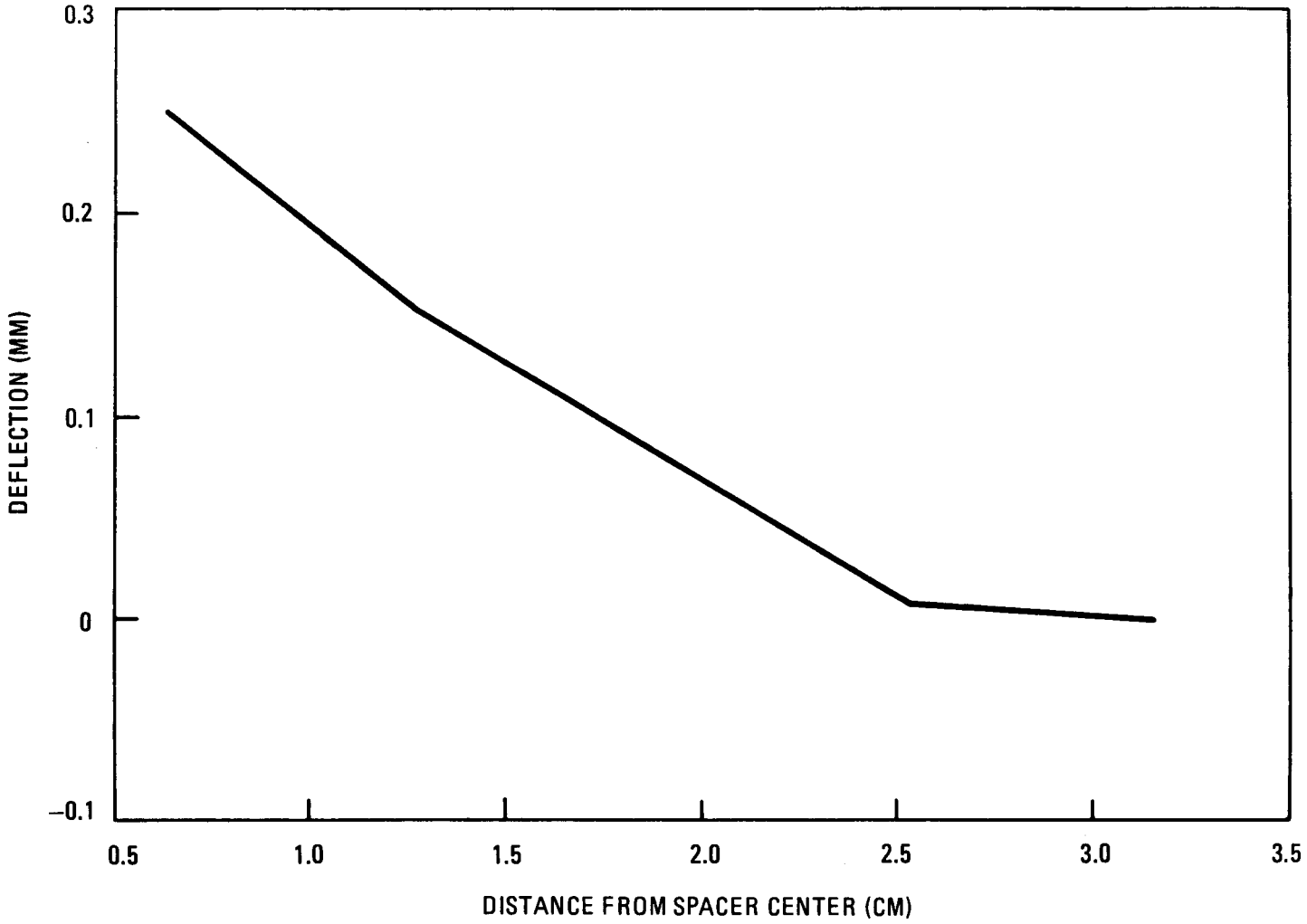

Fig. 2-23. Deflection for AGATHE HEX II spacer grid (MODSAP model)

TABLE 2-12
COMPARISON BETWEEN AGATHE HEX II
RESULTS AND MODSAP PREDICTIONS

Boundary Condition	MODSAP Finite Element Prediction (mm/KN)	AGATHE HEX-II Test Results (mm/KN)
Simple support	1.045	1.142
Clamped support	0.308	0.343

are within 10% of the experimental results. This is considered excellent agreement.

Structural Evaluation of CFTL AG1 Spacer Grid. The CFTL AG1 spacer grid was analyzed to evaluate its structural performance during normal operating conditions. In addition, the possibility of excessive inelastic deformations from the thermal creep ratcheting during experiment startup and shutdown cycles was assessed. The spacer grid was assumed to be at the maximum operating temperature of 538°C and subjected to the loadings from the interaction between the fuel rods and the grid. The analysis has concluded that the CFTL AG1 spacer grid will maintain its structural integrity during normal operating conditions.

The CFTL AG1 spacer grid as shown in Fig. 2-24 was analyzed using the finite element code MODSAP (Ref. 2-21). The spacer grid was idealized as an assemblage of three-dimensional beams capable of axial and shear deformation torsion and bending about two axes. As shown in Fig. 2-25, only half of the spacer grid was modeled because of the symmetric conditions in loading and geometry. The applicability of this finite element structural analysis model to the spacer grid was demonstrated in the preceding section.

The spacer grid was assumed to be at a temperature of 538°C. The loading resulting from the mechanical interaction between the fuel rods and the grid was assumed to be linearily distributed between 10 N per cell in the edge row to zero at the central cell. Figure 2-26 shows the deflection curves along the spacer grid corner-to-corner and flat-to-flat directions. The maximum deflection is 0.00225 mm and the maximum rotation is 0.048 deg. Therefore, the deformations are far less than the limits set up in the structural criteria (Ref. 2-24).

Based on the forces and moments obtained by MODSAP, the maximum bending stress (α_{11}^{max}), shear stress (α_{12}^{max}), and stress intensity occurred at beam

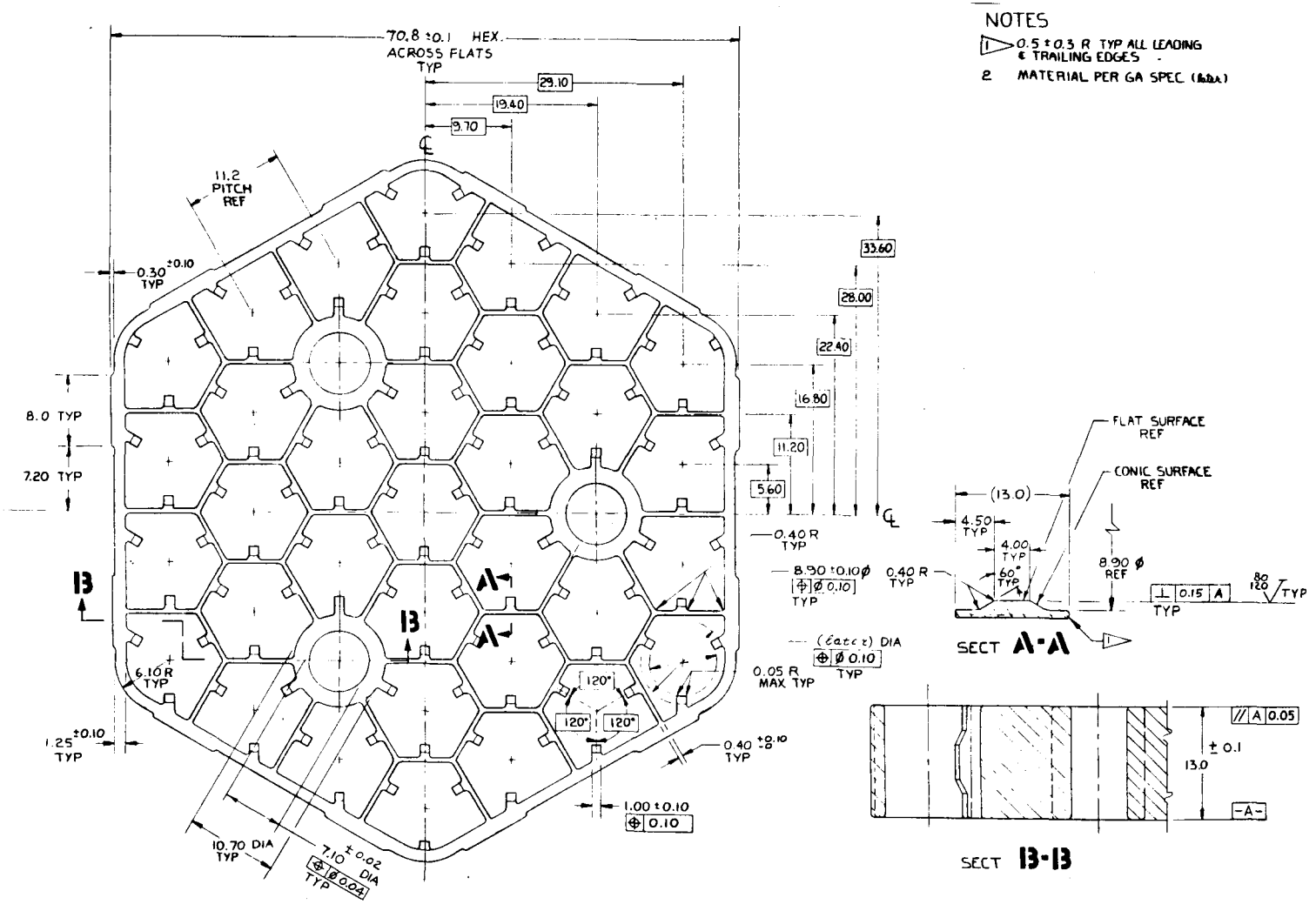

Fig. 2-24. CFTL AG1 spacer grid

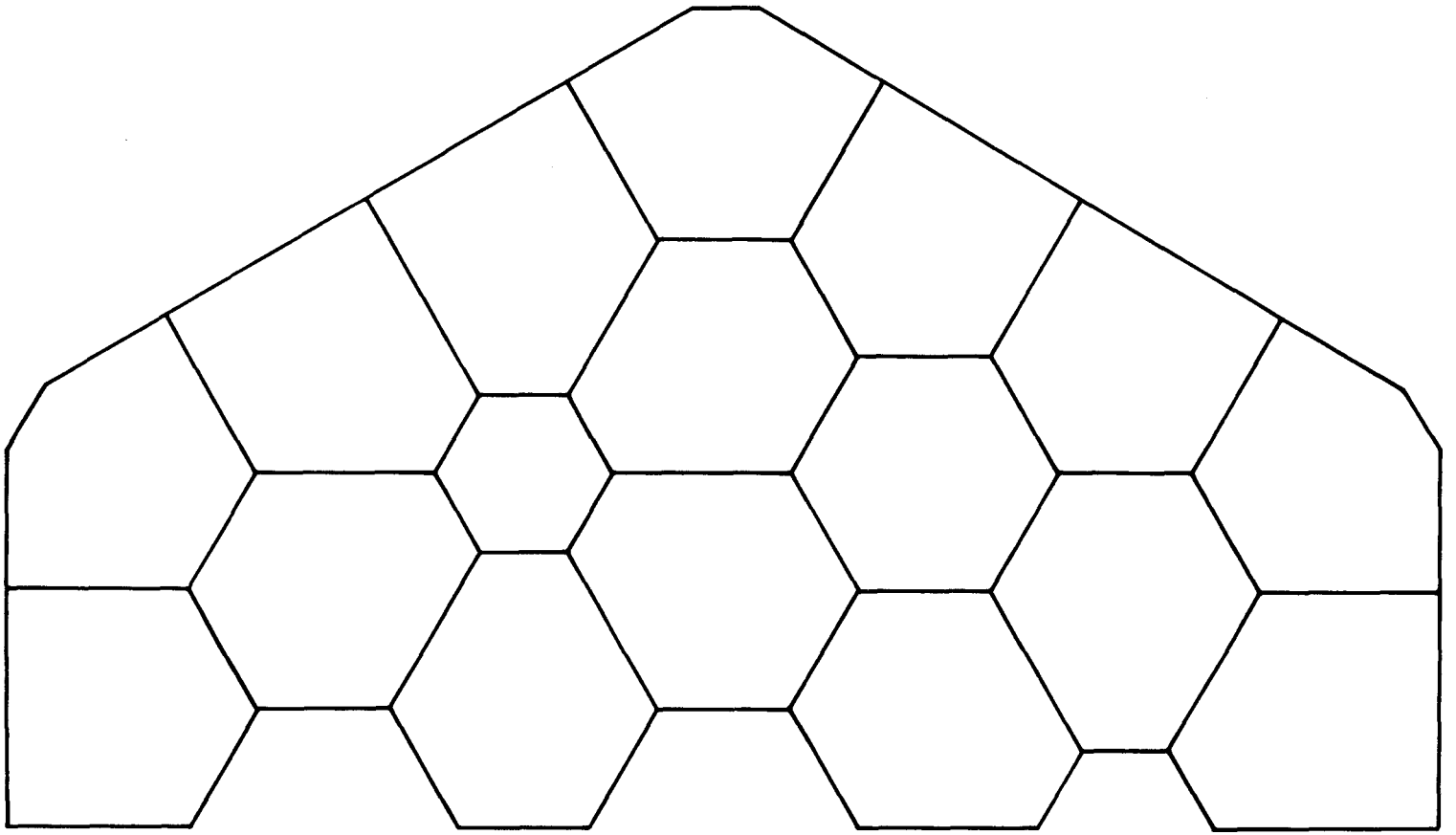

Fig. 2-25. CFTL AG1 spacer grid MODSAP structural model

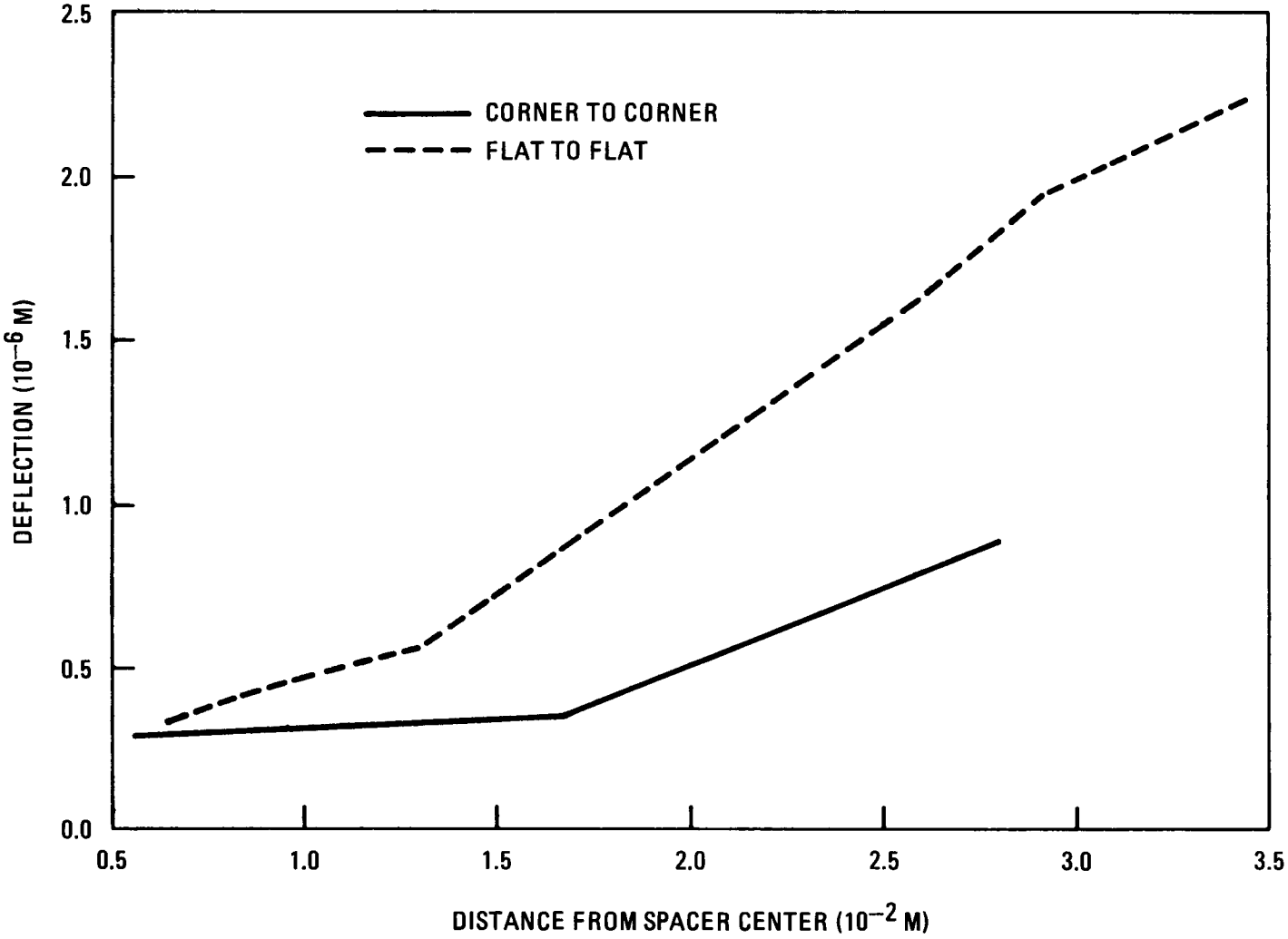

Fig. 2-26. Deflection for CFTL AG1 spacer grid at 583°C

number 60 (see Fig. 2-18) and were calculated as follows (coordinate system of the beam element shown in Fig. 2-27):

$$\sigma_{11}^{max} = 16.38 \times 10^6 \text{ Pa},$$

$$\sigma_{12}^{max} = 4.09 \times 10^6 \text{ Pa},$$

$$S_{12} = 18.3 \times 10^6 \text{ Pa}.$$

The stress intensity (18.3×10^6 Pa) is well below the stress limit (409×10^6 Pa) defined in RDT F9-7 (Ref. 2-25).

According to ASME Code Case 1592 (Ref. 2-26), when the maximum bending stress (16.38×10^6 Pa) is less than the stress limit (618×10^6 Pa = 1.25 x yield stress), inelastic strain limits as defined in the code are satisfied (elastic analysis test number 1). Therefore, the possibility of excessive inelastic deformations due to thermal creep ratcheting can be ignored.

In conclusion, these analyses demonstrate that the CFTL AG1 spacer grid will maintain its structural integrity when subjected to the loadings from the fuel rod and spacer grid mechanical interaction during normal operating conditions.

Fuel Rod Bundle Construction. As assessment of the current construction technique for GCFR fuel rod bundles was made. The results indicate that the current construction technique, which employs six tie rods consisting of concentric tension/compression members to space and support the grid spacers, cannot accommodate the effects of irradiation creep and probably cannot be made satisfactorily. As an alternative, the spacer grids could be attached directly to the tie rods, either by a mechanical interlock or by some sort of weldment.

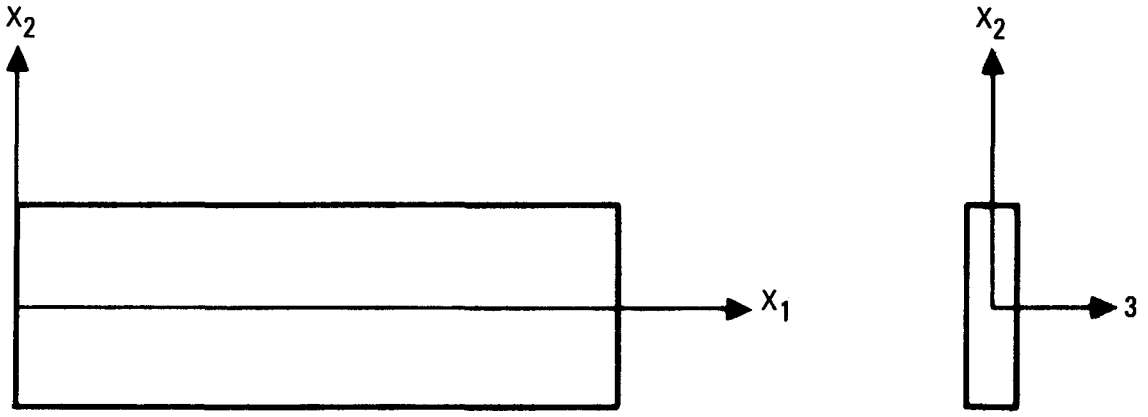

Fig. 2-27. Local beam element coordinate system

In the reference fuel assembly bundle construction, the spacer grids are spaced and supported by six tie rods located at or near the outer periphery of the grid. These tie rods consist of a central tension member (typically a hollow tube or a solid rod), over which spacer tubes and grid spacers are successively slipped. To ensure that the spacer grids do not come loose or become cocked, it is necessary that the spacer tubes be maintained in a state of compression. This condition can be met only if the upward force of the tension tubes is always greater than the downward forces exerted by the spacer grids. The initial preload of the tie rod must be somewhat higher than the minimum force required because the initial force will relax with time as a result of thermal and irradiation creep effects. A lower bound to the expected creep can be obtained by assuming that only the minimum load acts on the tie rod from BOL to EOL.

An estimate of the total spacer grid loading has been determined from CRASIB rod bowing studies and GCFR rod spacer interaction data. Assuming a peak rod-spacer interaction force of 10 N (∿2 lb), a coefficient of friction of 1 between rod and grid, and a linear loading distribution which decreases the load to zero at the center of the grid, a total grid load of 1760 N (∿400 lb) is calculated from the most highly loaded grid. From representative CRASIB data (Table 2-13), the total load exerted on the tie rods by all 10 spacer grids is found to be 3.23 times the load of the highest loaded grid. This works out to a total load of 5685 N (1280 lb) that must be carried by the tie rods, or, assuming six tie rods, a load of 950 N (215 lb) per tie rod.

Use of the above loading and representative values for the size of spacer tube (o.d. = 9 mm, i.d. = 7 mm) and the tension rod (o.d. = 7 mm, i.d. = 4 mm) results in a relatively modest tie rod stress of 37 MPa (5.4 ksi) and a tie rod elastic deflection of about 0.5 mm. From Fig. 1800 B-5 for 316 stainless steel at 1000°F [in Code Case 1592 of the ASME Boiler and Pressure Vessel Code (Ref. 2-26)], the thermal creep at 37 MPa (5.4 ksi) will be negligible.

TABLE 2-13
CRASIB SPACER GRID LOADING[a]

Grid	Load (N)	Normalized Load
1	0.18	0.02
2	-2.9	0.32
3	0.56	0.06
4	3.51	0.39
5	-2.51	0.28
6	-0.1	0.01
7	1.22	0.14
8	-4.20	0.47
9	9.05	1.00
10	-4.84	0.54
	Total	3.23

[a]GCFR design basis distributed grid load = 6 x 293.3 = 1760 N (400 lb); total GCFR grid loads = 3.23 x 1760 N = 5685 N (1280 lb).

Irradiation creep can be evaluated from Fig. 2-28, which is a plot of the Nuclear Systems Material Handbook (NSMH) (Rev. 5) irradiation creep equation for 316 stainless steel and gives creep strain per unit stress (in units of percent per MPa) as a function of temperature and fluence. An evaluation of the irradiation creep per unit stress for the tie rod is given in Table 2-14, and yields an approximate average value of 0.04% strain per MPa. For the expected tie rod stress of 37 MPa, this results in a 1.5% strain, which is equivalent to a 33-mm growth of the tension rod and is clearly unacceptable.

The most direct solution is to attach the grids directly to the tie rods, by either a mechanical device or weldment. This method would completely eliminate the possibility of loose or cocked spacer grids and would allow the use of larger diameter tie rods, which would serve to reduce tie rod stresses and, hence, tie rod creep.

An analysis of the current construction technique for GCFR fuel rod bundles indicates that the reference scheme would experience at least 33 mm of stretch in the tie rods as a result of irradiation creep. Unless soft springs are built into the system, such large amounts of creep are unacceptable.

As an alternative construction approach, it is proposed that the spacer grids be directly attached to the tie rods. Although significant tie rod creep will occur in this system also, the tie rod creep will not cause grids to become loose or cocked. Also, the possibility exists in this system for using a larger tie rod to reduce creep rates further.

2.1.2.3.3. Thermal-Hydraulic Methods Development

Introduction

Experimental data are being evaluated to develop the analytical basis for the design and development of the GCFR fuel, control, and blanket assemblies. Because complete prototype in-pile tests cannot be conducted,

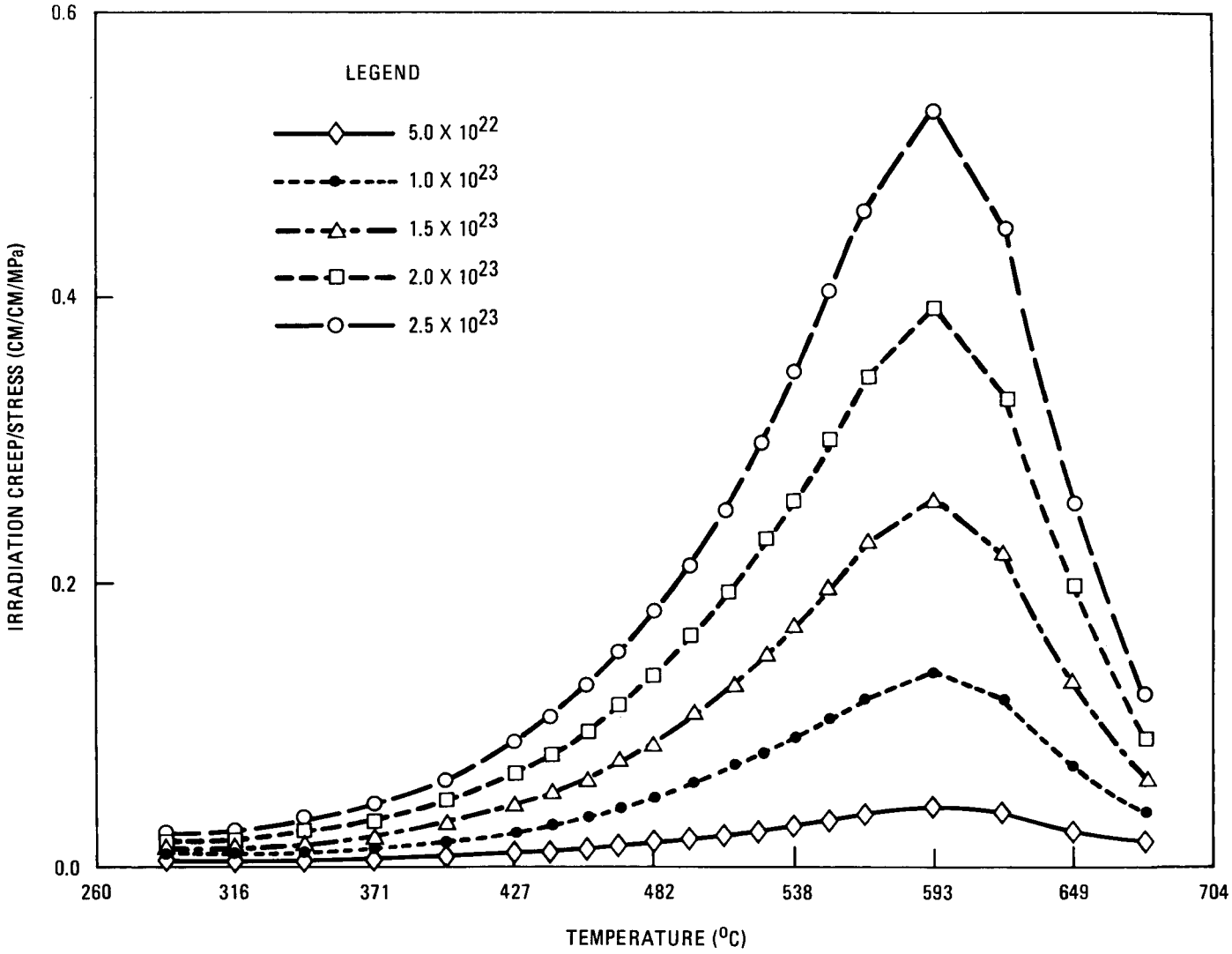

Fig. 2-28. Irradiation creep for 20% cold-worked 316 stainless steel (NSMH Rev. 5, MK5)

TABLE 2-14
TIE ROD IRRADIATION CREEP

Axial Location (mm)	Temperature [°C(°F)]	Fluence (n/cm^2)	Irr. Creep (%/MPa)
0	1112 (600)	2.0×10^{21}	0.001
600	1112 (600)	8.4×10^{22}	0.01
1200	1562 (850)	2.0×10^{23}	0.10
1800	1832 (1000)	8.8×10^{22}	0.07
2230	1832 (1000)	1.0×10^{22}	0.001
	Approximate weighted average		0.04

a strong analytical base supported by development tests is required to design the core assemblies. The current effort is devoted to the development of an adequate thermal-hydraulic steady-state and transient analysis capability to provide a basis for assembly design criteria and specific test requirements. The main efforts have focused on improvement of thermal-hydraulic correlations and development of methods for applying these correlations of the design and analysis of GCFR core assemblies.

Fuel Assembly Analysis

COBRA*GCFR Modification to Include Circumferential Rod Conduction. COBRA-IV-1 (Ref. 2-27) is a recent version of the COBRA series of codes for thermal-hydraulic analysis of nuclear fuel rod bundles. It was developed for analysis of sodium and water-cooled reactors. Major modifications to the COBRA code were necessary before the code could be used for GCFR thermal-hydraulic analysis. The modified code is called COBRA*GCFR (Ref. 2-11).

COBRA*GCFR code analysis has been compared to a number of experimental results and shows excellent agreement (Refs. 2-11, 2-28) with measured surface temperatures at locations where circumferential conduction* is not important, but it does not agree with the experimental results where circumferential conduction was significant. Hence, it was decided to develop a method to incorporate circumferential conduction in the COBRA*GCFR code.

Circumferential conduction is important in GCFR assemblies for the following reasons:

1. The edge rods are surrounded by different types of channels.

*The term "circumferential conduction" is used in this section to describe r-θ conduction mode.

2. The magnitude of heat transfer coefficients for gas coolants is low, particularly at low flows.

3. The flow distribution around the edge rods changes with flow rates.

The two-dimensional heat conduction equation in r-θ coordinates is

$$\rho c \frac{\partial T}{\partial t} = \frac{1}{r} \frac{\partial}{\partial r} \left(rk \frac{\partial T}{\partial r} \right) + \frac{1}{r^2} \frac{\partial}{\partial \theta} \left(K \frac{\partial T}{\partial \theta} \right) \tag{2-14}$$

subjected to the boundary conditions

$$\frac{\partial T}{\partial r} = 0 \quad \text{at} \quad r = 0,$$

$$-K \frac{\partial T}{\partial r} = h(T_s - T_B) \text{ at } r = R_0 , \tag{2-15}$$

and two boundray conditions in θ direction, which depend on whether a full or partial rod is analyzed.

A number of numerical procedures are available (Ref. 2-29) to solve the governing Eq. 2-14. Two classical procedures are the purely explicit procedure and purely implicit procedure (Ref. 2-29). These two methods suffer from the disadvantages of numerical instability and numerically expensive procedure for solving the resulting algebraic equations, respectively. Hence, an implicit alternating direction (IAD) procedure (Ref. 2-30) was adopted. This method combines the advantages of numerical stability (implicit method) with solution of tridiagonal system of equation (explicit method) and has been found successful in the solution of two- and three-dimensional conduction problems (Refs. 2-31, 2-32).

A subroutine CIRCON, which solves the conduction problem described by Eq. 2-14 and 2-15, was developed by using the IAD method. (Ref. 2-30). Fig. 2-29 shows the flow diagram of COBRA*GCFR with CIRCON. To minimize

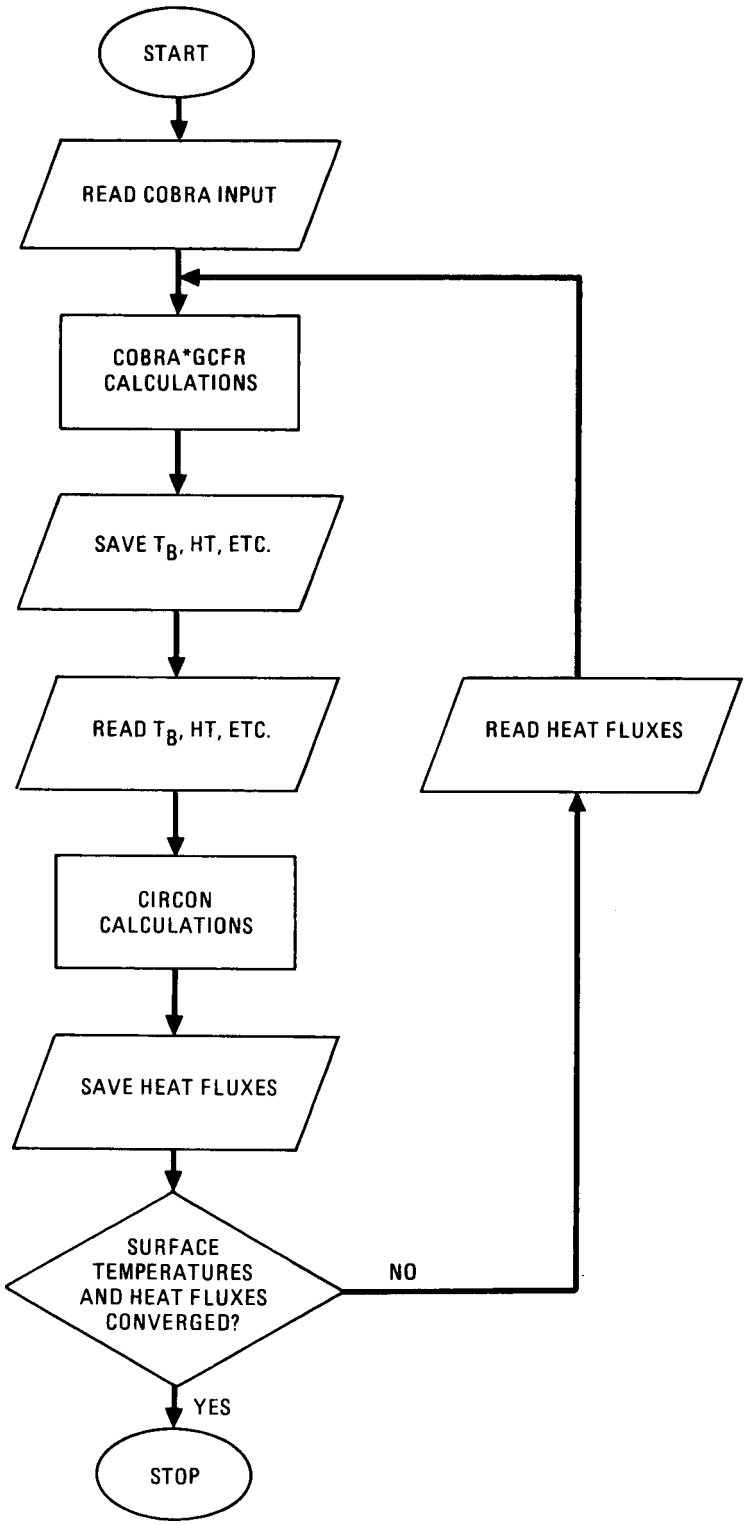

Fig. 2-29. Flow chart for COBRA*GCFR with CIRCON

changes to the COBRA*GCFR code, the following procedure was adopted for combined COBRA*GCFR and CIRCON calculating:

1. COBRA*GCFR calculates the flow distribution, heat transfer coefficients, and coolant temperatures in all channels at all levels.

2. CIRCON uses the heat transfer coefficient and coolant temperature for each rod and each level with the heat generation rates and rod description to solve Eq. 2-14 and calculates temperature distribution in the rod and the surface heat flux for each channel.

3. COBRA*GCFR uses the local heat flux values to calculate updated temperature and flow distribution.

4. Convergence is reached when the change in heat fluxes and surface temperatures is less than a predetermined convergence criteria.

The subroutine CIRCON and the modified COBRA*GCFR code were verified in two steps. During the first step, results from CIRCON were compared with the verified two-dimensional conduction code TAC-2D (Ref. 2-31). The comparison showed excellent agreement between the two programs for the sample problem.

The modified COBRA*GCFR code was verified by comparison with experimental results, where effect of rod conduction was known to be important (Ref. 2-28). Table 2-15 shows the comparison between COBRA*GCFR results without conduction and with conduction, and the measured results of AGATHE-1C tests (Ref. 2-28). The table lists some representative edge rods, since conduction effects are significant in these tests only for the edge rods. Close agreement is shown between COBRA*GCFR with conduction

TABLE 2-15
VERIFICATION OF COBRA*GCFR
(COMPARISON WITH AGATHE-1C EXPERIMENT)

Test No.	Rod No.[a]	Channel No.[a]	Axial Location (mm)	Surface Temperatures (°C)		
				COBRA*GCFR Without Conduction	COBRA*GCFR With Conduction	Measurement
1	7	10	310	620.1	554.5	550.9
	9	12C	310	528.2	515.9	500.4
	7	10	610	483.2	451.6	460.1
	8	7	610	454.0	442.7	437.8
	10	14	1160	611.8	603.0	599.8
	8	11C	1160	608.3	602.5	594.3
2	7	10	310	457.3	378.0	355.2
	8	11C	310	370.7	361.4	345.3
	7	10	610	466.1	419.8	411.9
	10	14	610	446.7	411.6	415.5
	7	10	1160	632.3	588.8	584.7
	9	12D	1160	554.8	575.1	582.5 563.0

[a] See Fig. 2-30.

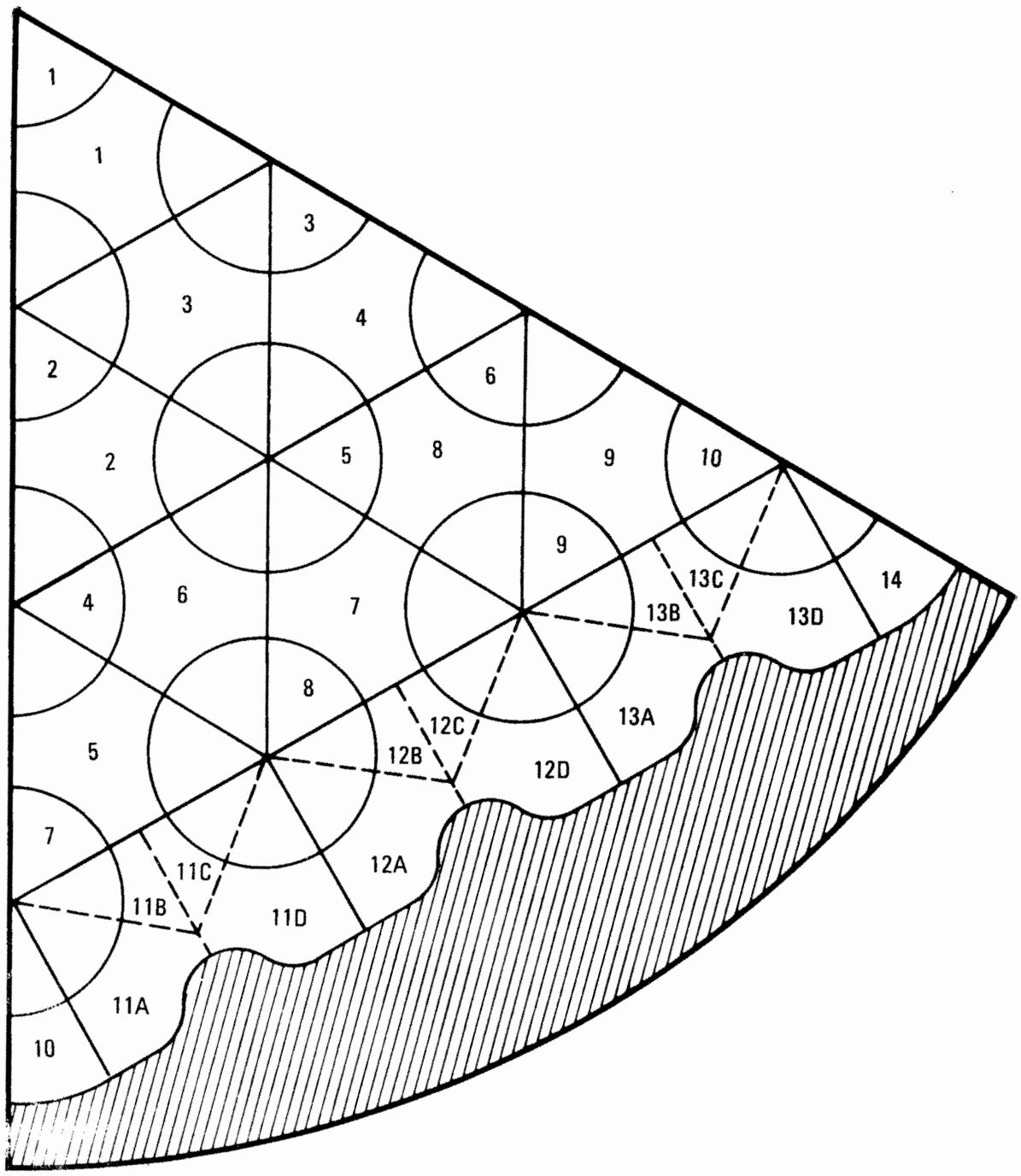

Fig. 2-30. AGATHE-1C bundle subdivision

and measured temperatures in most cases. In all cases, the agreement between analysis and experiment is closer with conduction than without conduction.

The modified code was also used to analyze various GCFR-type assemblies. Table 2-16 shows the temperature difference across rods in various gas-cooled assemblies with and without conduction. In all cases, the temperature gradients across the rods are reduced due to circumferential conduction. The results in Table 2-16 show that the effects of rod conduction are important in the following cases:

1. When the heat transfer coefficients are small.

2. When the conductivity of the rod is large as in the case of CFTL rods and AGATHE rods.

3. When the temperature difference across the rod is large.

Criteria 1 and 2 above can be concisely expressed in terms of a Biot number based on the rod diameter (see nomenclature listing at the end of this discussion).

$$Bi = \frac{hd_o}{K_{av}} \quad . \tag{2-16}$$

Results in Table 2-16 show that rod conduction is significant when the Biot number is smaller than 1 and negligible when the Biot number is greater than 10. This is expected, since the Biot number is a ratio of external to internal conductance, and thus, an inverse of the Biot number is a measure of rod conductivity effect. This range of Biot number can only be used as an approximate guideline, since the Biot number in Eq. 2-16 does not account for effects of coolant temperature distribution.

The results given in Table 2-16 are plotted in Fig. 2-31. The vertical axis is the ratio of temperature difference across the rod with and

TABLE 2-16
EFFECT OF CIRCUMFERENTIAL CONDUCTION ON TEMPERATURE DIFFERENCE ACROSS RODS IN GAS-COOLED BUNDLES

Example	Description of Bundle	Rough or Smooth Region	Coolant	Average Reynolds Number	ΔT Across Edge Rod (°C)		Biot No. $= \frac{hd_o}{k_{av}}$
					Without Conduction	With Circumferential Conduction	
1	CFTL[a]	R	He	10^5	24	12	1.9
2	AGATHE-1C	R	CO_2	2.5×10^5	27.7	7.3	1.5
3	AGATHE-1C	S	CO_2	3×10^5	80.5	13.7	0.6
4	AGATHE-1C	R	CO_2	1.3×10^4	34.9	0.5	0.07
5	AGATHE-1C	S	CO_2	1.7×10^4	54.6	0.7	0.03
6	GCFR fuel assembly	R	He	10^5	36	29	40
7	GCFR fuel assembly	S	He	1.6×10^3	167	48.3	1.2
8	GCFR blanket assembly	S	He	5×10^4	66	63	52
9	GCFR shield assembly	S	He	10^3	75	11.4	0.50

[a] Core flow test loop (Ref. 2-14) test assembly.

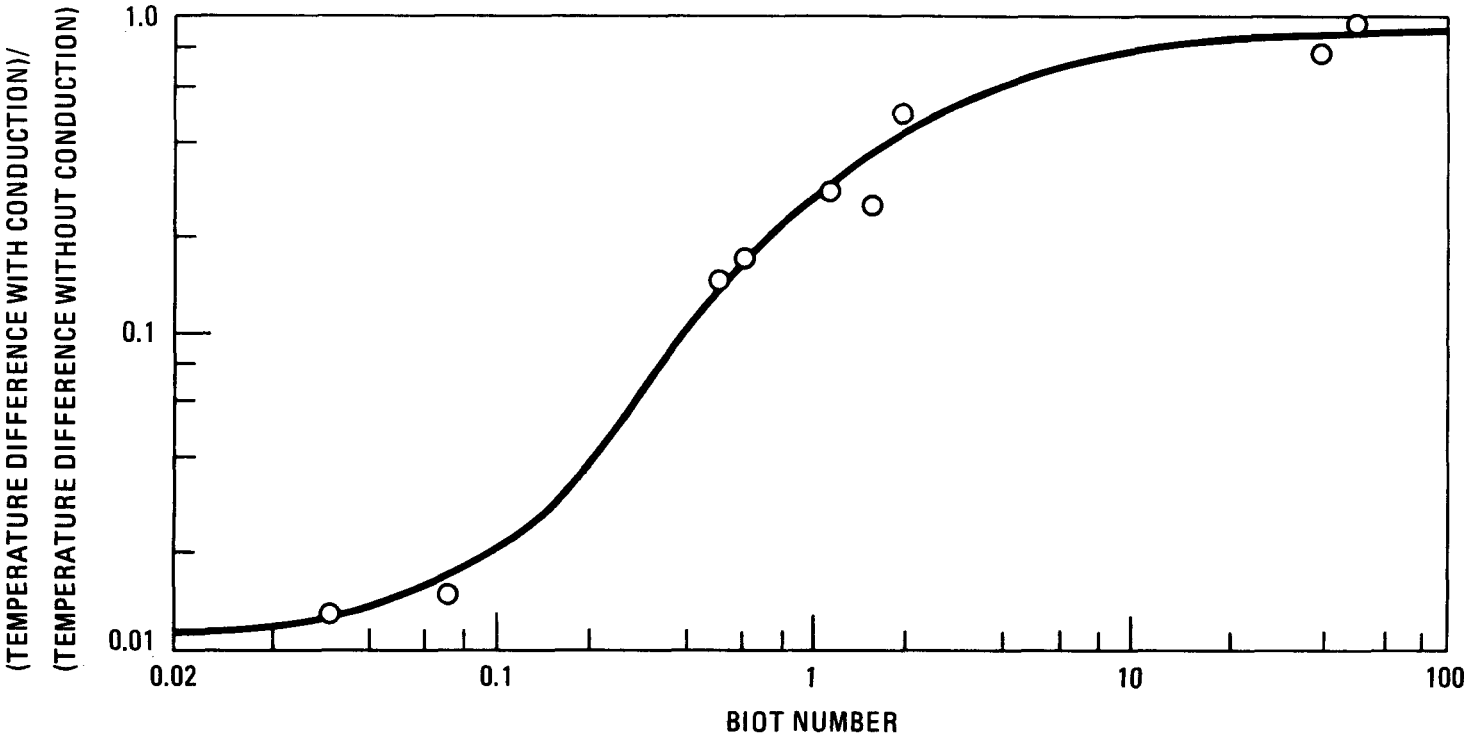

Fig. 2-31. Effect of Biot number on rod conduction in GCFR assemblies

without conduction. All results fall on a smooth curve; this curve can be used to obtain an approximation of the ΔT across the rods when tools to calculate conduction are not available.

Effect of Coolant Mixing on Maximum Fuel Rod and Fuel Assembly Duct Wall Temperature. For a particular reactor design defined by CALIOP (Ref. 2-33) fuel assemblies with different radial power tilts were analyzed with COBRA-IV-1 (Ref. 2-27). The object was to obtain a correction factor C_c (which can be added to the hot channel factor) to account for coolant mixing between subchannels. Since the edge subchannels are overcooled, the central subchannels are hotter than the average subchannel that CALIOP calculates for an assembly with no power tilt. For assemblies with power tilt, the effect of edge overcooling results in a lower maximum temperature than that estimated by CALIOP. CALIOP calculates the maximum and minimum exit coolant temperatures by assuming for the coolant a temperature profile having the same slope as the power profile. The difference in CALIOP and COBRA-IV-1 estimates is illustrated in Fig. 2-32 for exit coolant temperature. The corresponding effect on the fuel cladding midwall temperature is shown in Table 2-17. The correction C_c, shown in Fig. 2-33, can be defined by the equation

$$C_c = 0.052 - 0.225\ (T - 1.0).$$

Another outcome of this study was the effect of mixing on the duct wall temperatures. CALIOP predictions have always been used for mechanical analysis of the duct by assuming the duct walls to be at coolant temperature (points 1, 2, and 3 in Fig. 2-32). The actual temperature rise of the coolant at the duct wall from the inlet end to the exit end is only 80% of the previous estimates (Table 2-18). The temperature gradient on the duct is also lower than the previous estimates by 18.75%. Figure 2-34 expresses the temperature drop in terms of the coolant temperature rise ΔT_c and the radial power tilt T, as given by

$$\Delta T_{flats} = 1.625\ (T - 1.0)\ \Delta T_c\ .$$

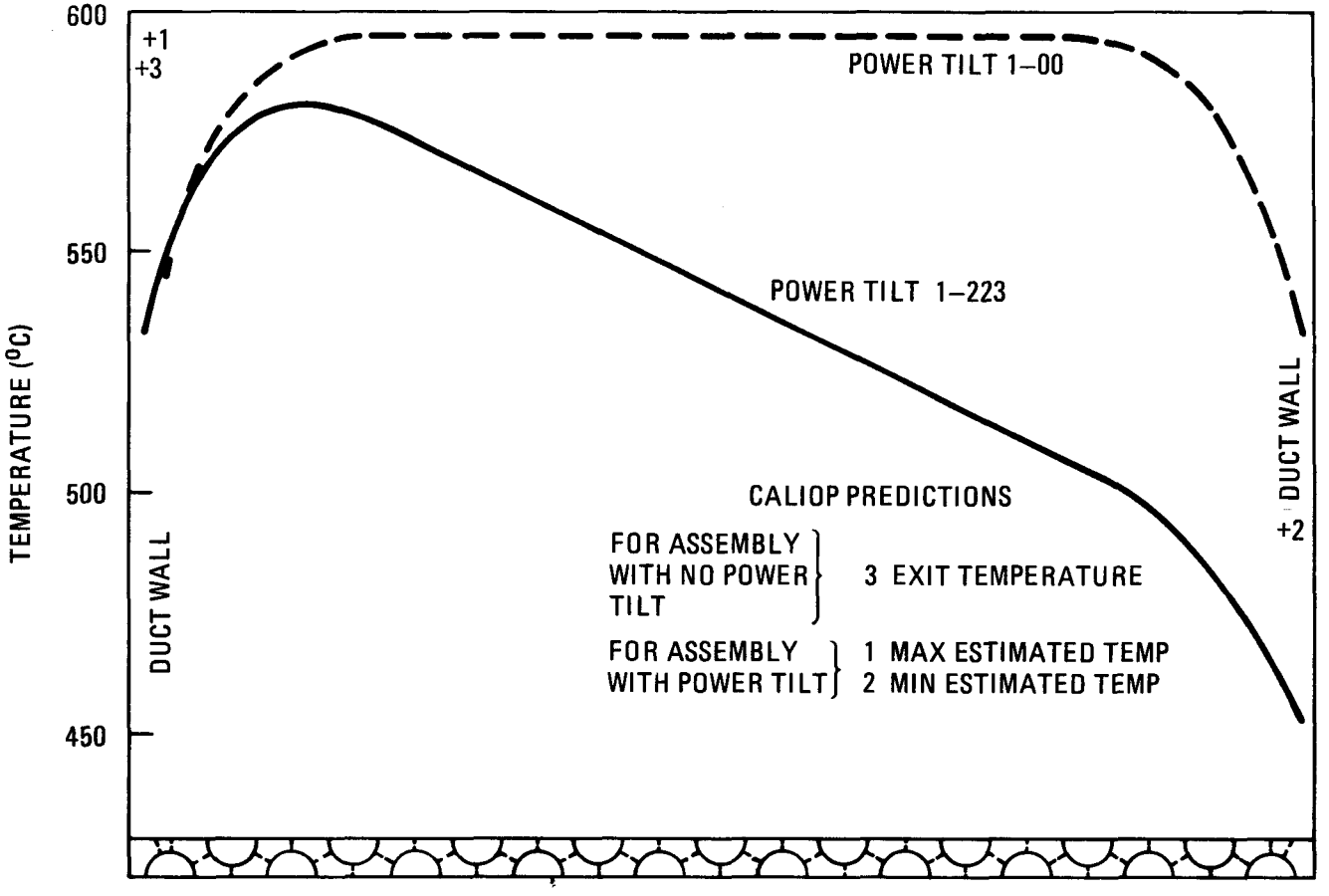

Fig. 2-32. Exit coolant temperature profile

TABLE 2-17
CORRECTION FACTOR C_c AS A FUNCTION OF POWER TILT

Radial Power Tilt T	Coolant Temp Rise ΔT_c (°C)	COBRA-IV Max Clad Midwall Temp T_{HS} (°C)	δT_{HS} $T_{HS}-713$ (°C)	C_c $\delta T_{HS}/\Delta T_c$
1.000	267.6	726.0	13.0	0.0490
1.050	258.5	723.2	10.2	0.0395
1.103	243.3	720.4	7.4	0.0304
1.223	215.8	713.2	0.2	0.0009

TABLE 2-18
TEMPERATURE DROP ACROSS FUEL ASSEMBLY AS A FUNCTION OF POWER TILT

Radial Power Tilt T	Duct Wall Temp Rise ΔT_d (°C)	$\Delta T_d/\Delta T_c$ (%)	CALIOP Estimate ΔT_{flats} (°C)	COBRA-IV Estimate ΔT_{flats} (°C)
1.000	213.0	79.97	0.00	0.00
1.050	207.4	80.23	25.85	21.55
1.103	194.4	79.92	50.11	40.72
1.223	172.9	80.12	96.25	78.28

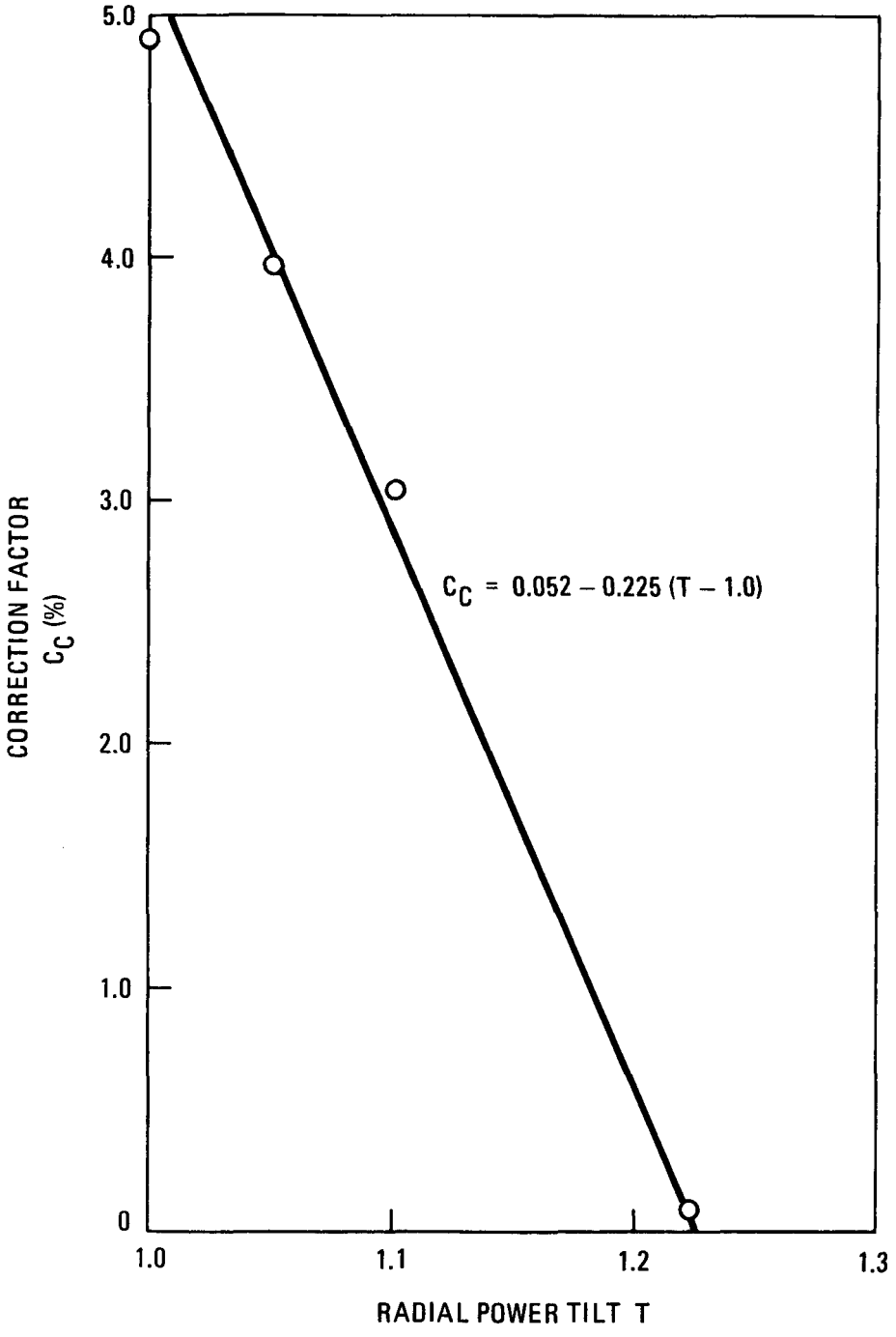

Fig. 2-33. Plot of correction factor versus radial power tilt

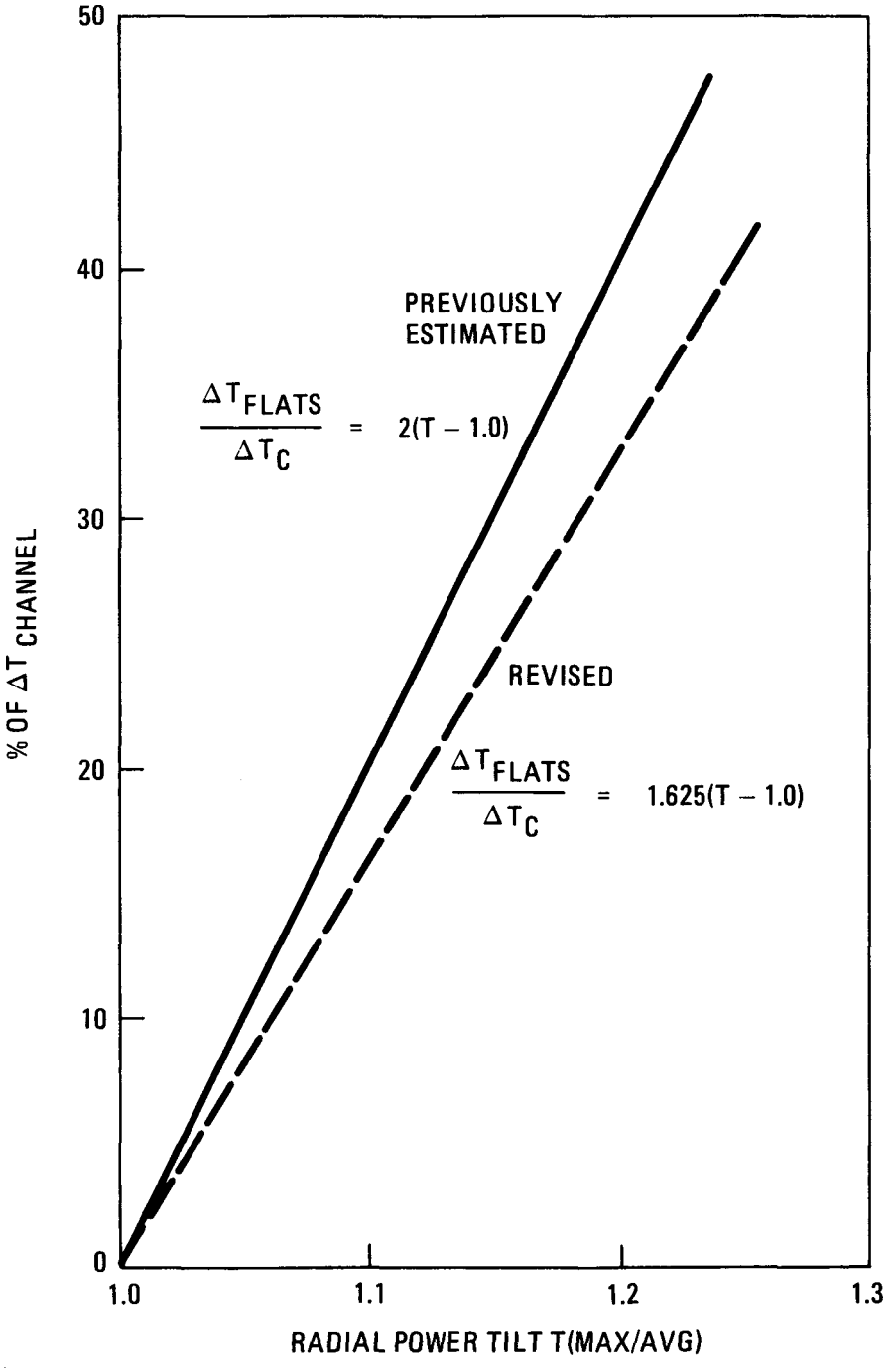

Fig. 2-34. Temperature drop across fuel assembly duct at exit end

A correction factor as a function of the power tilt will have to be included in CALIOP to account for the mixing effect on the maximum temperatures that it calculates. Currently, a constant factor (determined for an assembly with no power tilt) is being used for all assemblies. Since a smaller correction is needed for assemblies with power tilts, the result will be a gain in the coolant outlet temperature.

Nomenclature

Bi	Biot number = hd_o/K_{av}
C	Specific heat, W/hr/kg-°C
d	Rod diameter, m
h,HT	Heat transfer coefficient, W/m^2-°C
K	Thermal conductivity, W/m-°C
q	Heat flux, W/m^2
Q	Heat generation rate, W/m^3
r	Radial coordinate
R	Fuel pellet (or heater) radium, m
t	Time, s
T	Temperature at time t, °C
ΔT	Temperature difference across the rod, °C

Greek Symbols

ρ	Density, kg/m^3
θ	Coordinate in azimuthal direction

Subscripts

av	Average values
B	At bulk temperature
c	With conduction
o	Outside or without conduction
S	Surface

2.1.3. Core Design Verification and Support

2.1.3.1. Test Programs

2.1.3.1.2. Shielding Experiments

The purposes of the shielding task are to verify the adequacy of the methods and data for the nuclear design of GCFR shields, to evaluate the effectiveness of various shield configurations, and to provide an interface for mechanical and nuclear shield design activities. This task also coordinates and provides liaison with the analytical and experimental shielding program at ORNL.

During the last quarter, the approximate gamma dose on the service catwalk of the up-flow GCFR was calculated, and several up-flow GCFR inlet and outlet coolant duct shield configurations were assessed. A sensitivity study of the effect of radial blanket management or radial shielding requirements was conducted, and physics and materials-related design guidelines were determined, including nuclear heating rates, for radial reflector/shield assemblies. In addition, a test matrix was recommended for an FY-79 and FY-80 EBR-II irradiation experiment for tensile properties of structural 316 stainless steel and welds at high temperatures.

During this quarter, several new features were added to the one-dimensional discrete ordinates code DTFX (Ref. 2-34), and the DOT IV (Ref. 2-35) two-dimensional discrete ordinates code was obtained from ORNL and made operable on the UNIVAC computer system. The reference down-flow GCFR isoflux plots for the lower plenum were received from ORNL and analyzed. New reference shielding configurations were developed for the up-flow and down-flow GCFRs.

DTFX Improvements

The DTFX one-dimensional discrete-ordinates (Ref. 2-34) code has been updated to provide new capabilities for use in GCFR shielding analysis. The features added to the DTFX code include:

1. More general activity edits which remove the need for auxiliary editing codes to obtain irradiation damage rates, heating rates, etc.

2. An option to read the problem input and proceed directly to the final edits without performing any flux calculations so that old problems can be re-edited cheaply.

3. A zero input flux guess option to improve convergence of distributed source problems.

4. Options to delete selected portions of the final edits, some of which can be voluminous and not informative for large shielding problems.

5. The disadvantage factor calculations were revised to work correctly for mixtures of mixtures.

6. The exponential difference equations of Barbucci and di Pasquantonio (Ref. 2-36) were added as an optional alternative to the linear (diamond) difference plus negative flux fix-up equations that have been used in the DTFX code until now. The exponential difference equations yield non-negative angular fluxes when the angular source term is non-negative and are much more accurate than the linear difference plus negative flux fix-up schemes when coarse spatial meshes are used (real shielding problems almost always have coarse spatial meshes). The exponential

difference equations of Barbucci and di Pasquantonio are at least as accurate as the various weighted difference schemes used in the ANISN (Ref. 2-37) and DOT codes and have the outstanding advantage of not relying upon problem-dependent theta weighting coefficient. They apply equally well to source and eigenvalue calculations, require only a modest increase in the arithmetic per iteration, and provide a stable, easily accelerated solution.

7. A negative source fix-up scheme was incorporated after diagnostic tests showed that, particularly in the high-energy gamma groups, many negative flux fix-ups were occurring because of negative angular sources. The source fix-up algorithm sets the offending directional source to zero and modifies the other directional sources in that group and space point to preserve the total scattering cross section, which is usually much better known than the angular distribution of scattering events.

8. An improved coarse mesh rebalance inner iteration convergence acceleration algorithm was developed which is able to detect certain types of oscillatory instabilities and take corrective actions.

DOT IV Implementation

The DOT IV code (Ref. 2-35) (ORNL Version 4.3, GA Edition 1) has been made operable on the GA UNIVAC-1110 computer with the assistance of ORNL. The DOT IV code is a two-dimensional discrete ordinates transport theory code which solves the same basic equations as the TWOTRAN code (Ref. 2-38) but which has specialized features developed for large shielding problems.

Initial testing indicates that the DOT IV code may be superior to the GA version of the TWOTRAN code and that DOT IV has the potential to replace TWOTRAN as the GA standard two-dimensional transport theory code if and when satisfactory GA user experience with DOT IV is accumulated.

The DOT IV code is variably dimensioned and uses a sophisticated data management scheme by means of which very large problems may be run without requiring excessive fast memory. New flexibility in both space-mesh and directional-quadrature is allowed. For example, the radial mesh in an R-Z problem can vary with axial position. The directional quadrature can vary with both space and energy group. Diffusion theory options are also available. At ORNL, improvements in DOT IV are continuing, and new ORNL versions are expected to be received from time to time.

The DOT IV code is an improved, better documented code than the DOT 3.5 and DOT 2 codes. In addition, because of past difficulties (particularly with DOT 3.5), the major portion of the conversion of the DOT IV code to the GA UNIVAC-1110 was performed by W.A. Rhoades, who is responsible for the development and maintenance of DOT IV at ORNL. This procedure should yield a more reliable UNIVAC-1110 implementation than previous efforts. Rhoades has indicated that he plans to maintain a UNIVAC version of DOT IV at ORNL, and that most of the conversion work was performed using comment card flags to differentiate between versions and to facilitate the maintenance of a UNIVAC version.

2.2. REACTOR CORE ANALYSIS AND DESIGN

During the previous quarter, the final core assembly and core arrangement drawings were completed for the up-flow/down-flow configuration study. Final major core parameters for the up-flow and down-flow GCFR demonstration plants are given in Table 2-19, and the final core arrangement drawings for up-flow and down-flow are given in Figs. 2-35 and 2-36, respectively.

In summary, it appears that both the up-flow and the down-flow cores are technologically feasible. The down-flow core is preferred from the standpoint of alignment between the control rod drives and the control assemblies, while the up-flow core is preferred from the standpoints of seismic restraint and exit plenum shielding. On balance, the up-flow core appears to have a slight advantage.

2.2.1. Core Nuclear Analysis

Design Analysis. Results are presented for the initial physics analysis of grid-plate-supported reflector/shield (R/S) assemblies. Such assemblies are required in GCFR designs employing lateral core restraint (up-flow or down-flow) to reduce radiation damage and heating to the permanent core restraint system and outer radial shield to values below acceptable limits (Ref. 2-39). The R/S assemblies are an integral part of the core and subject to mechanical interaction with the fuel and blanket assemblies.

The analysis considered two types of R/S assembly mechanical concepts: (1) a block concept, in which hexagonal blocks of shield material with appropriate coolant passages are stacked into a steel hexagonal duct, and (2) a wire-wrap concept, in which a wire-wrapped bundle of 19 steel-clad tubes containing shielding material are within a steel hexagonal duct. The calculations were performed for the R/S assembly configurations shown in Fig. 2-37, which are different material arrangements for three different shield materials: (1) H-451 graphite (C); (2) boron carbide in a graphite matrix-25 wt % natural boron (C + B_4C), and (3) 316 stainless steel. Since

TABLE 2-19
UP-FLOW/DOWN-FLOW GCFR DEMONSTRATION PLANT
MAJOR CORE PARAMETERS

Parameter	Core Arrangement: 127-assembly, 19-control-rod core in 7 rows; 3-row blanket[a,b]; 2-row reflector/shield[a,b]	
	Up-Flow	Down-Flow
Assembly overall length	4650 mm	4208 mm
Core-blanket-shield diameter	4382 mm	4297 mm
Core lateral restraint	2 point, limited free bow	Single point constraint[b]
Core axial restraint	Individual mechanical lock for fuel and blanket (removeable lock actuator rod); pneumatic balance-shield assembly	Individual mechanical lock for all assemblies
PES manifold location	Top (hot end)	Top (cold end)
Exit plenum shielding	Incorporated in assembly	Replaceable lower shield elements
Temperature monitoring	Instrument trees	Thermocouples in assemblies

[a] Indicates change from interim design (9-78).
[b] Indicates change from Baseline Data Book.

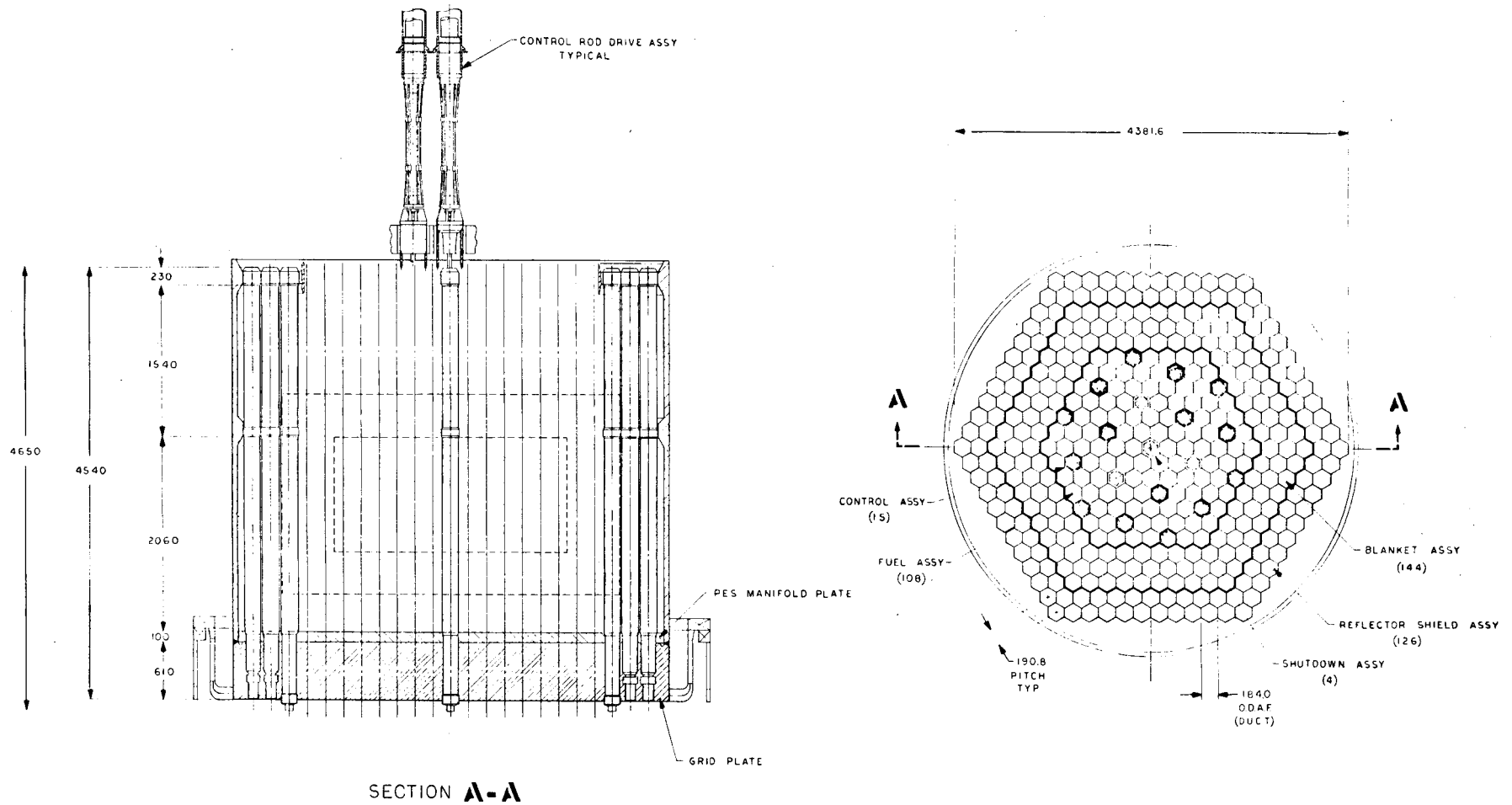

Fig. 2-35. Up-flow core general arrangement

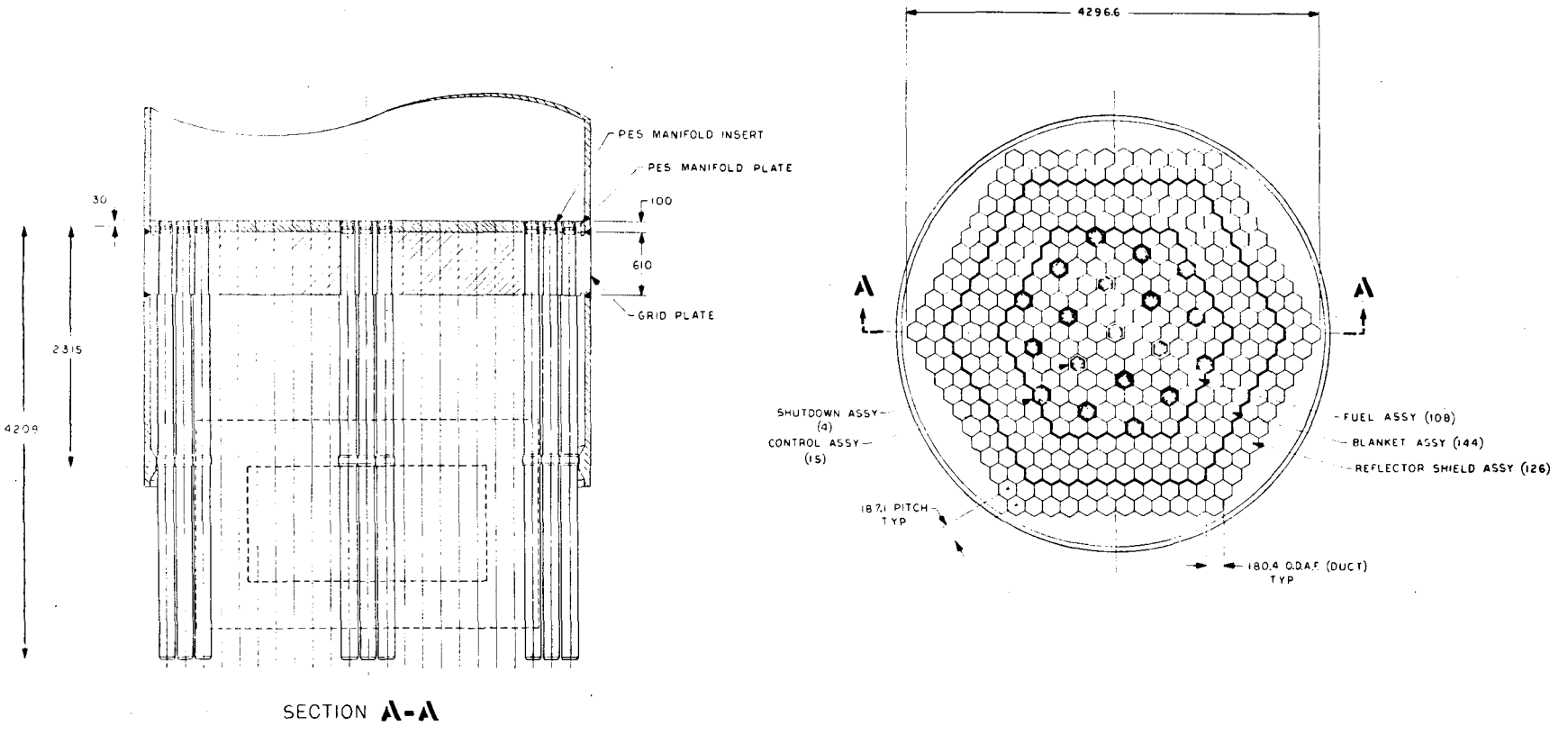

Fig. 2-36. Down-flow core general arrangement

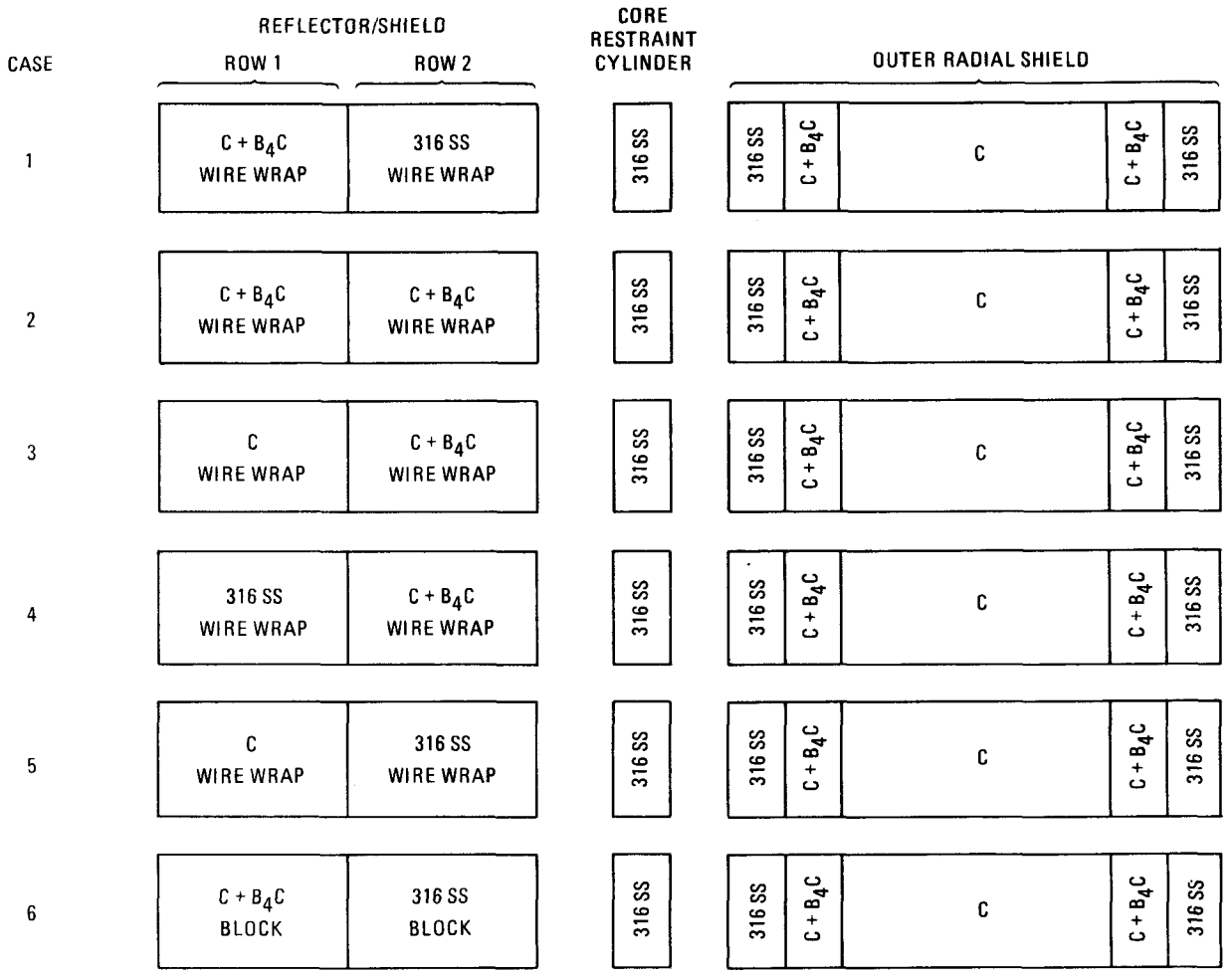

Fig. 2-37. Reflector/shield configurations

thermal-mechanical distortion and cooling of the R/S assemblies, core restraint cylinder, and outer radial shield could be an important consideration in the selection of the R/S configuration, results of relative comparisons of heating magnitudes and gradients in these components are presented. The one-dimensional discrete ordinates calculations were done for the core midplane axial level.

The materials radiation exposure criteria used in this study are summarized later in this section. The uncertainty associated with the operating temperature of the permanent core restraint system and the structural steel in the permanent outer radial shield results in two potential criteria for these components. In the event that either component operates at high temperature ($\geq$550°C), presumably with core outlet gas cooling, stringent limits of $\leq 10^{21}$ n/cm^2 total fluence exposure and a maximum 1 atoms part per million (appm) helium gas concentration apply to the 316 stainless steel. For a low operating temperature (<550°C), presumably with core inlet gas cooling, an 8 x 10^{21} n/cm^2 total fluence limit is applied to assure 10% residual ductility based on total elongation (RTE) in 308L stainless steel weld deposit. The exposure margins used to account for modeling, methods, and data uncertainties are summarized later in this discussion.

Analysis

One-dimensional 36-group (26 neutron and 10 gamma) discrete ordinates calculations were carried out using S_8 quadrature (Ref. 2-40) for the 6 two-row R/S configurations described in Table 2-20. Table 2-20 indicates the R/S concept, the basic shield materials, material volume fractions, and number of coolant flow holes (block concept) for each case.

Table 2-21 gives the geometry for the one-dimensional cylindrical equivalent model. For all cases, the helium flow gaps and outer radial shielding were the same. The R/S assemblies were homogenized according to the material volume fractions given in Table 2-20. Full material densities were assumed for the outer radial shielding (i.e., no allowance for manufacturing and construction tolerances).

TABLE 2-20
SPECIFICATIONS FOR TWO-ROW REFLECTOR/SHIELD ASSEMBLY CONFIGURATIONS

Parameter	Cases					
	1	2	3	4	5	6
Blanket fertile material	U	U	U	U	U	U
R/S assembly characteristics						
Row 1 concept	Wire wrap $C + B_4C$	Wire wrap $C + B_4C$	Wire wrap C	Wire wrap SS	Wire wrap C	Block 7 holes
Material, vol %						
He	0.191	0.191	0.191	0.114	0.191	0.267
SS	0.170	0.170	0.170	0.886	0.170	0.185
$C + B_4C$	0.639	0.639	0.0	0.0	0.0	0.548
C	0.0	0.0	0.639	0.0	0.639	0.0
Row 2 concept	Wire wrap SS	Wire wrap $C + B_4C$	Wire wrap $C + B_4C$	Wire wrap $C + B_4C$	Wire wrap SS	Block 3 holes, SS
Material, vol %						
He	0.114	0.191	0.191	0.191	0.114	0.105
SS	0.886	0.170	0.170	0.170	0.886	0.895
$C + B_4C$	0.0	0.639	0.639	0.639	0.0	0.0
C	0.0	0.0	0.0	0.0	0.0	0.0

TABLE 2-21
ONE-DIMENSIONAL EQUIVALENT CYLINDER MODEL FOR
REFLECTOR/SHIELD TRANSPORT CALCULATIONS

Zone	Material	Zone Δ Radius (mm)
1	EOEC core	1088.15
2	EOEC three-row uranium blanket	501.39
3	R/S row 1	154.73
4	R/S row 2	155.70
5	Helium gap	408.78
6	316 SS core restraint cylinder	44.45
7	Helium gap	51.00
8	Outer radial shield:	
	316 SS	51.00
	C + B_4C	51.00
	C	226.00
	C + B_4C	51.00
	316 SS	51.00
9	Helium gap	356.00
10	Iron PCRV liner	19.0
11	PCRV concrete	--

The distributed fission source used in the analyses was for end-of-equilibrium cycle (EOEC) (actually, end-of-cycle 7) for the case of a three-row uranium radial blanket managed according to a row 3 to row 1 to row 2 shuffling scheme (Refs. 2-41, 2-42). The maximum flux and heating levels in the shielding occur at EOEC.

The various configuration and material arrangements were investigated to determine relative advantage in achieving the following objectives:

1. Limit exposures to permanent components of the core restraint, outer radial shielding, and primary coolant system boundary systems to values below the exposure limits specified later in this section.

2. Minimize nuclear heating and heating gradients (and thus thermal stress) in the inner and outer radial shielding and the core restraint cylinder.

3. Minimize the total nuclear heating (and thus cooling requirements) for all related internal components.

4. Determine shielding physics advantages for block versus wire-wrap R/S concepts.

5. Determine if one type (with one material) of R/S assembly can satisfy exposure and heating limits.

Radiation Exposure Criteria

References 2-43 and 2-44 and associated references provide background on radiation exposure criteria for GCFR out-of-core structural components. Data for evaluating irradiation effects to metal alloys at high temperature (>550°C) are not currently available, bur helium damage is a primary concern for high-temperature lower-plenum metal components.

The conclusions of this study are based on the proposed radiation exposure criteria outlined below:

1. Removable Core R/S Assemblies

   a. Metal alloys and weldments

      (1) Physical criteria: Same as for fuel or blanket assemblies.

      (2) Exposure limit: Since 30 effective power years (EPY) exposures to R/S assemblies are less than for fuel assemblies with 3-year residence, it is assumed that degration of duct or clad mechanical properties does not limit the life of R/S assemblies to values less than plant life.

   b. Graphite (H-451)

      (1) Physical criteria: Zero expansion in radial direction (related to extrusion axis).

      (2) Exposure limit: Lifetime fluence $\leq$ 3.8, 3.5, and 1.4 x 10^{22} (EFFGD*) at 400°C, 600°C, and 800°C, respectively (Ref. 2-45).

   c. Boronated graphite

      (1) Physical criteria: Mechanical property, burnup, and temperature limits not defined.

      (2) Exposure limit: Not defined.

*EFFGD = equivalent fission fluence for graphite damage.

2. Permanent Core Restraint System and Outer Radial Shield Components

a. Metal alloys and weldments

(1) Physical criteria: (a) residual ductility based on total elongation (RTE) $\geq$ 10% (Refs. 2-44, 2-46, and 2-47); (b) temperature $\leq$ 650°C (Ref. 2-48).

(2) Exposure criteria for 316 stainless steel: (a) For temperature <550°C, total (E > 0) fluence limit for 316 stainless steel base metal = 4×10^{22} n/cm^2 and total (E > 0) fluence limit for 308L stainless steel (weld) = 8×10^{21} n/cm^2 (Ref. 2-49); (b) for temperature $\geq$550°C, total (E > 0) fluence limit for 316 stainless steel base and welds = 1×10^{21} n/cm^2 (Ref. 2-44) and an allowable helium gas concentration of 1 appm (atomic) (Refs. 2-50, 2-51).

b. Graphite (same as 1b)

c. Boronated graphite (same as 1c)

3. Primary Coolant System Boundary (PCSB)

a. PCRV liner

(1) Physical criterion: nil ductility temperature shift $\leq$47°C.

(2) Exposure limit: $\sim$1 to 4×10^{19} total fluence by damage function analysis.

b. PCRV tendon lubricant

(1) Physical criterion: lubricant adherence and corrosion protection.

(2) Exposure limit: 10^9 rad (Ref. 2-44).

The 1-appm helium gas concentration limit for 316 stainless steel base and weld metal operating at $\geq$550°C is only for interim guideline use, and an assessment of available data is required to obtain a more reliable limit.

Figures 2-38 and 2-39 (from Ref. 2-49), which show the recent HEDL results on the irradiation effects of 316 stainless steel and 308L stainless steel weld ductility, are the basis for the 2a(2) fluence limits for steel operating at <550°C. Note that the irradiation temperatures T_i varied from 371°C to 399°C and that the chosen fluence limits for 10% RTE correspond to the data points for the highest mean neutron energy E. Since the mean neutron energy in the vicinity of the GCFR core restraint system and outer radial shield is $\leq$0.25 MeV, the chosen fluence limits are expected to be conservative by about a factor of 2.

Exposure Margins

All radiation transport calculations include uncertainties in the computed flux values due to:

1. Analytical methods approximations.
2. Geometric modeling simplifications.
3. Nuclear cross-section uncertainties.

Uncertainties in computed flux values due to cross-section uncertainties increase with increasing penetration of the shield structures. Since the GCFR demonstration radial shielding attenuates the total neutron flux by about five orders of magnitude between the inside of the radial blanket and the PCRV liner, it is easy to understand how a few percent error in the cross-sections is manifested as a substantial flux uncertainty at the PCRV liner. The assumption of azimuthal symmetry for the one-dimensional calculations results in an underprediction of exposure levels at locations near the midpoint of the side flats of the hexagonal core (the mid-flat is closest to the reactor core center). This underprediction is estimated

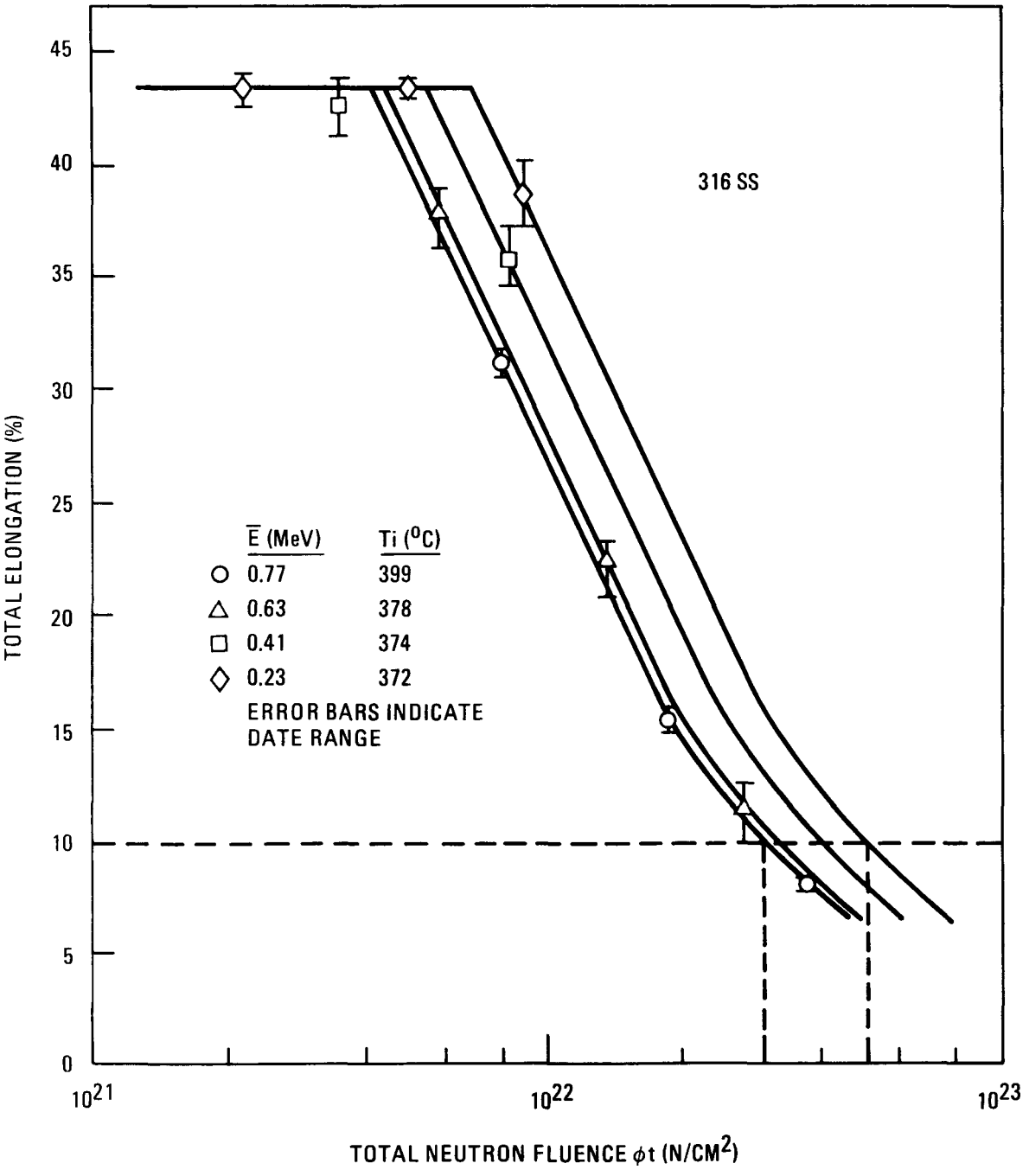

Fig. 2-38. Irradiation effects on 316 stainless steel ductility

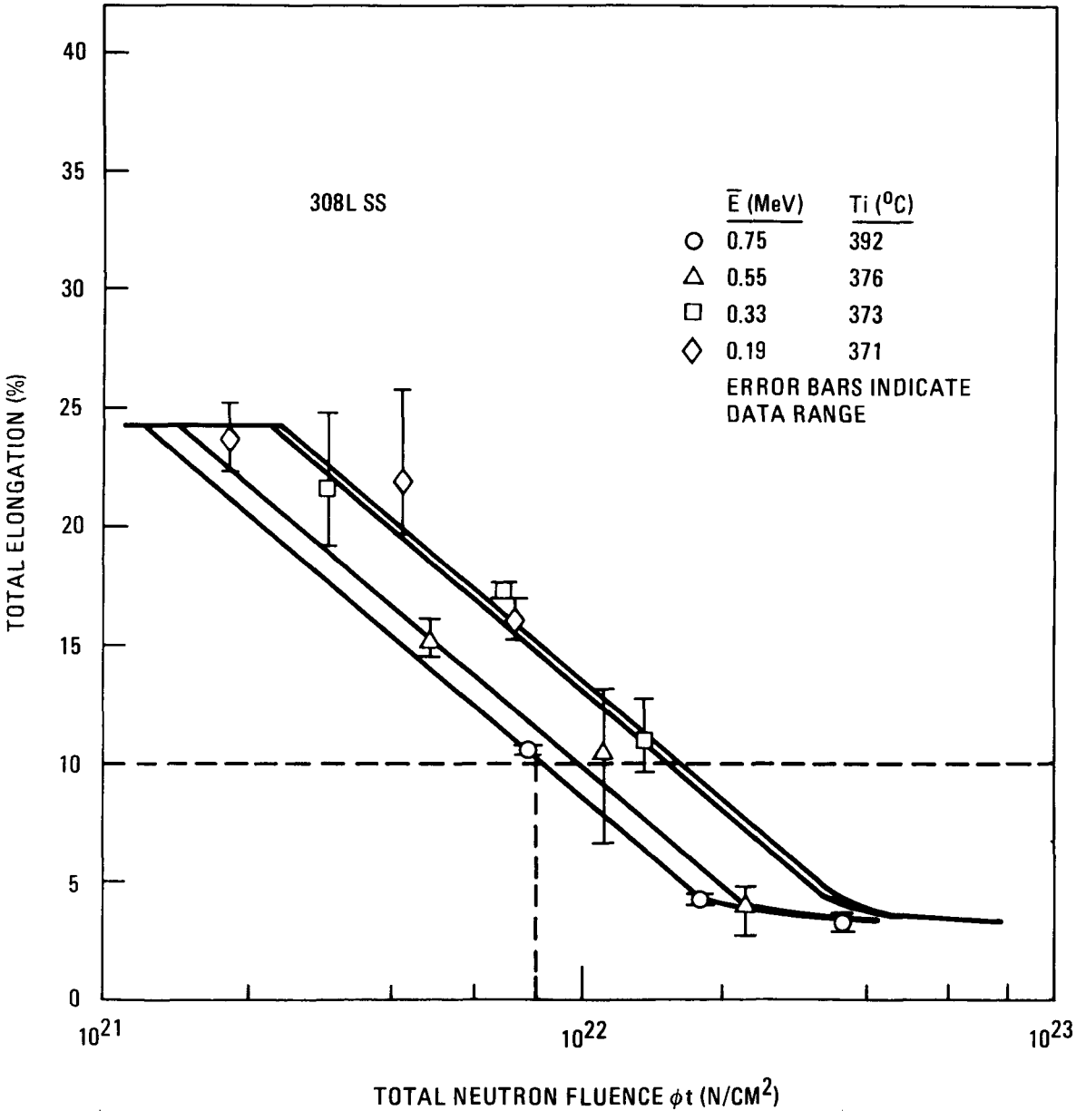

Fig. 2-39. Irradiation effects on 308L stainless steel (weld) ductility

to be 30% at the core-radial blanket interface (Ref. 2-52). The assumption of azimuthal symmetry also has the effect of neglecting some heterogeneity and streaming effects. For example, streaming takes place in void gap spaces and tolerances occurring during component fabrication and construction. Also, the transport characteristics of solid steel, such as in an R/S assembly duct wall or in outer radial shield section steel encasements, are considerably less effective than those of the solid shield materials, graphite and boronated graphite. Such gaps and steel casings are perpendicular to the azimuthal symmetry plane and cannot be modeled in a one-dimensional calculation.

The state of the art of transport sensitivity analysis techniques is not sufficiently advanced that percentage uncertainties can be calculated. Furthermore, uncertainties in raw nuclear data and processed multigroup cross-sections are generally unknown for specific applications. For these reasons, the estimation of uncertainties in computed fluxes and spectra due to methods, modeling, and data must be based on good engineering judgment and experience. Quantification of total (combined) uncertainties requires shielding experiments which simulate the actual system as closely as possible. The uncertainties discussed above will be quantified in the FY-79 GCFR radial shield experiment to be conducted at ORNL.

To evaluate the radial shielding requirements at the core midplane level, the following total uncertainties were assigned to the computed flux values:

Inner radial shields	50%
Core restraint cylinder	100%
Outer radial shield	100%
PCSB	500%

Therefore, desired exposure margins are 0.5, 1.0, and 4.0 for the inner shields, outer shield, and PCSB, respectively, where margin is defined by

$$\text{margin} = \left(\frac{\text{exposure limit}}{\text{calculated exposure}}\right) - 1 \quad .$$

Thus, for a PCRV heating rate limit of 1 mW/cc, the desired calculated heating rate is $\leq$0.2 mW/cc, giving the desired margin of (1/0.2 - 1) = 4.0.

Results

Tables 2-22 through 2-26 give, for each case considered, the nominal values (as computed values without uncertainties) for maximum inner-surface radiation exposure, damage, and heating for row 1 R/S assemblies, row 2 R/S assemblies, the core restraint cylinder, the outer radial shield, and the primary coolant system boundary, respectively. Note that the maximum nuclear heating rates given in the tables are for heating in full-density steel, graphite, or boronated graphite. Table 2-27 gives volume averaged (core midplane level) heating rates for each material and for each component, i.e., R/S assemblies, core restraint cylinder, and outer radial shield. Table 2-27 thus provides a relative comparison for each case of total energy deposition in the various components. Table 2-28 gives peak to volume-averaged heating rate ratios in each material of each component, giving a relative comparison of heating gradients with the different R/S assembly configurations. Finally, Tables 2-29 and 2-30 give the exposure margins for the permanent core restraint cylinder and outer radial shield based on the proproposed exposure criteria. All time-integrated values conservatively correspond to accumulated exposure for 30 effective power years (EPY - years of 0.8 capacity factor) for an EOEC power distribution.

Reflector/Shield Assemblies. From Tables 2-21 and 2-22, it is seen that for all cases, the total fluence exposures are less than that experienced by core fuel assemblies for a 3-year core residence. In addition, 30 EPY graphite EFFGD values are less than the 2.4×10^{22} n/cm^2 limit for H-451 graphite at 600°C and not more than 30% greater than the 1.4×10^{22} n/cm^2 limit for H-451 graphite at 800°C. Thus, based on the assumption that core and blanket assembly structural criteria are applicable to R/S assemblies and that the plant has a three-row blanket, it can be concluded that lifetimes for the grid plate supported R/S assemblies can be expected to

TABLE 2-22
NOMINAL MAXIMUM RADIATION EXPOSURE, DAMAGE, AND HEATING VALUES
FOR ROW 1 REFLECTOR/SHIELD ASSEMBLIES

Parameter	Cases					
	1	2	3	4	5	6
Row 1 R/S type	C + B_4C, WR[a]	C + B_4C, WR	C, WR	316 SS, WR	C, WR	C + B_4C, block
Row 2 R/S type	316 SS, WR	C + B_4C, WR	C + B_4C, WR	C + B_4C, WR	316 SS, WR	316 SS, block
30 EPY[b] neutron fluence, n/cm^2						
E > 0.1 MeV	1.77+22	1.76+22	1.83+22	2.48+22	1.84+22	1.80+22
2.38 eV (E < 0.1 MeV)	3.75+22	3.72+22	6.23+22	6.14+22	6.51+22	3.86+22
E < 2.38 eV	3.23+16	3.22+16	1.09+21	6.04+19	1.79+21	3.71+16
Total	5.52+22	5.48+22	8.12+22	8.62+22	8.47+22	5.66+22
Displacement per atom (dpa) at 30 EPY						
316 SS, dpa	7.03	6.99	7.37	9.35	7.42	7.15
Graphite EFFGD[c]	1.71+22	1.69+22	1.80+22	NA	1.81+22	1.74+22
Maximum nuclear heating[d], mW/cm^3						
316 SS	355	347	601	520	770	355
Graphite	NA[e]	NA	120	NA	154	NA
Boronated graphite	795	787	NA	NA	NA	819

[a] WR = wire wrap R/S assembly concept.
[b] 30 EPY = 30 years operation at 0.8 capacity factor.
[c] EFFGD = equivalent fission fluence for graphite damage.
[d] Heating rate in full-density material.
[e] NA = not applicable.

TABLE 2-23
NOMINAL MAXIMUM RADIATION EXPOSURE, DAMAGE, AND HEATING VALUES
FOR ROW 2 REFLECTOR/SHIELD ASSEMBLIES

Parameter	Cases					
	1	2	3	4	5	6
Row 1 R/S type	C + B_4C, WR[a]	C + B_4C, WR	C, WR	316 SS, WR	C, WR	C + B_4C, block
Row 2 R/S type	316 SS, WR	C + B_4C, WR	C + B_4C, WR	C + B_4C, WR	316 SS, WR	316 SS, block
30 EPY[b] neutron fluence, n/cm^2						
E > 0.1 MeV	3.52+21	2.65+21	2.65+21	5.60+21	3.57+21	4.53+21
2.38 eV (E < 0.1 MeV)	7.67+21	5.19+21	1.23+22	1.01+22	2.76+22	9.82+21
E < 2.38 eV	3.50+18	4.11+14	8.76+19	4.04+18	2.08+21	9.22+17
Total	1.12+22	7.84+21	1.50+22	1.57+22	3.25+22	1.37+22
Displacement per atom at 30 EPY						
316 SS, dpa	1.40	1.11	1.14	1.92	1.47	1.67
Graphite EFFGD[c]	NA[e]	2.56+21	2.69+21	5.14+21	NA	NA
Maximum nuclear heating[d], mW/cm^3						
316 SS	124	129	328	155	588	138
Graphite	NA	NA	NA	NA	NA	NA
Boronated graphite	NA	126	833	321	NA	NA

[a] WR = wire wrap R/S assembly concept.
[b] 30 EPY = 30 years operation at 0.8 capacity factor.
[c] EFFGD = equivalent fission fluence for graphite damage.
[d] Heating rate in full density material.
[e] NA = not applicable.

TABLE 2-24
NOMINAL MAXIMUM RADIATION EXPOSURE, DAMAGE, AND HEATING VALUES
FOR CORE RESTRAINT CYLINDER

Parameter	Cases					
	1	2	3	4	5	6
Row 1 R/S type	C + B_4C, WR[a]	C + B_4C, WR	C, WR	316 SS, WR	C, WR	C + B_4C, block
Row 2 R/S type	316 SS, WR	C + B_4C, WR	C + B_4C, WR	C + B_4C, WR	316 SS, WR	316 SS, block
30 EPY[b] neutron fluence, n/cm^2						
E > 0.1 MeV	7.95+20	4.07+20	3.93+20	6.83+20	7.83+20	9.47+20
2.38 eV (E < 0.1 MeV)	1.57+21	8.03+20	9.63+20	1.60+21	2.38+21	1.90+21
E < 2.38 eV	1.09+19	2.31+17	3.27+17	4.43+17	7.63+19	1.33+19
Total	2.36+21	1.21+21	1.35+21	2.28+21	3.20+21	2.85+21
Displacement per atom at 30 EPY	0.261	0.163	0.158	0.236	0.259	0.310
Maximum nuclear heating, mW/cm^3	20.0	18.1	41.2	30.5	53.5	24.2
Helium concentration in 316 SS at 30 EPY, appm	0.22	0.066	0.082	0.098	0.70	0.27

[a] WR = wire wrap R/S assembly concept.

[b] 30 EPY = 30 years operation at 0.8 capacity factor.

TABLE 2-25
NOMINAL MAXIMUM RADIATION EXPOSURE, DAMAGE, AND HEATING VALUES
FOR OUTER RADIAL SHIELD

Parameter	Cases					
	1	2	3	4	5	6
Row 1 R/S type	C + B_4C, WR[a]	C + B_4C, WR	C, WR	316 SS, WR	C, WR	C + B_4C, block
Row 2 R/S type	316 SS, WR	C + B_4C, WR	C + B_4C, WR	C + B_4C, WR	316 SS, WR	316 SS, block
30 EPY[b] neutron fluence, n/cm^2						
E > 0.1 MeV	5.25+20	2.79+20	2.68+20	4.51+20	5.15+20	6.25+20
2.38 eV (E < 0.1 MeV)	9.67+20	5.27+20	6.02+20	1.02+21	1.29+21	1.18+21
E < 2.38 eV	6.65+18	5.87+17	8.22+17	1.12+18	3.16+19	8.13+18
Total	1.50+21	8.07+20	8.71+20	1.50+21	1.82+21	1.81+21
Displacement per atom at 30 EPY						
316 SS	0.170	0.105	0.102	0.151	0.168	0.202
Graphite EFFGD[c]	2.33+20	1.34+20	1.28+20	2.01+20	2.27+20	2.76+20
Maximum nuclear heating[d], mW/cm^3						
316 SS	12.1	7.14	13.8	12.9	25.6	14.6
Graphite	1.02	0.58	0.86	1.06	1.60	1.23
Boronated graphite	12.7	6.48	7.42	12.0	17.7	15.2
Helium concentration in 316 SS at 30 EPY, appm	0.13	0.051	0.063	0.085	0.31	0.16

[a] WR = wire wrap R/S assembly concept.

[b] 30 EPY = 30 years operation at 0.8 capacity factor.

[c] EFFGD = equivalent fission fluence for graphite damage.

[d] Heating rate in full-density material.

TABLE 2-26

TABLE 2-26
NOMINAL MAXIMUM RADIATION EXPOSURE, DAMAGE, AND HEATING VALUES
FOR PRIMARY COOLANT SYSTEM BOUNDARY

Parameter	Cases					
	1	2	3	4	5	6
Row 1 R/S type	C + B_4C, WR[a]	C + B_4C, WR	C, WR	316 SS, WR	C, WR	C + B_4C, block
Row 2 R/S type	316 SS, WR	C + B_5C, WR	C + B_4C, WR	C + B_4C, WR	316 SS, WR	316 SS, block
30 EPY[b] neutron fluence, n/cm^2						
E > 0.1 MeV	4.28+17	6.03+17	5.69+17	3.61+17	4.04+17	4.82+17
2.38 eV (E < 0.1 MeV)	2.26+18	1.64+18	1.57+18	1.94+18	2.19+18	2.65+18
E < 2.38 eV	2.07+17	1.16+17	1.54+17	1.77+17	2.00+17	2.42+17
Total	2.86+18	2.37+18	2.26+18	2.44+18	2.76+18	3.33+18
Lower-bound 47°C NDTS[c] liner fluence limit, n/cm^2	3.10+19	2.06+19	1.81+19	3.12+19	3.17+19	3.21+19
Time to attain 47° liner NDTS	325	261	240	384	345	289
Liner steel at 30 EPY, dpa	1.37-4	2.18-4	2.06-4	1.18-4	1.29-4	1.53-4
Maximum concrete gamma ray heating rate, mW/cm^3	0.0307	0.0203	0.0342	0.0334	0.0367	0.0505
PCRV tendon lubricant gamma ray dose at 30 EPY, rads	7.22+7	5.49+7	7.79+7	7.44+7	1.12+8	8.53+7
Time to attain tendon lubricant dose of 10^9 rads, EPY	416	546	385	403	268	352

[a] WR = wire wrap R/S assembly concept.

[b] 30 EPY = 30 years operation at 0.8 capacity factor.

[c] NDTS = nil ductility temperature shift.

TABLE 2-27
ASSEMBLY VOLUME AVERAGED HEATING RATES IN EACH MATERIAL
AND FOR HOMOGENIZED R/S ASSEMBLIES, CORE RESISTANT
CYLINDER, AND OUTER RADIAL SHIELD

Parameter	Cases					
	1	2	3	4	5	6
Row 1 R/S type	C + B_4C, WR	C + B_4C, WR	C, WR	316 SS, WR	C, WR	C + B_4C, block
Row 2 R/S type	316 SS, WR	C + B_4C, WR	C + B_4C, WR	C + B_4C, WR	316 SS, WR	316 SS, block
Volume-averaged heating rates, mW/cm^3						
R/S Row 1						
316 SS	47.6	44.8	78.4	303	120	52.6
C + B_4C	260	244	NA	NA	NA	246
C	NA[a]	NA	53.3	NA	80.1	NA
Average	308	289	132	303	200	299
R/S Row 2						
316 SS	50.2	11.7	29.1	16.8	237	59.6
C + B_4C	NA	38.7	118	77.8	NA	NA
C	NA	NA	NA	NA	NA	NA
Average	50.2	50.4	147	94.6	237	59.6
316 SS core restraint cylinder	16.9	12.7	27.8	21.9	42.0	20.4
Outer radial shield						
316 SS	9.21	5.30	9.46	9.66	18.2	11.1
C + B_4C	10.2	5.57	6.14	10.1	12.3	12.3
C	0.43	0.25	0.41	0.46	0.74	0.52
C + B_4C	1.43	0.83	0.87	1.36	1.55	1.00
316 SS	0.44	0.26	0.46	0.48	0.79	0.53
Average	2.62	1.47	3.20	2.67	4.06	3.06

[a] NA = not applicable.

TABLE 2-28
PEAK TO AVERAGE HEATING RATE RATIOS IN EACH MATERIAL FOR R/S ASSEMBLIES, CORE RESTRAINT CYLINDER, AND OUTER RADIAL SHIELD

Parameter	Cases					
	1	2	3	4	5	6
Row 1 R/S type	C + B_4C, WR	C + B_4C, WR	C, WR	316 SS, WR	C, WR	C + B_4C, block
Row 2 R/S type	316 SS, WR	C + B_4C, WR	C + B_4C, WR	C + B_4C, WR	316 SS, WR	316 SS, block
Peak to volume average heating rate ratios						
R/S Row 1						
316 SS	1.27	1.32	1.30	1.52	1.09	1.25
C + B_4C	1.95	2.06	NA	NA	NA	1.82
C	NA[a]	NA	1.44	NA	1.22	NA
R/S Row 2						
316 SS	2.19	1.88	1.92	1.57	2.19	2.07
C + B_4C	NA	2.08	4.50	2.64	NA	NA
C	NA	NA				
316 SS core restraint cylinder	1.18	1.43	1.48	1.39	1.27	1.18
Outer radial shield						
316 SS	1.31	1.35	1.46	1.34	1.41	1.31
C + B_4C	1.25	1.16	1.21	1.19	1.44	1.24
C	2.36	2.33	2.12	2.29	2.18	2.36

[a] NA = not applicable.

TABLE 2-29
EXPOSURE MARGINS[a] FOR CORE RESTRAINT CYLINDER
AT 30 EPY (REQUIRED MARGIN $\geq$ 1.0)

Case	Row 1 R/S Type	Row 2 R/S Type	Exposure Criteria if Core Restraint Cylinder Temperature $\geq$ 550°C		Exposure Criteria if Core Restraint Cylinder Temperature < 550°C	
			1 appm Helium Concentration in 316 SS	10^{21} n/cm^2 Total Fluence	316 SS Base Metal 4×10^{22} n/cm^2 Total Fluence	308L SS Weld 8×10^{21} n/cm^2 Total Fluence
1	C + B_4C, WR	316 SS, WR	3.5	-0.58	16	2.4
2	C + B_4C, WR	C + B_4C, WR	14	-0.17	32	5.6
3	C, WR	C + B_4C, WR	12	-0.26	30	4.9
4	316 SS, WR	C + B_4C, WR	10	-0.56	17	2.5
5	C, WR	316 SS, WR	0.43	-0.69	10	1.5
6	C + B_4C, block	316 SS, block	2.7	-0.65	12	1.8

[a] Margin = (limit/response) -1.

TABLE 2-30
EXPOSURE MARGINS[a] FOR PERMANENT OUTER RADIAL SHIELD
AT 30 EPY (REQUIRED MARGIN = 1.0)

Row 1 R/S Type	Row 2 R/S Type	Criteria if Steel Temperature ≥ 550°C		Criteria if Steel Temperature < 550°F		
		1 appm Helium Concentration in 316 SS	10^{21} n/cm^2 Total Fluence	4×10^{22} n/cm^2 Total Fluence in 316 SS Base Metal	8×10^{21} n/cm^2 Total Fluence in 308L SS Weld Metal	1.4×10^{22} n/cm^2 EFFGD for H-451 Graphite at 800°
C + B_4C, WR	316 SS, WR	6.7	-0.33	24	4.3	59
C + B_4C, WR	C + B_4C, WR	19	0.24	48	8.9	103
C, WR	C + B_4C, WR	15	0.15	44	8.2	108
316 SS, WR	C + B_4C, WR	11	-0.33	24	4.3	69
C, WR	316 SS, WR	2.2	-0.45	20	3.4	61
C + B_4C, block	316 SS, block	5.2	-0.45	20	3.4	50

[a] Margin = (limit/response) -1.

approach that of plant life. This is most certain for row 2 R/S assemblies. The conclusion might not hold for boronated graphite (C + B_4C) R/S assemblies for which a C + B_4C exposure limit has not been specified.

Radiation heating and, in particular, thermal stresses due to temperature gradients, rather than lifetime, could be an important consideration for selection of the material arrangement for the R/S assemblies which are replaceable by normal fuel handling procedures.

Both the magnitude and the gradient of the heating determine the R/S assembly stresses and potential deformations. The following should be noted regarding the relative advantages of different R/S configurations in mitigating thermal effects in the R/S assemblies:

1. From Table 2-27 it is seen that row 1 R/S assembly volume-averaged heating rates for cases 3 (both row 1 and 2 R/Ss = C + B_4C, WR) and 5 (row 1 R/S = C, WR and row 2 R/S = SS 316, WR) are factors of about 2.3 and 1.5, respectively, below that for the other cases.

2. From Table 2-28 it is seen that the row 1 R/S peak to volume-averaged heating rates are lowest for case 5 (1.09 in 316 SS and 1.22 in C) and most severe for cases 1, 2, and 6 (about 1.3 in 316 SS and 1.9 in C + B_4C). Gradients for cases 3 and 4 are in between the former extremes.

3. For cases 3 and 5, which have the lowest row 1 R/S assembly-averaged heating rates, the row 2 R/S assembly heating rates are factors of about 3 and 4, respectively, greater than for the other cases.

4. Row 1 and row 2 R/S assemblies have nearly the same heating rates for cases 3 and 5.

5. The row 2 R/S assembly heating gradients are about the same for all cases except case 3, which has a peak to volume-averaged heating rate ratio of 4.5, or about 2 to 3 times greater than for the other cases.

Although it is apparent that the materials and material arrangements of the R/S assemblies strongly affect the heating rate magnitudes and gradients, thermal-mechanical analysis is required to identify potential problems and/or the preferred configuration(s) of the cases considered.

Core Restraint System. For this analysis, only a 4.4 cm (1-3/4-in.) thick core support cylinder (at the core midplane) was modeled. From Table 2-29 it is seen that if the core restraint cylinder operates at temperatures $\geq$550°C (core outlet helium cooling), none of the R/S configurations enable the 10^{21} n/cm^2 total fluence limit to be met with the required margin of 1.0; the 1 appm helium concentration limit is met with adequate margin for all cases except case 5. For cases 2 and 3, which have the lowest total fluence, 1.21×10^{21} and 1.35×10^{21} n/cm^2, respectively, the required value of 5×10^{20} could possibly be attained by increasing the B-10 enrichment in the boronated graphite. However, nuclear heating rates and gradients would increase. For cases 1, 4, 5, and 6, meeting the 10^{21} n/cm^2 limit would require the addition of a third row of R/S assemblies; there would then be three rows of blanket assemblies and three rows of R/S assemblies.

If the core restraint cylinder operates at temperatures <550°C, all R/S assembly configurations enable the limiting 8×10^{21} n/cm^2 total fluence exposure criterion for 308L stainless steel weld to be met with adequate margin, with the largest margins occurring for cases 2 and 3.

Table 2-27 shows that the average nuclear heating rate in the core restraint cylinder is lowest for case 2 and highest for case 5, and Table 2-28 shows that the heating gradient is smallest for cases 1 and 6. Again, thermal-mechanical analysis is required to determine the relative merits of the different R/S configurations in mitigating thermal effects.

Outer Radial Shield. As for the core restraint cylinder, Table 2-30 shows that if the outer radial shield structural steel operates at temperatures $\geq$550°C, none of the R/S configurations enable the 10^{21} n/cm^2 total fluence limit to be met with the required margin of 1.0; the 1 appm helium concentration limit is met with adequate margin for all cases. The additional required attenuation (see Table 2-25) varies from 40% for case 2 to a factor of about 4 for case 5. It is likely that the 10^{21} limit could be met for some configurations by one or more of the following means:

1. Increasing the B-10 enrichment in boronated graphite in the R/S assemblies.

2. Increasing the B_4C content in the C + B_4C (B_4C has a higher density than the graphite) in the R/S assemblies.

3. Replacing the 316 stainless steel in the core midplane region of the R/S assemblies with a high nickel alloy such as 718, which has a higher cross-section.

Table 2-30 shows that if the radial shield structural steel operates at temperatures <550°C (core inlet gas cooling required), all R/S assembly configurations enable the limiting 8 x 10^{21} n/cm^2 total fluence exposure criterion for 308L stainless steel weld to be met with adequate margin, with the largest margins occurring for cases 2 and 3.

Table 2-27 shows that heating rate magnitudes in the outer radial shield are significantly affected by the R/S assembly configuration. The heating rates for case 2 are about one-half and for case 5 are about twice as large as for cases 1, 3, and 4. However, the heating gradients in the outer radial shield, as characterized by the peak-to-average heating rate values in Table 2-28, are not strongly affected by the R/S assembly configuration.

Primary Coolant System Boundary. Table 2-26 shows that both the PCRV liner 47°C nil ductility temperature shift limit for the PCRV liner and the PCRV tendon lubricant gamma-ray dose limit are met by margins exceeding the

required margin of 4.0 (corresponding to a time to attain either exposure limit of 150 EPY years). However, the primary conclusion to be drawn from Table 2-25 is that the R/S assembly configuration has little effect on PCSB exposures and thus has little effect on outer radial shield thickness requirements.

Appendix. The helium production cross sections used in the analysis and the shield material specifications are given in Appendices A and B, respectively.

Conclusions

The following are the primary conclusions pertaining to the relative shielding effectiveness of the configurations that were considered to meet the exposure limits:

1. Based on the assumption that core and blanket fuel assembly structural and exposure criteria are applicable to the R/S assemblies and that the plant has a three-row blanket, lifetimes for the grid-plate-supported R/S assemblies can be expected to approach that of plant life, regardless of R/S assembly configuration.

2. For a high-temperature ($\geq$550°C) core restraint system, none of the configurations enable the 10^{21} n/cm^2 total fluence limit to be met with adequate margin. For cases 2 and 3, the limit might be met by increasing the B_4C content or B-10 enrichment in the R/S assemblies. For cases 1, 4, 5, and 6, a third row of R/S assemblies would probably be required. The above conclusion is valid for a multiple point constraint system where the core support cylinder extends to near or below the core midplane. Two-dimensional calculations could show that some or all of the R/S configurations would provide adequate shielding for a high-temperature single-point core restraint system extending to core-upper axial blanket (downflow core) interface.

3. For a high-temperature (>550°C) outer radial shield, none of the R/S assembly configurations enable the 10^{21} n/cm^2 total fluence limit to be met with adequate margin. The limit could be met for some and possibly all R/S configurations by one or more of the following means:

   a. Increasing the B-10 enrichment in B_4C in the R/S assemblies.

   b. Increasing the B_4C content in the C + B_4C in the R/S assemblies.

   c. Replacing 316 SS near the core midplane with a higher cross-section alloy such as 718.

4. For a low-temperature (<550°C) core restraint system or outer radial shield, all R/S assembly configurations enable the limiting 8 x 10^{21} n/cm^2 total fluence limit for 308L stainless steel weld to be met with adequate margin.

5. Based on overall attenuation effectiveness, R/S assembly configurations 2 and 3 are most effective and configuration 5 is least effective. Because of the larger shield material volume fraction, the wire-wrap R/S concept is preferred over the block concept.

6. The R/S assembly configuration has little effect on exposure levels at the PCSB (e.g., PCRV liner) and thus on outer radial shield thickness requirements. Outer radial shield optimization can be expected to be predominately independent of the R/S assembly configuration.

The following are the primary conclusions pertaining to the relative effectiveness of the R/S assembly configurations in reducing potential thermal-mechanical deformation and/or cooling requirements:

1. Heating rates and gradients in the R/S assemblies vary significantly between the different configurations. For cases 3 and 5, the

volume-averaged heating rates are nearly equal in R/S rows 1 and 2 and are factors of about 2.3 and 1.5 lower in row 1 and factors of about 3 and 4 higher in row 2, respectively, than for the other cases. Heating gradients are lowest for case 5 and relatively most severe for cases 1, 2, and 6 (e.g., for case 2, the peak to volume-averaged heating rate for C + B_4C in a row 1 R/S assembly is 1.95).

2. Volume-averaged heating rates and peak to volume-averaged heating rate ratios vary by factors of about 3 for the various R/S assembly configurations. Case 1 gives the best combination of low heating and low heating gradient.

3. Total energy deposition in the outer radial shield for case 2 is about one-half and for case 5 is about twice as large as for the other cases. The heating gradients are similar for all R/S configurations.

4. The row 1 and row 2 R/S assembly mechanical designs are the same for configuration 3.

5. The boronated graphite, for which an exposure limit has not been specified, is not located in the high-flux row 1 R/S position.

Additional physics analysis is required to determine how the shielding effectiveness of R/S assemblies can be increased with higher B_4C and/or B-10 contents or different metallic alloys such as 718 (high nickel). Current analysis should be refined by two-dimensional methods to better determine axial leakage effects.

Physics Analysis. The scope of activities planned under this subtask encompasses the application of nuclear design methods to the GCFR core design. Currently, the subtask includes additional activities on behalf of the Safety Analysis Branch in regard to evaluating recriticality potential during core disruptive accidents.

In the previous quarter, work was completed on the first stage of recriticality analysis for accident situations involving fuel crumbling and compaction. During the present quarter, a second stage of studies was finished and work on a third and final stage was initiated and is nearing completion. These second and third stages involve various configurations of molten fuel and steel relocations.

Distorted Core Analysis - Stage 2 Recriticality Analysis

A series of calculations were carried out to evaluate the prospects of fuel removal and of addition of neutron absorber (europium oxide, Eu_2O_3) toward maintaining subcriticality in the event of total slumping of molten fuel in a severe protected-loss-of-flow (PLOF) accident in the demonstration plant GCFR core. A distorted-core situation is postulated where all fuel has melted and slumped into a layer at full compaction between a layer of axial blanket plugged with refrozen clad and an upper layer of molten duct material. The objectives of these studies were to determine (1) what fraction of fuel drain-away would be required, or (2) what amount of poison material, soluble in the molten fuel, would have to be added to prevent recriticality even if the normal B_4C control rods were ejected or lost from the core.

Reactor Model. The model for the two-dimensional diffusion theory calculations was derived from the calculational setup used for the first stage of recriticality studies as described in the Ref. 2-53. For these total-slump cases, the geometric details are similar to the case for the 86% packing fraction of crumbled fuel reported earlier, except for the complete removal of the B_4C control rods from the core regions and subsequent flooding of the rod channels by molten-layer materials. As in the first-stage analysis, the fuel layer rests on top of the plugged axial blanket, which, in turn, is above the normal axial blanket and reflector regions. Above the molten fuel layer is a floating layer of molten steel with an axial thickness of 16.08 cm. The remainder of the normal core length above the steel layer is voided (except for helium and steel vapor), and above this are the normal, hot, upper axial blanket and reflector regions.

The core radial dimensions for the model were fixed at the normal hot-core specification, with the outer zone radius of 111.32 cm. Outward of the core are the normal hot radial blanket and radial reflector zones. In this series of calculations, the height of the molten fuel layer was varied according to the specific assumptions for each configuration, either a reduction for fractional drain-away of fuel, or an expansion for the homogeneous addition of europia to a fixed content of fuel. The reference configuration uses a fuel-only layer height of 32.50 cm, representing the total core inventory of 10905.3 kg of PuO_2UO_2 (16.7% fissile, average) with a density of 8.62 g/cm^3 (at 3200 K). For fuel drain-away, complete fuel removal from below the axial reflector is assumed, and the reduction in fuel layer thickness is accompanied by a corresponding increased height of voided region above the molten steel layer.

Specifications for europia were established on the basis of data reported by Simnad (Ref. 2-54). It was assumed that in the cold undistorted reactor, the europia was in the form of sintered or pressed pellets of cubic form granules with a smear density of 6.704 g/cm^3 (92% theoretical density for the cubic form). Also, in the molten state, a further density reduction factor of 0.90 was postulated, giving a molten, natural Eu_2O_3 density of 6.0336 g/cm^3 for blending with the molten fuel.

Calculational Methods. Cross sections for the reference molten core configurations, for the fuel-only layer at 3200 K, and for the drain-away situations were derived from the GGC-5 (Ref. 2-55) problem run previously during the first stage of core disruptive accident (CDA) analysis for crumbled, unmelted fuel compacted to 86% by volume. The Doppler broadening of resonances for these fuel cross sections was carried out for a temperature of 3000 K, and the 200 K difference in assumed temperature involves a reactivity discrepancy of less than $0.05. For the blanket and reflector regions, the material cross sections and densities were identical with those used in the first stage.

A new GGC-5 problem was run for the cases with the fuel mixed with europia. For the spectrum calculation and cross section generation, a two-region cell was specified, made up of small crumbled pieces of fuel pellets dispersed at 80% by volume in a matrix of molten Eu_2O_3. Again, a fuel temperature of 3000 K was used to match available temperature-broadened GGC-5 input data. New fine-group GAM data for the europia isotopes were prepared and added to the GAM data tape used by GGC-5. Macroscopic cross sections for fuel and europia were then derived from the GGC-5 output, using the natural abundances for the elemental Eu (47.8%, ^{251}Eu + 52.2% ^{253}Eu), for use in the 2DB (Ref. 2-56) calculations.

For these hypothetical situations, no boron carbide control rods are assumed anywhere in the reactor, giving the worst, most reactive configuration possible for the undrained, unpoisoned condition, with plugged blanket upholding the fuel and molten duct floating above the fuel as a reflector. The basic model for the 2DB diffusion calculations was adjusted to account for the removal of the control rod heterogeneity.

No diffusion modifiers were used in 2DB for the layers of fuel, fuel plus europia, molten steel, and plugged axial blanket. For the upper core void region (helium plus 1/4% steel vapor) modifiers were used to effect the special void diffusion coefficients (explained in Ref. 2-53), as used in the 86% crumbled fuel case. The sets of undistorted diffusion modifiers were used for the neutron streaming effects through the normal lattices in the radial and axial blankets.

Results of Calculations. Table 2-31 lists the series of 2DB calculations carried out for this stage of CDA analysis according to four sets of configurations in the order:

1. A slumped molten core retaining the three enrichment zones with progressive fuel drain-away.

2. The slumped molten core with three enrichment zones without drain-away but with added Eu_2O_3.

TABLE 2-31
SUMMARY OF REACTIVITY CALCULATIONS FOR MOLTEN CORE CONFIGURATIONS (FUEL DENSITY OF 8.62 g/cm^3 AT 3200K)

Case No.	Fuel Enrichment Distribution[a]	Configuration Details			Mass Ratio, Europia-to-Fuel[b]	2DB Results	
		% Fuel Drain-Away	Vol % Added Eu_2O_3	Fuel Height (cm)		Reactivity k	Reactivity in \$ (k-1)/kβ
1	3-zone	None	None	32.50	--	1.3122	+60.39
2	3-zone	50.0	None	16.25	--	1.0359	+8.80
3	3-zone	53.5	None	15.11	--	1.0041	+1.04
4	3-zone	57.0	None	13.98	--	0.9696	-7.96
5	3-zone	None	20.0	32.50	0.1750	1.0006	+0.15
6	3-zone	None	22.0	32.50	0.1974	0.9752	-6.45
7	Blended	None	None	32.50	--	1.3723	+68.86
8	Blended	58.0	None	13.65	--	1.0037	+0.94
9	Blended	60.0	None	13.00	--	0.9812	-4.86
10	Blended	62.0	None	12.35	--	0.9574	-11.29
11	Blended	None	22.0	32.50	0.1974	1.0074	+1.87
12	Blended	None	23.0	32.50	0.2091	0.9940	-1.53

[a] Normal 3-zone enrichments of 13.24, 17.47, and 22.10% in zones of radii 77.87, 94.40, and 113.20 cm, respectively. Core-average blended enrichment of 16.70%.

[b] Kg of Eu_2O_3 per kg of mixed oxide fuel (PuO_2UO_2) at average enrichment.

3. A slumped core with all fuel blended to the average enrichment, total inventory, and then fuel drain-away.

4. A slumped core with the total inventory, blended enrichment, and added Eu_2O_3.

The table includes the pertinent geometric details for the fuel region changes and the relative loading of europia. Results of the 2DB cases are given as the calculated k and equivalent configuration reactivities in dollars (derived using $\beta = 0.00394$).

As a reference configuration for this stage of analysis, the \$60.39 reactivity excess for case 1 in Table 2-31 represents a gain of about \$23.80 over that for the maximum packing (86 vol %) for unmelted crumbled fuel used in the previous stage (with control rods). About \$14.50 of this gain is due to loss of the B_4C rods, and the remainder, \$9.30, results from the compaction to the fuel-only layer at the molten density, plus the flooding of the rod channels, plus the build-up of the reflecting cover layer of molten steel. Compared to the molten-fuel layer thickness here of 32.5 cm, the previous 86% crumbled-fuel layer thickness was 39.28 cm (including unfueled rod channels), with the same total inventory of PuO_2UO_2.

Cases 2 through 4 in Table 2-31 represent fuel drain-away from the reference case 1 configuration with retention of enrichment zoning for the remaining fuel in the molten core layer. To achieve subcriticality it thus appears that 54% of the fuel would have to be removed uniformly from each zone at the molten-fuel temperature, and about another 0.6% would probably be required to compensate for a cool-down Doppler reactivity effect (3000 to 300 K).

For the three-zone, full-inventory fuel layer with added europia, cases 5 and 6, the poison addition to achieve subcriticality is seen to be slightly in excess of 20% by volume at the assumed molten fuel and Eu_2O_3 temperatures and densities. The more definitive criterion would be the

listed ratio of poison-to-fuel mass, a value of 0.175 kg europia per kg of average-enrichment fuel. The cool-down reactivity gain, estimated at $1.50, would require another 1/2% by volume europia for compensation.

Case 7 is a return to an unpoisoned situation with the total fuel inventory; here, however, the material from the three enrichment zones is blended into a homogenized layer with an average enrichment of 16.7% fissile plutonium. Compared with the reference case 1, the fuel blending is thus seen to significantly add reactivity, about $8.50. Interpolating between the results of the drain-away cases 8 and 9, the drain-away of the blended fuel layer would have to approach 58.4% to attain subcriticality for the molten state, and probably 59% for a cold refrozen layer.

The last two cases in Table 2-31 indicate the extent of poison mixing required for the total inventory of blended fuel to be subcritical, about 22.6 vol % for the molten state, near 23 vol % for covering the cool-down reactivity. It is interesting to note that the reactivity effect from blending the full inventory of fuel, from three enrichment zones to a uniform layer, when a sufficient poison is already mixed in (at 22 vol %, case 11 versus case 6) is $8.32, almost identical to the blending worth without poisoning.

Case 12 indicates that a homogeneous mix ratio of about 1 kg of europia per 4 kg of mixed-oxide fuel is sufficient to avoid recriticality in a total uniform slumping of fuel in the demonstration plant GCFR core, even to the most compact blended situation (assuming layer spread to full radius of original core). In terms of the essential reactive constituents, the mix equates to about 1.17 kg europium metal per kg of fissile plutonium (Pu-239 plus Pu-241) metal.

Requirement of an in-core poison-to-fuel ratio by volume of 0.299 (23/27) assuming Eu_2O_3 control rods, for instance, would mean a total shutdown core volume fraction of 7.77% for this poison material. This would require dedicated control elements (19 total) wherein the Eu_2O_3 rod material would constitute 52% by volume.

Distorted Core Analysis - Stage 3 Recriticality Analysis

Detailed configurations were supplied by the Safety Branch for a set of time points after circulator trip with subsequent total loss of flow for the 300-MW(e) GCFR. A reference geometry was selected at 770 s after trip, wherein fuel cladding has melted, slumped, and blocked the lower blanket. About 5% of the fuel has melted and slumped, and most of the duct has become molten and is floating on top of the molten fuel. The models were generated via an editing code for the SCORED code (Ref. 2-57) which follows the fuel and steel temperature rise due to decay heat and relocates materials upon melting and for refreezing. The models at the later time points, 870, 970, and 1110 s, trace the relocations with about 20, 30, and 43%, respectively, of the fuel molten.

Work is well under way toward calculating the reactivity progression in this sequence of configurations. Basic objectives for this third stage of analysis are to establish a time point for recriticality and the reactivity ramp rate at that time. Also, calculations have been initiated concerning complete fall-away of the entire core after the 770-s point but with control rods still affixed to the upper axial blanket. This will be to establish the recriticality potential and possible ramp rate for a hypothesized coherent fall-away.

2.2.2. Core Thermal-Hydraulic Analysis

Effect of Control Rod Withdrawal on Core Assembly Thermal

Reference 2-58 shows the effect of control rod withdrawal on the power levels, and on the axial and radial power profiles, of a central control assembly surrounded by two rows of fuel assemblies. The effects of these changes on the fuel rod temperature were checked by subchannel analysis of the three assemblies. No flow redistribution between assemblies was considered from beginning-of-equilibrium cycle (BOEC), when the control rod is at midplane of the core, to the end-of-equilibrium cycle (EOEC), when the control rod is withdrawn from the core.

Table 2-32 summarizes the results for the three assemblies. The control assembly produces 11% more power and the maximum rod temperature is 24°C higher at the EOEC (Fig. 2-40). The fuel assemblies have small changes in their power levels and the maximum temperature is lower at the EOEC (Figs. 2-41 and 2-42). The maximum temperature drops across the rods (peripheral rods in all six cases) showed only slight change during the cycle. This analysis indicates that a control assembly should be designed for EOEC conditions when it is generating higher power.

2.2.3. Core Configuration and Performance Analysis

2.2.3.1. Flow Redistribution in Ductless Core at Low Powers. The ductless core described in Ref. 2-59 was analyzed at approximately 1% power and flow. For the depressurized core, the buoyancy effect is negligible compared to the forced convection. Therefore, the temperature profile across the core follows the power profile, as the coolant moves from the hotter region to the cooler region (Fig. 2-43). As with full-power condition, the major flow redistribution occurs within each enrichment zone. A power tilt of 60% results in flow differences of 40% from one end of the zone to the other (Table 2-33), whereas the maximum deviation of average mass flux from the reactor average is less than 3%. This type of redistribution can also be expected in the ducted assemblies. For a pressurized reactor, however, the deviations from average are larger.

The buoyancy forces are proportional to the square of the coolant density; the effects can be easily seen in the pressurized core at low flows (Fig. 2-44). In the down-flow core, the buoyancy forces act against the forced convection, adding to the effect of flow reduction in hot subchannels. In the up-flow core, the buoyancy forces act together with forced convection, tending to smooth out the flow profile. Tables 2-34 and 2-35 summarize the results of the different zones.

COBRA-IV predicts that the ductless up-flow core may experience temporary local flow stagnation in the zone with the steepest power tilt.

TABLE 2-32
EFFECT OF CONTROL ROD WITHDRAWAL ON CORE ASSEMBLY

		Coolant Outlet Mixed Mean Temp (°C)	Power Change	Max Coolant Exit Temp (°C)	Max Rod Midwall Temp (°C)	Max Rod ΔT (°C)[b]
Control Assembly	BOEC	540		557	695	-45.4
	EOEC	565	+11%	583	719	-49.0
1st ROW FUEL ASSEMBLY	BOEC	560		571	695	-41.9
	EOEC	564	+2%	573	689	-41.5
2nd ROW FUEL ASSEMBLY	BOEC	564		573	695	-41.9
	EOEC	560	-2%	568	683	-40.5

Note: Fueled section ends at 1780 mm.

[a] Maximum rod temperature for all six cases occurred at axial location of 1635 mm.

[b] Maximum rod ΔT for all six cases occurred at axial location of 1834 mm.

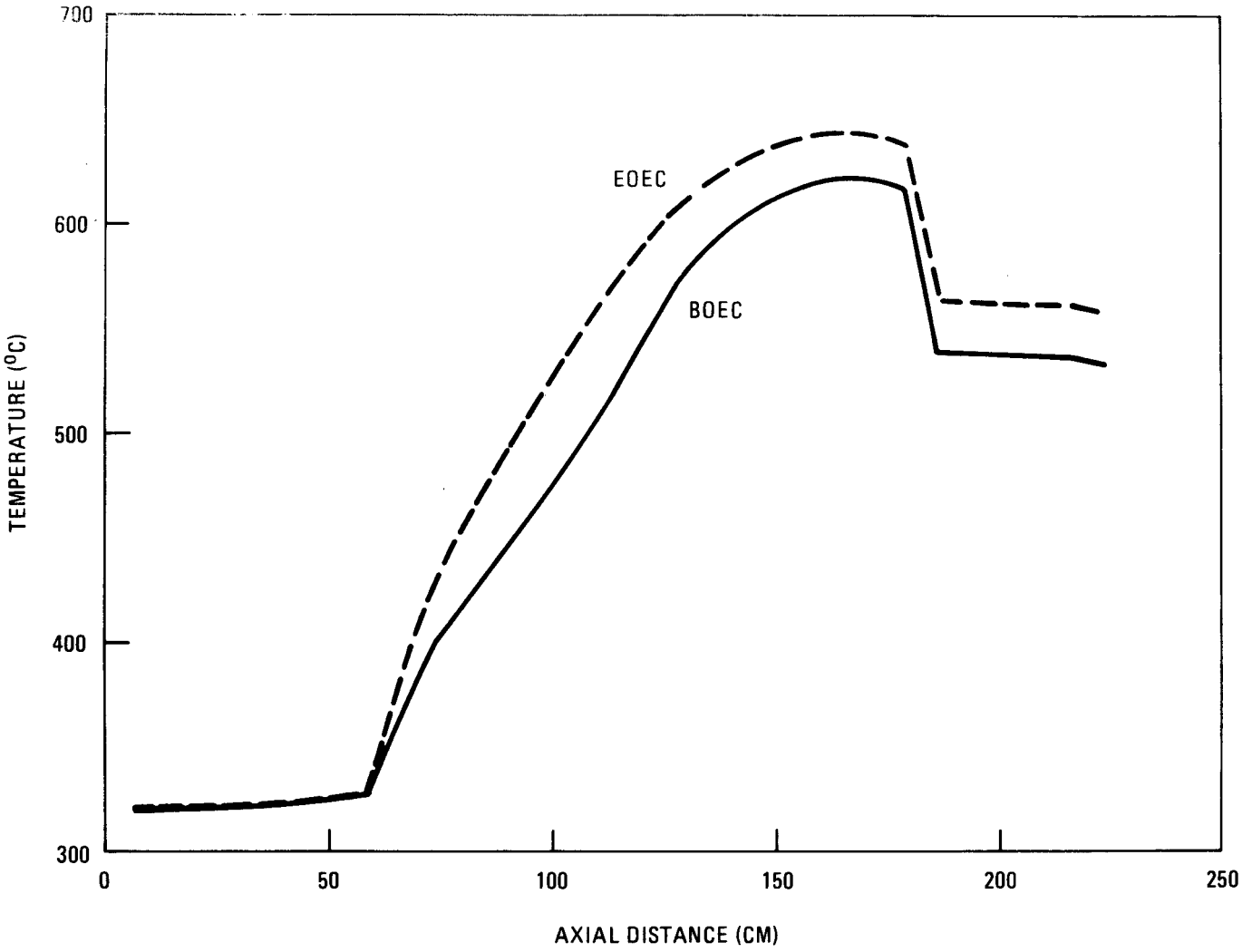

Fig. 2-40. Control assembly rod temperatures

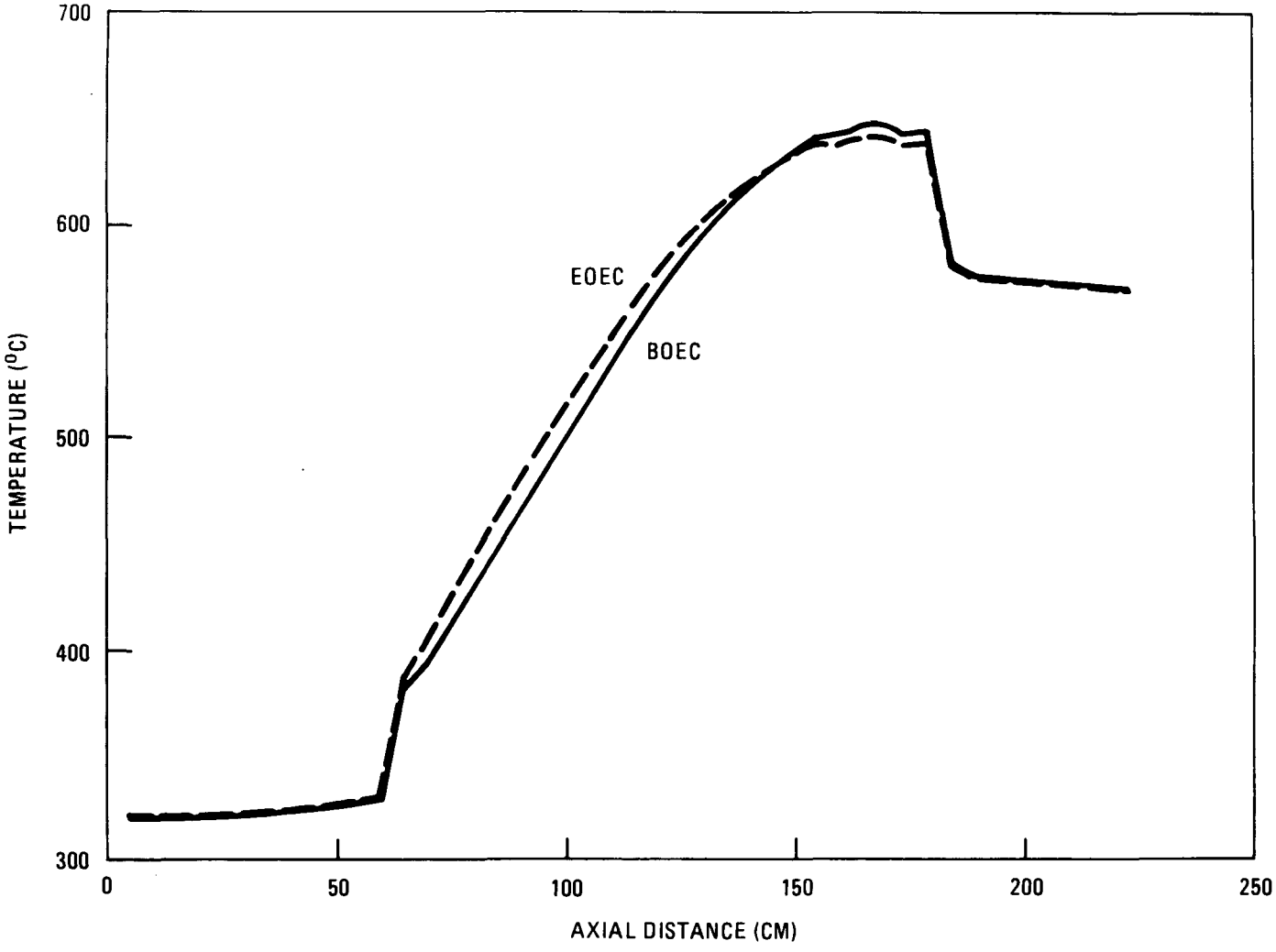

Fig. 2-41. Fuel assembly rod temperatures

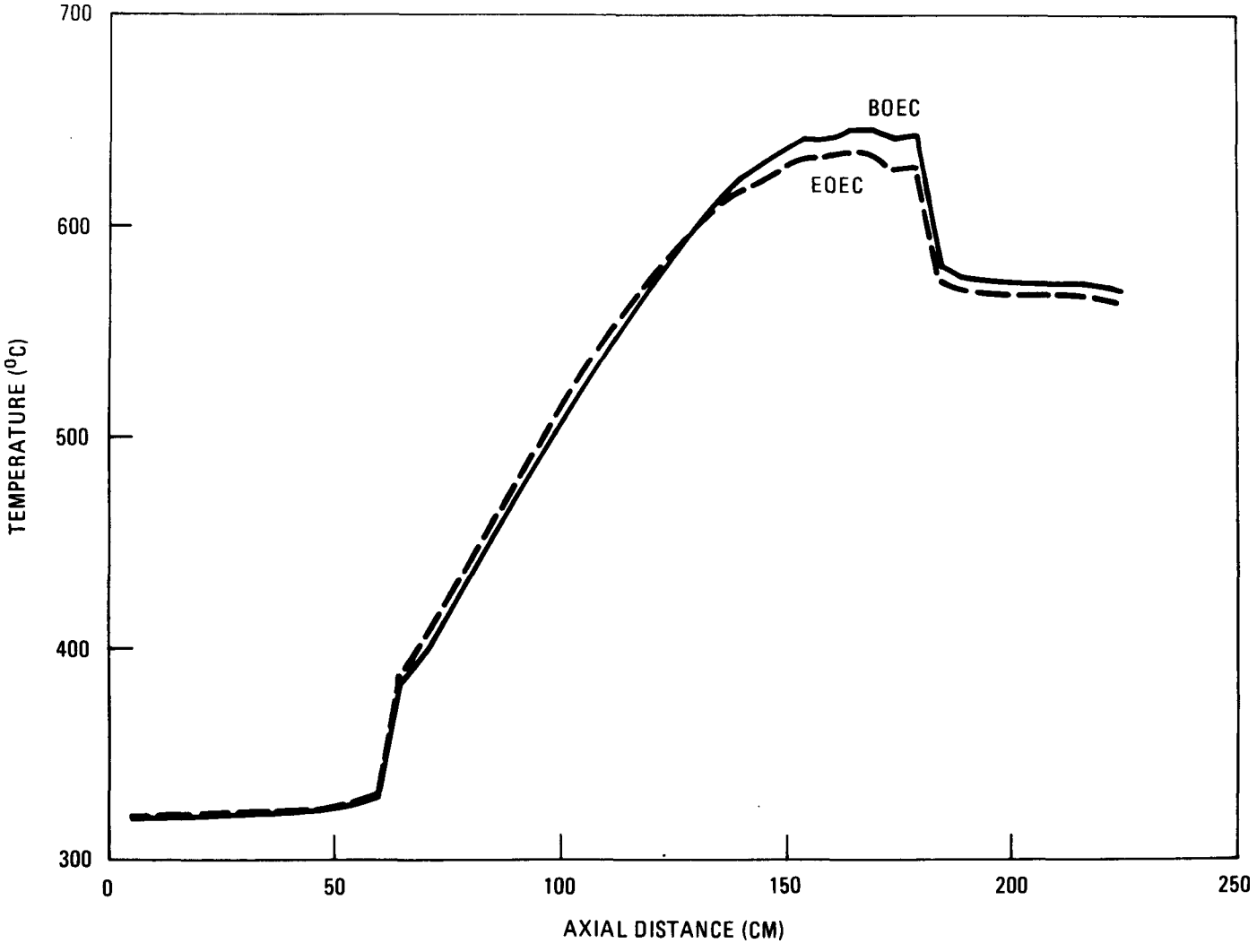

Fig. 2-42. Row 2 fuel assembly rod temperatures

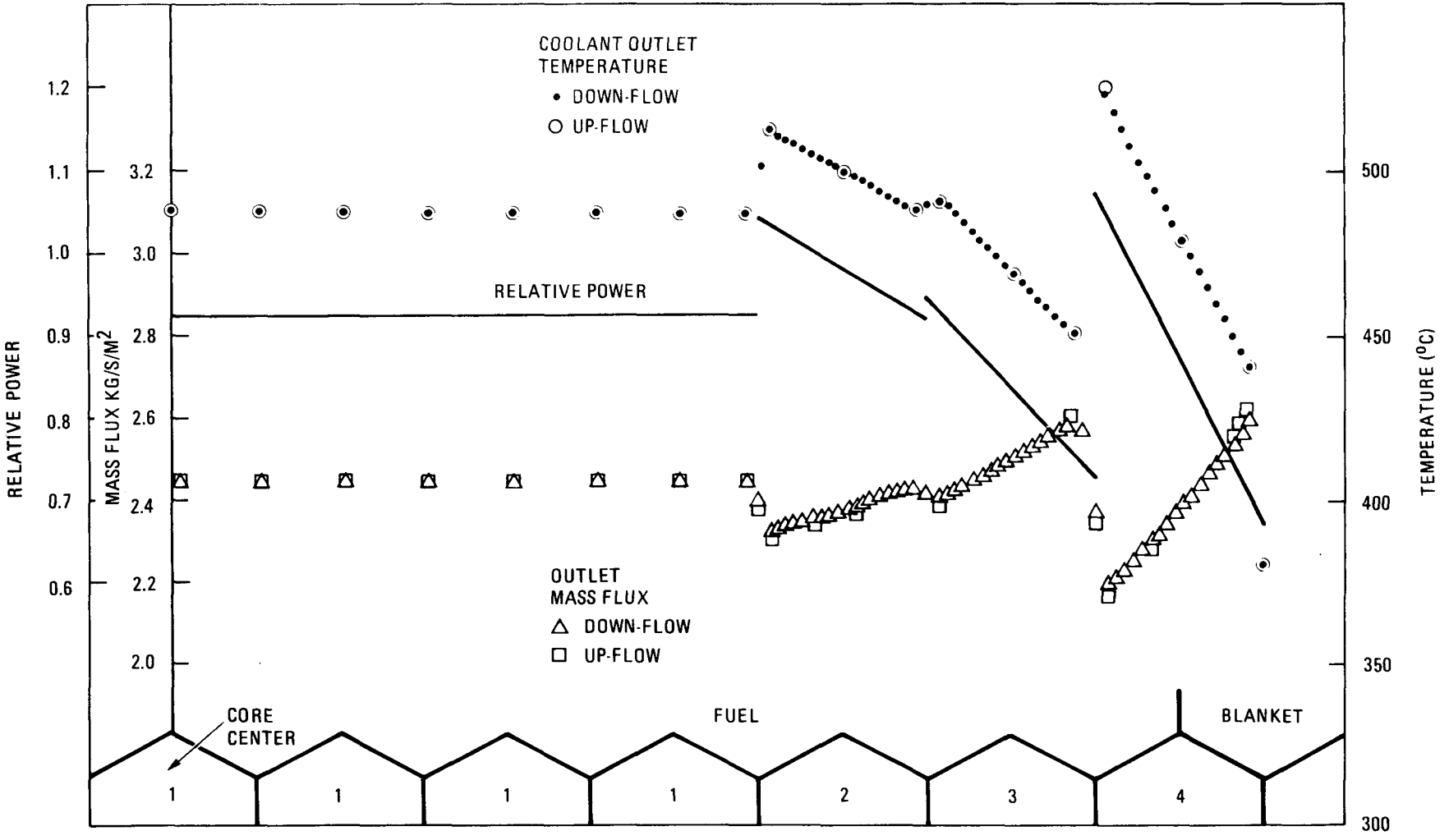

Fig. 2-43. Exit coolant conditions for a ductless core at low flows

TABLE 2-33
DEPRESSURIZED CORE AVERAGE MASS FLUX 2.44 kg/s/m^2

Assembly No.	Max/Min Ratio		Exit Mass Flux (kg/s/m^2)			% Deviation from Core Average
	Power	Flow	Min at Hot End	Max at Cold End	Average	
1	1.000	1.000	2.459	2.459	2.459	0.78
2	1.128	1.048	2.315	2.425	2.375	-2.66
3	1.299	1.083	2.398	2.596	2.494	2.21
4	1.608	1.401	2.172	3.042	2.420	-0.82

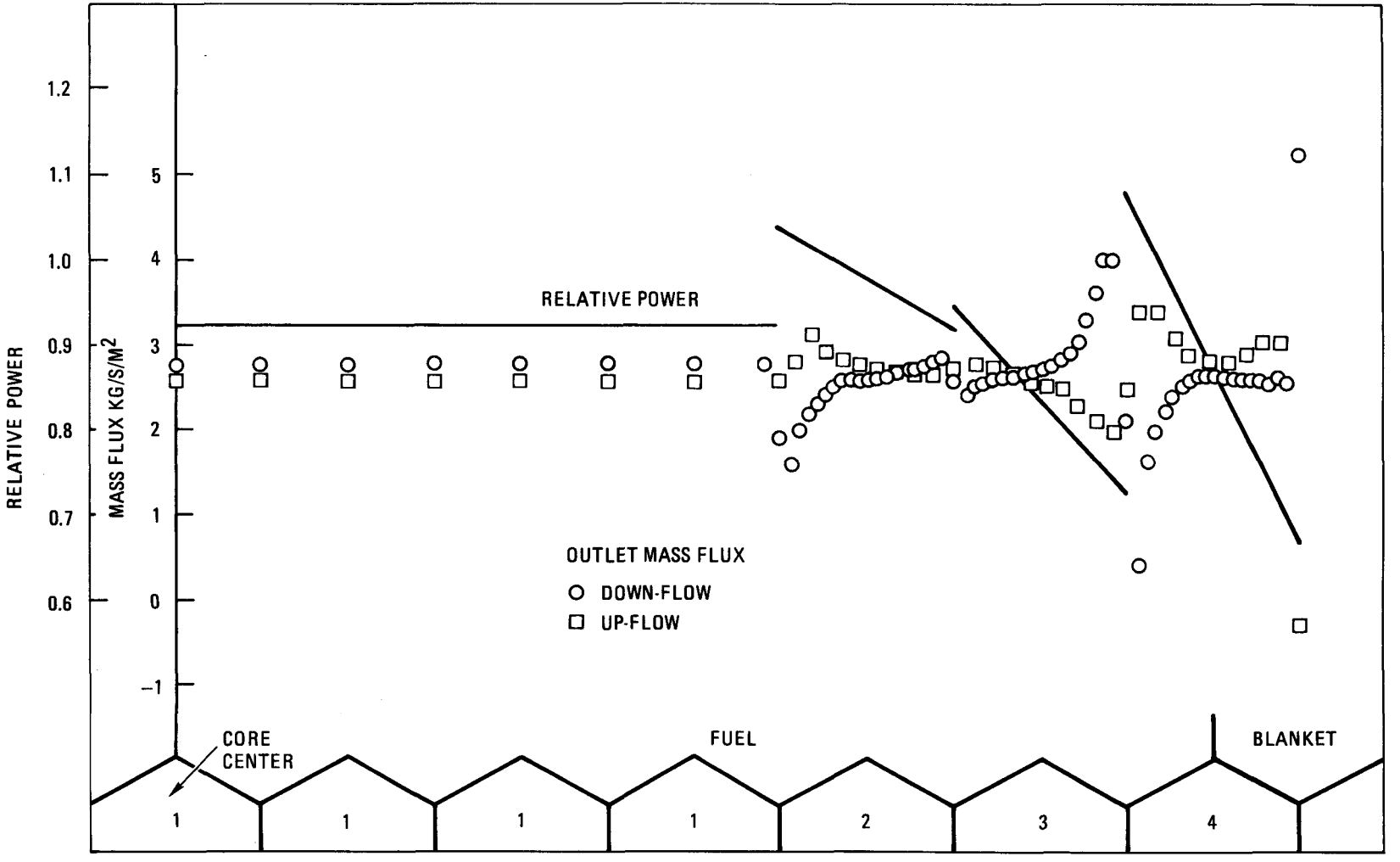

Fig. 2-44. Exit coolant conditions for a ductless core at low flows (pressurized reactor)

TABLE 2-34
PRESSURIZED DOWN-FLOW CORE AVERAGE MASS FLUX 2.70 kg/s/m^2

Assembly No.	Max/Min Ratio		Exit Mass Flux (kg/s/m^2)			% Deviation from Core Average
	Power	Flow	Min at Hot End	Max at Cold End	Average	
1	1.000	1.000	2.816	2.816	2.816	4.14
2	1.128	1.428	1.967	2.808	2.539	-6.10
3	1.299	1.649	2.464	4.064	2.920	8.00
4	1.608	3.107	1.692	5.257	2.527	-6.54

TABLE 2-35
PRESSURIZED UP-FLOW CORE AVERAGE MASS FLUX 2.70 kg/s/m^2

Assembly No.	Max/Min Ratio		Exit Mass Flux (kg/s/m^2)			% Deviation from Core Average
	Power	Flow	Min at Hot End	Max at Cold End	Average	
1	1.000	1.000	2.655	2.655	2.655	-0.19
2	1.128	1.151	2.696	3.102	2.826	6.24
3	1.299	1.401	2.024	2.835	2.566	-3.91
4	1.608	-13.97[a]	-0.252[a]	3.521	2.641	-0.71

[a] Flow reversal.

Since the implicit solution scheme in COBRA-IV cannot accurately handle flow reversals, this is just an indication that the margin to flow stagnation for this ductless core is small. The same zone was analyzed for a ducted assembly of the pressurized GCFR. Figures 4-45 and 4-46 show the exit flow and temperature conditions. From the flow distribution for 1% power and flow conditions, it is clear that there is a large margin before stagnation can occur in the up-flow or the down-flow assembly.

2.2.3.2. Integral Core Performance of Large Plants. Core studies were conducted for large GCFR plants [3600 MW(t)] to evaluate the effect of coolant pumping power requirements on core design and performance. In particular, the study objective was to explore low power density cores and the feasibility of pumping power reductions to about 10 MW per circulator. The results are documented in Ref. 2-60. The conclusion is that circulators with a power of 10 MW do not support competitive GCFR core designs at a system pressure of 9 MPa; however, circulator power requirements ranging from 15 MW to 22 MW per circulator would be sufficient to yield GCFR core designs and performances that are comparable to those of advanced oxide-fueled LMFBRs.

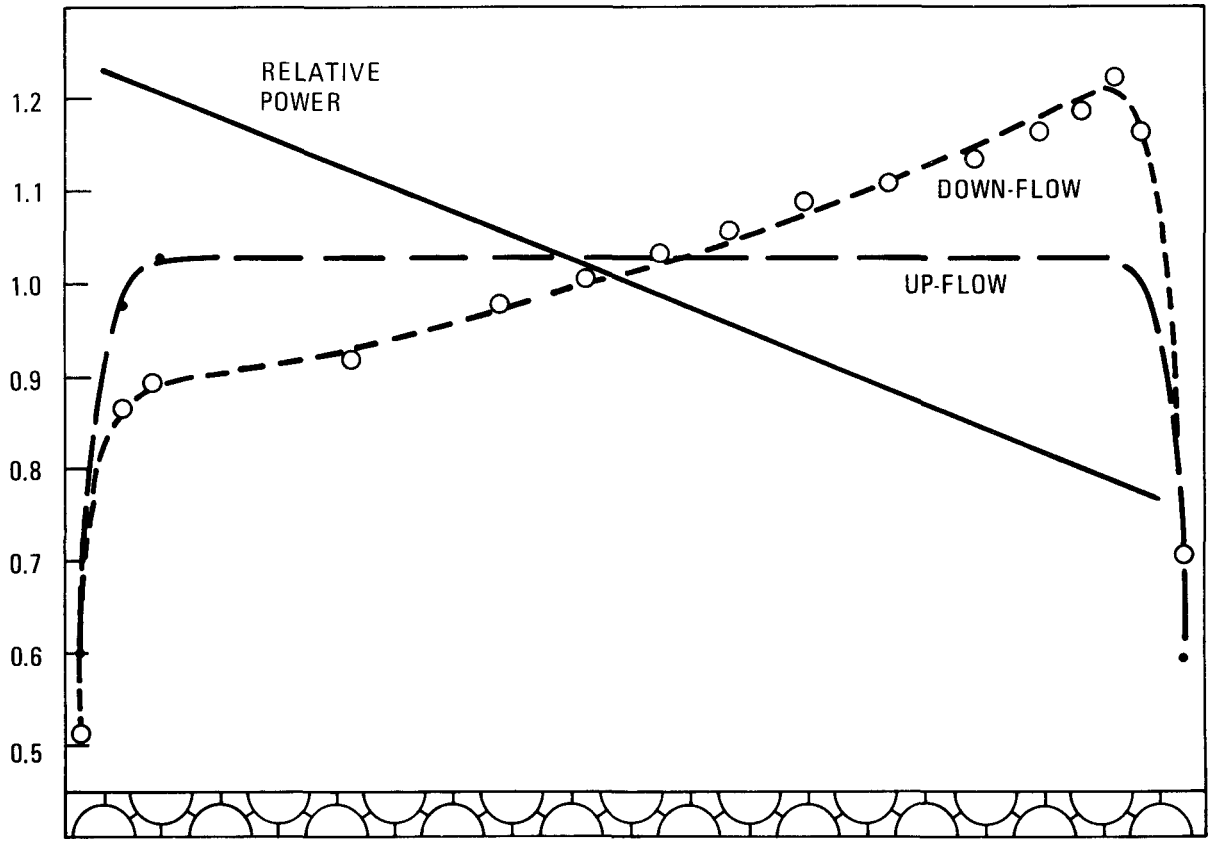

Fig. 2-45. Relative coolant mass flux at exit for GCFR fuel assembly (1% power + flow)

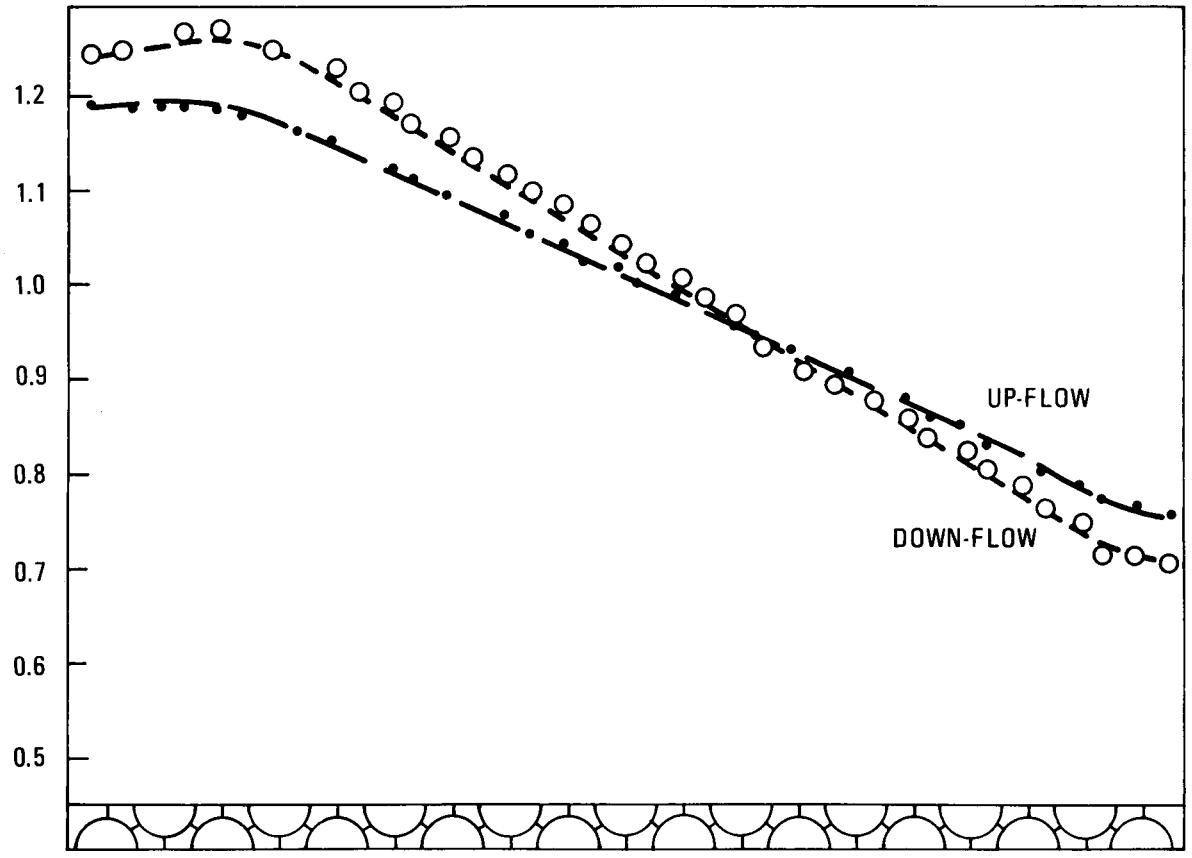

Fig. 2-46. Relative coolant temperature rise for GCFR fuel assembly (1% power + flow)

2.3. FUEL ASSEMBLY DESIGN AND ANALYSIS

2.3.1. Fabrication Development

2.3.1.1. Resource Evaluation and Control System. Some revisions were made to the input on GCFR core assembly fabrication development to the resource evaluation and control system (RECS). The input revisions are concerned with simplification and with the changes made in the work breakdown structure for (1) fabrication development of core assembly components and assemblies and (2) core manufacturing.

2.3.1.2. Rhombic Grid Spacers. Cold-rolled 316 stainless steel strips of a special thickness required for this design and tooling for stamping the grid spacer parts are being fabricated. The strip was received in the latter part of March 1979; the tooling is scheduled for completion in August 1979.

Welding trials on the thin stainless strip will be performed at GA and at Dimetrics, while the die tooling is being finished. To minimize distortion problems during assembly, several welding methods are being evaluated: standard TIG, pulsed high-frequency TIG, and pulsed laser welding.

2.3.1.3. Related Experience in Fabrication of Components

Duct Melting and Fall-Away Test Core Assembly Fabrication

Experience with fabrication of full-size GCFR core assembly components for the duct melting and fall-away test (DMFT) at Los Alamos Scientific Laboratory (LASL) is expected to be of value for achieving GCFR core assembly fabrication development objectives. As reported previously (Ref. 2-61), 20% cold-worked 316 stainless steel tubing has been received for use as DMFT cladding. Source inspection indicates that the tubing met all dimensional requirements. A chemistry analysis overcheck for composition and room temperature tensile tests showed the material to meet ASTM A269 requirements. Metallography showed that the ASTM grain size was 7 to 9

and the material was free of boundary carbide precipitates. Tubing has also been received for the DMFT grid skeleton assembly hanger and axial spacer tubes, and chemistry overcheck shows these tubes also meet ASTM A269 requirements.

Five spacer grids for the DMFT were fabricated from type 316 stainless steel plate by wire electrical discharge machining. These grids are of the modified hex design. Inspection of the grid spacers will be completed as soon as fixturing to hold the spacers in an automated optical measuring device becomes available. Results of the measurements to date indicate that except for some minor distortions from relaxation of stresses in the material during fabrication, affecting some cell locations, the grid spacer dimensions are within the specified tolerances.

Two hexagonal full-sized GCFR ducts of 20% cold-worked 316 stainless steel have been ordered and will be fabricated by drawing the material over a hexagonal mandrel to ensure close-tolerance finished dimensions.

CFTL Fabrication Support

A revised specification for CFTL fuel rod simulator cladding, based on ANSI/ASTM A213 76a, was issued to reflect technical considerations by GCFR and vendor capabilities. The starting material for this tubing is to be bar stock meeting RTD M7-23T requirements which will be gun drilled and o.d. ground to ensure concentricity, prior to drawing into 7.46-mm-o.d., 6.44-mm-i.d. tubing. One hundred pieces of the tubing, each 2420 mm in length, have been ordered for use as cladding for the CFTL AG-1 bundle. The FRS cladding tubes need to be ribbed over a length of 1150 mm, and work has been initiated to qualify a local vendor to perform the ribbing.

2.7. RADIAL SHIELD ASSEMBLY DESIGN AND ANALYSIS

The thermal analysis for both the concepts outlined is carried out at the end of life (EOL), when the shielding assembly is generating its maximum power. In an ideal design, there is expected to be a maximum of 2% radial shrinkage of the boronated graphite (B_4C), with the volume going back to its initial value at EOL. For this analysis, the maximum shrinkage is assumed at EOL (giving maximum cladding to B_4C gaps). The restriction on using B_4C is that the maximum temperatures should be about 700°C. The higher the B_4C temperature, the earlier in life it goes from shrinking to rapid swelling.

For the block assembly preliminary analysis, a section through the midplane (Fig. 2-47) was used with the TAC-2D code. The coolant was assumed uniformly distributed in the seven channels and at the same temperature. (Actual coolant temperatures would result in a higher gradient across the block than predicted by this analysis.) Figure 2-48 is the temperature map of the section. Although the maximum temperature is limited to 716°C, the temperature drop from one side of the duct wall to the other (due to the power gradient) is large (180°C) and cannot be eliminated easily in the design with segregated coolant passages. It is possible to reduce this gradient somewhat by adding a coolant passage between the two stainless steel duct walls. Positioning of the two ducts by pads similar to a wire wrap would further reduce this gradient by allowing the coolant to move from one side of the duct to the other.

The wire-wrapped assembly was analyzed using COBRA-IV (Ref. 2-27) assuming that all the wires started in the same azimuthal position. The maximum B_4C temperatures resulting from a coolant flow rate of 96 kg/hr is shown in Fig. 2-49. Since the heat transfer coefficient is small (the flow regime is laminar), circumferential conducting is dominant. The maximum temperature drop across any rod is less than 10°C.

The power produced in the shielding assemblies is small ($\sim$0.014 MW/assembly) and the coolant flow is in the laminar regime. At low powers, the

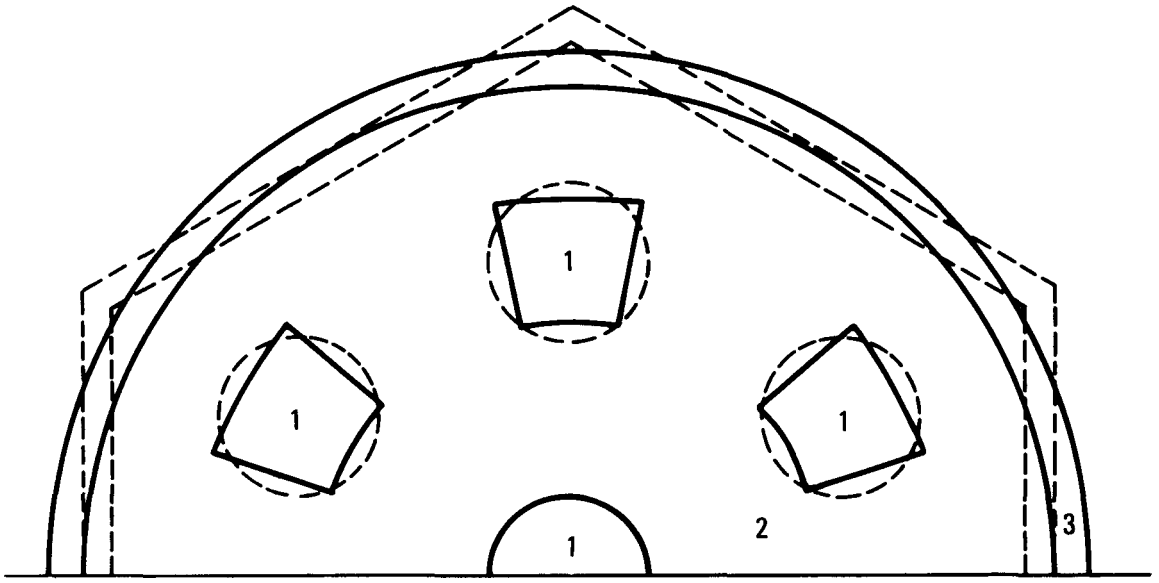

1. COOLANT PASSAGES
2. BORONALED GRAPHITE
3. 316 SS

Fig. 2-47. Section through radial reflector assembly (TAC-2D model)

TEMPERATURES (C)

THE RADIAL(I) DIRECTION IS HORIZONTAL
THE THETA (J) DIRECTION IS VERTICAL

32	C	-18	-18	-18	-18	-18	-18	-18	-18	-18	-18	-18	-18	-18	-18	-18	C
31	449	556	569	579	588	596	604	616	636	659	681	693	700	710	716	713	713	-18
30	449	556	569	579	586	593	600	611	630	651	674	686	695	705	712	711	711	-18
29	449	556	568	577	584	589	593	601	617	637	660	674	684	696	705	707	707	-18
28	449	555	567	576	581	583	584	588	600	617	638	658	671	685	696	703	703	-18
27	449	554	566	573	575	573	564	449	449	449	449	630	647	666	680	694	694	-18
26	449	551	563	569	571	567	558	449	449	449	449	617	634	652	666	682	682	-18
25	449	550	560	567	570	570	568	564	571	584	604	624	637	652	663	675	675	-18
24	449	548	559	566	570	572	572	574	584	599	618	632	641	652	661	671	671	-18
23	449	547	557	564	569	572	575	580	592	608	625	636	643	652	659	665	665	-18
22	449	545	556	563	568	572	576	582	595	610	626	635	641	648	654	659	659	-18
21	449	543	554	560	565	570	574	581	593	607	622	630	635	642	647	652	652	-18
20	449	542	552	558	562	566	569	575	586	599	613	621	626	632	638	644	644	-18
19	449	540	549	555	558	561	562	566	575	586	599	607	613	620	626	635	635	-18
18	449	538	547	552	555	555	554	556	562	571	582	592	599	608	615	627	627	-18
17	449	535	543	547	548	545	537	449	449	449	449	563	574	586	595	612	612	-18
16	449	531	538	541	541	536	528	449	449	449	449	547	556	567	576	592	592	-18
15	449	528	535	538	538	535	530	522	522	526	536	547	555	563	570	583	583	-18
14	449	527	534	536	537	535	532	528	529	534	544	551	556	562	567	578	578	-18
13	449	525	532	535	535	534	533	531	534	539	547	552	556	560	564	573	573	-18
12	449	524	530	533	534	533	532	532	535	541	547	552	554	558	561	569	569	-18
11	449	522	528	531	532	531	531	531	534	539	545	549	551	554	557	564	564	-18
10	449	521	527	529	530	529	528	528	530	534	540	544	546	549	552	559	559	-18
9	449	519	525	527	527	526	524	523	524	527	533	536	539	543	546	555	555	-18
8	449	518	524	526	525	523	520	516	516	518	523	528	532	537	541	551	551	-18
7	449	517	522	523	522	518	512	449	449	449	449	513	519	526	532	544	544	-18
6	449	515	520	521	519	515	509	449	449	449	449	508	514	521	526	539	539	-18
5	449	514	519	520	519	516	511	505	503	504	509	515	518	523	527	538	538	-18
4	449	514	519	520	519	516	513	509	508	511	515	519	521	525	528	537	537	-18
3	449	513	518	520	519	517	515	513	513	515	519	522	524	527	529	537	537	-18
2	449	513	518	520	519	518	516	514	515	517	521	524	525	528	530	537	537	-18
1	C	-18	-18	-18	-18	-18	-18	-18	-18	-18	-18	-18	-18	-18	-18	-18	C
	1	2	3	4	5	6	7	8	9	10	11	12	13	14	15	16	17	18

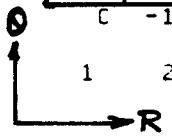

Fig. 2-48. Temperature distribution at the midsection of the radial reflector assembly

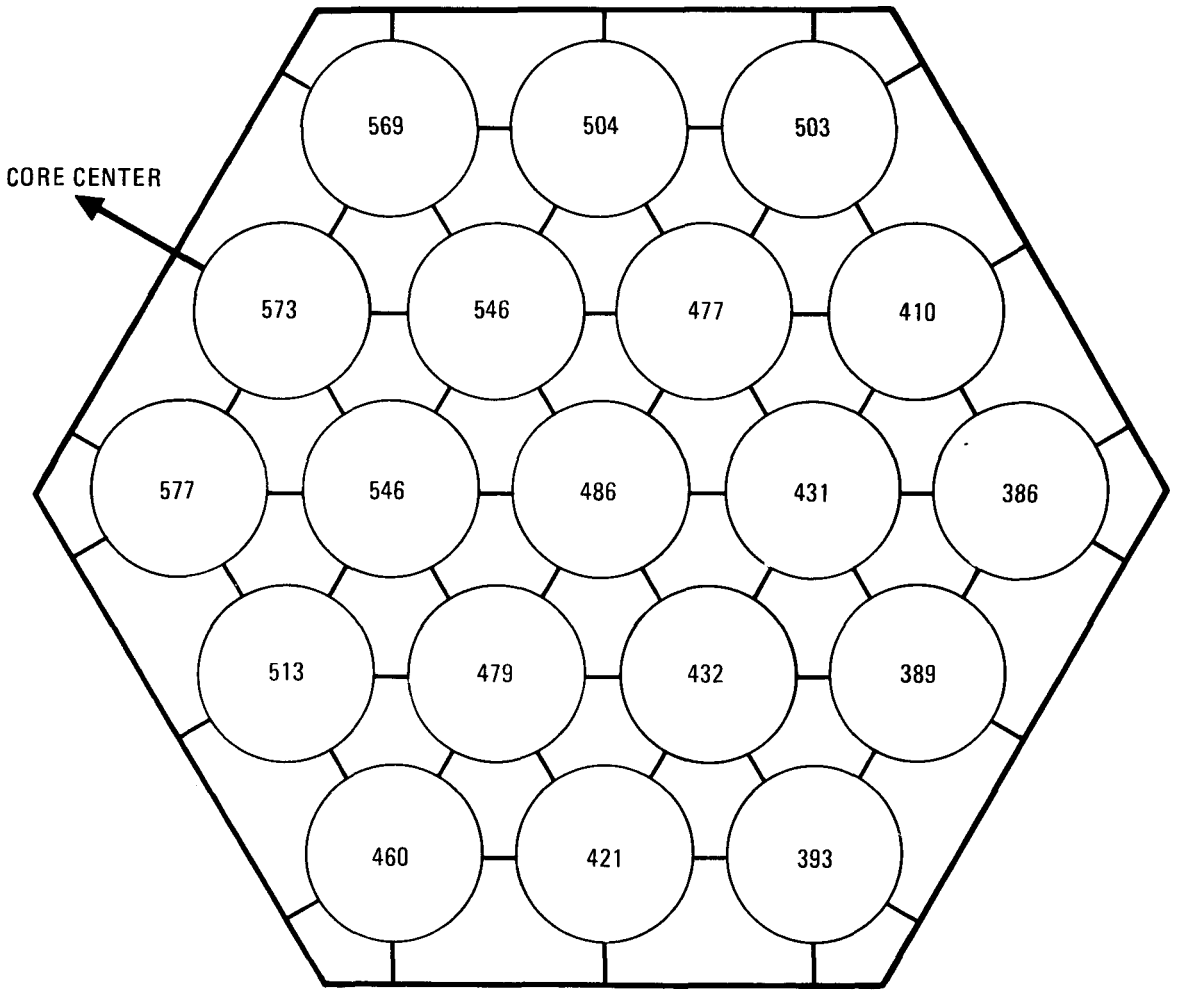

Fig. 2-49. Maximum graphite centerline temperatures (all not occurring at same axial location)

hydraulic resistance of these assemblies will increase sharply. Since the change in the resistance of the fuel assemblies is slight, providing coolant at the required proportions to different core assemblies at low powers is a problem. A possible solution is to overcool these assemblies at full power. Increasing the flow to 10 times the required amount makes the coolant flow turbulent, and the core outlet temperature deterioration is less than 10°C. Together with this increase in flow, a control device can be installed such that the resistance of the shielding assembly changes in the same proportion as that of the rest of the core, from full flow to low flows.

REFERENCES

2-1. Billone, M. C., et al., "The LIFE-III Fuel-Element Performance Code," ERDA Report 1756, Argonne National Laboratory, July 15, 1977.

2-2. Chang, K. H., M. P. LaBar, and R. J. Campana, "Modeling of Isotopic Fission Gas Release in the GCFR Vented Fuel Rod," Proceedings, International Conference on Fast Breeder Reactor Fuel Performance, Monterey, California, March 1979, pp. 423-432.

2-3. Longest, A. W., and J. A. Conlin, "Results from Irradiation of Vented GCFR Fuel Rods in the GB-9 and GB-10 Capsule Experiments," Oak Ridge National Laboratory Report ORNL-5259, September 1978, Appendix B.

2-4. Jadhav, K. B., and B. W. Roos, "SLIDER, A Fortran V Program for the Computation of the Release of Fission Products from One-Dimensional Multilayered Fuel Configurations," USAEC Report GA-8566, Gulf General Atomic Company, 1969.

2-5. Krug, W., et al., "Testing of GCFR Fuel Assemblies in the BR-2 He-Loop-Mol," Trans. Am. Nucl. Soc. 28, 220 (1978) and accompanying handout.

2-6. Jung, W., and W. Krug, "Gas-Cooled Fast Breeder Reactor Fuel Bundle Irradiations in the BR-2 Helium Loop," Nucl. Eng. Design 40, No. 1, 157-170 (1977).

2-7. Norman, J. H., et al., "Spheres: Diffusion-Controlled Fission Product Release and Absorption," Advances in Chemistry Series 93, 13 (1970).

2-8. Campana, R. J., et al., "Interdiffusion of Krypton and Xenon in High Pressure Helium," International Symposium on Thermodynamics of Nuclear Materials, IAEA-SM-236/65, February 1979.

2.9. Baxi, C. B., C. J. Burhop, and F. O. Bennet, "COBRA*GCFR, A Computer Code for Thermal-Hydraulic Analysis of GCFR Fuel Assembly," Trans. ANS 29, 743-5 (1978).

2.10. Dalle Donne, M., et al., "BR2 Bundle Mockup Heat Transfer Experiments," Nucl. Eng. Design 40, No. 1, 143-156 (1977).

2.11. Bolch, W. E., R. E. Selleck, and J. Kaufman, "Gas Dispersion in Porous Media Peclet-Reynolds Number Correlations," USAEC Report SERL 67-10, Sanitary Engineering Research Laboratory, University of California, Berkeley, 1967.

2-12. Strong, W. R., and H. C. Hopkins, "Core Assembly Helium Flow Test Program Plan," General Atomic unpublished data, September 14, 1978.

2-13. "Gas Cooled Fast Breeder Reactor Quarterly Progress Report for the Period August 1, 1978 through October 31, 1978," DOE Report GA-A15144, General Atomic Company, November 1978.

2-14. Hopkins, H. C., Jr., "Program Plan for GCFR Core Flow Test Loop," USAEC Report GA-A13080, General Atomic Company, August 9, 1974.

2-15. Hopkins, H. C., Jr., "TSPEC - A Computer Program to Predict Approximate Model Performance in the Core Flow Test Loop," ERDA Report GA-A14057, General Atomic Company, November 1976.

2-16. Flynn, P. W., "Specification for Cladding for the Core Flow Test Loop (CFTL) First Bundle AG-1," Document No. 903944, General Atomic unpublished data, February 23, 1979.

2-17. "Core Element Development Program Plan for the Gas-Cooled Fast Breeder Reactor Demonstration Plant," ERDA Report GA-A13312, General Atomic Company, May 6, 1975.

2-18. Snyder, H. J., "Fuel, Material and Core Component Work Statement," General Atomic unpublished data, June 3, 1977.

2-19. "GT-HTGR Program Semiannual Progress Report for the Period Ending June 30, 1976," ERDA Report GA-A13950, General Atomic Company, July 1976.

2-20. Lund, K. D., and C. J. Burhop, "SINDA/PES: A Transient Flow Network Code," DOE Report GA-A15220, General Atomic Company, to be published.

2-21. Johnson, J. J., "MODSAP, A Modified Version of the Structural Analysis Program SAP IV for the Static and Dynamic Response of Linear and Localized Nonlinear Structures," DOE Report GA-A14006 (Rev.), General Atomic Company, June 1978.

2-22. Sutherland, W. H., and V. B. Watwood, Jr., "Creep Analysis of Statically Indeterminate Beams," Batelle Northwest Laboratory Report BNWL-1362, June 1970.

2-23. Timoshenko, S. P., and J. N. Goodier, Theory of Elasticity, McGraw Hill, New York, 1970.

2-24. Lee, G. E., "Structural Functional Criteria for CFTL AG1 Spacer Grids," General Atomic unpublished data, February 27, 1979.

2-25. "Structural Design Criteria, Structural Design Guideline for FBR Core Components," RDT F9-7, August 1978.

2-26. ASME Boiler and Pressure Vessel Code, Section III.

2-27. Wheeler, C. L., et al., "COBRA-IV-1: An Interim Version of COBRA for Thermal-Hydraulic Analysis of Rod Bundle Nuclear Fuel Elements and Cores," Battelle Northwest Laboratory Report BNWL-1962, 1976.

2-28. Barroyer, P., M. Hudina, and M. Huggenberger, "Benchmark Calculation III/Summary of Results," Institut fur Reakorforschung, EIR Report No. AN-IN-720, 1978.

2-29. Carnaham, B., H. A. Luther, and J. O. Wilkes, Applied Numerical Methods, John Wiley & Sons, Inc., New York, 1969.

2-30. Peaceman, D. W., and H. H. Rachford, Jr., "The Numerical Solution of Parabolic and Elliptic Differential Equations," J. Soc. Indust. Appl. Math. 3, 28-41 (1955).

2-31. Clark, S. S., and J. F. Peterson, "TAC-2D, General Purpose Two-Dimensional Heat Transfer Computer Code," USAEC Report GA-9262, Gulf General Atomic, September 1969.

2-32. Peterson, J. F., "TAC3D, A General Purpose Three-Dimensional Heat Transfer Computer Code," USAEC Report GA-9236, Gulf General Atomic Company, September 1969.

2-33. Thompson, W. I., "CALIOP--A Multichannel Design Code for Gas-Cooled Fast Reactors," General Atomic unpublished data.

2-34. Lathrop, K. D., "DTF-IV, a FORTRAN-IV Program for Solving the Multigroup Transport Equation with Anisotropic Scattering," Los Alamos Scientific Laboratory Report LA-3373, 1965.

2-35. Rhoades, W. A., et al., "The DOT IV Two-Dimensional Discrete-Ordinates Transport Code with Space-Dependent Mesh and Quadrature," Oak Ridge National Laboratory Report ORNL/TM-6529, 1978.

2-36. Barbucci, P., and F. di Pasquantonio, "Exponential Supplementary Equation for S_n Methods: The One-Dimensional Case," Nucl. Sci. Eng. 63, 179-187 (1977).

2-37. Engle, W. W., Jr., "ANISN, A One-Dimensional Discrete Ordinates Transport Code With Anisotropic Scattering," K-1693, Oak Ridge National Laboratory, March 1967.

2-38. Lathrop, K. D., and F. W. Brinkely, Jr., "Theory and Use of the General Geometry TWOTRAN Program," Los Alamos Scientific Laboratory Report LA-4432, 1970 (see also LA-4848-MS, 1973).

2-39. Perkins, R. G., and C. A. Rouse, "Preliminary Considerations for Design of Grid-Plate-Supported Inner Radial Reflector/Shield Assemblies," General Atomic unpublished data.

2-40. Perkins, R. G., and J. Hom, "Sensitivity of Boronated Radial Shielding Response Values to Group Structure and Quadrature," General Atomic unpublished data.

2-41. Rucker, R. A., "GCFR Demo Radial Blanket Management," General Atomic unpublished data.

2-42. Perkins, R. G., "Sensitivity of Radial Shielding to Blanket Shuffling Scheme," General Atomic unpublished data.

2-43. Perkins, R. G., "Irradiation Effects to Out-of-Core Structural Components," General Atomic unpublished data, November 1977.

2-44. Perkins, R. G., "Proposed Out-of-Core Component Exposure Criteria for GCFR Based on LMFBR Criteria," General Atomic unpublished data.

2-45. Price, R. J., Beavan, L. A., and G. B. Engle, "Graphite and Boronated Graphite Assessment for GCFR Design," General Atomic unpublished data.

2-46. Moen, R. A., et al., "Neutron Fluence Limit Determinations for Some Fast Flux Test Facility Components," Iradiation Effects on Structural Alloys for Nuclear Reactor Applications, STP 484, ASTM, 1970.

2-47. "National Program Plan - Irradiation Effects on the Mechanical Properties of LMFBR Structural Materials," TC-810, Hanford Engineering Development Laboratory, March 1, 1977.

2-48. Perkins, R. G., "EBR-II Irradiation in Support of GCFR Materials Data Requirements," General Atomic unpublished data.

2-49. Rosenwasser, S. N., and R. G. Perkins, "National Coordination Meeting on Irradiation Effects on Breeder Reactor Structural Materials," General Atomic unpublished data.

2-50. Rosenwasser, S., General Atomic unpublished data.

2-51. Goel, B., "Importance and Status of (n,α) Cross Sections for a Reliable Prediction of Radiation Damage in Stainless Steel," EURFNR-1465, KFK (Germany), June 1977.

2-52. Rucker, R. A., and R. G. Perkins, "Decay Heating of Radial Blanket Fuel Rods Including Gamma Transport," General Atomic unpublished data.

2-53. "Gas Cooled Fast Breeder Reactor, Quarterly Progress Report for the Period November 1, 1978 through January 31, 1979," DOE Report GA-A15237, General Atomic Company, February 1979, Section 7.

2-54. Simnad, M. T., "Shielding and Control Materials for the Gas Cooled Fast Breeder Reactor," DOE Report GA-A14478, General Atomic Company, December 1977.

2-55. Mathews, D. R., et al., "GGC-5, A Computer Program for Calculating Neutron Spectra and Group Constants," Gulf General Atomic Report GA-8871, September 27, 1971.

2-56. Little, W. W., Jr., and R. W. Hardie, "2DB, A Two-Dimensional Diffusion-Burnup Code for Fast Reactor Analysis," USAEC Report BNWL-640, Battelle Northwest Laboratory, January 1968.

2-57. Joseph, W. M., "SCORIA Editing Routine SCORED," General Atomic unpublished data, March 1979.

2-58. Tang, I. M., "Effect of Control Rod Insertion on Power Tilting," General Atomic unpublished data, 1978.

2-59. Rao, S. B., "Flow Redistribution in a Ductless Core," General Atomic unpublished data, December 1, 1978.

2-60. Macken, T., et al., "Preliminary Evaluation of the Effect of Varying Helium Circulator Pumping Power on the Design and Performance of a Large GCFR," DOE Report GA-A15311, General Atomic Company, March 1969.

3.0. PROJECT SUPPORT

3.3. SYSTEMS ENGINEERING

3.3.1. Systems Integration

A Change Request covering licensing criteria for GCFR core disruptive accidents was approved through the resource organizations and transmitted to the project office for approval.

The overall GCFR planning effort--resources evaluation and control system (RECS) implementation--is progressing. The hand-drawn system-level logic networks which show time span and estimated costs were completed and are being computerized. The resulting computer-produced drawings are being reviewed, modified, and interfaced to overall milestones. The next phase of the implementation program, which involves modification of networks to reflect changes in design and the generation of more detailed networks for FY-80 and FY-81, was initiated.

Definitions of conceptual, preliminary, and final design and other major NSSS and reactor core milestones were provided. Efforts are under way to plan and schedule the work required to set commercial and demonstration plant parameters and to resolve major areas of concern regarding the feasibility/desirability of a two-loop, 400-MW(e) demonstration plant.

3.3.2. Systems Design (NSSS)

3.3.2.1. Up-Flow/Down-Flow Studies

General Status

The up-flow versus down-flow study is nearing its conclusion. Most of the design and analytical work has been completed. The down-flow design was changed considerably, and the up-flow design was modified to incorporate the latest GA/KWU design convergence features.

A detailed evaluation of about 40 design elements was reviewed by the Technical Management Committee in discussions with cognizant Resources personnel. The expected impact on engineering schedule and cost of a change in core flow direction from down-flow to up-flow has been assessed. A cost trend study of the two concepts has also been carried out to evaluate capital cost differences between the two.

The judgment of the Technical Management Committee is that the advantages of up-flow are sufficient to select an up-flow core. The following are the major factors favoring this recommendation:

1. Natural circulation core cooling has clear licensing advantages based on pressurized cool-down reliability and diversity.

2. Refueling appears inherently better in up-flow with either a rotating plug or fixed plug.

3. Plant capital cost disadvantages with up-flow may diminish or become gains if horizontal circulators are adopted.

4. Core disruptive accident (CDA) mitigation schemes (in core) were evaluated for both core flow directions with inconclusive results. Mitigation of CDAs at the containment systems level may provide a more practical approach.

Major factors against an up-flow recommendation are the expected increase in design and development costs and a small front-end schedule delay. Plant capital costs have also increased but are considered acceptable.

During the up-flow versus down-flow investigation, the potential for improvements in the current up-flow reference conceptual design was recognized. Concomitant with its up-flow recommendation, the Technical Management Committee suggested follow-on activities in this area. Some of the major items would be the evaluation of a horizontal main helium circulator and the substitution of a fixed core cavity plug for the rotating plug. There is also the possibility of flooding the reactor cavity for major maintenance. The advantage of having the capability of doing major maintenance in a manner similar to that for light-water reactors has been clearly recognized; however, to develop such a capability would require a major design effort.

The following is a summary of major design work completed in conjunction with the up-flow versus down-flow study. The down-flow core design was substantially modified. Additional removable shielding elements were required by Clinch River Breeder Reactor dose criteria at elevated temperatures. A core lateral restraint was added above the plane of the top of the active core in an attempt to reduce grid plate and core element seismic loads while retaining individual duct fall-away as a means to mitigate CDAs. Additional removable shielding elements were required to protect this structure. Removable radial shielding elements were placed in the lower plenum to limit radiation damage to the permanent lower shield. Loop layouts were changed to accommodate an electric drive main circulator and a bayonet tube CAHE. The core cavity closure plug was recessed to accept toggle hold-down loads directly into prestressed concrete, as required for the commercial-size plants. The size of the in-vessel molten fuel containment system was revised. Revised PCRV and containment arrangements incorporating these changes were completed. The refueling scheme was evaluated for scale-up and for handling of removable shielding elements. (Refueling time is a major concern for large plants.)

The up-flow design (NEU D) selected jointly with KWU in November 1978 was refined in many respects. The up-flow core element designs were refined. A design of a full-core lateral restraint system with appropriate removable shield elements was completed. Seismic and deformation analyses were completed to show that the lateral restraint was acceptable. A revised, recessed, dual rotating plug with toggle hold-down against prestressed concrete was designed. Plug penetration service connections were sized and congestion problems identified. A control rod guide tube scheme to eliminate the internal support grid structure was developed, as well as radial shielding with cross-duct shadow shields. The core support skirt design was refined to reduce thermal stresses. An in-vessel molten fuel containment system was sized. Top exit steam generator designs were successfully developed to accommodate thermal expansion/seismic stress problems, reducing a major concern in this area.

Dynamic natural circulation calculations were extended to show sensitivity to various events in the primary coolant system. The first-row blanket assemblies appear to require some changes to be compatible with available natural circulation head. Static natural circulation calculations were performed for the water and air systems. Elevations required are compatible with mounting of water-to-air coolers in the upper sections of the confinement building.

Revised PCRV and containment arrangements for the up-flow design were developed incorporating the above work. The refueling scheme was evaluated for commercial plants with acceptable results. Back-up evaluations were performed on fixed-plug and seven-element refueling schemes, and on horizontal circulators, all of which show considerable promise.

Core cooling reliability analyses indicate that for current designs, depressurized events dominate the failure probability. Since natural circulation is not adequate for the depressurized primary coolant system, up-flow does not show a large reliability advantage. However, it is likely that a depressurized CDA (during refueling or maintenance not including a

DBDA) has lower consequences than a pressurized CDA. Also, much more time for operator action is available. For pressurized conditions, natural circulation significantly enhances core cooling reliability. Also, natural circulation provides inherent diversity in cooling, which enhances plant licensability.

Systems Design Activities

The shutdown cooling system, primary coolant system helium flow conditions, and steam cycle were examined and found to have no significant differences between up-flow and down-flow designs.

Availability was compared; the availability evaluation considered planned outages (refueling, turbine overhaul, etc.) and unplanned outages (equipment failure). In evaluating planned outages, refueling and maintenance/in-service inspection (ISI) were shown to be advantages for up-flow. Refueling times were about 6 to 9 days/year shorter for the up-flow demonstration plant, and ISI about 1 day/year shorter. Unplanned outage of the steam generator, main helium circulator motor, and compressor showed that the down-flow design has about 18-1/2 hr/year less outage than the up-flow demonstration plant.

Economic evaluation of these differences was done using a replacement power cost of 20 mills/kWh and an 18% interest rate. This resulted in an advantage for the up-flow design of $5.2 to $7.7 million in equivalent capital cost. For a large plant, this advantage increased to $33.5 to $78.3 million in equivalent capital cost. Even considering the uncertainty in this conceptual estimate, availability differences are a major factor favoring up-flow. If down-flow is selected, significant improvement in refueling time is required, especially for large plants.

The CACS design with natural convection was reviewed. Up-flow and down-flow residual heat removal (RHR) both are considered feasible. Assuming both are licensable, down-flow is preferred because up-flow RHR (with

natural convection in CACS loops) has several technical problems that require additional engineering effort to remove technical uncertainties. (However, both may not be equally licensable.)

3.3.2.2. Residual Heat Removal. Results of a preliminary screening of shutdown cooling systems (SCSs) were presented to management and HBA. Data were presented showing the matrix of candidates considered, rationale for screening candidates, design information on four promising systems, and a preliminary evaluation. Two concepts were selected for detail study: concept A, in which the NSS has separate SCS circulators, heat exchanger, and water pump, and concept B, in which the NSS uses main steam generator and pony electric drive on the main helium circulator. The requirements are the same for both concepts. Means to improve these two designs will be investigated further.

Performance requirements for the concept A circulator and heat exchanger were transmitted for component sizing. Input for reliability assessments of the SCS alternates have been provided.

A preliminary evaluation of the operation of the SCS and CACS in parallel for a DBDA was completed. The results indicate that if a separate primary loop SCS (with separate SCS circulators and heat exchangers) is selected, SCS and CACS loops operating in parallel could be used for a DBDA. This concept would improve reliability under DBDA conditions (except $\leq$10 min considering common mode failure), reduce CACS circulator power (by a factor of $\sim$2), and reduce the size of the CACWS water/air heat exchanger (by a factor of $\sim$2). If an SCS using a pony drive on the main helium circulators and using the main steam generators is selected, parallel operation is not recommended.

Evaluation of the natural convection CACS gave the following preliminary results:

1. Detailed evaluation of the sizing of the CACS has not been performed to date; however, preliminary investigation indicates that natural convection mode operation will probably fix the component sizes (CAHE and auxiliary loop cooler).

2. The CAHE geometry and flow configuration will have to be carefully established to prevent CAHE water-side flow instabilities during natural circulation operation.

3. In conjunction with the Control and Electrical Branch, it has been concluded that a serious auxiliary circulator motor controller problem will exist in trying to operate at both DBDA conditions, when there is minimal natural circulation, and at pressurized conditions, when the natural circulation flow will be about 50% of the total required flow rate.

   The circulator motor must be designed to deliver full pumping power at DBDA conditions. During pressurized cool-down, it is necessary to reduce the circulator speed (helium flow) to the point where there will be no local boiling in the CAHE. For the down-flow design, where natural circulation effects are small, the low speed requirements are in the range from 6 to 10%. These requirements are at the outer edge of the controller limits. In the up-flow design, the driving head of the always-present natural circulation will reduce the required motor speed below the limits of state-of-the-art for induction motor controllers.

   One possible solution for this problem is to increase the CAHE subcooling margin, thus allowing larger gas flows. This solution, however, requires reducing the water-side hot leg temperature, which in turn reduces the water-side natural circulation head and requires the use of a large ALC.

4. Natural circulation is always available in the pressurized mode. Therefore, it is possible to have a pressurized cool-down with forced flow on one or two loops and natural circulation on the remainder of the loops. This mixed-mode operation should be evaluated. Natural circulation will be sized for two loops, each removing 50% of the heat load from a 100% power condition. It is not clear how three loops will operate, or what will be the effect of lower power level on the natural circulation cooling effectiveness.

Steam generator flow stability during RHR was investigated briefly. Using flow rates available from the back-up HTGR-type CACWS, unstable operation is predicted. Solutions are possible, such as changing the steam generator outlet location from the bottom to the top or increasing the flow rate.

The importance of steam generator ISI was identified. Potential use of the steam generator in the SCS system may require more stringent ISI than is anticipated for the HTGR. This may impact future plans for steam generator ISI development.

The ECSEL code (under development) has been modified to allow either steady-state performance or sizing analyses. The performance calculation that has been added to the code iterates on water temperatures to reach a steady-state heat balance between the helium, water, and air. This performance calculation has been used to evaluate performance of the air-blast heat exchangers for the two SCS concepts.

3.3.2.3. Steady-State Performance and Primary Coolant System. An analysis was made to compare overall plant performance for two candidate steam cycles, one incorporating steam reheat and one with no steam reheat. Two computer codes were used in the analysis: SCAP (Ref. 3-1), which was developed for analyzing the HTGR-SC plant, and COMB (Ref. 3-2), which was developed for the GCFR plant. An HTGR design of 2338 MW(t) was used as a base for the comparison.

In general, there is little difference in the thermodynamic calculations between the two codes. For the small amount of steam reheat studied, the plant efficiency between steam reheat and non-reheat cases is practically the same. For SCAP, the plant efficiencies for reheat and non-reheat are 38.48% and 38.43%, respectively. For COMB, the plant efficiencies are 38.59% and 38.62%, respectively. These differences in plant efficiency are mainly due to different steam tables used; physical components modeled, such as type of steam turbine and its extractions and the HP and LP feedwater trains; feedwater booster pump; and the deaerator.

It was concluded that SCAP has several advantages: (1) SCAP uses the 1967 ASME Steam Tables (COMB uses the older Keenan-Keyes), (2) SCAP allows more turbine types, e.g., cross compound and tandem compound, (3) SCAP allows up to four LP feedwater heaters (COMB only allows three), (4) SCAP appears to have more efficient methods for performing uncertainty analyses, resulting in less computer time and cost.

A comparison was made of the total primary circuit pressure drop for the up-flow and down-flow designs for the 300 MW(e) size plant. The helium pressure drops for the core and steam generators were determiend to be the same for both concepts (per cognizant branches). The other helium pressure drop around the loops (core inlet plenum, outlet plenum, hot duct, cold duct, etc.) was calculated to be 1.93 kPa (0.28 psi) greater for the down-flow design. The difference in overall plant efficiency was estimated to be 0.02% lower for the down-flow design.

3.3.2.4. Parametric Design Models. Development work on the parametric design program SOFAST continued. The major accomplishments during the reporting period are as follows.

Subroutines were written for sizing and costing the containment-confinement building, and for defining the main circulator design parameters. (These routines have not yet been incorporated into the main program.)

Work is in progress on integrating the steam generator sizing routines into SOFAST. The steam generator model being used consists of helical coiled tube bundles for the economizer, evaporator, and superheater. The model is similar to the one used for the large-HTGR studies, except that it does not include a straight tube superheater. The main dependent variables considered in the steam generator design are overall height and pressure drop for the helium flow and steam flow. The main parameters considered as input to the steam generator design are overall cavity diameter and the necessary performance parameters specifying the helium and steam inlet/outlet conditions. Two options are presently being developed. One will allow for holding a constant stress margin in the tubes by varying the tube diameter. The second will allow the tube diameter to be fixed but let the stress margin vary. This work is expected to be completed early in the next quarter. A cost subroutine for the steam generator has been written but has not yet been integrated into the main program.

Work is also in progress to develop an operational version of SOFAST that can be used in studying plant parameters for the commercial size plant. This first operational version will incorporate a simplified steam generator size and cost routine, plus simplified relations for costs of the turbine steam system and balance of plant.

3.3.2.5. Advanced Concepts. The objective of this task is to develop and evaluate alternate design concepts for the GCFR 300-MW(e) plant NSSS configuration, components, and related plant facilities and equipment.

Alternate Residual Heat Removal (RHR) System Study

The purpose of this subtask is to study and evaluate alternate RHR concepts with the objective of improving the RHR system of the present reference design or developing RHR concepts that would be applicable to the reference design and larger GCFR plants. Emphasis is placed on improving the reliability and availability of the RHR system by providing diversity and reducing system complexity.

Preliminary aerodynamic design and performance calculations were made to ascertain the design feasibility of two continuously running circulators (two circulators per loop) placed either in series or in parallel. These circulators must meet the requirements for normal (fully pressurized) operation and also provide adequate flow during a DBDA assuming two out of three safety class circulators are operating. Prior analysis carried out for the main and auxiliary circulators for the GCFR demonstration plant show the volumetric flow and head requirements for normal and DBDA to be essentially the same, although the power requirement is significantly different. This analysis showed that the series circulator arrangement appears not to be feasible on the grounds that the loop would be lost once one of the circulators in that loop is shut down or inoperative.

The parallel flow arrangement is also shown to be marginally feasible since to meet the head and the flow requirements when one of the circulators is lost will require 33% overspeed of the remaining circulator. A similar increase in speed would need to be applied to each of the safety class circulators to meet the required head and flow requirements for DBDA. Additional analysis will be required to determine whether designing the circulators for nonoptimum design for normal operation and making the DBDA the design point could make this circulator arrangement acceptable.

Reliability analysis is being performed on two alternate RHR concepts to determine whether they can satisfy the probability goal for loss of primary cooling of 10^{-6}/year, and to determine whether these systems offer improvement over the presently proposed reference design RHR system.

Core Power Density Variation and Scale-Up Studies

During this reporting period, preliminary studies were performed to investigate the effect of varying pumping power on plant nuclear performance (breeding ratio and doubling time), power production, and major plant components as applied to a scaled-up [3600 MW(t)] GCFR. The primary intent of the studies was to make a scoping examination of the plant design and investment trade-offs associated with improved nuclear performance, thus

aiding in providing a basis for selection of commercial size GCFR parameters and additional guidance to the GCFR demonstration plant effort. A particular objective of this work was to determine if limiting circulator electric motor drive power per loop to between 11 to 22.4 MW (15,000 to 30,000 hp) in conjunction with primary system pressure of 9 to 12 MPa (1300 to 1740 psia) would allow competitive nuclear and power performance without the need for extensive electric motor development.

Summaries of these two studies are reported in Refs. 3-3 and 3-4, and the combined and more detailed reporting of the work results and recommended future work are given in Ref. 3-5.

The plant basic criteria, parameters, and ground rules for the studies were established in agreement between HBA and GA and, in addition to the circulator power and primary system pressure ranges previously noted, included a 3600-MW(t) [nominally 1200-MW(e)] six-loop system with a $(U,Pu)O_2$ fuel and UO_2 or ThO_2 blanket, maximum clad temperature of 750°C (1382°F), core inlet temperature of 260° to 315°C (500° to 600°F), maximum fuel linear rating of $\leq$49.2 kW/m (15 kW/ft), main turbine steam conditions of 12.5 MPa (1800 psig) 510°C (950°F). Output variables included net electrical output, plant efficiency, core geometry, breeding performance, fissile inventory, doubling time, breeding ratio, end-of-life fluence, refueling interval, and steam generator dimension and surface area. It was required that the breeding performance goal be at least comparable to the mixed-oxide-fueled LMFBR as specified in the proliferation resistance large-core design study.

For component design evaluation, an up-flow core configuration was selected, with the reactor internal arrangement being generally consistent with the GCRA demonstration plant up-flow core study design.

Nuclear Performance. The nuclear performance of the plant, including doubling time, breeding ratio, and fissile inventory, depends on the reactor design, which in turn depends on the principal plant parameters of pressure level and circulator pumping power. Circulator power is determined by the gas mass flow rate, the total loop pressure drop, and the density of the cooling gas at the circulator inlet. A parametric study was made to determine

the nuclear performance as a function of these plant parameters and of varying the core inlet temperature.

Principal assumptions for the core performance study include the following:

Core structural material	316 stainless steel
Load factor	0.75
Out-of-pile time	1 year
Reprocessing loss	2%
Burnup	100 (max) MWd/kg
Fluence limit	3×10^{23} nvt > 0.1 MeV
Pin diameter	8 mm (0.315 in.)
Core inlet temperature	293°C (560°F)
Core outlet temperature	566°C (1050°F)
Max mid-cladding temperature	750°C (1382°F)
Number of fuel elements	366
Fuel pins/element	264
Number of control elements	31

The nuclear performance parameters which are generally used to judge the merit of the reactor system are shown in Fig. 3-1. These include compound system doubling time, reactor fissile inventory, and breeding ratio. The breeding ratio is defined as reactor production of fissile material per unit loss of fissile material (Pu-239, Pu-241) in the core and blankets. All calculations refer to a reactor and processing system which has operated through sufficient cycles to be in equilibrium with respect to fissile inventory. Calculation methods were checked by comparing a test calculation with results reported by the INFCE* Working Group 5 on an identical lattice configuration. The agreement between the calculated value of breeding ratio and doubling time was considered satisfactory.

Steam Cycle Performance. Performance calculations for the associated steam system are shown in Fig. 3-2. Thermal efficiency (defined as net

*International Nuclear Fuel Cycle Evaluation.

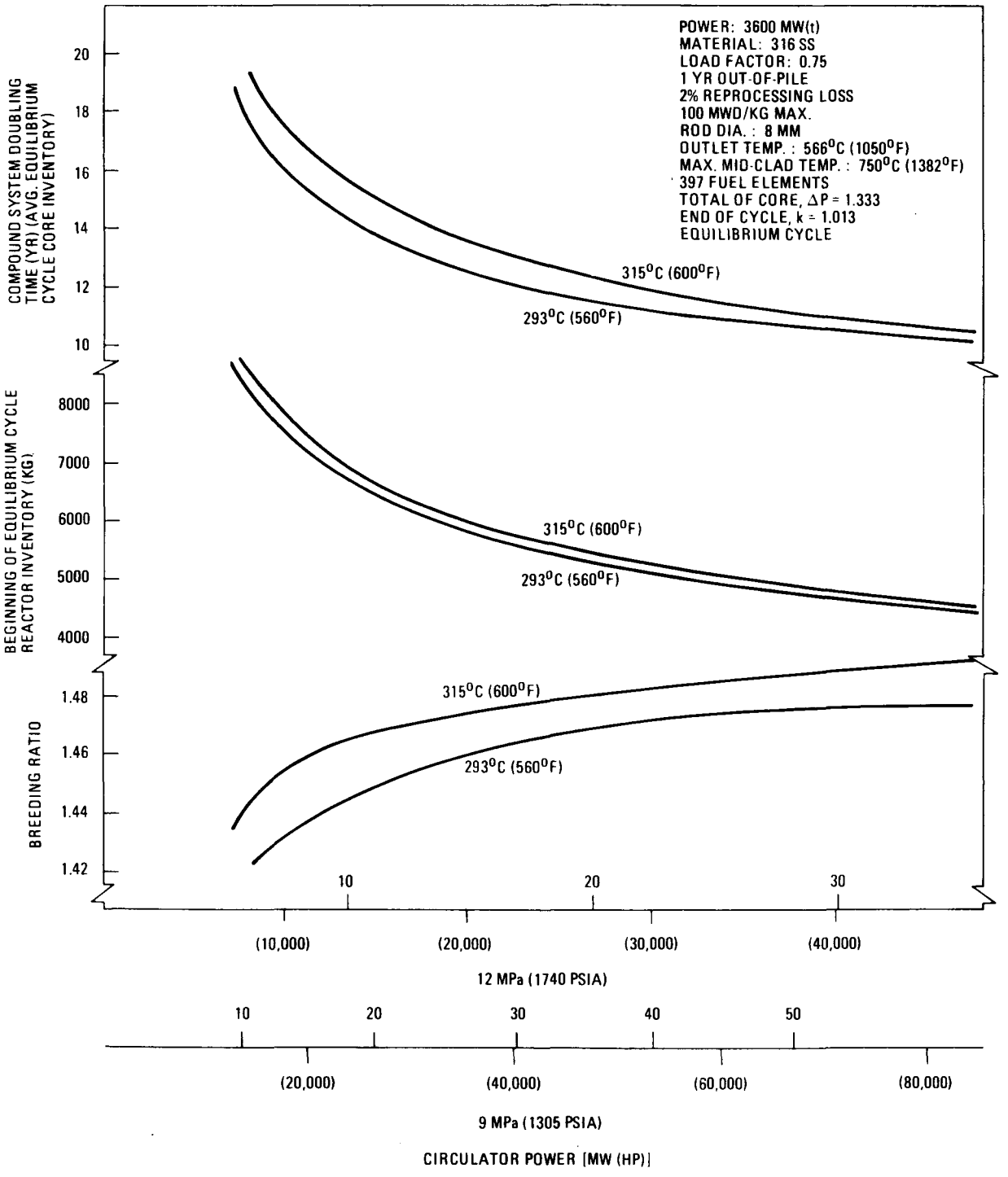

Fig. 3-1. Reactor core performance versus circulator power at different system pressures and inlet temperatures

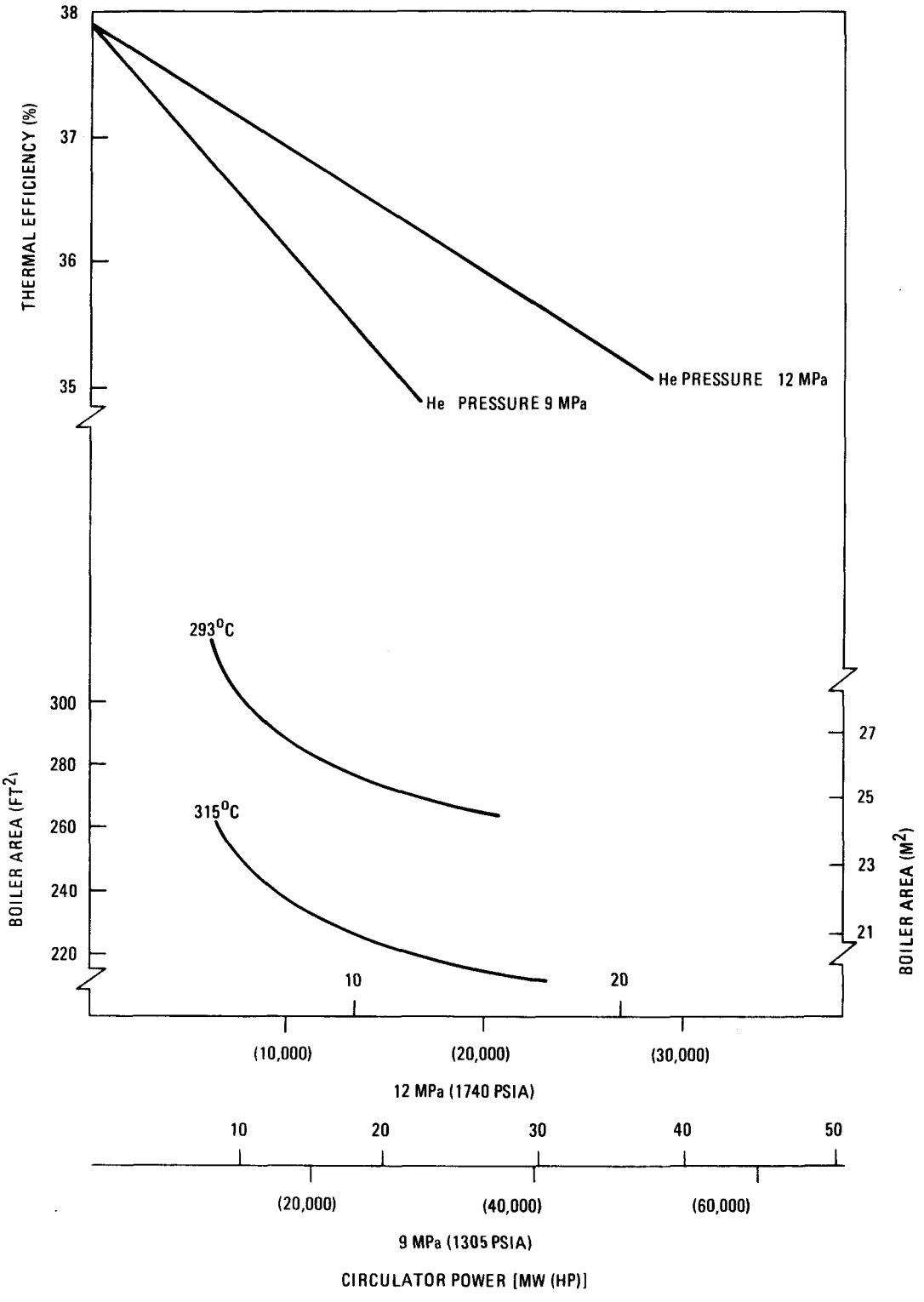

Fig. 3-2. Thermal efficiency and boiler area versus circulator power at different system pressures and core inlet temperatures

electric output per unit reactor heat input) decreases as circulating power increases. Steam generator diameter and heat transfer area both decrease with increase of helium pressure or circulating power. Steam generator sizes were based on the use of 25.4-mm (1.0-in.) diameter tubing in the superheater and 19.0-mm (0.75-in.) tubing in the economizer and evaporator sections. Separate curves are shown for reactor inlet temperatures of 293°C (560°F) and 315°C (600°F).

Economic Evaluation. Figure 3-3 shows a rough economic evaluation of the investment in fissile material, at an assumed cost of $25/g, for a plant with 12.0 MPa (1740 psia) helium pressure. The figure of $25/g is a rough estimate of the cost of recovering plutonium from LWR fuel waste, which could be the primary source of fuel for the first generation of breeders. At a thermal output of 3600 MW, the electric output of the plant varies from 1340 to 1280 MW as the circulator power per loop is increased from 3.73 to 18.65 (5000 to 25,000 hp). Assuming the plant investment, excluding fissile inventory, to be $1 billion, the total investment per unit electric output goes through a minimum at around 12.7 MW (17,000 hp) circulator power per loop.

This economic analysis neglects other capital cost item changes, such as boiler surface and circulator cost. This approach appears justified by the cost estimates of NSSS and related balance-of-plant (BOP) components. Over the range of potential circulator power, the variance in component cost is approximately 3%, which represents about 1% cost variance of the total plant.

Since the plant capital cost and plutonium cost shown in Fig. 3-3 may be significantly different from the assumed values selected (i.e., $1 billion and $25 per gram, respectively), additional data points were generated assuming $1.5 billion per plant capital cost and $50/g for the plutonium value (Figs. 3-4 and 3-5). The results indicate that increased capital costs tend to shift the optimum to lower pumping power requirements, and that increased plutonium costs tend to shift the optimum to higher pumping power requirements. At a system pressure of 9.0 MPa (1305 psia), the optimum circulator power appears to be in the range from 12.7 to 22.3 MW (17,000

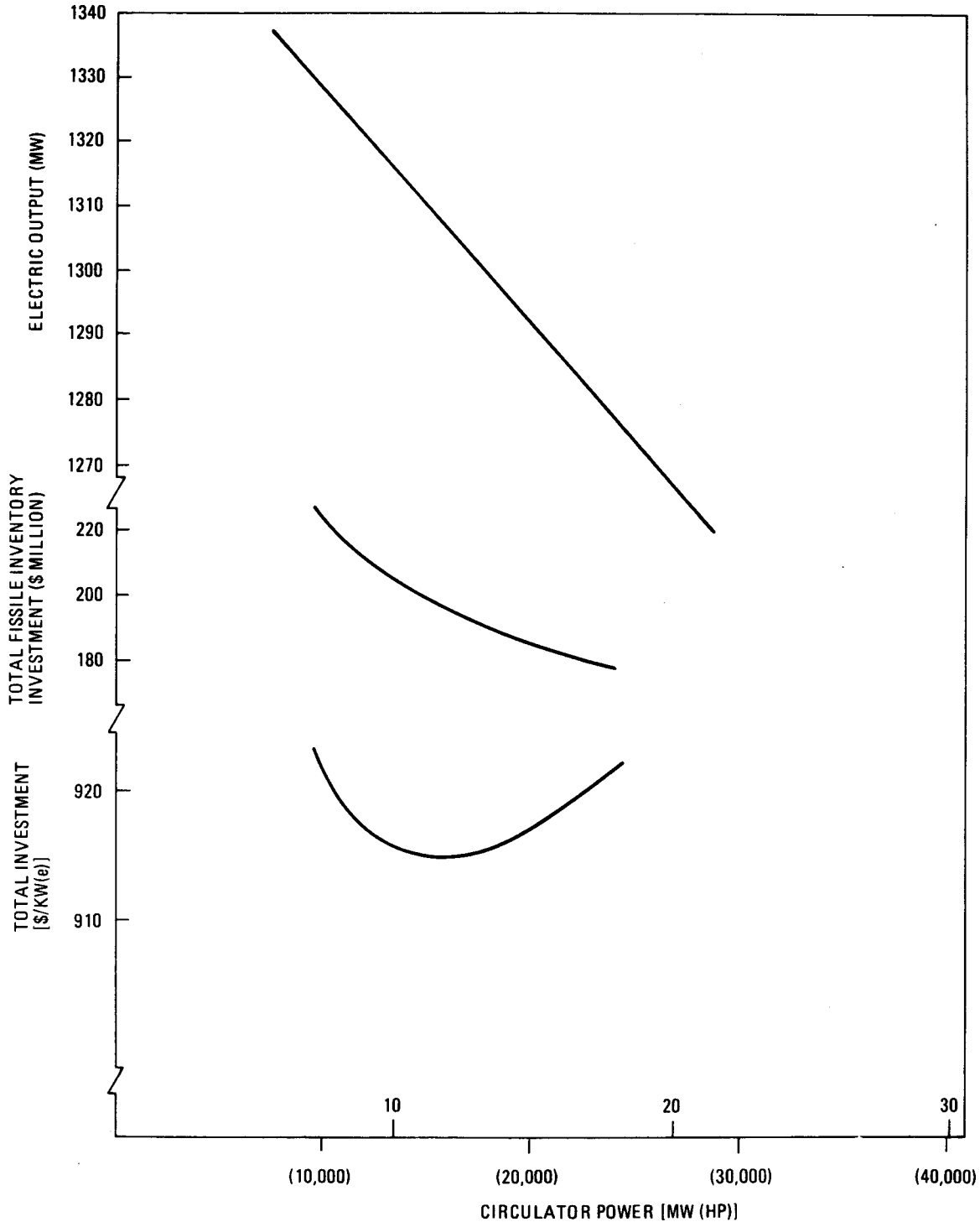

Fig. 3-3. Electric output and fissile investment versus circulator power at 12 MPa (1740 psia) system pressure

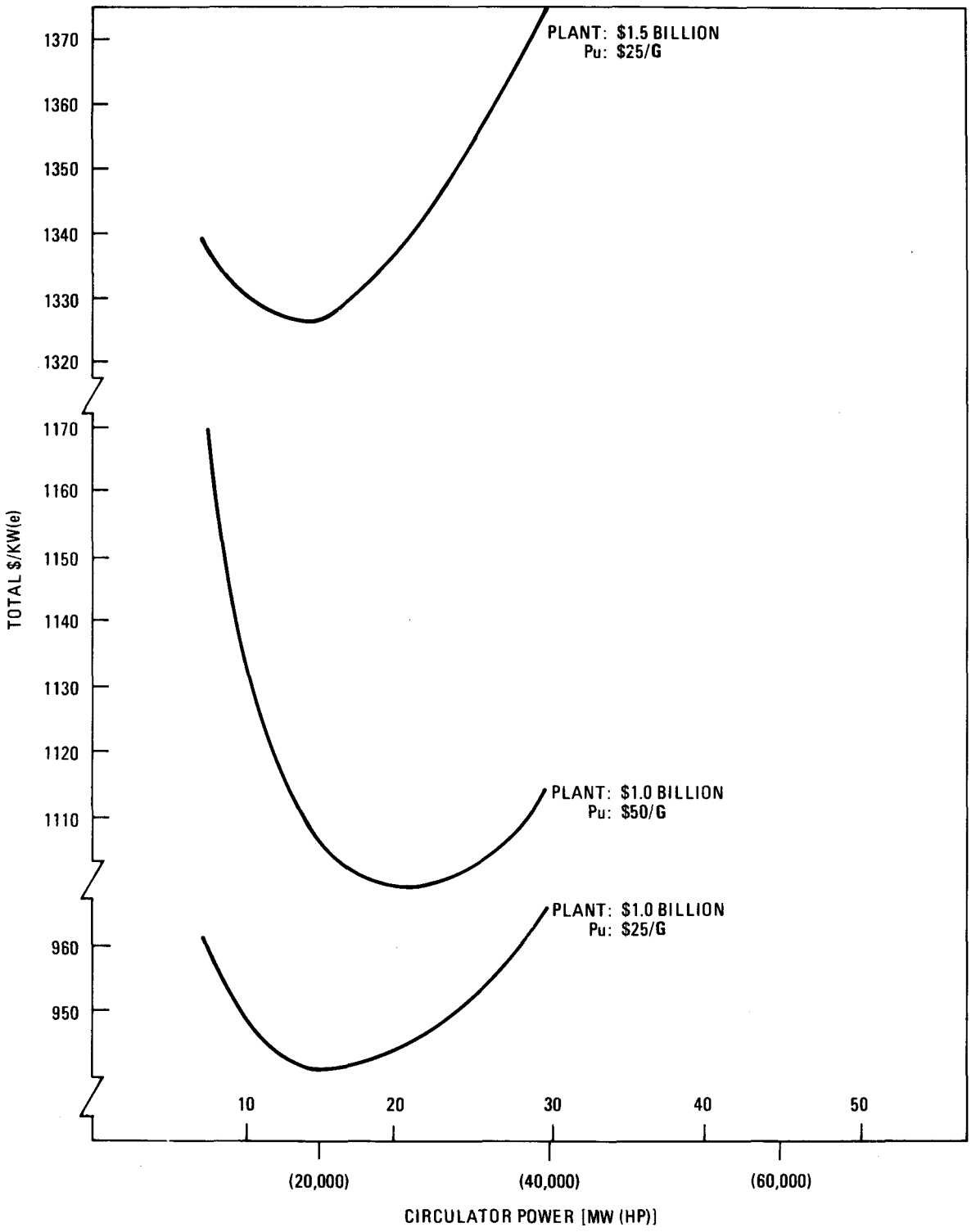

Fig. 3-4. Capital cost versus circulator power at 9 MPa (1305 psia) system pressure

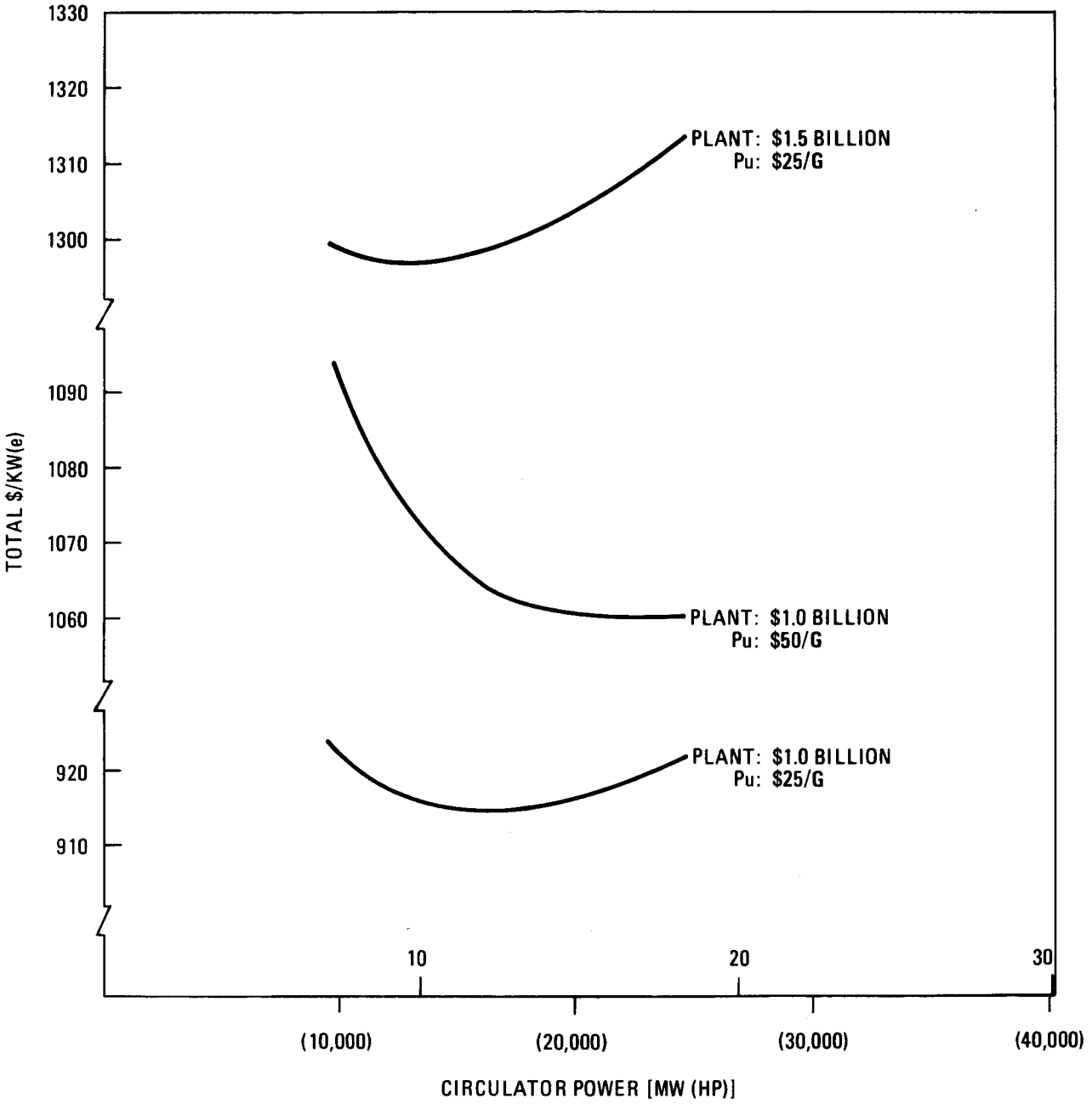

Fig. 3-5. Capital cost versus circulator power at 12 MPa (1740 psia) system pressure

to 30,000 hp). For a system pressure of 12.0 MPa (1740 psia), the optimized circulator powers appear to range from 9.0 to 22.3 MW (12,000 to 30,000 hp).

The results of the above optimizations must be used with extreme caution, since the cost curves used in determining minima are very flat. The foregoing economic analysis was based on a fixed power output of 3600-MW(t) and a varying net electrical output. An additional preliminary analysis was made based on a plant to produce a fixed net output of 1260 MW(e).

Configuration Description and Component Design Evaluation. The basic configuration selected for the 3600-MW(t) GCFR scale-up study is a six-main-loop, three-auxiliary-loop, up-flow core arrangement contained within a PCRV, as shown in Figs. 3-6 and 3-7. The individual designs selected for component evaluation are defined as follows:

Configuration No. 1 represents the design with the highest primary coolant pressure, 12.0 MPa (1740 psia) and with 19.7 MW (26,425 hp) circulators. It constitutes the reference high nuclear performance within the guidelines of the study.

Configurations No. 2 and 3 represent two intermediate designs in which the plant nuclear performance remains constant but the circulator power per loop and coolant pressure are varied from 11.5 to 20.4 MW (15,400 to 27,375 hp) and 12.0 to 9.0 MPa (1740 to 1305 psia), respectively.

Configuration No. 4 represents the lower limit of the nuclear performance and core power density and is based on a 9.0 MPa (1305 psia) coolant pressure and 11.5 MW (15,450 hp) per loop circulator power.

An additional plant configuration, No. 5, was also considered. This configuration has a 35.0 MW (46,975 hp) loop circulator and 9.0 MPa (1305 psia) coolant pressure. While outside the specified range, this plant was included to provide an additional data point, since it furnishes further insight into the variation of plant cost and performance.

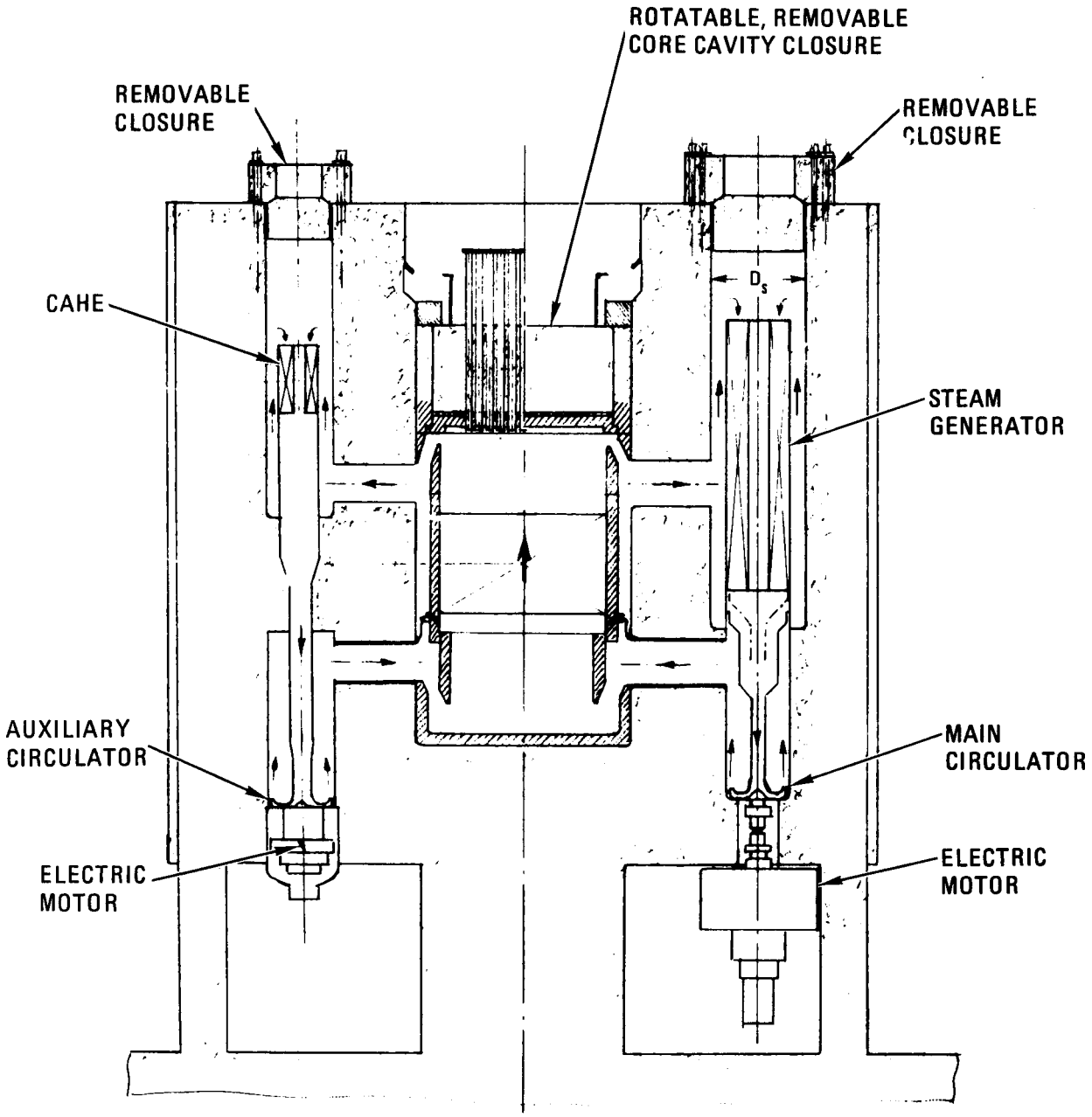

Fig. 3-6. Basic configuration, vertical section

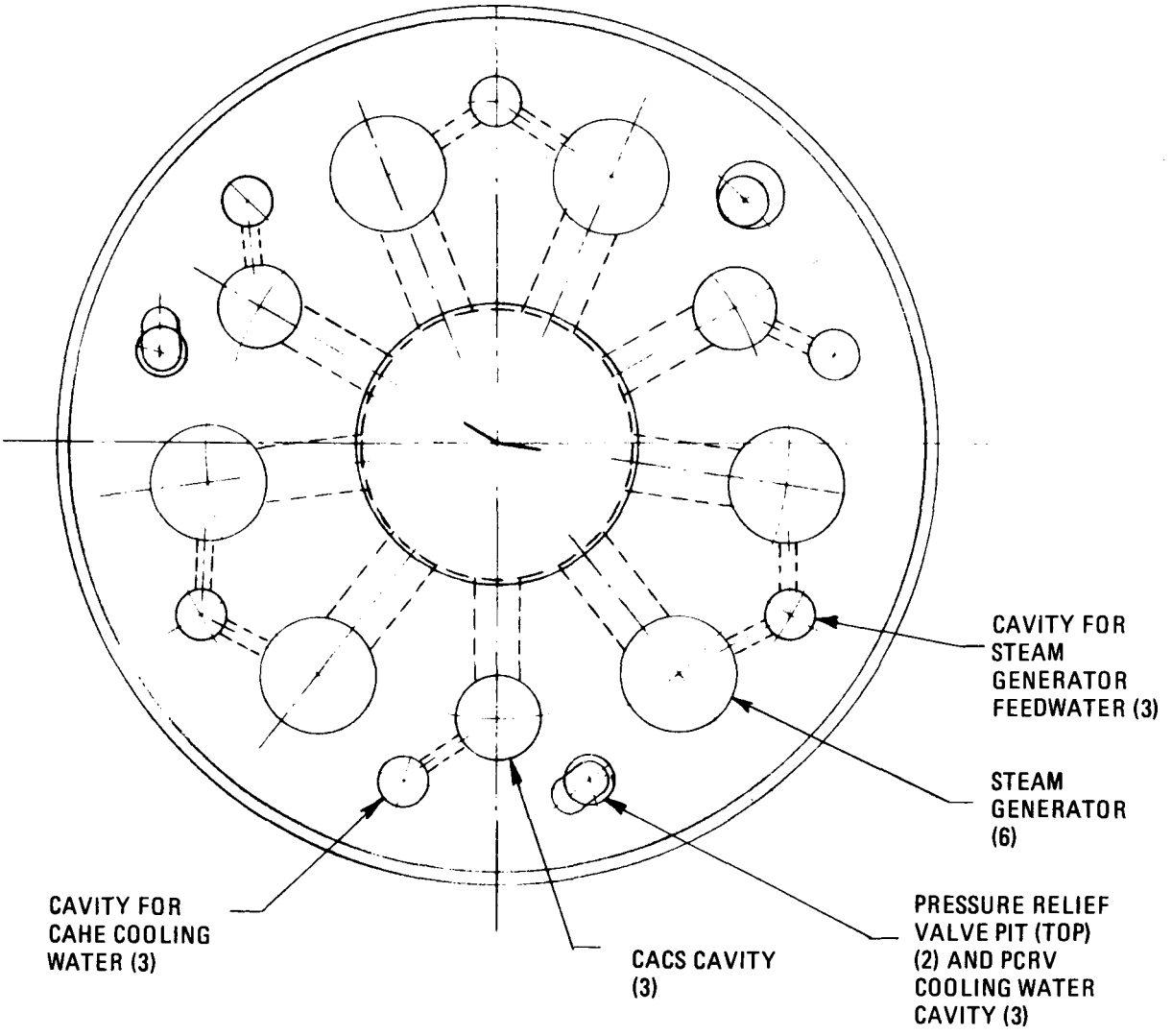

Fig. 3-7. Basic configuration, top view

The PCRV contains a central core cavity surrounded by nine cylindrical cavities. Six contain the steam generators and main helium circulators with loop isolation valves. The other three contain the CAHEs and auxiliary circulators with loop isolation valves.

In evaluating the multicavity PCRV design, particular reference has been made to determining design limits for the vessel pressure ranges considered in the study. While there appears to be no feasibility limitation to the basic vessel design, there are concerns with all designs (particularly at higher pressures) with respect to tendon, rebar, aggregate congestion, and concrete stresses in critical ligament areas between the cross ducts. Alternate design possibilities to alleviate the tendon and rebar congestion and high concrete stresses include (1) use of higher strength concrete, (2) increased PCRV diameter, (3) reduced cross duct diameter, and (4) rearrangement of the CACS loops and cross ducts.

The configurations incorporate a rotating plug for the reactor core cavity closure similar in design to that proposed for the up-flow core demonstration plant study. Closure design is not considered a feasibility concern, but large multisection high-pressure closures present a number of design problems, including load transfer between the closure plug and the PCRV and sealing between the individual elements of the plug and between the plug and the PCRV structure.

The grid plate and core support diameters are substantially larger than for the demonstration plant. This introduces a new consideration, namely, the compatibility of the vertical natural frequency and seismic amplification of the grid plate and core assembly with the PCRV. The design feasibility is further compromised by the fabrication limitations (size and weight) of a single-piece forging. A number of solutions were advanced to respond to these limitations, including the favored one of increasing the grid plate ligament efficiency. A general recommendation was made to keep the core diameter (including removable inner shielding) to a minimum to ease the grid plate, reactor cavity closure, and PCRV

tendon designs and to investigate alternate grid plate fabrication methods. Other components, including the steam generator, CAHE, auxiliary circulator containment, and confinement buildings were sized and evaluated.

Incremental costs were developed for the major NSSS and nuclear island components over the range of circulator power and helium pressures. It was shown that the total costs of these components, including the PCRV, steam generators, circulators, and containment and confinement buildings, varied little (3%) over the range of interest. The total cost differential was considered to be less than 1% of the total plant cost.

Conclusions and Recommendations. The studies showed that a commercial GCFR plant with system pressure of 9.0 MPa (1305 psia) and circulator power of 11.2 MW (15,000 hp) would not yield plant performance that is competitive with long-range planning of the LMFBR program. Since system pressures of 9.0 to 10.0 MPa (1305 to 1450 psia) appear to be feasible, and electric motors for coolant circulator drives should be feasible and reliable at power levels of 15.0 to 22.0 MW (20,000 to 30,000 hp), the following commercial plant scenario was suggested.

The first commercial-size GCFR plant with a nominal net output of 1200 MW(e) should yield a doubling time of about 14 years. This goal can be accomplished with a system pressure of 9.0 MPa (1305 psia) and six circulators of about 19.0 MW (25,000 to 30,000 hp) each. With increased operating experience and confidence in high pressures and circulator powers, subsequent GCFR plant generations should aim at a higher system pressure of 12.0 MPa (1740 psia), motor power of 29.8 MW (40,000 hp), and the use of ferritic steels in the core design. The doubling time of these advanced GCFR commercial plants is currently predicted to be about 8 to 9 years.

The cost optimization curves display rather flat characteristics, so that no strong economic conclusions can be drawn. However, it is worth noting that even with large variations in assumptions for plant capital and fuel investment cost, the economic optima fall within the circulator and system pressure ranges discussed above.

With regard to components evaluation, for the range of parameters considered, the principal feasibility concern is the pressure limit of the PCRV. The study concluded that the PCRV pressure should be maintained below ∿9 MPa (1305 psia) pending more detailed analysis of critical areas and confirmation of the structural design margins.

Preliminary calculations for the rotating plug, reactor cavity closure, and grid plate indicated no fundamental feasibility problems. However, additional detail design and analyses will be required to fully verify the design.

Fabrication limitations, specifically for a single-piece grid plate forging, are of some concern for the lower power density designs, but a number of options are available to control grid plate thickness requirements. Possible fabrication alternates include multipiece welded grid plate designs.

The steam generator design does not appear to present any major design problem, although the final length and diameter need to be optimized with respect to seismic loadings, helium inlet and outlet temperatures, and feedwater temperature. A preliminary study of the CACS, including sizing of the CAHE and auxiliary circulator, discloses no particular technical problems.

Although the refueling system was not investigated in detail in this study, a preliminary estimate of the anticipated refueling time was shown to be 23 days using a single transfer machine. It is possible that refueling time could be lessened by using two machines and by reducing the number of core elements (from 397 to 331) and inner shield assemblies.

This study covered the nuclear island components of the balance of plant (BOP), including the containment and confinement buildings. The scale-up study evaluation indicated no feasibility problems. A preliminary assessment of equipment and piping below the PCRV and within the containment building was also made, and the arrangement is considered feasible. A list of recommended future work required in support of the large plant design is included in Ref. 3-5.

3.3.3. Systems Design (BOP)

The purpose of this subtask is to develop preliminary system designs and general arrangements of the nuclear island so that the feasibility of several nuclear island concepts can be evaluated and the principal dimensions of the major buildings can be established. During this quarter, the following were accomplished:

1. The up-flow core evaluation study was completed. Input on the BOP assessment of up-flow core plant compared with the reference (down-flow) plant was provided to the Technical Management Committee for final reactor concept selection. Included in the assessment were relative costs for the two plant designs.

2. A study was conducted to determine the feasibility of providing the necessary support services (electric power, instrumentation, cooling water) for the PCRV top head penetrations for the rotating plug refueling concept. The study showed that severe congestion would result on the top head, making accessibility extremely difficult.

3. Conceptual procedures were developed to accomplish unscheduled maintenance (removal/replacement) of reactor internals under water (floodable core cavity). While difficult, such procedures appear to be feasible.

4. Work is in progress on the arrangement and layout of two alternate shutdown cooling system (SCS) designs for the purpose of evaluation and selection of the preferred scheme.

5. Requirements for planned maintenance and in-service inspection were defined, and the impact of these requirements on the up-flow/down-flow reactor concepts was identified for inclusion in the up-flow/down-flow plant evaluation.

3.3.4. Seismic Engineering

The derivation of the mathematical dynamic model of the down-flow GCFR was studied with respect to its usage as the simulation of the up-flow GCFR. In addition, all major NSSS systems within the down-flow PCRV were compared to those used in the up-flow design. These studies indicated that the up-flow PCRV, pedestal support, containment building, confinement building, and almost all NSSS equipment within the PCRV were significantly different. New simulations in terms of mass and stiffness representations were derived for these items. These new values have been coupled with soil compliances representing a parametric range of soil sites to form the completed dynamic model of the up-flow GCFR plant. Eigenvalues and seismic response data for the plant subjected to an operating basis earthquake (OBE) on each site will be determined.

Verbal and written comparisons of the seismic response differences between the up-flow and down-flow GCFR were presented to the decision task force. Attention was focused on the benefits of placing safety-related NSSS structures in seismically desirable locations. The effect of a seismic event and the resulting overturning loads on the design of the PCRV support was discussed. In conjunction with an agreement formulated between Bechtel National Inc. and GA, preliminary seismic data for the conceptual design of a PCRV support system were made available to Bechtel.

A complete set of level 2 RECS were submitted. The RECS were written for (1) GCFR Seismic Program Plan, (2) GCFR Plant Specification: Seismic Requirements, and (3) GCFR Seismic Design Support and Review.

3.3.5. Materials Engineering

The major effort during this reporting period was aimed at incorporating the GCFR structural component radiation damage data needs into the national FBR testing program. The additional materials irradiations and property tests required for GCFR and not originally included in the national

program are shown in Table 3-1. This list is the result of an analysis that categorized GCFR structural components; defined service environments, baseline materials, and property data required for design/verification of these components; and compared these requirements with the available information and the existing national program test matrix.

The information in Table 3-1 is based on an analysis of the projected data requirements for key internal components in the upper reactor plenum, core support system, and lower reactor plenum of the reference down-flow design. Although it appears that these data needs will not change significantly for the reference up-flow configuration, a detailed review is being performed.

The highest priority requirement was determined to be the establishment of tensile, stress rupture, and low cycle fatigue data on 316 stainless steel parent metal and welds at the high temperatures (up to 650°C) and high fluences (10^{22} n/cm^2) for components in the lower reactor plenum where helium embrittlement mechanisms may be dominant. The previous National Program Plan did not adequately cover this alloy-environment regime. Property data on 316 stainless steel structural welds at the lower temperatures (325°C to 425°C), which are required for design of core support system components, are also a high priority item. The original program emphasized 304 stainless steel weldments. The high cycle fatigue data, which are not currently being obtained in the national program, are considered important because of the possibility of cyclic loading from high-frequency, flow-induced vibrations.

The GCFR requirements were incorporated into the National Program Plan (Ref. 3-6) and several actions were taken at the January National Coordination Meeting to adapt the currently planned program to meet the GCFR data needs. It was decided that the GCFR tensile, low-cycle fatigue, stress rupture, and creep-fatigue specimen irradiation requirements would be incorporated as effectively as possible into the initial structural material irradiations in the FTR materials open test assembly. The tensile program was modified to increase the number of 316 stainless steel parent metal

TABLE 3-1
MATERIALS IRRADIATIONS AND PROPERTY TESTS REQUIRED FOR GCFR STRUCTURAL COMPONENTS AND NOT INCLUDED IN ORIGINAL NATIONAL PROGRAM PLAN

Priority	Material	Temperature Range (°C)	Fluence Range [n/cm^2 (E > 0.1 MeV)]	Fast Flux Fraction Range[a]	Required Tests
1	316, 316 welds	550-650	$5 \times 10^{21} - 5 \times 10^{22}$	0.04-0.60	Tensile, low cycle fatigue, stress-rupture
2	316 welds	325-425	$5 \times 10^{21} - 5 \times 10^{22}$	0.1-0.4	Tensile, low cycle fatigue, in-reactor creep
3	316, 316 welds	550-650	$5 \times 10^{21} - 5 \times 10^{22}$	0.04-0.60	Creep-fatigue, in-reactor creep, high cycle fatigue
4	316, 316 welds	325-425	$5 \times 10^{21} - 5 \times 10^{22}$	0.1-0.4	High cycle fatigue
5	304, 304 welds	325-425	$5 \times 10^{19} - 5 \times 10^{21}$	0.05-0.40	High cycle fatigue
6	718, 718 welds	325-425	$5 \times 10^{21} - 2 \times 10^{22}$	0.05-0.60	High cycle fatigue
7	316, 800H	550-650	$1 \times 10^{18} - 5 \times 10^{19}$	0.15-0.40	Tensile, low cycle fatigue, stress rupture
8	Ferritic steel	550-600	$1 \times 10^{18} - 5 \times 10^{19}$	0.15-0.4	Tensile
9	316, 800H	550-650	$1 \times 10^{18} - 5 \times 10^{19}$	0.15-0.4	High cycle fatigue, in-reactor creep, creep fatigue

[a] Range given is for actual component service conditions. It is understood that it is not possible to attain high fluence exposures in soft spectra with existing facilities.

specimens and to include 316 stainless steel weldments. High-cycle and low-cycle fatigue specimen irradiations in FTR were also modified to include 316 stainless steel and 316 stainless steel weldments.

In addition to the FTR experiments, an EBR II irradiation to obtain nearer-term high-temperature tensile data for setting fluence limits on 316 stainless steel GCFR shielding was implemented based on a GA-HEDL recommendation and national committee agreement. The test matrix, shown in Table 3-2, includes irradiations at 550° to 650°C of 316 stainless steel parent metal and three different weldments at total fluences of 0.5 to 2 x 10^{22} n/cm^2. The experiment, which consists of three B-7 pins in row 7 of EBR II, will be fabricated by the end of FY-79. Irradiations will be completed by the end of FY-80

TABLE 3-2
TEST MATRIX FOR GCFR EBR-II MATERIALS IRRADIATION EXPERIMENT

Irradiation Temperature (°C)	Total Fluence (10^{22} n/cm^2)	Number of Specimens				Number of Tension Tests
		Base Metal		Weld Metal		
		No. of Heats	Replicates	No. of Welds[a]	Replicates	
550°C	0.5	3	2	3	2	12
	1	3	2	3	2	12
	2	3	2	3	2	12
650°C	0.5	3	2	3	2	12
	1	3	2	3	2	12
	2	3	2	3	2	12

[a]Three different welds made in 2.54-cm (1-in.) plate using 316 SS filler metal and gas tungsten arc, shielded metal arc, and submerged arc processes, respectively.

3.4. REACTOR SAFETY AND RELIABILITY

The purpose of this task is to investigate and quantify GCFR safety characteristics. In accordance with the GCFR safety program plan, the DOE-sponsored GCFR safety task has been organized into five subtasks.

1. An overall safety program definition and integration task defines and organizes the activities in the individual tasks, provides for coordination of the national and international GCFR safety programs, and ensures that all important aspects of GCFR safety are studied with a balanced set of priorities.

2. The probabilistic technology task is aimed at defining event sequences leading to loss of coolable core geometry and at quantifying their probability of occurrence.

3. The core accident technology task focuses on the core response to events involving loss of coolable core geometry. The objective of this task is to quantify core energy release and fuel vapor generation that may occur before a permanently subcritical configuration is established.

4. The primary containment technology task focuses on the response of the PCRV to the conditions established at permanent core subcriticality by the core accident technology task. The objective of this task is to quantify the consequence mitigation characteristics provided by the PCRV, principally with respect to molten fuel containment, energy release containment, and fuel aerosol containment, to ensure protection of secondary containment integrity. Furthermore, this task will establish a mechanistic basis to demonstrate the conservatism of the secondary containment site suitability source term.

5. The secondary containment technology task focuses on the performance of the secondary containment as a barrier to the release of radioactivity. The objective of this task is to quantify the secondary containment response to the conditions established by the primary containment technology task to ensure that secondary containment integrity is maintained for a significant period of time and that the radiological consequences are limited to acceptable levels for extremely low probability events. Furthermore, this task will ensure that the radiological consequences of a site suitability source term release to the containment are within 10CFR100 guidelines.

Work is currently in progress toward attaining the objectives identified above. Logical probabilistic methods are employed to determine the probabilities associated with various accident initiation and progression sequences and to identify potential design modifications that would help reduce risks. A reliability data bank is maintained and continuously updated to support these analyses. A methodology for integrating reliability considerations into the GCFR engineering effort at the system, subsystem, and component levels has been developed for trial use on a selected system, with the objective of determining the optimal use of reliability engineering methods in the GCFR. Core accident consequence analyses are concentrating on the protected loss of flow (PLOF) accident sequence, which has been identified as a dominant event sequence leading to core melting. Recriticality in this accident sequence is the phenomenon that could most significantly influence consequences. The conditions that may lead to recriticality are therefore the principal object of current investigations. Post-accident fuel containment (PAFC) analyses are being performed to assess the capability of the design and to identify potential modifications that could improve the molten fuel containment capability.

3.4.1. Safety Program Definition and Integration

The objectives of this task are the technical definition of the overall GCFR safety program and the technical coordination of GCFR safety-related work being performed by GA, the national laboratories, and international participants of the GCFR program under the umbrella agreement.

During this reporting period all work concentrated on completing the safety comparison between an up-flow core and a down-flow core. The technical assessment was completed and documentation is currently in progress.

Five papers were presented at the Specialist Meeting on GCFR Safety and Associated Design Features in Brussels, March 13-15, 1979. The meeting was jointly sponsored by the Nuclear Energy Agency (NEA) of the Organization for Economic Cooperation and Development (OECD) and the International Atomic Energy Agency (IAEA). A. Torri presented three papers and A. P. Kelley (HBA) presented two papers on the GCFR safety program in the United States. The five papers are listed in Table 3-3. Representation at the Specialist Meeting is shown in Table 3-4. Papers were presented basically in three categories: (1) papers dealing with safety considerations of the U.S./FRG design concept (nine papers were contributed from the U.S., Germany, and Switzerland); (2) papers discussing safety analyses for the Gas Breeder Reactor Associates (GBRA) design concept (seven papers were contributed from Belgium, Japan, and England), and (3) papers addressing design-independent considerations (two papers were contributed from England and Sweden). The following major conclusions are drawn from the overall assessment of the meeting. The strength of the coordinated U.S. safety program became clearly evident. The completeness of definition of the U.S. safety program and the accomplishments in each specific task area working toward defined objectives have no apparent counterpart in the European GCFR safety

TABLE 3-3

U.S. PAPERS PRESENTED AT THE SPECIALIST MEETING ON GCFR SAFETY AND ASSOCIATED DESIGN FEATURES, BRUSSELS, BELGIUM, MARCH 13-15, 1979

1. "The GCFR Safety Program in the U.S. - Overview and Status," by A. Torri (GA), A. P. Kelley (HBA), and D. Emon (DOE).

2. "The Role of Probabilistic Analysis in the GCFR Program," by A. P. Kelley (HBA), A. Torri (GA), and D. Emon (DOE).

3. "Improvement in Residual Heat Removal Reliability in the GCFR Demonstration Plant," by A. Torri, T. Taniguchi, and P.H. Raabe (GA).

4. "A Core Melt-Down Assessment in the GCFR," by A. Torri, M. V. Frank, and C. Kang (GA).

5. "The Gas Reactor In-Pile Safety Test Project (GRIST-2)," by A. P. Kelley (HBA), E. Arbtin (EG&G), and R. St. Pierre (ANL).

TABLE 3-4
REPRESENTATION AT THE SPECIALIST MEETING ON GCFR SAFETY AND ASSOCIATED DESIGN FEATURES, BRUSSELS, BELGIUM, MARCH 13-15, 1979

Country	Attendees	Papers
Belgium	6	3
France	2	0
West Germany	3	3
Japan	1	2
Sweden	3	1
Switzerland	4	1
United Kingdom	8	3
U.S.A.	2	5
International Organizations	5	0
Total	34	18

program. The safety program supporting the GBRA design appears to be currently very small and fragmented among the contributors from Belgium, England, and Japan. The large contingent of attendees from England resulted from the need for British authorities to prepare for a fast reactor inquiry and the opportunity provided by this meeting to gain an overview of the status of GCFR safety programs. Japan is reported to have a steady four-man effort to perform safety and physics analyses of the GBRA design.

3.4.2. Probabilistic Technology

In support of the up-flow/down-flow study, a probabilistic evaluation was performed with the objective to assess the maximum potential improvement in RHR reliability attainable by adding a natural convective core auxiliary cooling system (CACS) capability to the basic forced convective cooling capabilities.

3.4.2.1. RHR Systems Considered. The probabilistic evaluation of forced convective RHR cooling was based on the following operational sequence assumed for the primary and backup forced convective cooling systems: first, the main cooling system (MCS); then, the shutdown cooling system (SCS); and last, the CACS. The probabilistic evaluation of a plant augmented with a natural convective cooling capability in the CACS added a fourth operational option to the three listed above: natural convective cooling by the CACS, where natural convection occurs in the primary, secondary, and tertiary coolants.

Two basic design configurations for the MCS/SCS were evaluated, the so-called reference design and the revised design. There are two principal differences between the reference design and the revised design: (1) the revised design includes a steam generator floodout capability in the SCS by the addition of a safety-class floodout pump and water supply to the SCS, and (2) the revised design includes a dedicated emergency

power supply for each of the three SCS loops and for each of the three CACS loops, while the reference design utilizes a shared emergency power supply between the SCS and the CACS.

3.4.2.2. Summary of Results. For each RHR system investigated, natural circulation was considered in two modes. In the first mode, it was assumed that natural circulation on the helium side was only available with the PCRV pressurized. In the second mode, it was assumed that for intentionally depressurized conditions such as refueling, it was possible to repressurize the PCRV, if necessary, to that pressure level needed to accomplish natural circulation cooling of the core. Reliability data from the reference gas-cooled reactor reliability data bank (Ref. 3-7) was used to quantify the reliability of the RHR heat removal trains and power supply.

Common mode failure analyses were performed using the β-factor method (Ref. 3-8) to yield an indication of the upper limit failure rate that might be expected. Common mode estimates are considered conservative when interpreted as the reliability potential represented by a given design configuration.

The results from this RHR reliability study are summarized in Table 3-5. For each configuration studied, the results are separated into the contribution to the total failure probability from events in which the PCRV remains pressurized and events that cause or require depressurization. It should be noted that depressurized events control the failure probability of all statistically independent failure estimates, particularly for the revised design, whereas for common cause events, the pressurized and depressurized events are of roughly equal importance within a factor of 3. The reason for this dominance of depressurized events is three-fold:

1. Helium natural circulation is not effective with the PCRV depressurized.

TABLE 3-5

RHR FAILURE PROBABILITY SUMMARY FOR HEAT REMOVAL TRAIN AND POWER SUPPLY SYSTEMS: COMPARISON OF FORCED CIRCULATION AND FORCED/NATURAL CIRCULATION

Configurations	RHR Failure Probability Per Year	
	CACS FC Only[(a)]	CACS FC + NC[(a)]
Reference Design		
Statistical independence estimate:		
Pressurized events only	1.0×10^{-6}	3.3×10^{-8}
Depressurized events only	1.8×10^{-6}	1.7×10^{-6}
Depressurized events with repressurization		3.3×10^{-9}
Total: No repressurization	2.8×10^{-6}	1.7×10^{-6}
With repressurization		3.6×10^{-8}
Common cause estimate:		
Pressurized events only	9.8×10^{-5}	2.2×10^{-5}
Depressurized events only	8.5×10^{-5}	8.4×10^{-5}
Depressurized events with repressurization		1.0×10^{-6}
Total: No repressurization	1.8×10^{-4}	1.1×10^{-4}
With repressurization		2.3×10^{-5}
Revised Design		
Statistical independence estimate:		
Pressurized events only	2.3×10^{-10}	4.9×10^{-11}
Depressurized events only	5.2×10^{-8}	2.3×10^{-8}
Depressurized events with Repressurization		3.4×10^{-9}
Total: No repressurization	5.2×10^{-8}	2.3×10^{-8}
With repressurization		3.4×10^{-9}
Common cause estimate		
Pressurized events only	9.0×10^{-6}	1.3×10^{-6}
Depressurized events only	3.2×10^{-6}	1.6×10^{-6}
Depressurized events with repressurization		5.2×10^{-7}
Total: No repressurization	1.2×10^{-5}	2.9×10^{-6}
With repressurization		1.8×10^{-6}

(a) FC = forced circulation, NC = natural circulation.

2. The RHR failure probability is dominated by running failures of RHR equipment during long downtime events. These long downtime events are identical with events that require PCRV depressurization.

3. The annual expected downtime derived from the initiating event frequencies and repair times for the 47 design duty cycle events is much greater with the PCRV depressurized than for pressurized downtime. The annual pressurized downtime is probably underestimated because shutdowns not related to the design duty cycle were not considered and because the repressurization and rise-to-power portion of the downtime was not included. Most of this unquantified downtime is probably with the PCRV pressurized. If the entire balance between a 20% unavailability and the accounted-for downtime were pressurized, the total pressurized downtime would become comparable to the depressurized downtime. Even in this case, the depressurized events in the revised design would still dominate the statistically independent failure rate.

The full benefit of natural circulation will be considerably larger than this numerical study would indicate, for the following reasons:

1. For common cause events, the RHR failure rate contribution from pressurized and depressurized events is about equal. A substantial increase in pressurized downtime would cause the pressurized events to control the common cause RHR failure rate and increase the importance of natural circulation to guard against common cause failures or design errors.

2. Natural circulation as a last line of defense can probably be designed such that it requires no control action and no instrumentation. Therefore, the dependence on controls and

instrumentation for a system with natural circulation may be significantly reduced. This could mean a large benefit of natural circulation.

3. Early GCFR plants and particularly the demonstration plant will have higher initiating event frequencies and failure rates in addition to being more susceptible to common cause failures. A naturally convecting RHR system will provide an inherent defense against such early plant design deficiencies, which are an unavoidable part of the system commercialization process.

3.4.3. Core Accident Technology

3.4.3.1. Core Disruptive Accident Assessment for Up-Flow Versus Down-Flow Concept. During the reporting period, the assessment of core melt accidents in a GCFR with an up-flow core compared to a down-flow core GCFR design was completed. Documentation is in progress. The most significant results are summarized below.

This discussion examines the differences between the up-flow and down-flow designs in the context of core disruptive accidents (CDAs). Four elements are considered:

1. Determine the consequences of an unmitigated PLOF (GA and ANL).

2. Determine the feasibility of PLOF consequence mitigation concepts (GA).

3. Assess the flow blockage accident (GA).

4. Assess unprotected LOF and transient overpower (TOP) accidents (GA and ANL).

The key findings are:

1. The consequences of an unmitigated PLOF accident are larger than for the unprotected accidents and likely to become a major focus in the GCFR safety program.

2. The PLOF mitigation concepts of drainage or poison, investigated in this study, are not considered feasible. Further work in combining drainage and poison is warranted.

3. Duct fall-away in the down-flow core is potentially feasible. The principal concerns are neither the ability of ducts to fall nor the hold-up of ducts by adjacent assemblies, but the potential for fuel-crumbling-induced criticality before fall-away.

4. The down-flow core can prevent damage propagation during a complete flow blockage of a single assembly via duct fall-away.

3.4.3.2. Summary of Results

Consequences of Unmitigated PLOF Accident

Detailed core heatup and recriticality calculations were performed at GA to determine the core heatup sequence, cladding and fuel melting rate, and time of fuel melting. The core heatup analysis did not include convection effects in the central cavity, which may delay recriticality. However, the time of recriticality is sensitive also to the particular assumptions of molten fuel spreading over a single assembly and from one assembly to another. In general, spreading a molten fuel layer over more assemblies reduces the reactivity. Since the molten fuel was assumed to spread uniformly over adjacent circumferential rings of assemblies, the time to recriticality may be overestimated. Hence, the calculated time

of 970 s should be considered a best estimate. Central cavity convection would also raise the PCRV pressure and could cause relief valve opening prior to cladding melting. This effect was not assessed. The unmitigated PLOF consequences were calculated by ANL in terms of the fraction of core fuel vaporized and the mechanical work energy release. In a pressurized condition [8.6 MPa (85 atm)], fuel vaporization on the order of 5% and a mechanical energy release on the order of 150 MW-s are estimated. This estimate increases to approximately 9% fuel vaporized and 300 MW-s mechanical energy release. Fuel behavior phenomena which tend to prevent criticality in a depressurized condition have not been investigated. The calculated work potential is not considered a threat to PCRV structural integrity but may affect PCRV internals, liner cooling potential, and PCRV relief valves. The analyses were not intentionally biased toward conservative consequences. The simplifying assumptions necessary for the analysis may be both conservative and optimistic. The results should be regarded as the preliminary best estimate of the PLOF consequences. The most important conclusions are as follows:

1. The RHR reliability analysis indicates that in the revised design the most likely PLOF event occurs with the PCRV depressurized. The PLOF consequences increase with decreasing system pressure. Additional analyses for depressurized cases will be required, but it appears that the dominant consequences may result from the long downtime depressurized events.

2. Multiple criticality events are neither certain nor can they be ruled out at this time. Fuel boil-up is not expected to prevent criticality for pressurized cases and may not for depressurized cases at low decay heat.

3. Mitigation of the predicted core consequences at the primary coolant boundary (PCRV) and by the containment are under investigation, to determine whether there is a need for containment features beyond those currently provided.

PLOF Consequence Mitigation

Early accident termination mechanisms that would prevent criticality for the PLOF accidents were investigated. Duct fall-away was investigated for the down-flow core. The poison solution concept and the external drain concept are currently considered not technically feasible. The internal drain concept is technically feasible but requires the elimination of a large portion of the lower axial blanket in most of the core assemblies. Further work on combining drains with poison is warranted. The only CDA consequence-mitigating concept with a small design impact that is currently considered feasible is duct fall-away for the down-flow core. The principal remaining uncertainty is whether fuel crumbling will lead to recriticality before duct fall-away occurs.

Assessment of Flow Blockage Accidents

A complete flow blockage in a single assembly was investigated to determine the potential for damage propagation to neighboring cooled assemblies. Cladding melting leads to a blockage in the lower axial blanket of the blocked assembly similar to the PLOF. However, in contrast to the PLOF, fuel melting and slumping precedes duct wall melting. A molten fuel pool with temperatures above the liquidus would collect on the steel blockage and begin melting the duct wall as the reactor power and flow rate decreased after trip. Within a few tens of seconds, the molten pool in an up-flow core is calculated to melt through the duct wall of a neighboring assembly despite a continued, albeit decaying, flow rate. (The average post-trip flow rate is 10% of full flow.) This sequence would lead to welding together of the seven-assembly group that has the blocked assembly at its center. An increased post-trip flow rate in the unblocked assemblies could prevent damage propagation.

A down-flow core designed for fall-away during a PLOF would automatically provide an early accident termination mechanism without damage

propagation. When the molten pool raises the duct wall temperature to its yielding point under the assembly weight, the assembly would drop from the core. This would occur prior to melting of neighboring assemblies.

Unprotected Accidents

Two unprotected accidents, the transient overpower (TOP) and the loss of flow (LOF), have been investigated by ANL with respect to flow direction and support direction. The TOP consequences are insensitive to flow direction and ought to be substantially less than an LOF. The key uncertainties in TOP consequence determination are clad failure location, fuel particle sweepout from the core, and primary side damage from dispersed fuel.

Best estimates for unprotected LOF accident fuel vapor fraction and energy release are one to two orders of magnitude below the PLOF. This consequence assessment has been performed by ANL using the accident analysis code SASGAS, which attempts to treat the phenomena mechanistically rather than conservatively. The up-flow has been compared to the down-flow for two potentially sensitive phenomena: (1) clad motion versus residual coolant flow, and (2) fuel motion versus residual coolant flow. In addition, fuel plugging potential in the inlet nozzle region of an up-flow core was studied. The major analytical uncertainty pertains to the potential for swelling fuel columns to block neutron streaming paths and add a positive prompt reactivity mechanism. Within the model and phenomenology uncertainties, neither the flow direction nor support direction made a significant difference in the results.

3.4.4. Primary Containment

A feasibility evaluation for the up-flow core design with bottom control rod drives was described in Ref. 3-9. During the present reporting period, an analysis of core meltdown conditions in an up-flow core was completed. Some preliminary results of follow-up PAFC analyses were also obtained. The consequences of fuel spillover into side cavities was assessed.

3.4.4.1. Analysis of Up-Flow Core Meltdown Conditions. Following a core meltdown accident in an up-flow GCFR, the extent of meltdown depends on the failure modes of the core support plate. The earliest failure of the core support plate would occur when molten fuel and steel refreeze and plug the coolant channel in the core support plate. One-third of the fuel and fuel cladding may be contained in the void spaces of the core support plate. By adiabatic heating, the average temperature of the core support plate would reach the failure limit (1100°C) 3 hr after the accident.

If molten fuel and steel do not refreeze in the core support plate, they would be relocated to the core cavity floor, forming a debris pool. Due to the large amount of steel on the cavity floor, the molten pool is expected to remain at the melting temperature of steel until all the steel has become molten. A radiation heat transfer model was developed to calculate the transient heat-up of the core support plate. The remaining core, the upper and lower plenum, and the cavity liner cooling were included in the model. The volatile fission products were assumed to remain in the central cavity and uniformly distributed in the helium. The transient heat-up of the core support plate is shown in Fig. 3-8 for three locations. It is seen that the midplane of the core support plate would reach the 1100°C assumed failure limit about 9 hr after the accident.

It is concluded from the above two cases that the core support plate would fail from 3 to 9 hr after a core meltdown accident.

3.4.4.2. Analysis of Up-Flow Core Post-Accident Fuel Containment. A two-dimensional heat transfer model was developed for PAFC analysis following the initial meltdown phase. Materials from the center portion of the core barrel were assumed to drop to the core catcher after the failure of the core support plate. The outer rim of the grid plate (outside the radial blanket) with shielding assemblies was assumed to remain in place. It is the purpose of this analysis to determine whether subsequent heating in the PAFC phase would fail the remaining grid plate and shielding, as well

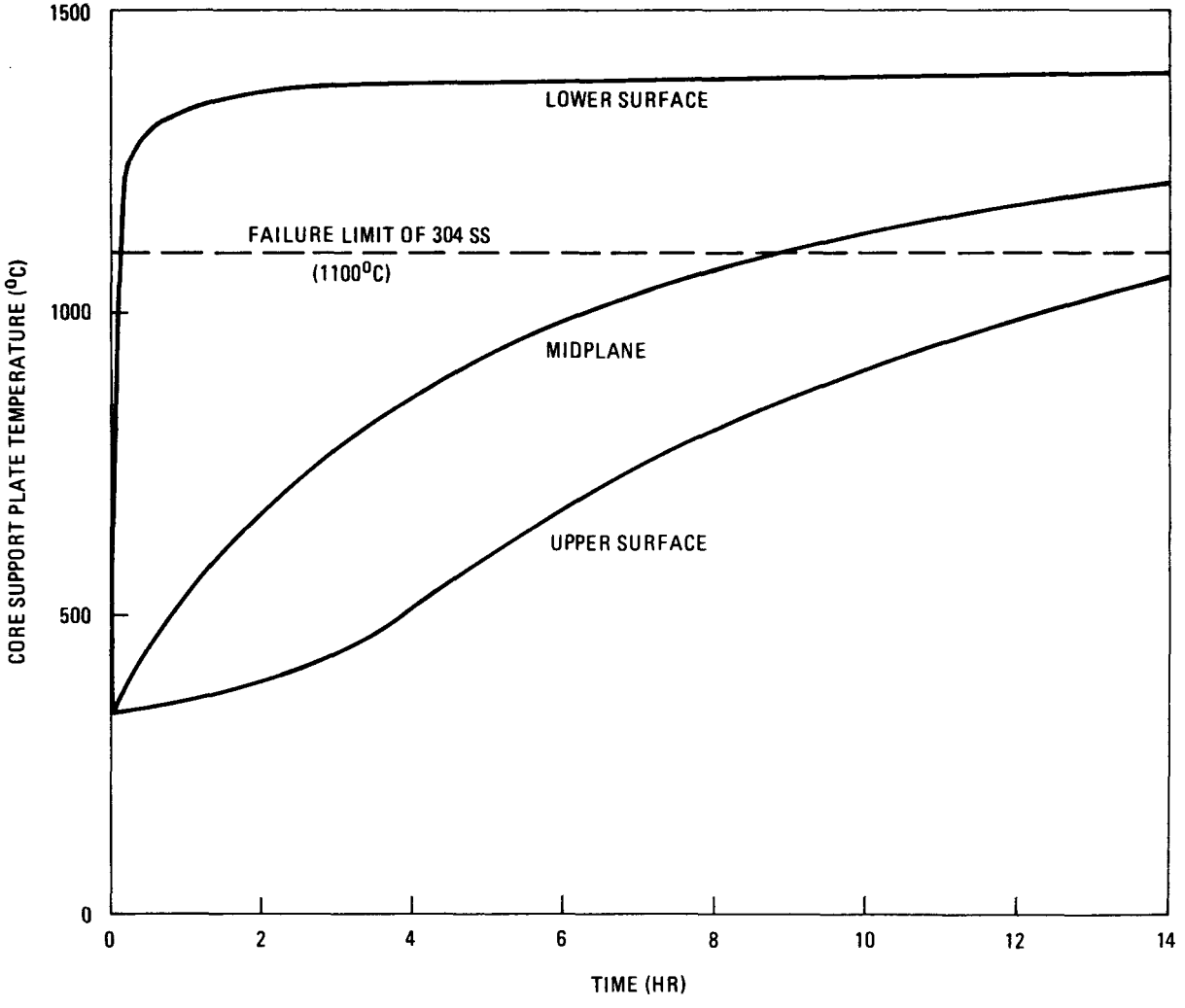

Fig. 3-8. Core support plate temperatures at various locations

as the outer radial shield. A steel overlaying the UO_2 debris model was assumed. Only the cavity liner cooling system was assumed for the PAFC cooling.

Results of the transient analysis are shown in Fig. 3-9. It is seen that the temperature of the remaining grid plate would reach 1100°C about 85 hr after the accident. The radial shield may also reach 1100°C at a time beyond 100 hr. The sideward cavity liner temperature, which is the highest of all cavity liner locations, is below 200°C for the first 100 hr.

It appears that, without forced or natural helium convection, the core support plate and radial shield may approach a peak temperature of 1100°C. Therefore, it is important to establish the failure temperature of these structures to determine whether their failure would be expected.

3.4.4.3. Fuel Spillover into Side Cavities. The inlet coolant ducts connecting the reactor cavity with the side cavities are situated low in the reactor cavity for the up-flow design. Molten debris spillover could occur if the entire grid plate and radial shield were to accumulate in the debris. An evaluation was made to determine the consequences of fuel spillover into the side cavities following radial shield failure. Part of this evaluation required a recalculation of material volumes for both the up-flow and down-flow core designs. The minimum core catcher volumes are 13 m^3 for the down-flow and 24 m^3 for the up-flow. Fuel spillover will not occur in the up-flow core until the radial shields fail. The two likely consequences of fuel spillover are steam ingress from the main steam generator and PCRV failure from fuel melting through the circulator. Spillover of steel alone would not constitute a significant problem.

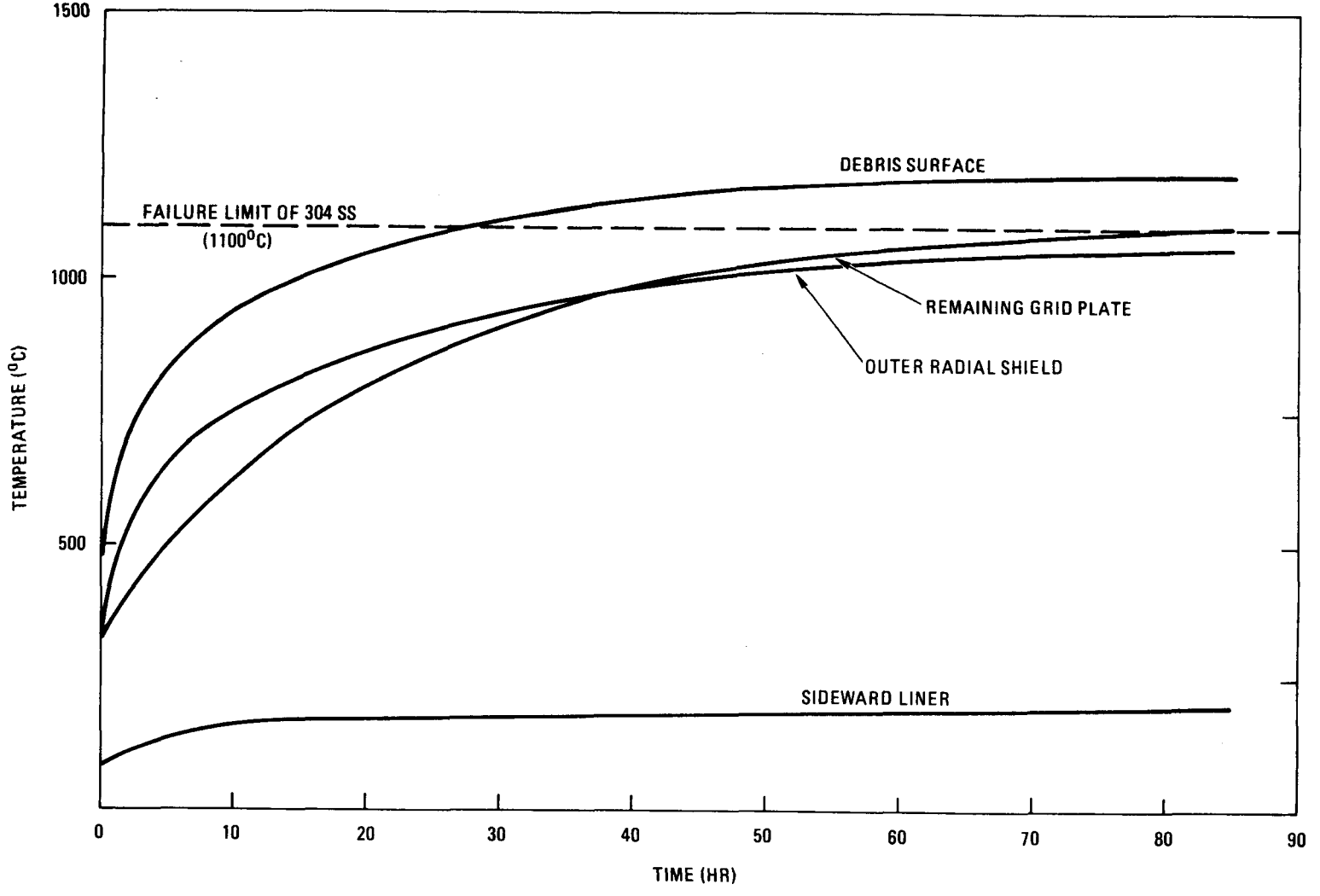

Fig. 3-9. Reactor cavity temperatures at key locations

REFERENCES

3-1. "SCAP, Steam Cycle Analysis Program User's Manual," GA-A15151, prepared for General Atomic by Jaycor (J78-6067-TR-1), August 1978.

3-2. Thompson, W. I., "COMB-GCFR Plant Design Scoping Program," General Atomic unpublished data, April 30, 1976.

3-3. Thompson, W. I., and T. Macken, "Summary Report on a Core Power Density Variation Study for a 3600-MW(t) GCFR Concept," DOE Report GA-A15341, General Atomic Company, March 1979.

3-4. Macken, T., "Summary Report--Conceptual Scale-Up Study for 3600-MW(t) GCFR Plant," DOE Report GA-A15345, General Atomic Company, March 1979.

3-5. Macken, T., et al., "Preliminary Evaluation of the Effect of Varying Helium Circulator Pumping Power on the Design and Performance of a Large GCFR," DOE Report GA-A15311, General Atomic Company, March 1979.

3-6. Knecht, R. L., "National Program Plan, Irradiation Effects on the Mechanical Properties of LMFBR Structural Materials," TC-810-2 Supplement, Hanford Engineering Development Laboratory, September 1978.

3-7. Hannaman, G. W., "GCR Reliability Data Bank Status Report," ERDA Report GA-A14839, General Atomic Company, July 1978.

3-8. Fleming, K. N., "A Reliability Model for Common Mode Failures in Redundant Safety Systems," ERDA Report GA-A13284, General Atomic Company, April 18, 1975.

3-9. "Gas-Cooled Fast Breeder Reactor Quarterly Progress Report for the Period November 1, 1978 to January 31, 1979," ERDA Report GA-A15237, General Atomic Company, February 1979.

4.0. CIRCULATOR TEST FACILITY

The objective of this task is to develop a facility for the development, qualification, and acceptance testing of the GCFR main helium circulator. The scope of this task involves (1) evaluation of alternative test facility concepts in terms of technical feasibility and cost; (2) identification of the most promising test facility concept; (3) establishment of an architect/engineer conceptual design; and (4) final design, construction, and checkout of the facility.

A contract was approved and issued to The Ralph M. Parsons Company of Pasadena, California, in November 1978 for the following work:

1. Perform an economic and technical evaluation of two external helium loop cooling configurations.

2. Update the facility design to reflect the latest circulator, electric motor, service system, and motor controller requirements.

3. Produce an updated design report describing the changes and associated costs.

The evaluation of the helium loop cooling configurations was completed during the previous quarter. The direct cooling concept, whereby a helium-to-air heat exchanger is used to remove thermal energy from the helium loop, was found to be more expensive than the indirect configuration. The indirect concept uses an intermediate Dowtherm G fluid loop to cool the helium and transfer the thermal energy to the ambient air. As a consequence, the updating of the facility design and the design report are based on the Dowtherm G cooled helium loop configuration. The updating of the facility design and development of the associated costs have been completed. Documentation is in the review phase, to be followed by distribution.

The updated design of the GCFR circulator test facility is shown in a perspective view in Fig. 4-1. The helium test loop configuration is shown in Fig. 4-2.

When construction of the facility is completed, tests will be conducted on the following GCFR demonstration plant prototype and production components:

1. Prototype main motor controller, pony motor controller, main circulator service system, diffuser, thermal barrier, circulator control system, and steam generator inlet.

2. Prototype/spare main motor, pony motor, main helium circulator, and isolation valve.

3. Production units 1, 2, and 3 main motors, pony motors, and main helium circulators.

The facility will have the capability to perform development, qualification, and acceptance tests at the same conditions of pressure, temperature, helium flow rate, and rotating machinery speed as expected in the demonstration plant. Included in the project are the design, fabrication, and installation of a Dowtherm G cooled helium loop and an electrical supply and distribution system housed in a building located on an appropriate site. Supporting facilities are provided for the supply of helium, nitrogen, purified water, cooling water, and compressed air. When completed, this non-nuclear facility will be capable of establishing the behavior of demonstration plant components during design and off-design operation, operational transients, and depressurization accidents.

The updated conceptual design is a 1420-m^2 (15,310-ft^2) (gross) steel-framed, braced structure with insulated metal siding and roofing. The building will have a high bay area flanked by a two-story bay. The high bay will contain a test pit to house the helium loop and the main circulator

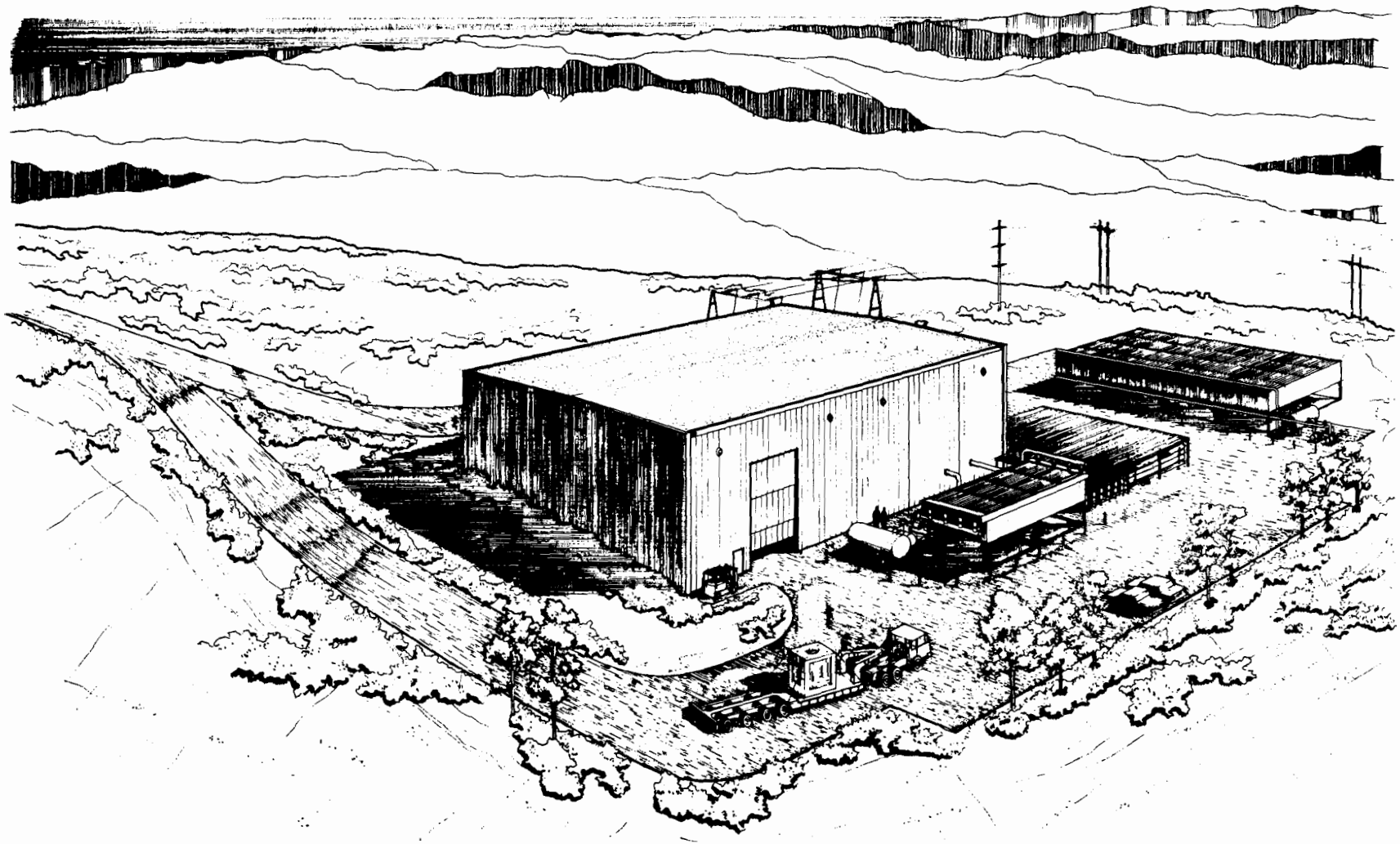

Fig. 4-1. GCFR circulator test facility

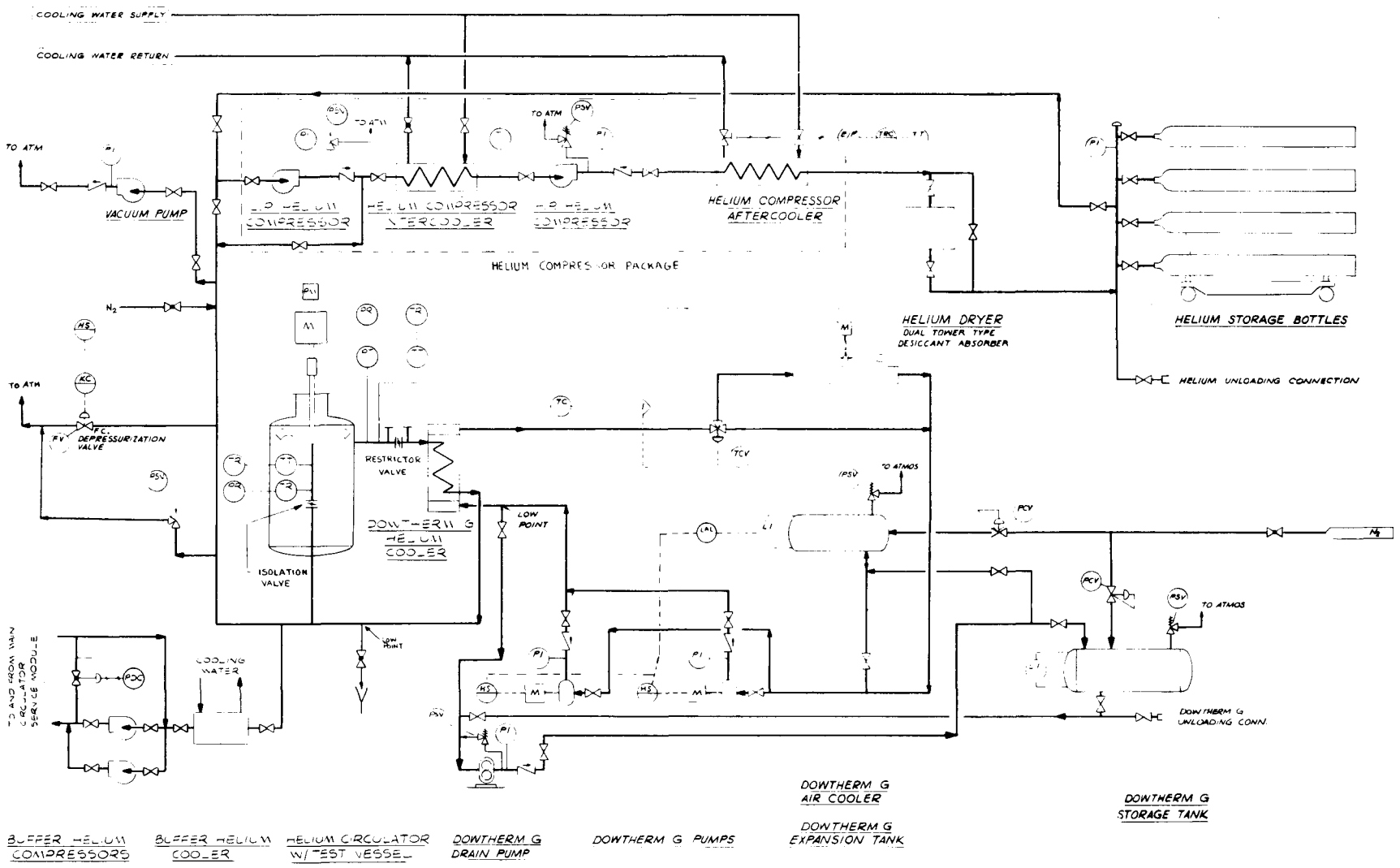

Fig. 4-2. GCFR helium test loop configuration

service system, a main motor storage and assembly pit, a test bay, and a receiving/lay-down area accessible by a vertical lift service door. A 99,800-kg (110-ton) overhead crane will run the full length of the high bay.

The two-story bay will also run the full length of the building. The second floor will contain the motor controller room and the facility electrical and mechanical equipment room. An overhead monorail with two 9100-kg (110-ton) hoists will permit installation and removal of motor controller modules from the controller room. Helium compressors, a helium dryer, air handling units, and motor control and load centers will occupy the equipment room. The ground floor will provide space for a battery room, a small machine shop, storage, locker and toilet facilities, control room, and office. The office, control room, and locker rooms will be air conditioned. All other interior space will be serviced by heating and ventilating systems. Fire protection will be provided by a wet pipe sprinkler system in all areas except the control room complex and within the motor controller modules, where Halon 1301 will be used. Outside of the building will be located a covered storage area housing rented helium and nitrogen gas supply and storage trailers, a Dowtherm G storage tank, air cooler, expansion tank and pump, and the facility cooling water heat exchanger, expansion tank, and pumps. A parking lot suitable for 20 cars will be provided.

The helium loop will provide a circulation path for component testing. The loop will consist of the circulator, its diffuser, a circulator test vessel, large diameter external piping, a restrictor valve, a helium/ Dowtherm G heat exchanger, internal flow ducting within the vessel, and an isolation valve. The helium circulator and its drive motor will be mounted on a flange at the top of the test vessel. A diffuser assembly within the upper head of the vessel will expand the helium flow stream from the radial compressor into the vessel. The helium will then flow through the vessel discharge nozzle into the external piping and through the restrictor valve. The speed of rotation of the circulator and the degree of closure of the

restrictor valve will control the rate of helium flow. The helium will flow through the helium/Dowtherm G heat exchanger, which will be an integral part of the helium flow path in the piping system.

The energy imparted by the circulator to the helium will be transferred to the Dowtherm G coolant in the heat exchanger. The Dowtherm G will then transport the energy to an outdoor Dowtherm G/air heat exchanger, where it will be dissipated to the atmosphere. Upon leaving the helium/Dowtherm G heat exchanger, the helium will return through the remainder of the helium loop piping to the intake nozzle of the vessel. Here it will flow into the return flow ducting within the vessel and then through the isolation valve to the inlet of the circulator.

Connections and a valve will be provided for helium flowing out of the loop through other test sections temporarily installed in the test bay and back into the loop. A separate valve with a controllable opening rate will be connected to the large diameter pipe run of the helium loop and will exhaust to the atmosphere outside of the building. This valve will permit the simulation of a design basis helium depressurization accident (DBDA).

The electric motor circulator drive will consist of a main motor, pony motor, main motor controller, and pony motor controller. The main motor will be a 17,700 kW (24,000 hp), brushless-exciter, synchronous machine rated for full-power operation at 3600 rpm. The motor will be totally enclosed within a missile-proof housing containing the rotor, stator, brushless exciter, bearings, bearing lubrication system, and heat exchangers for cooling. The voltage rating will be 6900 V at full load with starting at zero frequency by a variable frequency controller. The pony motor will be a three-phase induction motor rated at 224 kW (300 hp) and suitable for variable speed operation over a range of 150 to 1800 rpm. This motor will be coupled to the top end of the main motor drive shaft. The main motor controller will be a solid-state, adjustable frequency power supply with output rating compatible with motor operating and stability requirements

over the entire speed range. The controller power supply will consist of two three-phase thyristor bridges linked together through a smoothing reactor (dc link). One three-phase bridge will be connected to the facility power system and will operate as a phase-controlled rectifier to supply power to the dc link. The second bridge will be connected to the synchronous motor and will invert the power from the dc link back to variable frequency current to power and control the circulator main motor.

The forced commutated inverter power supply (control) for the pony motor will be a three-phase, bridge-type inverter supplied by an adjustable voltage dc thyristor rectifier. Frequency control will be achieved by frequency gating of the forced commutated three-phase bridge, and the inverter voltage output will be controlled by the dc input. Power supply will be rated at 500 hp at 460 V, 60 Hz.

A transmission line belonging to a local utility will be extended to the facility electrical switchyard, where the voltage will be stepped down through a power transformer to the required voltages for the helium circulator electric motor drive and for facility auxiliary power needs. Facility auxiliary power will be supplied at 4.16 kV. Two outdoor power transformers will provide power to two double-ended 480-V load centers for smaller electrical loads. The electrical and mechanical equipment room will house the 480-V load centers, motor control centers, panelboards, and dry transformers for stepping the voltage down for 120/240-V service.

A battery and charger will supply dc power for the switchyard and the forklift. Utilities will include sanitary waste, water, and telephone. Standard equipment will include office furnishings and shop equipment.

Supporting efforts of particular significance in arriving at the described facility configuration include initial efforts to resolve potential acoustic problems associated with the nature of the test equipment. Technical discussions were held with acoustic specialists and considerable information was exchanged. Analysis was initiated to calculate the noise levels inside the test loop due to the throttle valve, based on

newly acquired data. In turn, this will help determine whether the throttle valve noise is less than that of the circulator. Since one of the purposes of the facility is to learn how much acoustic noise the circulator introduces into the loop, the analysis will help determine if the circulator noise will be masked by the valve noise.

A second area subject to specific investigation is that of fabrication/ transportation of the large and very heavy test vessel. Two basic options are being investigated, one involving a vessel which is shop fabricated in the Eastern United States and shipped to the facility site, the other a vessel which is field erected at the facility site from components manufactured in Eastern U.S. shops.

A Schedule 44 - Construction Project Data Sheet entitled "GCFR Circulator Test Facility" was prepared, reviewed and approved by GA management, and submitted to DOE.

5.0. ALTERNATE FUEL CYCLES

5.1. ALTERNATE FUEL CYCLE STUDIES

The purpose of this task is to determine the characteristics of a GCFR fueled with a variety of fissile and fertile materials. These characteristics will be used to evaluate various reactor fuel strategies which could be employed to improve the proliferation resistance and/or energy capability of future nuclear power systems. The GCFR mass flow information for the Non-Proliferation Alternate Systems Assessment Program (NASAP) and International Nuclear Fuel Cycle Evaluation (INFCE) studies are also prepared and reviewed under this task.

A general outline for the study was established previously, and the preliminary analysis and evaluation phase has been completed (Ref. 5-1). Preliminary fuel strategy studies indicate that the fuel cycles of greatest interest for the GCFR are:

1. Pu/U core with uranium or thorium blankets.
2. Pu/Th core with thorium blankets.
3. (Low-enriched) U-233/Th core with thorium blankets.

During the second phase of the program, core materials and configuration studies are being performed to identify the optimum states for the various parameters for each fuel composition.

Approximate parametric studies have been completed on two of the fuel cycles of interest (Pu/U and Pu/Th cores). The design characteristics of large core designs for the NASAP have been documented, and fuel strategy studies have been initiated to help identify optimum core characteristics for the various roles that an FBR may be required to fulfill. During the

last quarter, a sensitivity study was completed on the effect of GCFR fuel rod diameter on energy availability for symbiotic systems. An appropriate fuel pin diameter for either symbiotic or all FBR strategies appears to be 8 mm.

During this quarter, efforts were made to determine the sources of differences noted in the General Atomic GCFR NASAP submittal and the subsequent ANL INFCE calculations; the impact of withdrawn control rod position on breeding performance was established. The fast mixed spectrum reactor proposed by Brookhaven National Laboratory was reviewed, and an initial attempt was made to select the major core and plant parameters for a large GCFR.

5.1.1. Comparison of Mass Flow Calculations for the Large Core GCFR

In March 1978, GCFR mass flow and fuel cycle information was supplied to DOE for the NASAP study by General Atomic (Ref. 5-2). This mass flow information was revised in June to reflect the lower allowable linear heat rates suggested in the interim (Ref. 5-3). Both submittals were generated to be consistent with the "prudently aggressive" FBR guidelines (Ref. 5-4) established in the Proliferation Resistant Large Core Design Study (PRLCDS). The mass flow information supplied by GA was used along with that supplied by other FBR contractors in DOE's NASAP study.

For the INFCE study (Ref. 5-5), ANL was the technical integrator for U.S. information. In this role, ANL personnel chose to modify the ground rules used in the NASAP calculations and to recalculate the mass flow and breeding performance characteristics of the various FBR designs. The GCFR core design which eventually emerged from the ANL calculations differed significantly from that supplied in the NASAP submittal. Breeding performance was significantly reduced by the following ANL decisions:

1. Derate the reactor core by ∿20% to reduce the linear heat rate.

2. Shorten the fuel residence time by ∿33% to reduce the fluence and burnup.

3. Include solid stainless steel rod followers for all control and shutdown rods.

After much review of the ANL design and calculations, it has been concluded that the ANL GCFR design is not representative of a reasonably optimized configuration and, as a result, seriously underestimates the breeding performance of the GCFR concept.

Comparing the original GCFR NASAP submittal and the final ANL INFCE design, the following sequence of changes can be identified:

	Doubling Time* (Yr)	Approx. Change in Doubling Time
GCFR NASAP submittal (Ref. 5-2)	∿13.2	
Including U-235 as fissile	14.2	1.0
Reduction in fuel lifetime from 3 to 2 years	15.2	1.0
Revised ANL zoning, blanket shuffling, etc.	15.6	0.4
Derating plant from 1200 to 988 MW(e)	18.1	2.5
Inclusion of SS rod followers	20.8	0.2

*Compound system doubling time $= 0.693 \times \dfrac{M\left(1 + RF \times \dfrac{Tex}{1\ cycle}\right)}{(G - Lp - Ld) \times cycles/year}$

where M = equilibrium fissile fuel inventory for core and blanket elements,

RF = fraction of core replaced at refueling,

Tex = external cycle time = 1 year,

T cycle = cycle length between refuelings,

G = fissile gain per cycle of operation, 75% capacity,

Lp = processing losses = 2%,

Ld = Pu-241 decay loss for external cycle.

In reviewing each of these design or definitional modifications, the magnitude of the penalty introduced relative to other FBR can be estimated.

The decision to include the U-235 tails as fissile represents a departure from general practice and a departure from the standard doubling time definition proposed in Ref. 5-6 by the same personnel. While this definitional variation tends to increase all FBR doubling times, the impact on the GCFR with its three-row blanket and higher core inventory is almost twice as large as for the homogeneous oxide LMFBR.

Reducing the GCFR fuel lifetime from 3 years to 2 years basically increases the material inventory being processed from 33% to 50% of the in-core inventory. This represents a significant relative penalty for the GCFR since this modification reduces the average burnup in the GCFR to ∿45 MWd/kg or ∿15% less than that for other FBRs being studied. A more appropriate comparison would be achieved if a constant burnup or fluence were the basis for consistency.

The ANL redefinition of the GCFR design included reducing the core to two fuel zones, modifying the blanket shuffling scheme, and other changes. While these modifications appear to have only a minor impact on doubling time, the calculated power distribution for both core and blanket is unacceptable. A core zoning and blanket shuffling scheme similar to that originally submitted would be required to produce reasonable power, burnup, and fluence distributions.

A major modification made by ANL included derating the GCFR design from 1200 to 988 MW(e). This deration was made to reduce the peak linear heat rate from ∿52 kW/m (∿17 kW/ft) to the ∿43 kW/m (∿14 kW/ft) used for the other oxide FBR designs. Based on preliminary GA calculations, the linear heat rate was reduced to ∿39 kW/m (∿12.9 kW/ft), thereby penalizing the GCFR. Furthermore, the means chosen to reduce the heat rate, i.e. deration, leads to a direct reduction in fissile production with no compensating reduction in inventory. A similar heat rate reduction was achieved between the first and second GCFR NASAP submittals (Refs. 5-2, 5-3)

by increasing the active core length by ∿170 mm. The resulting increase in doubling time was negligible, since the production was increased to compensate the increased inventory. Based on this experience, the doubling time penalty resulting from deration could potentially be compensated by a reduction in fissile (and fertile) inventory to reoptimize the design while maintaining the linear heat rate that ANL wishes to impose.

The inclusion of stainless steel rod followers in the GCFR has been determined to be an oversight in the ANL model. The extra 20% of stainless steel has never been suggested for the GCFR and should not be included. The resulting 2.7-year penalty in doubling time is inappropriate.

In summary, it is estimated that the ANL INFCE calculations for the GCFR overstate the doubling time by at least 3 years and more probably by ∿5 years, even with the ground rules selected for the study. These calculations are being reviewed at ANL.

5.1.2. Withdrawn Control Rod Positioning

One of the physical core design parameters that may have a significant impact on reactor breeding performance is the configuration of the control assemblies and the associated control rod programming. During this quarter, the impact of the withdrawn control rod position on breeding performance was quantitatively explored and a recommendation developed.

The withdrawn control rod position is important for the following reasons:

1. The control rods in the axial blanket compete for neutrons which breed additional fissile material in the blankets.

2. A significant radiation dose to the rods can occur in the withdrawn position.

3. Fuel element length and PCRV dimensions can be affected by required rod withdrawal.

A decision on how far control rods should be withdrawn into the axial blanket must consider each of these factors.

Calculations for typical GCFR core designs indicate that if control rods are withdrawn no further than the core blanket interface, enough neutrons will be lost to the B_4C in a uranium blanket to reduce the breeding ratio by $\sim$0.033. In addition, the end-of-cycle reactivity will be reduced by $\sim$0.5% Δk, requiring $\sim$1% increase in core inventory. These factors would increase doubling time by $\sim$8%. The impact on a thorium blanketed core would be somewhat larger due to the reduced density of cross section of the thorium blanket. These calculations also indicate that the control rod tips will receive a fast neutron dose which each year is a large fraction of the currently established radiation limit. This dose could limit control rod lifetime to some value less than the desired 3-year in-core, time.

Based on the value of the bred material and approximate plant costs, the optimum economic position for withdrawn control rods appears to be somewhere between 10 cm and 30 cm above the upper axial core/blanket interface. Pending further resolution, the large plant designs provide for rod withdrawal approximately 20 cm above the core/blanket interface.

5.1.3. Technical Review of the Fast Mixed Spectrum Reactor Proposed by BNL

The FMSR concept proposed by BNL (Ref. 5-7) was reviewed and discussed with the BNL technical staff. The concept proposed would be started up on 10% enriched uranium and would require only natural uranium feed at equilibrium. Such a system could increase the energy available from current uranium resources by a factor of 15 without reprocessing.

Neutronic calculations that have been performed at BNL suggest that the concept may be feasible. In addition to the obvious questions concern-

ing fuel material fluence capability, several issues of a neutronic nature must be resolved before feasibility is clearly demonstrated. Among the issues are:

1. Capacity to Achieve and Maintain Criticality

The equilibrium calculations performed by BNL indicate that with an equilibrium plutonium loading the core will be slightly subcritical at the beginning of cycle, with enriched uranium control rods being employed to achieve criticality. Considering the fact that virtually all means of increasing reactivity, i.e., metal fuel, high fuel volume fractions, fueled control, and high exposure, have already been employed, it seems highly likely that an enriched fissile feed will be required at equilibrium to accommodate licensing requirements and uncertainties.

For start-up, BNL has proposed that a 10% enriched uranium initial core could be employed to achieve initial criticality. Depletion analysis is required to determine if such a U-235 fueled core would have the $\sim$1.6 breeding ratio required to breed enough fuel to sustain the reactivity following refueling with natural uranium. Since U-235 has a significantly lower number of neutrons emitted per fissile absorption (compared to Pu-239), it seems likely that, at a minimum, a number of the early reloads will require enriched fuel.

2. Reactor Control Requirements

The fueled movable control system proposed may be adequate to achieve criticality, but it will be extremely difficult to cool since its linear heat rate could be twice as high as that in the core. An additional backup shutdown system will probably be required to meet the general design criteria for licensing. Provisions will have to be made to deal with single failures, stuck rods, and rod ejection events. Requirements for additional

control volume within the core will make achieving and maintaining criticality even more difficult.

3. Power Distribution Concerns

As illustrated in the BNL calculations, the radial power distribution has more variations with time than the traditional FBR. A more complex and time-dependent orificing scheme will be required to match the core power and flow distribution. In addition, the axial power distribution can be expected to be strongly peaked at the core midplane prior to the attainment of the equilibrium fissile concentration at all axial positions. The high midplane peak will increase hotspot temperatures and probably require some unusual orificing considerations.

4. Uncertainties

While a number of uncertainties can be identified, there are at least two of a neutronic character which may raise questions of feasibility. First, experimental evidence suggests that the ENDF/B4 cross-sections used will tend to overpredict breeding ratio by 0.08. Such a reduction in breeding would reduce fissile production by $\sim$12% and, at constant fluence, appreciably reduce reactivity. Second, the effect of fission products in the fuel elements near the beryllium locations must be treated more rigorously to determine the reactivity impact more precisely.

These issues have been discussed briefly with BNL staff, who had already recognized the need for further studies on many points.

Based on the considerations noted, a realistic assessment of the concept will probably focus on determining the enrichment requirements of such a system for the initial core and the reloads. The desirability of

continuing the development will then hinge primarily on how much resource extension can be accomplished with a once-through FMSR that is licensable and that is deemed feasible with regard to material exposures.

5.2. ALTERNATE FUEL CYCLE MATERIALS

Advanced fuel designs incorporating (U,Pu)C are being developed for use in FBRs. Carbide fuels offer several advantages over the current reference $(U,Pu)O_2$ fuels, including:

1. Higher metal atom density.

2. High melting point.

3. Good thermal conductivity.

4. High burnup potential.

5. Good dimensional stability at high temperature and under irradiation (Ref. 5-8).

However, before (U,Pu)C can be considered for use in the GCFR, the following characteristics of carbide fuels need to be addressed:

1. Carbide pellet pyrophoricity and its impact on manufacturing and handling requirements.

2. Swelling under irradiation and its effect on potential fuel clad-mechanical interaction (FCMI).

3. Carburization of cladding.

4. Hydrolysis, swelling, and potential loss of thermal and mass flow conductances under leaking rod conditions.

Each of these is reviewed below along with areas requiring additional study.

5.2.1. Properties of Carbide Fuel

Potential carbide fuels for FBRs are generally composed of uranium monocarbide, UC, or uranium-plutonium monocarbide [$(U_xPu_y)C$], where $X \cong 0.75$ to 0.85 and $y \cong 0.15$ to 0.25. In addition to the monocarbide, the sesquicarbide (M_2C_3) may be present in concentrations up to ~10% (Ref 5-9). The principal reason for considering carbide fuel is the high heavy metal atom density attainable in the core compared to oxide fuels. This leads to higher breeding ratios and shorter doubling times. In addition, the high melting point of carbides and their good thermal conductivity under irradiation permit the use of larger diameter fuel rods and higher power densities. These properties likewise lead to larger breeding ratios. An additional benefit of using carbide fuel is the significantly lower fission product release that takes place during irradiation. Whereas only 5 to 10% of the fission gas is retained in mixed oxide fuels, the fraction of fission gases held in carbide fuels approaches 70 to 80% (Ref. 5-10). This comes about in part because of the lower operating temperature of carbide fuels compared to oxide temperatures. As a consequence, fuel-clad chemical interaction (FCCI) resulting from the migration of volatile fission species does not occur to any significant degree with carbide fuels (Refs. 5-2, 5-3).

Use of carbide fuels in the GCFR is not without important problems. The carbides are known to react slowly in air when in the bulk form, while the dust is pyrophoric. This can present special handling problems during fuel fabrication. Current GCFR design uses sintered and ground fuel pellets. Having to grind and maintain the pellets in an inert atmosphere at all times prior to irradiation may introduce additional complications to fuel fabrication. The use of sphere pac fuel may reduce some of the concerns associated with pyrophoric carbide dust, but special inert-atmosphere handling conditions will still be required. In addition, sphere

pac fuel results in lower attainable metal atom densities in the core and high fission product release, partly offsetting the incentive to use carbide fuels. These concerns can probably be handled with an extension of current fuel fabrication technology being developed for LMFBR carbide fuels.

Although carbide fuels show greater fission product retention than oxide fuels, carbide fuels swell more than twice as fast ($\sim$1.7% per percent burnup at $\leq$1323 K) as a function of burnup as oxide fuels (Ref. 5-11). This can lead to FCMI and potential cladding failure if fuel smear densities and cladding gaps are not properly coupled to minimize that effect. Fuel-clad mechanical interaction was an important mechanism leading to cladding breach in exploratory irradiations of carbide fuels (Ref. 5-12). However, subsequent irradiations have demonstrated that with proper selection of fuel smear density, sesquicarbide concentration, and fuel-cladding gap, FCMI will not result in significant cladding failures (Ref. 5-9). Swelling may pose more serious problems in GCFR fuel rods due to the necessity to retain flow conductance under failed rod conditions where moisture ingress can occur (see below). Lower smear densities may be required to ensure that flow conductance is not jeopardized by FCMI.

The presence of carbide fuel raises the specter of cladding carburization. Single-phase monocarbide fuels with stoichiometric ratios of heavy metal and carbon atoms and with low (<0.1%) oxygen concentration do not carburize inner cladding surfaces. However, impure monocarbides containing O_2(>0.3%) do result in inner clad carburization, apparently as a result of carbon transport in the fuel aided by the presence of oxygen. Hyper-stoichiometric fuel, i.e., that containing the sesquicarbide M_2C_3, also brings about increased carburization (Ref. 5-10). Recent irradiation results indicate that carburization can be controlled by the proper selection of monocarbide/sesquicarbide ratios and by the exclusion of oxygen-bearing impurities. It is worth noting that sesquicarbide is included to reduce fuel swelling (Ref. 5-9).

5.2.2. Carbide Fuel Hydrolysis

The single greatest uncertainty in using carbide fuel in the GCFR is the potential for hydrolysis under leaking rod conditions. Since the primary coolant in the GCFR may contain up to 100 ppm (860 Pa) water in helium under normal operating conditions, hydrolysis may occur when moisture flows into the rod and the pressure equalization system via a cladding breach. Since this is not a problem for the LMFBR, little work has been done on (U,Pu)C hydrolysis. However, studies have been performed on uranium monocarbide.

5.2.3. Thermodynamics

A variety of reactions can occur between UC and H_2O depending on the temperature (Ref. 5-13):

$$UC + 2H_2O \rightarrow UO_2 + 2H_2 + C \qquad 573\text{-}773\ K \qquad (5\text{-}1)$$

$$UC + 2H_2O \rightarrow UO_2 + CH_4 + \text{higher hydrocarbons} \qquad 783\ K \qquad (5\text{-}2)$$

$$UC + 4H_2O \rightarrow UO_2 + 4H_2 + CO_2 \qquad 973\text{-}1273\ K \qquad (5\text{-}3)$$

$$UC + 3H_2O \rightarrow UO_2 + 3H_2 + CO \qquad 1873\text{-}2773\ K \qquad (5\text{-}4)$$

All of these reactions have a large negative free energy of formation at the temperature ranges of interest, as shown in Fig. 5-1 (Refs. 5-14 through 5-16). This provides a large thermodynamic driving force favoring the formation of hydrolysis products. In addition, the equilibrium H_2/H_2O association with each of these reactions is $>10^5$, a value far in excess of the expected primary coolant H_2/H_2O ratio of 0.1 to 10.0. This implies that prevailing conditions in the primary coolant will not limit the extent of hydrolysis on thermodynamic grounds.

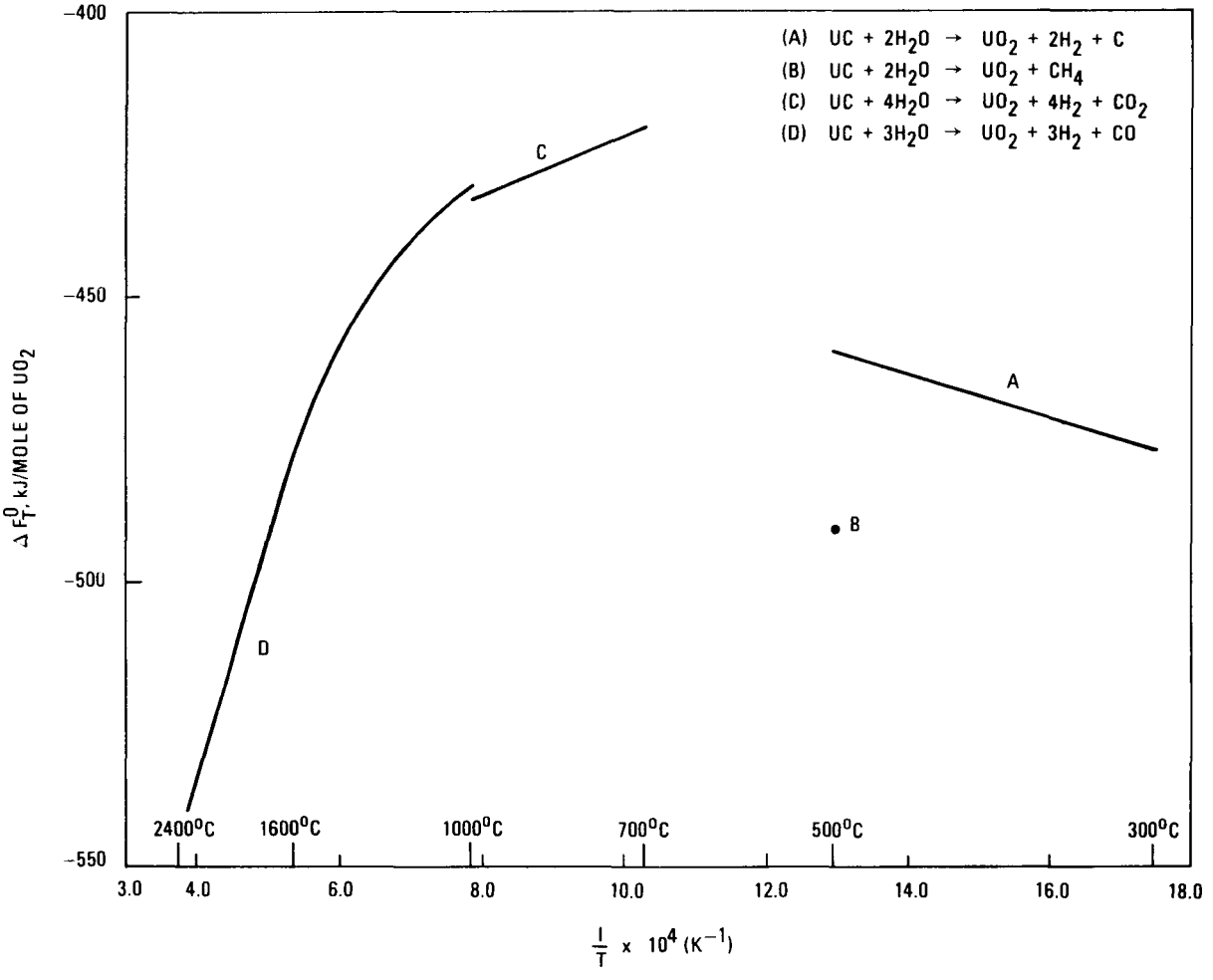

Fig. 5-1. Gibbs free energy of reaction as a function of temperature

5.2.4. Kinetics

The reactions shown in Eqs. 5-1 through 5-4 have been found to have different rate-limiting steps. The hydrolysis rate has been found to decrease with increasing temperature in the range 423 to 673 K. At 423 K, the basic chemical reactivity of uranium monocarbide and steam apparently determines the rate, with hydroxyl ions and atomic hydrogen being formed on the outer surface of the sample. At 673 K, an adherent coating of uranium dioxide is formed on the carbide surface and the reaction rate is established by diffusion of steam through the layer. Above 673 K, the hydrolysis rate increases but does not exceed the 423 K rate until ∿1273 K (Ref. 5-13).

Irradiation reduces the rate of hydrolysis at lower temperatures. At temperatures up to 673 K, samples irradiated to 17 MWd/kg showed a markedly lower reaction rate (Ref. 5-13). This effect may help reduce the rate of reaction of GCFR blanket material, which is maintained at ∿573 K. It is unknown how the rate is affected by increasing neutron fluences and burnup. Irradiation has little effect on hydrolysis rates at 973 K (Refs. 5-13, 5-17). Unirradiated and irradiated carbides react at comparable rates at 1173 K and above. These findings indicate that irradiation will have no passivating effect on the monocarbide in the fuel region of the GCFR rod.

In terms of the GCFR 3-year fuel residency time in core, the reaction rate is very rapid at all temperatures. At 573 K, unirradiated samples are over 60% reacted within 8 hr, although a significant diminution of the rate is noted after this time. Irradiated samples (17 MWd/kg) showed a significantly lower rate, being ∿1% reacted after 7 hr (Ref. 5-13). At 973 K, unirradiated and irradiated samples show reaction rates comparable to those at 573 K. At 1173 K, complete reaction of the monocarbide is approached within 10 hr. At 1873 to 2773 K, the reactions are over 50% complete within 2 to 3 min. The rate studies show significant variation from sample to sample, in part because the UO_2 coatings tend to sluff off during the reaction. Nonetheless, reaction kinetics are unlikely to be

the rate-limiting step to fuel hydrolysis during leaking rod conditions. Instead, the rate of moisture ingress through the cladding breach and the diffusion time for moisture within the rod are likely to limit reaction rates.

5.2.5. Hydrolysis Effects

The most significant problems associated with carbide hydrolysis are fuel swelling and the accompanying loads applied to the cladding (FCMI) and the loss of thermal conductivity of the fuel. No data apparently exist on the volume increases of hydrolyzed UC, but UC_2 has been found to show over a factor of two volume increase after hydrolysis (Ref. 5-18). Expansion of this order would clearly be unacceptable for GCFR fuel rods if the reaction rate were not limited prior to completion of the reaction. The possibility exists, however, that defective rods may plug as a result of hydrolysis, thereby limiting the amount of moisture that can reach the fuel. While this is a benefit in restricting hydrolysis, it also poses the potential for loss of flow conductance in the rod downstream of the cladding breach. This is clearly undesirable since it leaves open the possibility for fission gas venting from the defective rod into the primary coolant.

5.2.6. Areas Requiring Additional Study

The results summarized above indicate that UC or (U,Pu)C hydrolysis is not likely to be limited thermodynamically or kinetically under GCFR operating conditions. As such, a series of questions require additional study before carbide fuels can be considered for GCFR application.

For normal operating conditions, the international effort devoted to carbide fuel irradiations will continue to provide data for optimizing fuel configurations, fuel properties, and fuel chemistry (Ref. 5-9). The following specific questions related to the GCFR need to be addressed:

1. What are the measured release to birth fractions (R/B) of important fission gases as a function of burnup?

2. What fractions of cesium and iodine are released from the fuel as a function of burnup?

3. Will fuel swelling under dry conditions lead to FCMI and flow restrictions in the fuel region that would jeopardize pressure equalization system performance?

For leaking rod conditions, the presence of water vapor in the GCFR primary coolant requires that additional work be done to define the impact of the following considerations:

1. How much moisture can be expected to enter a leaking rod as a function of time and fuel swelling?

2. Does (U,Pu)C react with moisture in a manner analogous to UC?

3. Will hydrolysis result in unacceptable loss of thermal conductivity, fuel swelling, and cladding failures?

4. How is fission gas and volatile fission product release affected by hydrolysis?

5. How would leaking carbide fuel rods respond to moisture during low-temperature, high-moisture shutdown conditions?

6. Is contamination of the circulating reactor coolant by fissionable, powdery, hydrolyzed mixed oxide through a cladding breach a serious problem?

Answers to these questions require additional research and development on representative GCFR fuel samples.

REFERENCES

5-1. Hamilton, C. J., "A Preliminary Study of Alternate Fuel Cycles for the Gas-Cooled Fast Breeder Reactor," ERDA Report GA-A14536, General Atomic Company, August 1977.

5-2. Broido, J. H., General Atomic Company, letter to L. M. Welshans, DOE, March 13, 1978.

5-3. Broido, J. H., General Atomic Company, letter to L. M. Welshans, DOE, May 24, 1978.

5-4. "The Proliferation Resistant Preconceptual Core Design Study," Hanford Engineering Development Laboratory Report TC-1082, March 1978.

5-5. "INFCE/5 Fast Breeder Reactor Studies; Design and Performance Characteristics of Alternative Fuels and Fuel Cycles," Argonne National Laboratory Report INFCE/5 TM-3, July 1978.

5-6. Barthold, W. P., and Y. I. Chang, "Breeding Ratio and Doubling Time Definitions Used for Advanced Fuels Performance Characterization," Trans. Am. Nucl. Soc. 26, 588 (1977).

5-7. Fisher, G. J., and R. J. Cerbone, "The Fast-Mixed Spectrum Reactor Interim Report Initial Feasibility Study" (Draft), Brookhaven National Laboratory Report, December 1978.

5-8. Jones, R. W., and J. L. Crosthwaite, "Uranium Carbide Fuel for Organic Cooled Reactors," Atomic Energy of Canada Limited Report AECL-4443, 1973.

5-9. Latimer, T. W., et al., "Irradiation Performance of Helium-Bonded Uranium-Plutonium Carbide Fuel Elements," International Conference on Fast Breeder Reactor Fuel Performance, 1SBN:0-89448, 1979, p. 816.

5-10. Kleykamp, H., "The Chemical State of Irradiated Carbide Fuel Pins," Advanced LMFBR Fuels, Topical Meeting Proceedings, ERDA 4455, 1977, p. 166.

5-11. Dienst, W., et al., "Swelling, Densification and Creep of Oxide and Carbide Fuels Under Irradiation," International Conference on Fast Breeder Reactor Fuel Performance, 1SBN:0-89448, 1979, p. 166.

5-12. Simmons, J. M., et al., "The U. S. Advanced LMFBR Fuels Development Program," Advanced LMFBR Fuels, Topical Meeting Proceedings, ERDA 4455, 1977, p. 2.

5-13. Dyck, R. W., R. Taylor, and D. G. Boase, "A Study of the Hydrolysis of Uranium Monocarbide, Part 1: Reactions in Steam in the Temperature Range 150°C to 2500°C," Atomic Energy of Canada Limited Report AECL-4917, 1975.

5-14. JANAF Thermochemical Tables, Second Ed., National Bureau of Standards, NSRDS-NBS 37 (1971).

5-15. Schick, H. L., Thermodynamics of Certain Refractory Compounds, Academic Press, N. Y,. 1966, p. 2-255.

5-16. Holley, C. E., and E. K. Storms, "Actinide Carbides - A Review of Thermodynamic Properties," Thermodynamics of Nuclear Materials, Proceedings of Symposia, IAEA, 1967, p. 397.

5-17. Flanary, J. R., et al., "Hot Cell Studies of Aqueous Dissolution Processes for Irradiated Carbide Reactor Fuels," Oak Ridge National Laboratory Report ORNL-3660, 1964.

5-18. "HTGR Fuels and Core Development Development Program Quarterly Progress Report for the Period Ending May 31, 1975," ERDA Report GA-A13444, General Atomic Company, May 31, 1975.

APPENDIX A

HELIUM PRODUCTION CROSS SECTIONS

TABLE A-1
SPECTRAL AVERAGED CROSS SECTIONS FOR EVALUATING HELIUM PRODUCTION
AND DISPLACEMENT PER ATOM AT INNER SURFACE
OF CORE RESTRAINT CYLINDER

Spectral Averaged Cross Section (barns)	Cases					
	1	2	3	4	5	6
Composite stainless steel threshold (n,α)	2.64-6	1.74-5	1.36-5	2.59-6	1.81-6	2.30-6
$Ni^{58}(n,\gamma)Ni^{59}$	0.0331	0.0228	0.0245	0.0246	0.0633	0.0333
$Ni^{59}(n,\gamma)Ni^{60}$	4.25	1.78	2.72	2.02	6.53	4.28
$Ni^{59}(n,\alpha)Fe^{56}$	0.757	0.313	0.485	0.356	1.15	0.762
$B^{10}(n,\alpha)Li^{7}$	17.9	7.32	9.29	7.97	44.7	18.1

TABLE A-2
SPECTRAL AVERAGED CROSS SECTIONS FOR EVALUATING HELIUM PRODUCTION
AND DISPLACEMENT PER ATOM AT INNER SURFACE OF
OUTER RADIAL SHIELD

Spectral Averaged Cross Section (barns)	Cases					
	1	2	3	4	5	6
Composite stainless steel threshold (n,α)	1.80-6	1.10-5	9.57-6	1.79-6	1.40-6	1.57-6
$Ni^{58}(n,\gamma)Ni^{59}$	0.0321	0.0252	0.0271	0.0269	0.0516	0.0323
$Ni^{59}(n,\gamma)Ni^{60}$	3.95	3.08	3.79	3.18	5.44	3.97
$Ni^{59}(n,\alpha)Fe^{56}$	0.702	0.550	0.679	0.567	0.959	0.706
$B^{10}(n,\alpha)Li^{7}$	17.0	10.5	12.3	10.9	34.2	17.1

APPENDIX B
SHIELDING MATERIAL SPECIFICATIONS

LOWER PLENUM 316 STAINLESS STEEL

General characteristics: Annealed 316 stainless steel per ASME Specifications SA=182 neglecting trace elements [see Nuclear Systems Material Handbook (NSMH) Part I, Group I, Section 4, Property Code 1100].

Density: 8.0271 g/cm^3

Average chemical composition (wt %): Fe (66.5), Cr (17.0), Ni (12.0), Mo (2.5), Mn (2.0).

Nuclide densities [atoms/(barn-cm)]:

$Fe = 5.7570 \times 10^{-2}$
$Cr = 1.3699 \times 10^{-2}$
$Ni = 9.8819 \times 10^{-3}$
$Mo = 1.2602 \times 10^{-3}$
$Mn = 1.7601 \times 10^{-3}$

SHIELDING GRAPHITE

General characteristics: Grade H-451, extruded near-isotropic graphite produced by Great Lakes Carbon Co.

Mean bulk density: 1.76 g/cm^3

Nuclide density: $C = 8.8255 \times 10^{-2}$ atoms/(barn-cm)

SHIELDING BORONATED GRAPHITE

General characteristics: 25 wt % natural boron in a near-isotropic graphite matrix.

Bulk density: 1.6 g/cm^3

Nuclide densities [atoms/(barn-cm)]:

B (natural) = 2.2287×10^{-2} (19.8 at. % B-10)
C = 6.0174×10^{-2}

SHIELDING BORON CARBIDE

General characteristics: Boron carbide granules, with 19.8 at. % B-10 content, dispersed in a graphite matrix neglecting trace impurities.

Density: 2.38 g/cm^3 (95% theoretical density)

Nuclide densities [atoms/barn-cm)]:

B-10 = 2.0596×10^{-2}
B-11 = 8.3224×10^{-2}
C = 2.5943×10^{-2}